Bridge between Transcriptomics and Histopathology: Seq-Scope Reveals Molecular Pathologies Underlying Muscle Degeneration

by

Jer-En Hsu

A dissertation submitted in partial fulfillment
of the requirements for the degree of
Doctor of Philosophy
(Molecular and Integrative Physiology)
in the University of Michigan
2026

Doctoral Committee:

Professor Jun Hee Lee, Chair
Professor Hyun Min Kang
Professor Liangyou Rui
Professor Yatrik Shah

Jer-En Hsu

jerenhsu@umich.edu

ORCID iD: 0000-0002-2968-1853

© Jer-En Hsu 2026

Dedication

I would like to dedicate this dissertation to my mother, Jane Lu, who encouraged me to begin this journey and supported me along the way.

Acknowledgements

Flashing back on this six-year journey has just made me realize how fortunate I am to be standing at this moment. I will be forever thankful for the support of everyone along the way. First and foremost, I would like to thank my mentor, Jun Hee Lee, who took me in without any hesitation while knowing that I was barely out of undergrad. You saw my potential and pushed me hard, sometimes even drove me crazy, but now, looking back at what we built together, everything was worth it. As a foreigner in this country and society, thank you for making the working environment encouraging, motivating, and still warm, and thank you for shaping me into a true scholar. I also want to thank Susan Brooks, who has been a co-mentor to me throughout the whole time. It has always been your kind words and knowledgeable suggestions that have pushed and pulled the muscle projects, and me, forward.

Next, I want to thank all of my dissertation committee members, Hyun Min Kang, Yatrik Shah, Liangyou Rui, and Ling Qi. I know we only met once in a while, and that my projects changed constantly (pretty much a whole new project every year), but I still thank you for attending and for sharing your valuable insights. A year ago in the meeting, it was your encouragement that made me realize my dissertation was achievable, and that I was already almost there.

I also want to thank all the present and past members of Lee Lab, Kang Lab, and our collaboration teams, who have constantly been bombarded by my questions. I want to thank Chun-Seok Cho, Yongsung Kim, and Myungjin Kim for your patient and wise guidance in experiments and in life. They will always be good memories for me. I want to thank my lab-mate/gym-mate, Angelo Anacleto, for bringing the energy to the lab. I enjoyed every moment chatting with you about baseball in the lab while Jun Hee thought we were having serious scientific debates. I wish you all the best with your academic journey. I want to thank Qingyang Zhao for completing all the tasks I asked for. I am truly appreciative of your contribution to my projects, and I wish you a bright future ahead. Yichen Si, Weiqui Cheng, and Yongha Hwang, you guys are my lifesavers. If it were not for you, I wouldn't be able to do a single computational

analysis that I now perform on a daily basis. Thank you for answering my ignorant questions and unreasonable requests in coding whenever and wherever you were. Lloyd Ruiz, Steve Guzman, and Peter Macpherson, thank you for always saying yes to helping me collect the muscle samples. It is an honor for me to share my accomplishments in the muscle field with you. For the rest of the members, I apologize for my lack of words. I will be forever grateful to have known and worked with each and every single one of you during this journey.

I want to thank the Department of Molecular and Integrative Physiology and my cohort. It was you who gave me the opportunity (through a slightly unconventional route in the first place) to let me be who I am now. I am forever appreciative of it. Thank you, Dan Michele, for the support from the very beginning to the very end, from lending a poor student his first dinner table set to writing a supporting letter to help that student find his first job. Thank you, Michele Boggs, for your patience in working through the tedious paperwork for me year after year, with your always-lighthearted spirit. Quoc Huynh, Garrett Chavis, Jessica Maung (and David), and LeeAnn Flowers (and Steph), it is so nice to be in the same cohort with you. I will remember all the nights out with you.

I also want to express my gratitude to all my friends who support me, wherever you are around the world. Tzi-Li Liu, Yun-Chung Hsiao, Hua-Yi Lee, and Tung-Che Hsieh, it is my life fortune to be friends with you. You are always there through the ups and downs, and I thank you from the bottom of my heart. I want to honorably mention Yun-Chung (as he strongly demanded) for keeping our regular gaming time. It has been a great stress reliever along this frustrating and never-ending PhD journey. Thank you, my NCRB badminton people. Playing badminton with you every Monday and Wednesday for six years has been one of the best parts of my life outside of lab (shout-out to Dr. Grant for giving me a new ACL and the chance to walk onto the court again).

Last but not least, I want to thank and express my love to my family. Thank you, Mom. I have always been the most troublesome child, but you supported my dream every step of the way, without a moment of doubt. I am proud to be your son, and I hope I make you proud. Dad, thank you for trying to stay in my life. I love you no matter what. Cherie and Jeffrey, thank you for being such considerate siblings. We are scattered around the world, yet we still manage to find each other from time to time. These wonderful memories will forever stay with me. Finally,

thank you, Chun-Chen and Aunt Chiu. Thank you for always being there for me. I would never be able to achieve this without you.

Table of Contents

Dedication ii

Acknowledgements iii

List of Figures ix

Abstract xii

Introduction 1

Chapter 1 Seq-Scope Technology and Applications: Repurposing Illumina Sequencing Flow Cells for Microscopic Spatial Transcriptomics 7

1.1 Abstract 7

1.2 Introduction 8

1.3 Results 10

1.3.1 Seq-Scope technology overview - experimental 10

1.3.2 Seq-Scope technology overview - computational 14

1.3.3 HDMI-array captures spatial RNA footprint of tissues 17

1.3.4 Seq-Scope captures transcriptome information with high efficiency 20

1.3.5 Seq-Scope reveals nuclear-cytoplasmic transcriptome architecture from tissue sections 22

1.3.6 Seq-Scope pathophysiological applications 24

1.4 Discussion 44

1.5 Methods 47

1.6 References 51

Chapter 2 High-Resolution Spatial Transcriptomic Atlas of Mouse Soleus Muscle: Unveiling Single-Cell and Subcellular Heterogeneity in Health and Denervation 58

2.1 Abstract 58

2.2 Introduction 58

2.3 Results 61

2.3.1 Overview of the experiments and dataset 61

2.3.2 Single-myofiber transcriptome analysis of normal muscle 67

2.3.3 Subcellular anatomy of the hybrid myofiber transcriptome 67

2.3.4 Identification of neuromuscular junction (NMJ) transcriptome 72

2.3.5 Spatial resolution of postsynaptic and schwann cell-associated NMJ domains 72

2.3.6 Distinct transcriptomic programs within the NMJ microenvironment 73

2.3.7 Characterization of non-myocytes in the Seq-Scope dataset 76

2.3.8 Fiber type-specific responses to denervation 78

2.3.9 Subcellular heterogeneity in denervation responses 79

2.3.10 Denervation preserves postsynaptic NMJ identity while inducing extrajunctional acetylcholine receptors 83

2.3.11 Denervation elicits robust extracellular matrix remodeling in the perisynaptic NMJ microenvironment 84

2.3.12 Non-myocyte responses to denervation 87

2.4 Discussion 90

2.5 Methods 92

2.6 References 96

Chapter 3 Histopathology and Spatial Transcriptomics Jointly Map Myofiber-specific Pathological Programs in mTORC1-driven Myopathy 102

3.1 Abstract 102

3.2 Introduction 103

3.3 Results 105

3.3.1 Seq-Scope enables combined analysis of histopathology and single-myofiber transcriptomics 105

3.3.2 Identification of fiber type-specific responses to mTORC1 hyperactivation 110

3.3.3 Distinct mTORC1-driven adaptations of type IIx myofibers in different muscles 115

3.3.4 Type IIx myofibers in Soleus undergo hypertrophy with structural remodeling... 120

3.3.5 Central nuclei are prevalent across various types of myofibers 121

3.3.6 Basophilic fibers activate lipid and oxidative metabolism to sustain elevated RNA synthesis 127

3.3.7 Stress-induced reprogramming of type IIb fibers in EDL reveals transcriptional adaptability 132

3.3.8 mTORC1 hyperactivation drives macrophage–fibroblast accumulation in soleus muscle 138

3.4 Discussion 141

3.5 Methods 144

3.6 References 149

Chapter 4 Conclusions and Future Directions 154

4.1 Summary 154

4.2 The future of Seq-Scope: beyond spatial transcriptomics 154

4.3 Muscle atlas and muscular microenvironments 156

4.4 mTORC1 hyperactivation-driven myopathies 157

4.5 Perspectives 157

4.6 References 158

List of Figures

Figure 1.1 Seq-Scope experimental procedure – Part 1 12

Figure 1.2 Seq-Scope experimental procedure – Parts 2 & 3 13

Figure 1.3 Seq-Scope computational procedure 16

Figure 1.4 HDMI-array captures spatial RNA footprint of tissues 18

Figure 1.5 Seq-Scope has an outstanding transcriptome capture performance 19

Figure 1.6 Seq-Scope captures transcriptome information with high efficiency 21

Figure 1.7 Seq-Scope visualizes subcellular spatial transcriptome 23

Figure 1.8 TREM2 macrophages are recruited to lesion hair follicle 25

Figure 1.9 Seq-Scope enables single-cell spatial transcriptome analysis in p21-Cre mouse liver 27

Figure 1.10 Identification of liver zonation and immune cell infiltration in aged liver 29

Figure 1.11 Cell-type landscape of p21-Cre aged mouse liver 30

Figure 1.12 p21-Cre fluorescence guides cell-type assignment of senescent cells 32

Figure 1.13 Senescence emerges in parallel across multiple liver lineages in aged liver 33

Figure 1.14 Distinct SASP programs reveal heterogeneity among p21-expressing senescent cells 35

Figure 1.15 Cell types exhibit distinct transcriptome profiles within the senescent niche 38

Figure 1.16 Senescence undergoes transcriptional shifts across distinct stages 41

Figure 1.17 Interferon-stimulated gene activation in aging is independent of p21 status 43

Figure 2.1 High-resolution spatial transcriptomic analysis of mouse soleus muscle in healthy and denervated conditions 64

Figure 2.2 Transcriptome-based identification of cell types from Seq-Scope data 65

Figure 2.3 Data integration identifies canonical myofiber types and major muscle cell populations 66

Figure 2.4 Single-myofiber transcriptome analysis of normal muscle 69

Figure 2.5 Fiber type-specific gene expression in single-segmented myofibers 70

Figure 2.6 Characterization of myofiber type transcriptomes using hexagonal grid analysis 71

Figure 2.7 High-resolution spatial profiling of neuromuscular junction-associated transcriptomes 74

Figure 2.8 Expression of distinct marker genes in the neuromuscular junction region 75

Figure 2.9 Non-myocyte transcriptomic heterogeneity revealed in the Seq-Scope dataset 77

Figure 2.10 Heterogeneous transcriptome responses to denervation in single myofibers 81

Figure 2.11 Fiber type-specific denervation responses 82

Figure 2.12 Denervation-induced changes in the neuromuscular junction region 85

Figure 2.13 Neuromuscular junction responses to denervation 86

Figure 2.14 Denervation responses in non-myocytes 89

Figure 3.1 Seq-Scope enables histopathology-guided single-myofiber transcriptome analysis. 107

Figure 3.2 mTORC1 hyperactivation-induced muscular pathologies 108

Figure 3.3 Stratification of single-myofiber transcriptome into classical myofiber types 109

Figure 3.4 Identification of fiber type-specific responses to mTORC1 hyperactivation 112

Figure 3.5 Functional analysis of fiber type-specific responses to mTORC1 hyperactivation .. 113

Figure 3.6 Validation of fiber type-specific and global gene expression comparisons 114

Figure 3.7 Distinct hyperactive mTORC1 responses of type IIx myofibers in different muscles 117

Figure 3.8 Systematic revelation of distinct responses from type IIx myofibers in different muscles 118

Figure 3.9 Validation of MF2X fiber responses under mTORC1 hyperactivation 119

Figure 3.10 Type IIx myofibers in Soleus undergo hypertrophy with structural remodeling 123

Figure 3.11 Schematic of soleus Type IIx hypertrophy with structural remodeling 124

Figure 3.12 Transcriptomic characteristics of pathological features in myofiber enlargement . 125

Figure 3.13 Transcriptomic characteristics of pathological features in central nuclei 126

Figure 3.14 EDL myofiber type IIx develops basophilia with high RNA content 129

Figure 3.15 Basophilic fibers activate lipid and oxidative metabolism to sustain elevated RNA synthesis 130

Figure 3.16 Supporting data for oxidative metabolism and RNA synthesis in basophilic fibers 131

Figure 3.17 Type IIb fibers in EDL exhibit three distinct stress adaptation states without gross morphological alterations 134

Figure 3.18 Overview of distinct stress adaptation states in EDL Type IIb fibers 135

Figure 3.19 Diversification of MF2B responses to mTORC1 hyperactivation 136

Figure 3.20 Expression of genes in MF2B subtypes in response to mTORC1 hyperactivation 137

Figure 3.21 mTORC1 hyperactivation drives macrophage-fibroblast accumulation in SOL muscle 139

Figure 3.22 Hexagonal grid analyses of non-myocyte populations 140

Abstract

Traditional molecular biology approaches have defined many of the cellular pathways that govern tissue development, homeostasis, and disease. With continued technological advances, *omics* approaches ("measuring at a system-wide scale") have emerged, aiming to resolve biological questions comprehensively and efficiently. Among the omics worlds, transcriptomics is the field studying RNA expression systematically, bridging the information stored in genomics to the action carried out in proteomics. To fill the gap in our understanding of cellular heterogeneity hidden beneath the histological architecture, spatial transcriptomics (ST) was further developed to map captured transcripts to their *in situ* spatial coordinates. Here, we present the methodology and the applications of a cutting-edge ST, Seq-Scope, with near-optical microscopic resolution and whole-transcriptome coverage. Seq-Scope leverages solid-phase amplification of randomly barcoded oligonucleotides on Illumina sequencing platforms to generate spatially indexed clusters that function as RNA-capturing arrays with probes spaced approximately 0.5 to 0.8 μm apart. This technology not only achieves comparatively high RNA capture efficiency relative to currently available ST platforms but also maintains sub-micrometer resolution, enabling digital delineation of intercellular compartments. The technical upgrade from MiSeq to HiSeq and NovaSeq platforms was described with a substantial expansion of imaging area up to 7 mm x 7 mm, together with additional implementations such as multi-round on-array imaging, DAPI-based spatial single-cell segmentation, and fluorescence-guided spatial mapping.

This thesis then applies Seq-Scope to skeletal muscle, an organ that exhibits pronounced cellular and subcellular heterogeneity. A high-resolution spatial transcriptomic atlas of mouse soleus muscle was built in longitudinal sections. Combining histology-guided myofiber segmentation with unbiased grid-based mapping, we recovered canonical fiber types and revealed widespread hybrid myofiber states *in situ*. At the subcellular scale, we delineated the neuromuscular junction (NMJ) as a multi-compartment niche containing postsynaptic myonuclei and spatially distinct peri-synaptic and myelinating Schwann cell-associated regions, each with

characteristic gene programs. Applying this framework to denervation (3 and 7 days) identified robust fiber-type-specific stress responses, coordinated remodeling of macrophage and fibroblast transcriptomes, marked intramyofiber heterogeneity, and distinct transcriptional domains associated with the NMJ.

Seq-Scope's ability to link histopathology to molecular states at single-fiber resolution was further demonstrated in a rodent model of sustained mTORC1 hyperactivation. The results showed that mTORC1-driven pathology was strongly fiber-type dependent. Type I and IIa fibers exhibited relative resistance, while type IIx fibers diverged into distinct fates across muscles, including hypertrophic growth programs with impaired proteostasis in soleus and basophilic states supported by lipid-driven respiration and RNA accumulation in extensor digitorum longus. In parallel, type IIb fibers displayed pronounced intra-muscle heterogeneity spanning stress responses, oxidative metabolic activation, and developmental reprogramming.

Together, this thesis establishes Seq-Scope as a flexible, scalable, high-resolution spatial transcriptomics platform and demonstrates its ability to bridge histological architecture to genome-wide molecular programs. By applying Seq-Scope to inflammatory skin disease, senescence-associated niches, and muscle biology and pathology, this work provides a framework for resolving how gene regulation is organized within cells, across cells, and across tissue microenvironments in health and disease.

Introduction

Gene regulation lies at the core of physiology. The selective activation and repression of genes enable cells with an identical genome to perform distinct functions, sustain tissue homeostasis, and adapt to changing internal and external conditions (1,2). In development, gene regulatory programs drive cell fate specification and tissue organization (3). In adult tissues, they preserve functional identity while allowing flexible responses to stress, injury, and metabolic demand (1). When these regulatory mechanisms become altered, physiological balance can shift toward dysfunction and disease.

Skeletal muscle represents a highly organized and physiologically essential tissue in which gene regulation is fundamental to the maintenance of function and adaptability. As the main tissue driving movement, skeletal muscle also contributes to posture, whole-body metabolism, and energy homeostasis (4,5). These functions depend on substantial cellular and functional heterogeneity within the tissue. Myofibers are classified into distinct fiber types that differ in contractile speed, fatigue resistance, and metabolic preference, including type I, IIa, IIx, and IIb fibers, as defined by their physiological properties and myosin heavy chain isoform expression (6). Different muscle groups contain these fiber types in different proportions, reflecting their specialized physiological roles. Muscles involved in sustained postural activity are generally enriched in slow oxidative fibers, whereas muscles adapted for rapid and forceful movement contain a greater proportion of fast glycolytic fibers (6). In addition to myofibers, skeletal muscle contains multiple non-myocyte populations, including satellite cells, fibroblasts, immune cells, and endothelial cells, each of which contributes to tissue maintenance, remodeling, and adaptation to physiological demand (7). Together, these features establish skeletal muscle as a dynamic and heterogeneous system in which tightly controlled gene regulatory programs are essential, highlighting the need for technologies that can unravel gene expression within its native histological context.

Spatial transcriptomics (ST) technologies aim to advance gene expression studies by profiling the entire transcriptome while preserving spatial information from a single histological

section (8). ST emerged from earlier in situ hybridization methods, such as fluorescence in situ hybridization (FISH) (9), single-molecule fluorescence in situ hybridization (smFISH) (10), RNA in situ hybridization assay (RNAscope) (11), sequential fluorescence in situ hybridization (seqFISH) (12), and multiplexed error-robust fluorescence in situ hybridization (MERFISH) (13), which localized a limited number of transcripts directly within tissue, as well as from sequencing-based approaches, including Illumina next-generation sequencing (14) and single-cell RNA sequencing (15,16), which enabled broader transcriptome-wide analysis. By integrating the strengths of these approaches, ST was developed to bridge molecular profiling with tissue architecture. By assigning RNA molecules or captured transcripts back to their original positions in the tissue, ST makes it possible to study gene expression while preserving the spatial relationships among cells, structures, and microenvironments (8).

The emergence of sequencing-based spatial transcriptomics (ST) platforms began in 2016 with the development of barcoded mRNA-capturing spots arranged on an array chip at 100 μm resolution, enabling transcriptome-wide visualization across tissue sections (17). This design was later commercialized as 10x Genomics Visium, which improved usability while reducing spot size to 55 μm. Subsequent platforms pushed spatial resolution closer to the cellular scale, including Slide-seq (18) and Slide-seqV2 (19) at approximately 10 μm, High-Definition Spatial Transcriptomics (HDST) (20) at approximately 2 μm, and Stereo-seq (21) at sub-micrometer resolution. Despite the rapid expansion of ST technologies, their broad adoption has remained limited by low spatial resolution, restricted transcript capture, complex procedures, limited scalability, and the high cost of platform setup or individual experiments. These limitations highlight the need for platforms that provide substantially improved spatial precision for resolving tissue architecture at true single-cell and subcellular levels, while also offering a more cost-efficient and accessible workflow for general use.

In this thesis, we report Seq-Scope, a spatial barcoding technology with a resolution almost comparable to an optical microscope (22,23). Seq-Scope is based on solid-phase amplification of randomly barcoded single-molecule oligonucleotides using an Illumina sequencing platform, which is accessible to most researchers. These RNA-capturing barcoded clusters define the pixels of Seq-Scope that are approximately 0.5-0.8 μm apart from each other. We describe the preparation of a fresh frozen tissue section for both histological imaging and sequencing library preparation and provide a streamlined computational pipeline with

comprehensive instructions to integrate histological and transcriptomic data for high-resolution spatial analysis. This includes the use of conventional software tools for single-cell and spatial analysis, as well as our recently developed segmentation-free method for analyzing spatial data at sub-micrometer resolution. Aside from array production and sequencing, which can be done in batches, tissue processing, library preparation, and running the computational pipeline can be completed within three days by researchers with experience in molecular biology, histology, and basic Unix skills. Over time, we have upgraded Seq-Scope from its original MiSeq flow cell platform to HiSeq 2000 and, most recently, to NovaSeq 6000, enabling the profiling of multiple tissue sections over areas of 7 mm × 7 mm or larger. The workflow has also been advanced through enhancements such as multi-round on-array imaging and fluorescence-guided spatial mapping, establishing Seq-Scope as a valuable tool for researchers in molecular biology and histology.

In this thesis, Seq-Scope was applied to profile skeletal muscle under both physiological and perturbation conditions, revealing spatially resolved features of muscle organization and adaptation that were previously difficult to capture. In one study, we mapped skeletal muscle and its response to denervation along the longitudinal axis of myofibers. This analysis provided high-resolution views of neuromuscular junction architecture and uncovered substantial heterogeneity in how individual myofibers respond to loss of neural input. It also revealed dynamic transcriptional changes in both myofibers and surrounding non-myocyte populations, highlighting coordinated cellular responses during muscle remodeling. Together, these findings demonstrate the value of spatial transcriptomics for resolving the complex cellular interactions that underlie muscle homeostasis and injury responses.

In a second study, we used Seq-Scope to investigate skeletal muscle pathology driven by sustained mammalian target of rapamycin complex 1 (mTORC1) hyperactivation, a condition that can arise naturally during aging and is associated with progressive myopathy marked by fiber degeneration, metabolic stress, impaired proteostasis, and loss of regenerative capacity (24). By profiling distinct muscle groups with different fiber-type compositions, we found that mTORC1 activation induces both shared stress responses and muscle- or fiber-specific remodeling programs. These analyses revealed marked plasticity among myofibers, including divergent responses in the same fiber type across different muscle contexts and shifts away from canonical metabolic identities under pathological conditions. In addition, histopathological

features such as myofiber enlargement and basophilia were linked to distinct transcriptional states. Overall, this work establishes a spatial, single-fiber framework for understanding how pathological signaling reshapes muscle organization and function, and provides novel insights into the molecular basis of myofiber-specific disease progression.

References

1. Buszczak M, Signer RAJ, Morrison SJ. Cellular differences in protein synthesis regulate tissue homeostasis. Cell. 2014;159(2):242–51.

2. Carthew RW. Gene Regulation and Cellular Metabolism: An Essential Partnership. Trends Genet. 2021;37(4):389–400.

3. Lokken AA, Ralston A. The Genetic Regulation of Cell Fate During Preimplantation Mouse Development. Curr Top Dev Biol. 2016;120:173–202.

4. Mukund K, Subramaniam S. Skeletal muscle: A review of molecular structure and function, in health and disease. Wiley Interdiscip Rev Syst Biol Med. 2020;12(1):e1462.

5. Argilés JM, Campos N, Lopez-Pedrosa JM, Rueda R, Rodriguez-Mañas L. Skeletal Muscle Regulates Metabolism via Interorgan Crosstalk: Roles in Health and Disease. J Am Med Dir Assoc. 2016;17(9):789–96.

6. Schiaffino S, Reggiani C. Fiber types in mammalian skeletal muscles. Physiol Rev. 2011;91(4):1447–531.

7. Yin H, Price F, Rudnicki MA. Satellite cells and the muscle stem cell niche. Physiol Rev. 2013;93(1):23–67.

8. Moses L, Pachter L. Museum of spatial transcriptomics. Nat Methods. 2022;19(5):534–46.

9. Pinkel D, Straume T, Gray JW. Cytogenetic analysis using quantitative, high-sensitivity, fluorescence hybridization. Proc Natl Acad Sci U S A. 1986;83(9):2934–8.

10. Raj A, van den Bogaard P, Rifkin SA, van Oudenaarden A, Tyagi S. Imaging individual mRNA molecules using multiple singly labeled probes. Nat Methods. 2008;5(10):877–9.

11. Wang F, Flanagan J, Su N, Wang LC, Bui S, Nielson A, et al. RNAscope: a novel in situ RNA analysis platform for formalin-fixed, paraffin-embedded tissues. J Mol Diagn. 2012;14(1):22–9.

12. Lubeck E, Coskun AF, Zhiyentayev T, Ahmad M, Cai L. Single-cell in situ RNA profiling by sequential hybridization. Nat Methods. 2014;11(4):360–1.

13. Chen KH, Boettiger AN, Moffitt JR, Wang S, Zhuang X. Spatially resolved, highly multiplexed RNA profiling in single cells. Science. 2015;348(6233):aaa6090.

14. Bentley DR, Balasubramanian S, Swerdlow HP, Smith GP, Milton J, Brown CG, et al. Accurate whole human genome sequencing using reversible terminator chemistry. Nature. 2008;456(7218):53–9.

15. Tang F, Barbacioru C, Wang Y, Nordman E, Lee C, Xu N, et al. mRNA-Seq whole-transcriptome analysis of a single cell. Nat Methods. 2009;6(5):377–82.

16. Hwang B, Lee JH, Bang D. Single-cell RNA sequencing technologies and bioinformatics pipelines. Exp Mol Med. 2018;50(8):1–14.

17. Ståhl PL, Salmén F, Vickovic S, Lundmark A, Navarro JF, Magnusson J, et al. Visualization and analysis of gene expression in tissue sections by spatial transcriptomics. Science. 2016;353(6294):78–82.

18. Rodriques SG, Stickels RR, Goeva A, Martin CA, Murray E, Vanderburg CR, et al. Slide-seq: A scalable technology for measuring genome-wide expression at high spatial resolution. Science. 2019;363(6434):1463–7.

19. Stickels RR, Murray E, Kumar P, Li J, Marshall JL, Di Bella DJ, et al. Highly sensitive spatial transcriptomics at near-cellular resolution with Slide-seqV2. Nat Biotechnol. 2021;39(3):313–9

20. Vickovic S, Eraslan G, Salmén F, Klughammer J, Stenbeck L, Schapiro D, et al. High-definition spatial transcriptomics for in situ tissue profiling. Nat Methods. 2019;16(10):987–90.

21. Chen A, Liao S, Cheng M, Ma K, Wu L, Lai Y, et al. Spatiotemporal transcriptomic atlas of mouse organogenesis using DNA nanoball-patterned arrays. Cell. 2022;185(10):1777-1792.e21.

22. Cho CS, Xi J, Si Y, Park SR, Hsu JE, Kim M, et al. Microscopic examination of spatial transcriptome using Seq-Scope. Cell. 2021;184(13):3559-3572.e22.

23. Kim Y, Cheng W, Cho CS, Hwang Y, Si Y, Park A, et al. Seq-Scope: repurposing Illumina sequencing flow cells for high-resolution spatial transcriptomics. Nat Protoc. 2025;20(3):643–89.

24. Castets P, Lin S, Rion N, Di Fulvio S, Romanino K, Guridi M, et al. Sustained activation of mTORC1 in skeletal muscle inhibits constitutive and starvation-induced autophagy and causes a severe, late-onset myopathy. Cell Metab. 2013;17(5):731–44.

Chapter 1 Seq-Scope Technology and Applications: Repurposing Illumina Sequencing Flow Cells for Microscopic Spatial Transcriptomics

1.1 Abstract

Spatial transcriptomics (ST) technologies aim to advance gene expression studies by profiling the entire transcriptome with intact spatial information from a single histological slide. However, the application of ST is limited by low resolution, limited transcript coverage, complex procedures, poor scalability, and high costs of initial setup and/or individual experiments. Here we report Seq-Scope, a spatial barcoding technology with a resolution almost comparable to an optical microscope. Seq-Scope is based on a solid-phase amplification of randomly barcoded single-molecule oligonucleotides using an Illumina sequencing platform. The resulting clusters annotated with spatial coordinates are processed to expose RNA-capture moiety. These RNA-capturing barcoded clusters define the pixels of Seq-Scope that are approximately 0.5-0.8 μm apart from each other. We describe the preparation of a fresh frozen tissue section for both histological imaging and sequencing library preparation and provide a streamlined computational pipeline with comprehensive instructions to integrate histological and transcriptomic data for high-resolution spatial analysis. This includes the use of conventional software tools for single-cell and spatial analysis, as well as our recently developed segmentation-free method for analyzing spatial data at sub-micrometer resolution. Aside from array production and sequencing, which can be done in batches, tissue processing, library preparation, and running the computational pipeline can be completed within three days by researchers with experience in molecular biology, histology, and basic Unix skills. Over time, we have upgraded Seq-Scope from its original MiSeq flow cell platform to HiSeq 2000 and, most recently, to NovaSeq 6000, enabling the profiling of multiple tissue sections over areas of 7 mm × 7 mm or larger. The workflow has also been advanced through enhancements such as multi-round on-array imaging and fluorescence-guided spatial mapping. Applied to diverse tissue sections, Seq-Scope resolves spatial transcriptome heterogeneity across multiple histological scales, capturing subcellular nuclear and cytoplasmic architectures, distinguishing macrophage subtypes and their roles in

acne-associated pathology, and revealing complex regulatory programs within senescent niches. Given its adaptability across various biological tissues, Seq-Scope establishes itself as an invaluable tool for researchers in molecular biology and histology.

1.2 Introduction

Conventional histology, employing methods such as immunohistochemistry and RNA in situ hybridization, is limited to detecting only a few specific molecular entities on a tissue slide. As a result, the information acquired from one experimental run is restricted, likely missing crucial biological details.

To address these challenges, the emerging field of spatial transcriptomics (ST) aims to analyze the entire transcriptome from a single histological slide. However, existing ST technologies face significant challenges due to their low resolution or limited capacity for high-throughput analysis. For example, the widely used Visium platform from 10x Genomics, based on the original ST technology (1), offers a resolution of 100 μm (2), which falls below the 40 μm resolution discernible by the naked human eye. Although newer methods employing microbead arrays or microfluidics (3–5) have enhanced resolution to approximately 10–20 μm, they have yet to match the precision of traditional optical microscopy. High-resolution techniques, such as sequential in situ hybridization and in situ sequencing, are available on commercial ST platforms, including 10x Xenium (6), Nanostring CosMx (7), and Vizgen MERSCOPE (8). However, these approaches involve extensive staining and imaging and require intensive computational image analysis, limiting the number of genes that can be analyzed simultaneously within a practical time frame and budget. Such constraints on the number of target genes per project likely restrict research focus and introduce bias, potentially impeding access to crucial biological insights that would otherwise be accessible with a more comprehensive approach.

Single cell RNA-sequencing (scRNA-seq) is an unbiased approach that comprehensively examines transcriptomic heterogeneity across individual cells (9). However, due to the nature of tissue dissociation and single-cell isolation, all current scRNA-seq methods have clear limitations. First, scRNA-seq omits many labile cell types that lyse during tissue dissociation and cell sorting. Second, extensive tissue dissociation and cell sorting procedures cause physical and chemical stresses that may elicit stress responses in cells and thus alter their transcriptomes. Large cells such as myofibers and lipid-laden cells such as adipocytes are not amenable for cell

sorting by microfluidics or microwells. Finally, and most obviously, scRNA-seq eliminates the spatial information of single cells in the histological space, resulting in loss of important biological information, such as tissue zonation niches and cell-cell interactions.

Therefore, improving the resolution, throughput, and scalability of ST is crucial for overcoming the limitations of currently available ST and scRNA-seq technologies. Recently, we developed Seq-Scope (10), which represents the first published high-resolution ST method capable of providing sub-micrometer resolution (0.5–0.7 μm on average), while monitoring the whole transcriptome at the sequence level. This enables single-cell and even subcellular analysis and represents a dramatic improvement in spatial resolution. For instance, the spatial throughput (spatial units per area) of Seq-Scope is over 10,000 times higher than that of conventional 10x Visium (with a 100 μm resolution) and 4–8 times higher than that of the new 10x Visium HD platform (released in January 2024, with a 2 μm resolution (11)).

Seq-Scope utilizes Illumina sequencing platforms, repurposing their flow cells into high-resolution spatially barcoded arrays. Publication of our method (10) was followed by several papers employing similar approaches utilizing independent sequencing platforms, such as DNA Nanoball (DNB) sequencing (12) and a custom polony sequencing platform (13) that can also provide resolutions similar to Seq-Scope. However, Seq-Scope's unique characteristics and capabilities, outlined below, make it especially useful and accessible for investigators seeking to utilize high-resolution spatial techniques.

The Seq-Scope protocol was developed by building upon existing scRNA-seq and ST technologies. The protocol incorporates well-established components from polymerase chain reaction (PCR)-based scRNA-seq library creation, as referenced in the Droplet sequencing (Drop-Seq) (14) and BD Rhapsody (15) protocols, along with general tissue handling techniques from ST protocols described in the original spatial transcriptomics methodology (16) and the commercially available 10x Visium kit protocols (17,18). It also utilizes the STARsolo scRNA-seq alignment tool (19) for data processing. These established methods, combined with our innovative adaptation of the Illumina sequencing flow cell for ST, have led to the creation of a new experimental and computational workflow, as outlined in our previous publications on the Seq-Scope methodology (10) and the STtools computational analysis package (20). Our method is compatible with most Illumina sequencing platforms, including MiSeq (10) and HiSeq (21–23), and has been independently adapted for 2- and 3-dimensional analyses on the NovaSeq

(24,25), demonstrating its wide applicability and reproducibility. We further optimized the method for a 7 mm × 7 mm imaging area on the NovaSeq 6000 flow cell. The imaging area size was selected for its suitability for the majority of histological applications and comparability with the 6.5 mm × 6.5 mm area used by 10x Visium. The procedure has also been updated to support multi-round on-array imaging and fluorescence-guided spatial mapping. Overall, the technology continues to evolve, with the promising potential to uncover previously inaccessible information within tissue microenvironments, intracellular space, and even subcellular compartments.

1.3 Results

1.3.1 Seq-Scope technology overview - experimental

The Seq-Scope experimental procedure can be divided into three major parts with two separate sequencing steps. The concept applies to all three platforms, including MiSeq, HiSeq, and NovaSeq, except for a few minor updates to match the nature of the style of the flow cell.

In Part 1, a spatially barcoded array is produced (Figure 1.1). The first array sequencing (1st-Seq) begins as conventional Illumina sequencing of a single-stranded oligonucleotide library encoding a high-definition map coordinate identifier (HDMI) as a random sequence that is attached to PCR adapters and an oligo-dT RNA capture probe (Figure 1.1.A-C). After 1st-Seq, the sequenced flow cell is retrieved and disassembled to expose the surface covered with amplified DNA clusters containing HDMI sequences. The 1st-Seq HDMI array is then biochemically treated to expose the 3' oligo(dT) probe head for poly-A capturing (Figure 1.1.D). The output of 1st-Seq is a data table that associates all HDMI barcode sequences from the physical array with their corresponding coordinates.

Part 1 of the procedure has undergone the most updates as we improved the imaging area by upgrading the platforms. Our initial MiSeq and HiSeq platforms contain 0.7 mm^2 and two 90 mm^2 imaging areas which cannot be dissected and requires the removal of the cover part of the flow cell. The most up-to-date NovaSeq platform, on the other hand, can be run as a batch, producing 18 chips, each with four separate 7 mm x 7 mm imaging areas, totaling 72 imaging areas per flow cell with 3,600 mm^2.

In Part 2, the tissue is placed on the array to prepare for library construction (Figure 1.2.A). Sectioned tissue is attached and briefly fixed on the surface of the array. Conventional

imaging, such as H&E histology staining or fluorescence imaging, can be performed at this stage.

In Part 3, the tissue transcriptome is captured through reverse transcription, and the spatially barcoded cDNA is processed into a next-generation sequencing library (Figure 1.2.B-C). RNAs are released by partial proteolytic digestion of tissues using collagenase and pepsin and captured onto the 1st-Seq HDMI array. The tissue-array sandwich then undergoes reverse transcription, labeling the HDMI-oligo-dT molecules with cDNA sequences (Figure 1.2.B). Through subsequent secondary strand synthesis, alkaline elution, and PCR amplification steps, the chimeric molecular library of HDMI-cDNA is prepared as an Illumina-compatible library that is then sequenced on an Illumina sequencer (Figure 1.2.C). The output of 2nd-Seq is another data table with two paired-end reads—one end with HDMI information and the other end with cDNA sequence information.

In the NovaSeq platform, full procedure in Part 2 and the initial on-array procedure in Part 3 (mRNA Release and Reverse Transcription, Tissue Removal, and Secondary Strand Synthesis procedures) apply to a single chip with four imaging areas. The Purification of the secondary strand solution, Library Amplification PCR reaction and Purification, and Indexing PCR and Size Selection procedures of Part 3 apply to each imaging area of the chip. These procedures can be conducted separately for individual imaging areas or in parallel for the entire chip or multiple chips, depending on the user's experimental goals and throughput requirements. The Library Sequencing procedure of Part 3 can be conducted in batches.

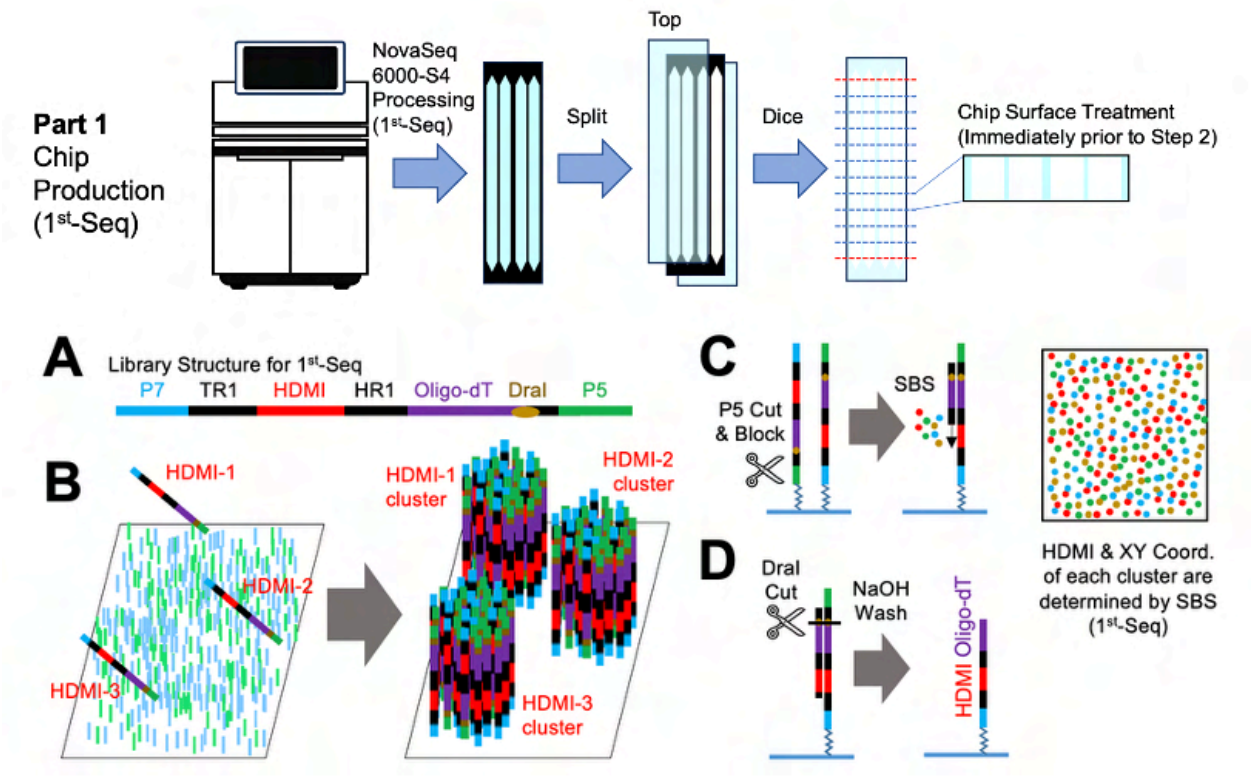


Figure 1.1 Seq-Scope experimental procedure – Part 1

Part 1 produces the chip through Illumina NovaSeq 6000 sequencing (1st-Seq), flow cell disassembly, dicing and chemical processing to expose oligo(dT) sequences. (A) Schematic representation of the HDMI-oligo library structure for 1st-Seq. P5/P7, PCR adapters; TR1, TruSeq Read 1; HR1, HDMI Read 1. (B) Solid-phase amplification of different HDMI-oligo molecules on the flow cell surface. (C and D) Illumina sequencing by synthesis (SBS) determines the HDMI sequence and XY coordinates of each cluster (C). Then, HDMI oligonucleotide clusters are modified to expose oligo(dT), the RNA-capture domain (D).

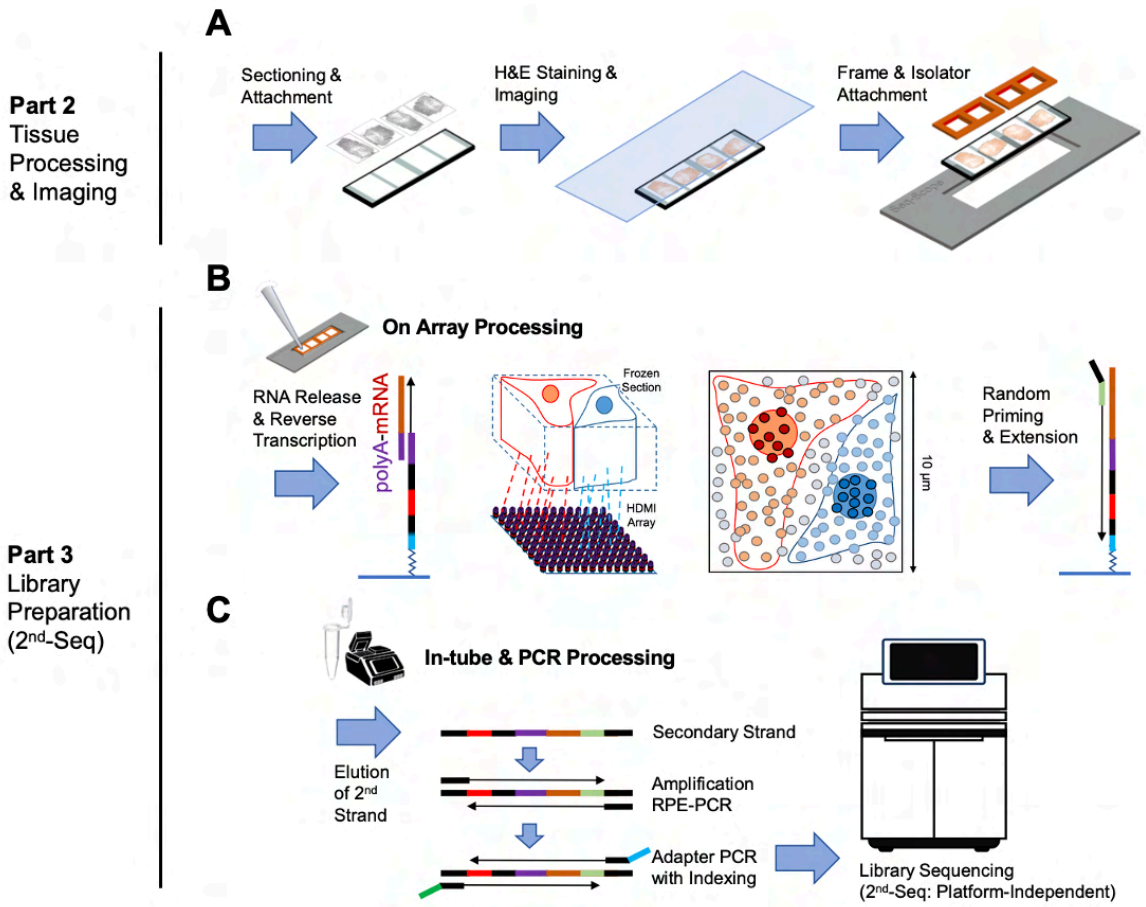


Figure 1.2 Seq-Scope experimental procedure – Parts 2 & 3

Part 2 processes and images tissue sections, preparing them for subsequent reverse transcription and library preparation in Part 3. Libraries produced in Part 3 are sequenced again (2nd-Seq) to complete the experimental procedure of Seq-Scope. In the schematic diagram, DNA segments are depicted in various colors: blue for the P7 sequence, green for the P5 sequence, red for HDMI, purple for oligo(dT), orange for mRNA/cDNA, light green for randomer-based UMI and black for other adapter sequences including sequencing read primers. RPE, random priming and extension. Images of 1.5-ml tube and PCR machine from Labicons.net.

1.3.2 Seq-Scope technology overview - computational

For each HDMI sequence, 1st-Seq generates spatial coordinate information while 2nd-Seq captures cDNA information. The analysis of sequence reads is also divided into three key stages (Figure 1.3): Part 4 builds the map of spatial barcodes (HDMI) from the single-ended sequence reads of the chip (1st-Seq). Part 5 generates a high-resolution spatial digital gene expression (SGE) matrix, by aligning the paired-end sequence reads of the prepared library (2nd-Seq) to the cDNA sequence while resolving the spatial positions of the HDMI barcodes. Optionally, if histology images are available, they can also be aligned to the HDMI coordinates in this part. Part 6 describes exemplary downstream analyses of the SGE matrix, including conventional single-cell optimized software packages such as Seurat (26) and Scanpy (27) and the identification of cell type factors and the inference of pixel-level factors at sub-micrometer resolution. Factors are transcriptome phenotypes expressed as the average expression levels of all genes across a tissue section, modeled using a multinomial distribution (28), and can represent cellular and subcellular transcriptome phenotypes specific to certain cell or organelle types as well as physiological or pathophysiological states. Parts 4 and 5 are implemented in the NovaScope pipeline (https://github.com/seqscope/NovaScope), which is an extension of the STtools pipeline (20). Part 6 primarily uses the FICTURE software tool (28) and the detailed steps to reproduce our exemplary analysis are provided in a public GitHub repository (https://github.com/seqscope/NovaScope-exemplary-downstream-analysis). Part 6 also provides examples of image-based single-cell segmentation, performed using either Watershed (29) or Cellpose (30,31) algorithms, and generates a single-cell SGE matrix, which can be subsequently used for spatial single-cell analysis. The aligned sequenced reads can be directly used for tasks that require read-level information, such as allele-specific expression or somatic variant analysis. The SGE matrix can also be analyzed with tools such as Giotto (32) and Squidpy (33), offering additional possibilities for downstream data analysis.

The up-to-date protocol is specifically optimized for the Illumina NovaSeq 6000 S4 flow cell. Previous studies have shown that Seq-Scope also works well with Illumina MiSeq and HiSeq platforms with minimal modifications in reaction scale and adaptation of bioinformatic workflow (10,21–23). Therefore, it is plausible that the protocol can also be made compatible with the NovaSeq-X 25B flow cell, a more recently released Illumina platform, provided this flow cell can be disassembled to expose the cluster surface. Additionally, it is possible that the

Seq-Scope strategy could be adapted for use with non-Illumina equipment. Indeed, several recent methodologies have utilized custom sequencing-by-synthesis platforms (e.g., Polony-indexed library-sequencing (Pixel-Seq) (13)) or a DNB-seq platform (e.g., Spatio-Temporal Enhanced REsolution Omics-sequencing (Stereo-Seq) (12)) to generate high-resolution spatial arrays using strategies similar to Seq-Scope.

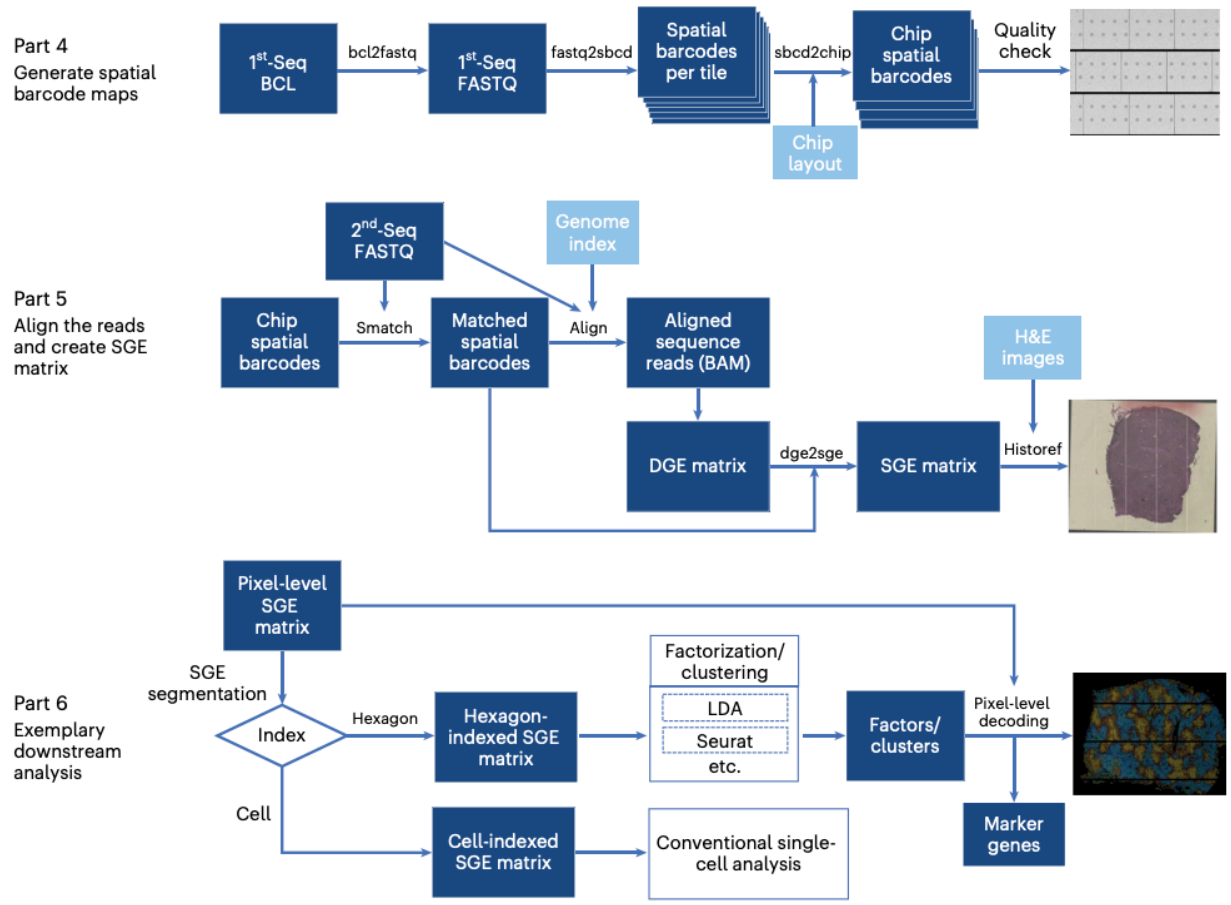


Figure 1.3 Seq-Scope computational procedure

This conceptual overview illustrates the main stages in the computational procedure. Detailed descriptions of all steps can be found in the publication (34). Part 4 generates spatial barcode maps by processing 1st-Seq data. Part 5 aligns the reads from 2nd-Seq and creates the spatial digital gene expression (SGE) matrix by using the spatial barcode information from Part 4. Part 6 describes exemplary downstream analyses for the SGE matrix produced in Part 5. These analyses include a pixel-level analysis, which identifies spatial factors at a pixel-level resolution by leveraging a hexagon-indexed SGE matrix, and a cell segmentation-based analysis, which explores cell type clusters on a cell-indexed SGE matrix, with cells segmented on the basis of histology images. A round rectangle represents data or a file, while a standard rectangle indicates a process or instruction. A diamond shape signifies a decision point. Text aligned with an arrow denotes a step or an option at a decision point. Navy blue and light blue colors represent input/intermediate/output files and additionally provided external files, respectively. DGE, digital gene expression.

1.3.3 HDMI-array captures spatial RNA footprint of tissues

Through a series of titration experiments, we produced the HDMI-array with a sequenced cluster density of up to 1.5 million clusters per mm^2 (Figure 1.4.A-C), which is sufficient to perform single-cell and subcellular analyses of the spatial transcriptome.

The RNA-capturing capability of the HDMI-array was first evaluated by performing a cyanine 3 (Cy3)-dUTP-mediated cDNA labeling assay using a fragmented frozen liver section. The HDMI-array successfully generated a spatial cDNA footprint that preserved the overlying tissue's gross shape (Figure 1.4.D). The labeling assay also revealed microscopic details of cDNA footprints that resemble a single cell morphology (Figure 1.4.D, insets), which has a fluorescence texture similar to the underlying clusters (Figure 1.4.A-B).

Then, we performed the complete Seq-Scope procedure on two representative gastrointestinal tissues, the liver and colon. The tissue sections were overlaid onto the HDMI arrays, examined by H&E staining, and subjected to 2^{nd}-Seq. Analysis of the 1^{st}-Seq and 2^{nd}-Seq data demonstrated that the RNA footprints were discovered mostly from tissue-overlaid regions (Figure 1.5.A), confirming that Seq-Scope can indeed capture and analyze the spatial transcriptome from the tissues.

The Seq-Scope analysis was robust against PCR and sequencing errors; >99% of all spatial assignments were estimated to be accurate, as detailed in the STAR method (Figure 1.5.B-D). The small number of transcripts discovered outside of the tissue-overlaid regions had a transcriptome profile similar to the tissue-covered area ($r = 0.9833$); therefore, these transcripts are likely derived from tissue debris or ambient RNAs released from the tissue.

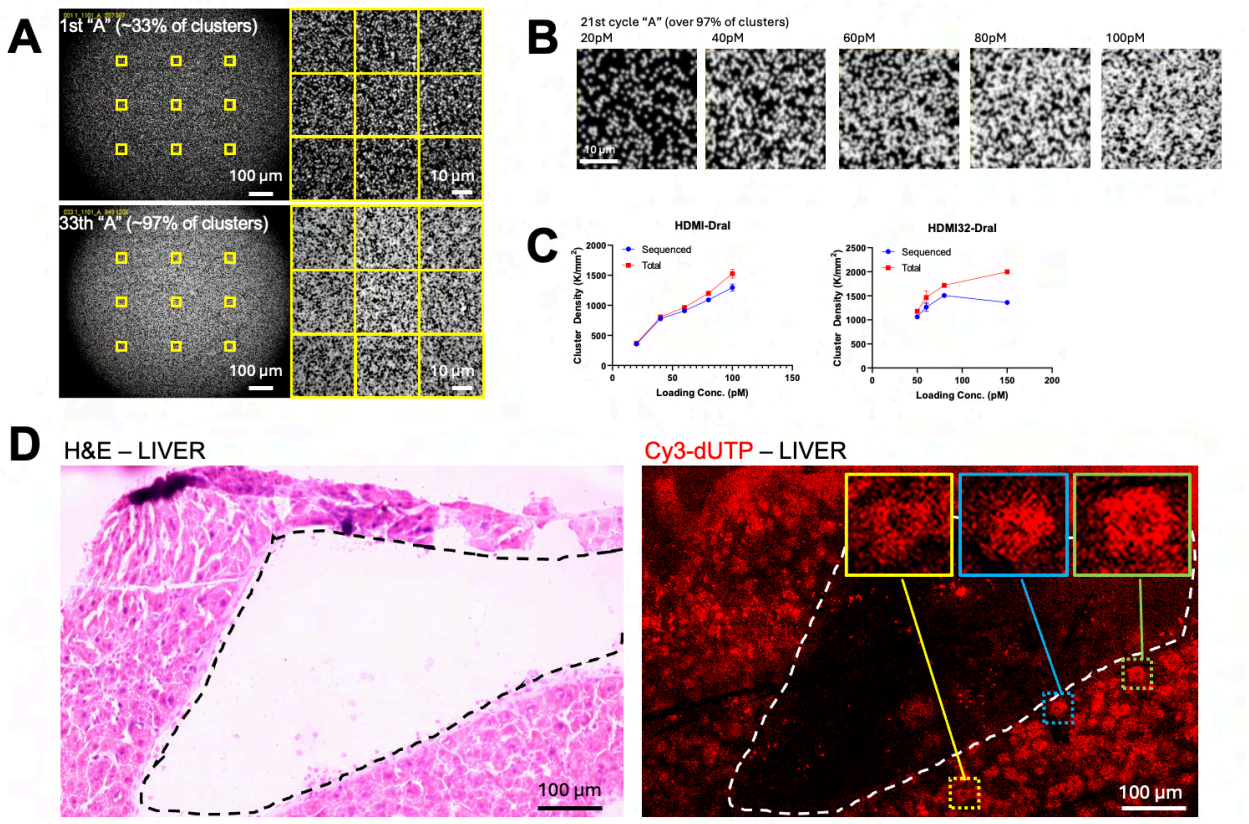


Figure 1.4 HDMI-array captures spatial RNA footprint of tissues

(A) Representative images of HDMI clusters visualizing "A" intensity at the 1st (upper) and 33rd (lower) cycles of the 1st-Seq SBS, where 33% and >97% of clusters exhibit fluorescence, respectively. Yellow squares in the left panels are magnified in the right panels. (B) Magnified images of HDMI clusters in the HDMI-array, retrieved from the Illumina sequence analysis viewer (SAV). Each picture represents the indicated HDMI-oligo library loading concentration for the visualization of "A" intensity at the 21st cycle of the 1st-Seq SBS, where >97% of HDMI clusters exhibit fluorescence. (C) Titration of HDMI-oligo library loading concentration for obtaining maximum number of sequenced clusters. Total (red) and sequenced (blue) cluster numbers were presented for indicated 1st-Seq conditions. Data are presented as mean ± SEM.

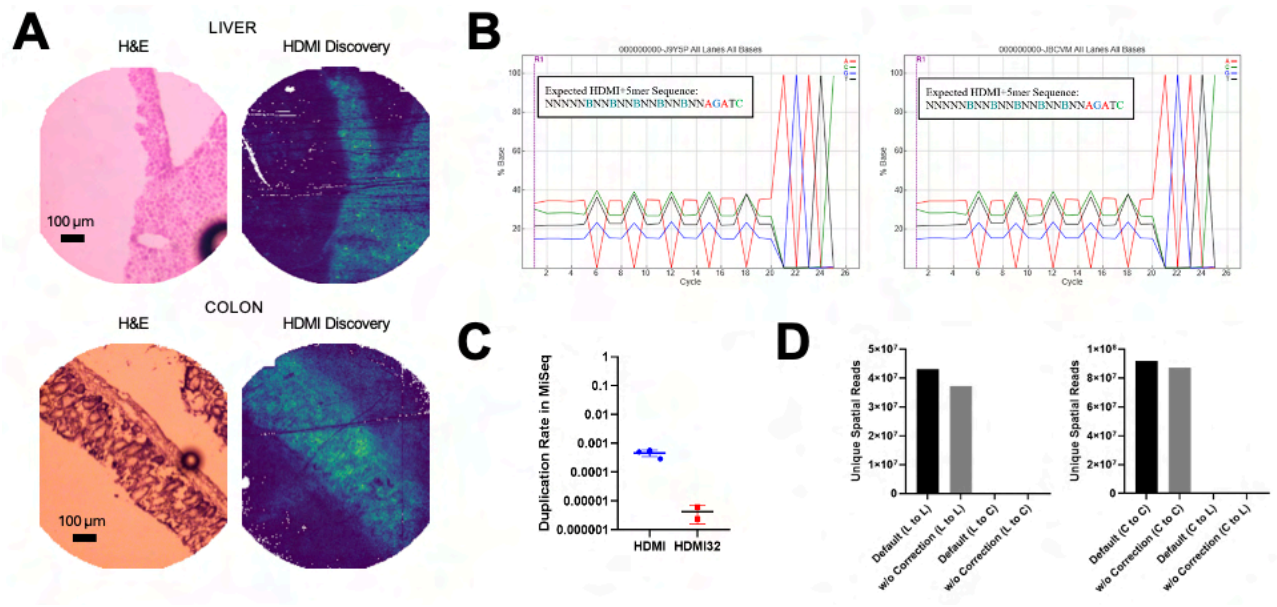


Figure 1.5 Seq-Scope has an outstanding transcriptome capture performance

(A) H&E staining and its corresponding HDMI discovery plot drawn from the analysis of 1st-Seq and 2nd-Seq outputs. Brighter color in the HDMI discovery plot indicates that more HDMI was found from 2nd-Seq in the corresponding pixel area. (B) HDMI sequencing results from 1st-Seq. Base incorporation rate (%) at each location of the HDMI sequences in liver (left) and colon (right) 1st-Seq is presented in a line graph. We used standard machine mixing for making random oligonucleotides. In this method, even though A:C:G:T was dispensed at 25:25:25:25, random bases potentially have variations from the designated ratio (in our case, A>C>G>T) due to the different chemical properties of the bases. (C) Duplication rate of HDMI (standard 25-mer) and HDMI32 (extended 32-mer). (D) Reciprocal misassignment analysis of HDMI spatial mapping. Liver 2nd-Seq dataset was analyzed with Liver 1st-Seq dataset (L to L) or Colon 1st-Seq dataset (L to C), and Colon 2nd-Seq dataset was analyzed with Colon 1st-Seq dataset (C to C) or Liver 1st-Seq dataset (C to L). Alignment was performed with default error correction algorithm of STARsolo (Default) or without any error correction implementation (w/o Correction).

1.3.4 Seq-Scope captures transcriptome information with high efficiency

Compared to previous ST solutions, Seq-Scope offers a dramatic improvement in resolution (Figure 1.6.A) and pixel density (Figure 1.6.B); the center-to-center distance between HDMI pixels was measured to be 0.633 ± 0.140 μm (liver) and 0.630 ± 0.132 μm (colon) (mean ± SD; Figure 1.6.A). Although each HDMI-barcoded cluster covers an extremely tiny area (<1 μm^2), single HDMI pixel in tissue-covered region was able to capture 6.70 ± 5.11 (liver) and 23.4 ± 17.4 (colon) UMIs (mean ± SD; Figure 1.6.C). The number of gene features identified per HDMI pixel was 5.88 ± 4.22 (liver) and 19.7 ± 14.3 `(colon) (mean ± SD; Figure 1.6.D). Per-pixel counts of UMIs and genes in Seq-Scope were larger than HDST but were smaller than other technologies (Figure 1.6.C-D). However, after normalization using the pixel density, Seq-Scope showed the best transcriptome capture performance per area among the datasets we examined (Figure 1.6.E-F; colon dataset). Overall, Seq-Scope provides an outstanding mRNA capture output, in addition to providing an unmatched spatial resolution output.

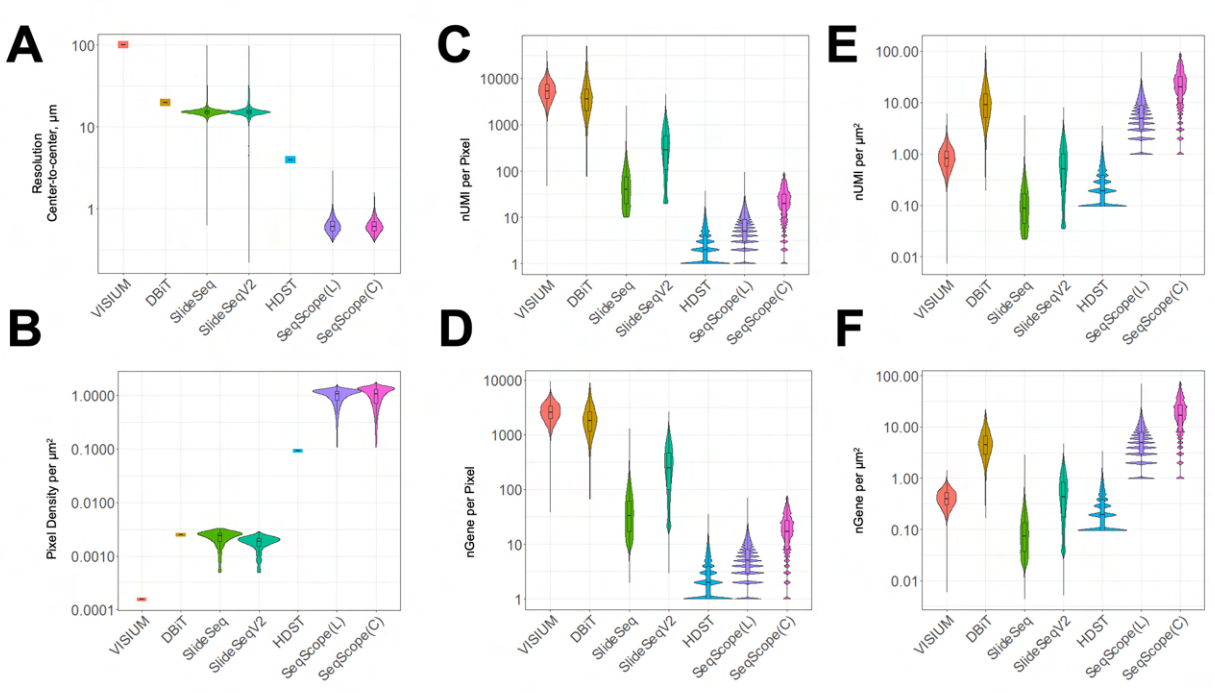


Figure 1.6 Seq-Scope captures transcriptome information with high efficiency

(A-F) Performance comparison of different ST solutions. The values were derived from each pixel (A and C-F) or gridded area (B). nUMI, number of UMI; nGene, number of gene features; SeqScope(L) and SeqScope(C), liver and colon Seq-Scope data.

1.3.5 Seq-Scope reveals nuclear-cytoplasmic transcriptome architecture from tissue sections

mRNA is transcribed and poly-A modified in the nucleus and transported to the cytoplasm after splicing (Figure 1.7.A). Several RNAs in the mouse liver, such as *Malat1*, *Neat1* and *Mlxipl*, exhibit strong nuclear localization (35). On the other hand, the cytoplasmic mitochondria contain many mitochondria-encoded RNAs (mt-RNA; Figure 1.7.A).

We spatially plotted all spliced and unspliced transcripts discovered from Seq-Scope. Intriguingly, unspliced transcript expression was restricted in tiny circles with a diameter of ~10 μm (Figure 1.7.B), which is about the size of hepatocellular nuclei (36). Spliced mRNAs were relatively scarce in the unspliced area, while nuclear-targeted RNAs were more abundant in the unspliced area (Figure 1.7.B). mt-RNAs were mostly in the spliced area (Figure 1.7.C). These observations were substantiated by correlation analysis of the single-cell images (Figure 1.7.D).

These results suggest that spliced and unspliced transcripts are useful to determine the nuclear-cytoplasmic structure from the Seq-Scope dataset. Indeed, when overlaid with H&E staining images, the unspliced RNA-enriched region generally agreed with the nuclear position (Figure 1.7.E; note that some hepatocytes are known to be multinucleate (37)). However, in some hepatocytes, the unspliced RNA-enriched regions were not observed (Figure 1.7.E), which can be explained by the absence of the cell's nucleus in the tissue slice (Figure 1.7.I), the inadequate positioning of the nucleus for RNA capture (Figure 1.7.J) or the intrinsic variations in the rates of transcription, splicing and nuclear export (Figure 1.7.K).

To further test the robustness of these observations, we randomly divided all genes into three independent subsets and examined the expressions of spliced and unspliced mRNAs from each subset. All three datasets similarly visualized a nuclear-cytoplasmic structure with a strong correlation (Figure 1.7.F).

Finally, we identified nuclear centers by using unspliced transcripts (Figure 1.7.G). Then, we searched for genes whose transcripts were enriched within 5 μm from the nuclear centers. Consistent with previous cell fractionation and RNA in situ hybridization studies (35) and our observations described above, *Malat1*, *Neat1,* and *Mlxipl* were identified as the top 3 genes enriched in the nuclear area (Figure 1.7.H). These results demonstrate that Seq-Scope can perform subcellular transcriptome studies.

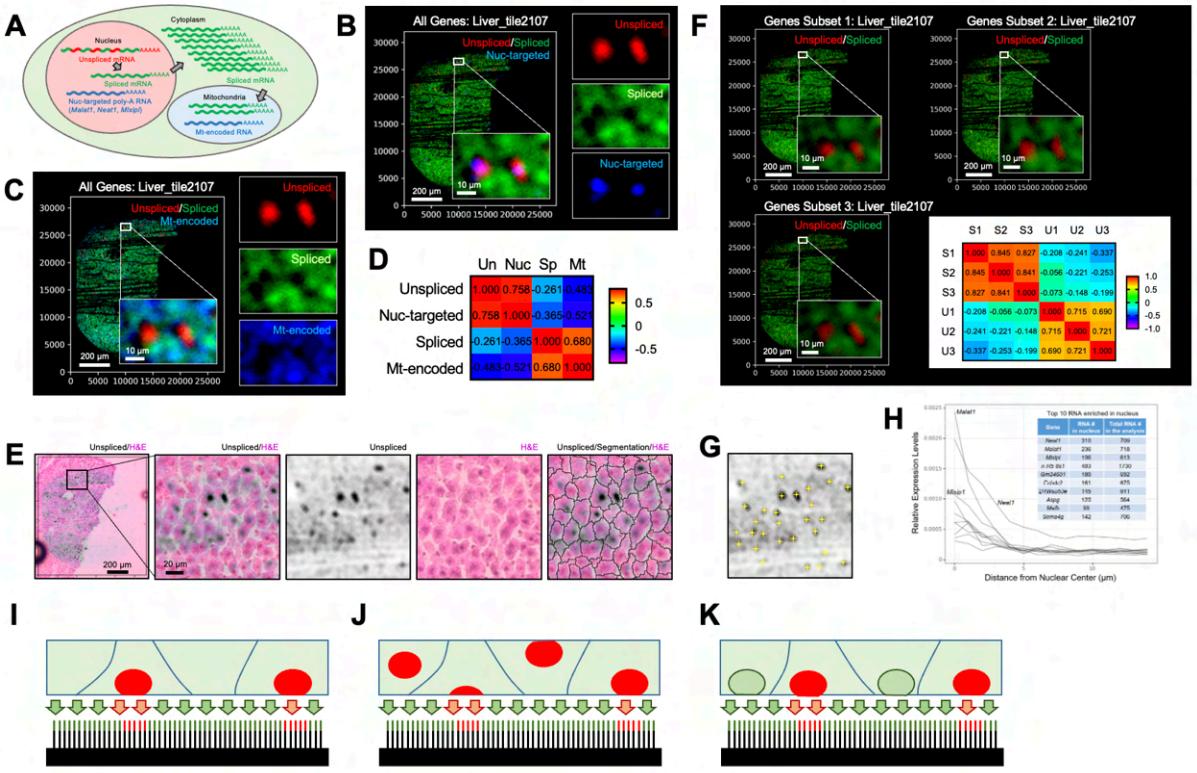


Figure 1.7 Seq-Scope visualizes subcellular spatial transcriptome

(A) Schematic diagram depicting the distribution of different RNA species in subcellular compartments. (B-D) Spatial plot of all unspliced and spliced transcripts, as well as nuclear-targeted (B) and mitochondria-encoded (C) transcripts. Pearson correlations (r) between these transcript intensities were presented in a heat map (D). (E) Images displaying unspliced RNA discovery, H&E histology and histology-based cell segmentation boundaries. Inset in the first panel is magnified in right panels. (F) Spatial plot of unspliced and spliced transcripts in three independent subsets of genes (Gene Subset 1-3). Pearson correlations (r) were presented as a heat map. S1-3, Spliced 1-3; U1-3, Unspliced 1-3. (G) Identification of transcriptomic nuclear centers (yellow crosses) through local maxima detection. (H) Identification of nuclear-enriched RNA species. Top 10 nuclear-enriched RNAs are shown. (I-K) Potential reasons of why some segmented hepatocellular area did not exhibit nuclear/unspliced RNA-enriched area. Section slice may not contain nucleus for the cell (I). Nuclear position in the section may not be ideal for the unspliced RNA capture (J). Transcriptionally inactive nuclei may express reduced levels of unspliced RNAs (K).

1.3.6 Seq-Scope pathophysiological applications

Taking advantage of Seq-Scope's sub-micrometer resolution and full-transcriptome coverage, we applied it to address pathophysiological questions across distinct disease contexts, including skin acne (22) and liver senescence with details demonstrated below.

1.3.6.1 Distinguishing TREM2 macrophages and their roles in acne-associated pathology

Acne affects 1 in 10 people globally, often resulting in disfigurement. The disease involves excess production of lipids, particularly squalene, increased growth of *Cutibacterium acnes*, and a host inflammatory response with foamy macrophages. Through single-cell sequencing and the utilization of 10X Visium, our collaborator, Dr. Johann E. Gudjonsson's Lab and Dr. Robert L. Modlin's Lab, has identified a macrophage subtype, which expresses TREM2 and regulates lipid metabolism and proinflammatory gene programs in acne biopsies.

To further validate the direct relationship between TREM2 macrophages and acne formation around hair follicles, we applied Seq-Scope to precisely localize and profile a longitudinally sectioned human hair follicle surrounded by an inflammatory infiltrate in a biopsy specimen. (Figure 1.8.A). We segmented the histology area with 10-μm-sided square grids, which revealed an average of 145 genes and 167 transcripts across 3558 grids in an acne lesion. We clustered and annotated the 10-μm-grid dataset using the cluster and subcluster signature genes from the acne scRNA-seq dataset, defining the location of TREM2 macrophages, other macrophages, $KRT5^+$ and $KRT16^+$ keratinocytes (KCs), fibroblasts, endothelial cells, and B cells (Figure 1.8.B). We then further refined the spatial resolution of the dataset by transferring the annotations obtained under 10-μm grids to the sliding-grid datasets with 5-, 2-, and 1-μm intervals between the center of two adjacent grids. $KRT5^+$ KCs were identified in the basal layer of the epidermis and the outer root sheath of the hair follicle, whereas $KRT16^+$ KCs were identified in the inner root sheath of the hair follicle. TREM2 macrophages, other macrophages, and fibroblasts were localized in close proximity as well as directly adjacent to the hair follicle (Figure 1.8.C). A magnified view of the region near the hair follicle at 1-μm resolution identifies TREM2 macrophages adjacent to $KRT5^+$ KCs in the hair follicle outer root sheath (Figure 1.8.C, inset). We also plotted the expression of individual genes, confirming the microanatomic location of KRT5 and KRT16 expression, with the localization of APOE, a key marker of TREM2 macrophages in the area surrounding the hair follicle (Figure 1.8.D)

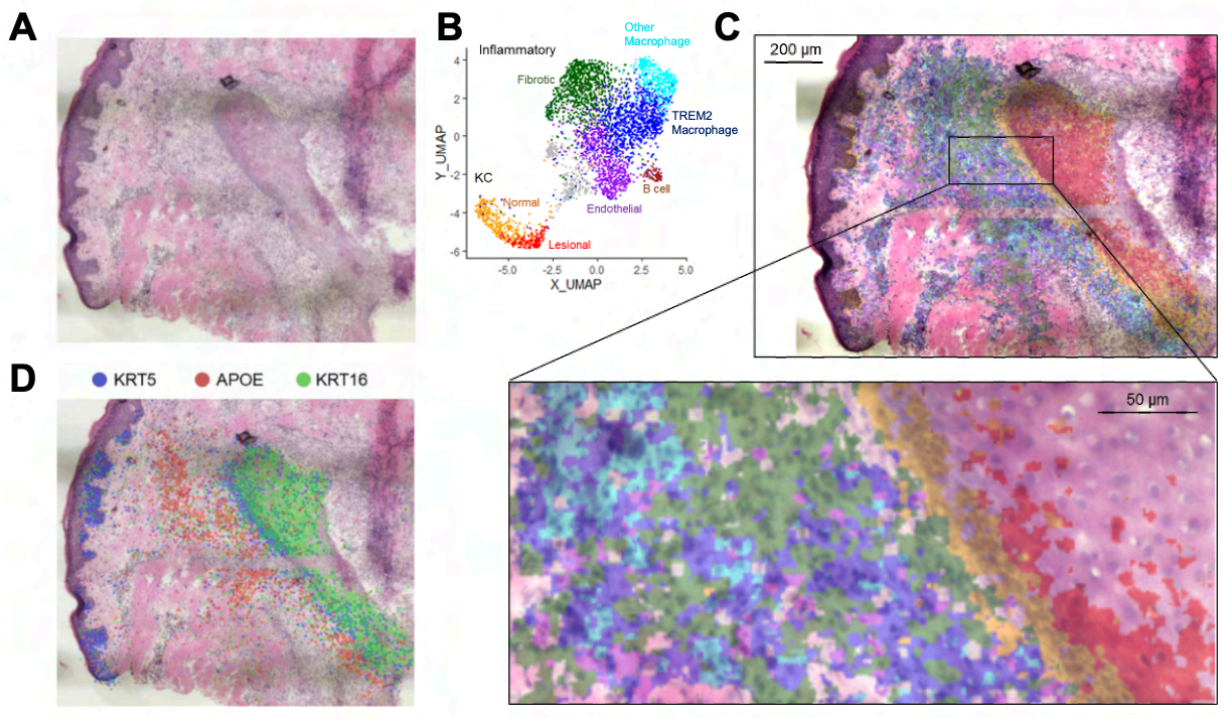


Figure 1.8 TREM2 macrophages are recruited to lesion hair follicle

(A) H&E staining of the acne biopsy used for Seq-Scope analysis. (B) UMAP manifold of cell type clustering in lesion area. (C) Spatial visualization of cell type clusters identified in (B) using 5-µm-sided square grids. Inset: Boxed region showing the magnified spatial plot with 1-µm intervals between grids. (D) Spatial plot showing overlay of KRT5 in blue, APOE in red, and KRT16 in green with 2-µm intervals between grids.

1.3.6.2 Unraveling the identities and the signatures of p21-expressing senescent cells in aged liver

Cellular senescence is a regulated aging process in which cells remain viable yet undergo stable cell-cycle arrest and acquire metabolic changes that can reshape tissue homeostasis (38). With age, senescent cells accumulate and have been implicated in diverse age-associated pathologies, in part through paracrine signaling mediated by senescence-associated secretory phenotypes (SASPs) (39,40). Among senescence-associated programs, upregulation of the cyclin-dependent kinase inhibitor p21 (*Cdkn1a*) is widely used as a hallmark of senescence and a key effector of cell-cycle arrest, acting downstream of damage and stress signaling to enforce growth inhibition (41). The accumulation of p21 positive ($p21^{+}$) cells has been identified in aged tissues in vivo, and clearance of this population in rodents has been shown to both extend lifespan and improve healthspan (42,43). Still, a persistent challenge remains as senescent cells are rare, heterogeneous, and context dependent, causing difficulties in identifying them and defining their tissue-level interactions (44).

To address this gap, we developed a fluorescence-guided spatial transcriptomic framework, branching out from our standard Seq-Scope procedure with DAPI-based single-cell segmentation to apply to a well-established p21-Cre dual-reporter mouse model (10,34,42,43,45). In this reporter system, a p21 promoter-driven Cre-GFP cassette reports ongoing p21 transcriptional activity, whereas a Cre-dependent loxP-tdTomato allele under a constitutive CAG promoter permanently labels cells with a history of p21 expression. Together, this model enables both spatial mapping of p21-lineage cells and discrimination between current and past p21 activity, providing a readout of senescent stage progression. This technological combination enables us to (i) precisely localize p21-expressing cells *in situ*, (ii) resolve their cellular identities and transcriptional states without restricting analysis to a limited marker panel, (iii) systematically characterizes the local cellular neighborhood sur-rounding senescent cells, and (iv) unravel the transcriptomic shift along the senescence progression (Figure 1.9).

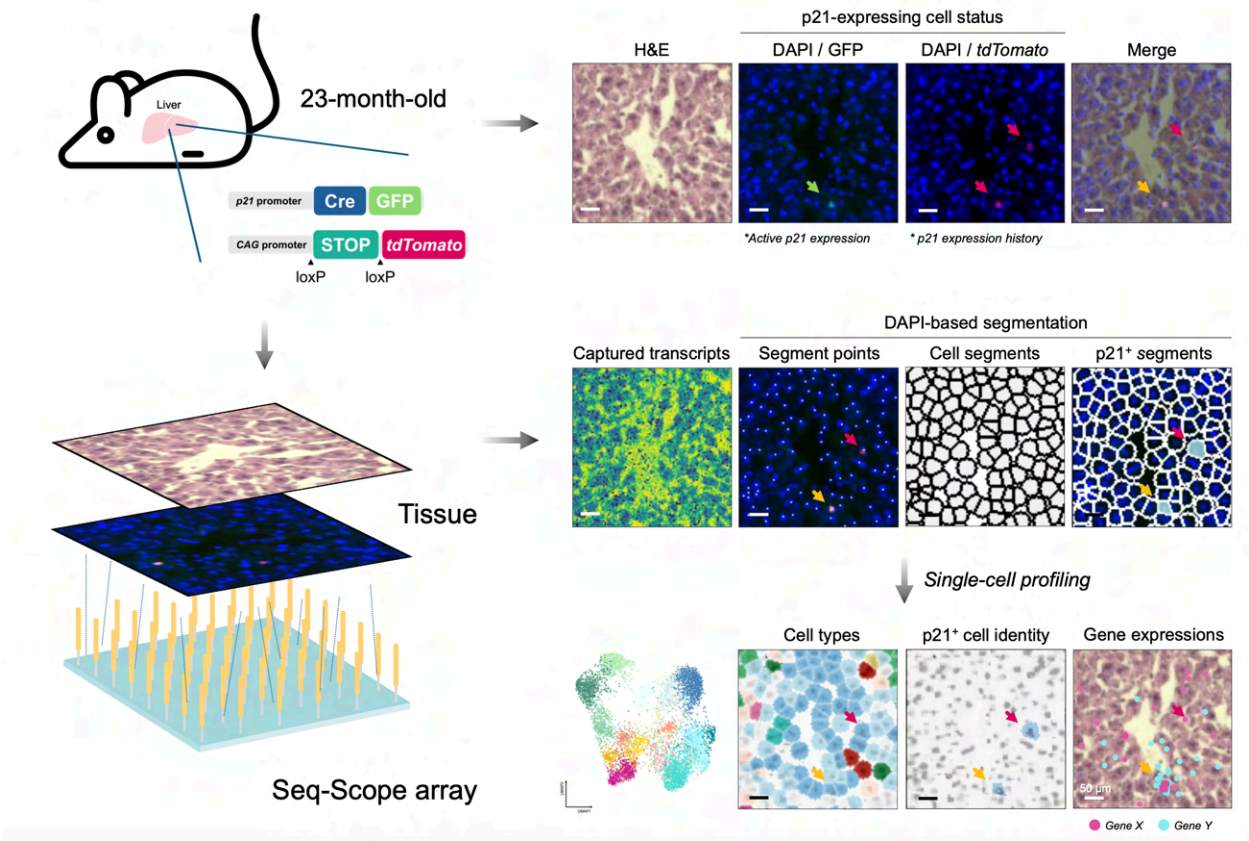


Figure 1.9 Seq-Scope enables single-cell spatial transcriptome analysis in p21-Cre mouse liver

p21-expressing senescent cells are visualized in aged p21-Cre-GFP/*tdTomato* dual-reporter mice, separating cells with current p21 transcriptional activity (GFP; green/yellow arrow) from cells with prior p21 activity recorded by *tdTomato* labeling (*tdTomato*; red arrow) (top). Liver sections are profiled by Seq-Scope using a barcoded array and multi-round on-array imaging. DAPI-marked nuclear positions are used as anchor points for cell segmentation and assignment of spatially barcoded reads to individual cells (middle). Cell identities and transcriptional signatures are resolved by dimensionality reduction and clustering of the single-cell spatial transcriptomes.

Identification of liver zonation and immune cell infiltration in aged liver

In this study, six liver sections from three biological replicates of 23-month-old p21-Cre reporter mice were profiled using the Seq-Scope HiSeq2500 platform. The same sections were sequentially subjected to H&E staining (Figure 1.10.A, first row) and DAPI/GFP/*tdTomato* imaging (Figure 1.10.A, second row) on the array surface. Transcripts were then released, spatially barcoded, and collected to construct a SGE matrix that stores each gene copy along with its spatial coordinates. The SGE matrix was visualized as an RNA density map (Figure 1.10.A, third row), revealing strong transcript localization to the cytoplasm, consistent with known cellular biology. Overall, 101,532 of high-quality segmented cells were identified across all sections.

On average, each segmented cell yielded 475 unique transcripts (Figure 1.11.A). Cells from each mouse were treated as independent groups for integration, followed by clustering. Output clusters were assigned to cell types based on canonical markers (Figure 1.11.B). Batch effects were minimal and did not dominate any major population structure (Figure 1.11.C). In this dataset, we identified hepatocytes (Hep), macrophages (M_{Φ}), neutrophils, plasma cells, hepatic stellate cells (HSCs), and hepatic progenitor cells (HPCs), with several populations exhibiting subtype structure. Hepatocytes were further sub-clustered into zone-specific populations ranging from Periportal (PP), Midzone (M), Pericentral (PC), to Centrilobular (CL). Injured hepatocyte subset was also identified by predominant expression of *Saa1* and *Saa2* (Figure 1.11.D). Macrophages could first be separated into resting and activated states, with the activated population expressing *Vcam1*, *Cd74*, and *H2-Ab1*. Surprisingly, building on this separation, we further identified an activated macrophage subset with high *Cxcl13* expression, indicating layered heterogeneity beyond the resting–activated split in aged liver. In addition, a distinct cell group enriched for type I interferon-stimulated gene (ISG) program was detected, with ex-pression of interferon-associated genes such as *Rsad2*, *Ifit1*, *Cmpk2*, and *Ifit3* (Figure 1.11.D) (46,47).

We next mapped the UMAP-defined cell types back to their spatial coordinates in situ (Figure 1.10.A, fourth row). Zoomed-in views highlighted the organization of major anatomical landmarks, including the portal and central veins, and showed the relative positioning of infiltrating versus resident macrophages, providing a comprehensive spatial view of liver cellular architecture (Figure 1.10.B).

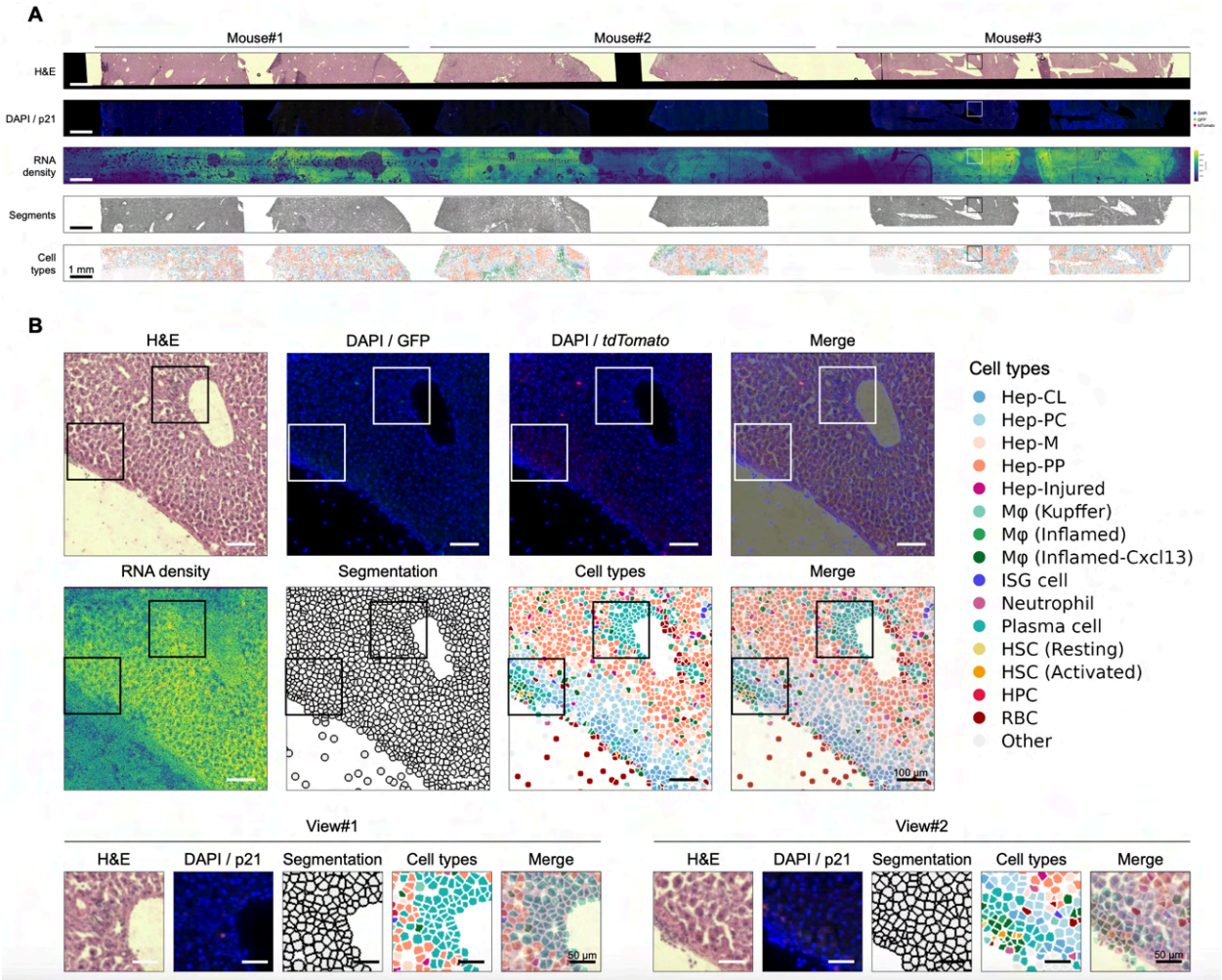


Figure 1.10 Identification of liver zonation and immune cell infiltration in aged liver

(A) Overview of six liver sections from three biological replicates examined by Seq-Scope. From top to bottom, images are displayed as H&E histology, DAPI/GFP/*tdTomato* fluorescence, Seq-Scope RNA density map, DAPI-based segmentation, and spatial cell type projection, according to the clusters identified in Figure 1.11.B. (B) Top: spatial maps of boxed region in (A). Bottom: higher-magnification views of the corresponding regions in (B) top, highlighting plasma cell infiltration (view #1) and macrophage infiltration (view #2).

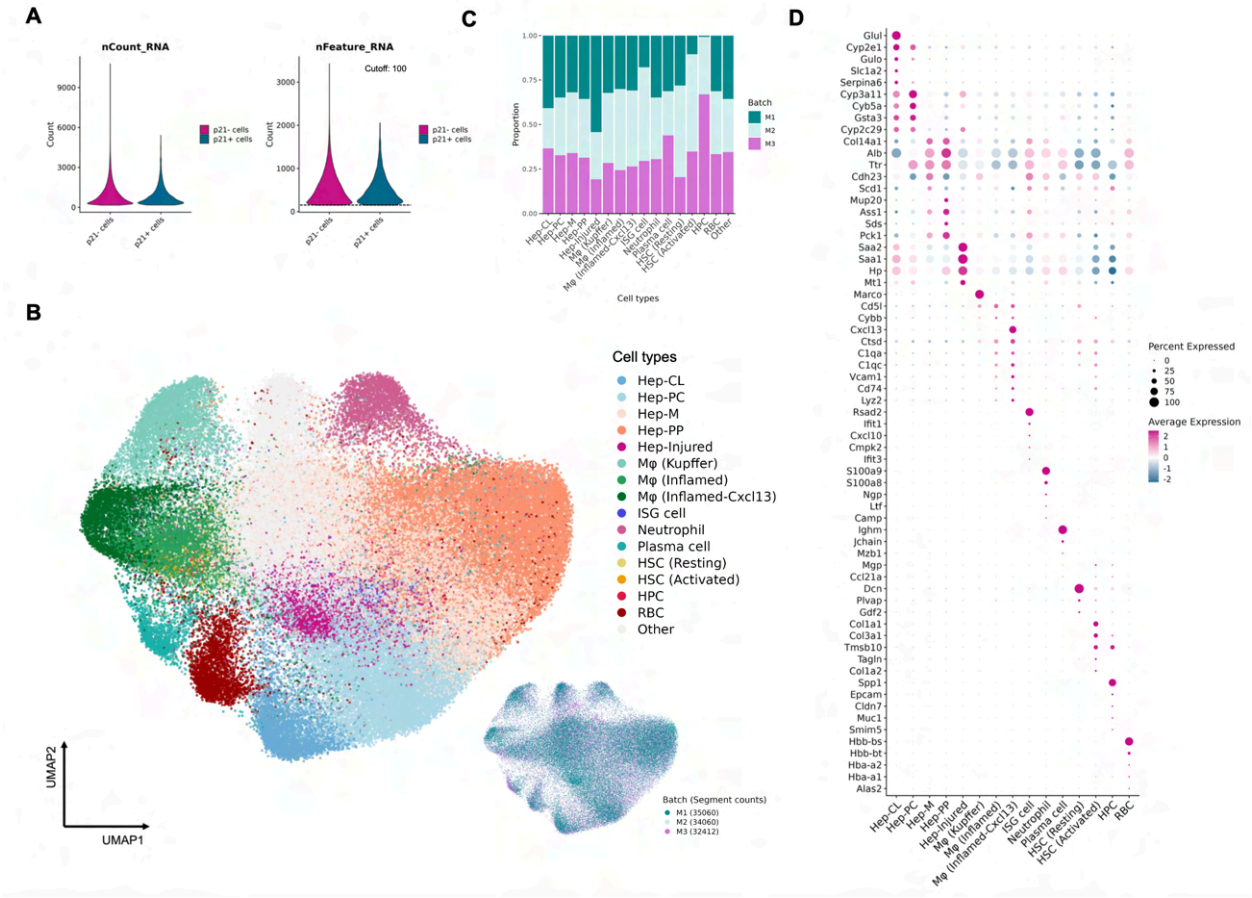


Figure 1.11 Cell-type landscape of p21-Cre aged mouse liver

(A) Distribution of transcript counts (left) and unique RNA features (number of detected genes; right) per segmented cell, shown separately for $p21^-$ and $p21^+$ cells. A minimum cutoff of 100 unique RNA features was applied prior to integration and downstream analyses. (B) UMAP embedding of major cell types identified by multidimensional clustering after integration across mice. Each point (n = 101,532) represents one cell and is colored by assigned cell type (center) or by originating mouse (lower right). (C) Contribution of each mouse to the indicated cell types. (D) Representative expression patterns of cell-type marker genes across clusters.

Cellular Identity of p21-expressing cells in aged liver

To further reveal the identity of p21-expressing cells within the whole aged liver population, we isolated segments with overlapping GFP or *tdTomato* fluorescence (Figure 1.12.A, first and second rows). As a result, 1,338 segmented cells were recognized as $p21^+$ cells. These cells were largely distributed across the tissue area, with a few exceptions forming local aggregates (Figure 1.12.B). Through cell type identification, we discovered a diverse lineage of senescent development across all major cell types (Figure 1.12.B and Figure 1.13.A-B), without a single population dominating the $p21^+$ cell group (Figure 1.13.C). The cell type composition of $p21^+$ cells was largely similar to the whole population ($p21^-$ cells). This diverse-lineage pattern resonates with our previous single-cell RNA-seq results in visceral fat and further supports the conclusion across organs and platforms (42).

By quantifying $p21^+$ cells across three biological replicates, we observed discrepancies in senescence occurrence among samples (Figure 1.13.D), although we cannot rule out factors such as section position or sampling depth within the liver. Still, senescence remained rare, as no batch contained more than 2% $p21^+$ cells. Over 50% of $p21^+$ cells were hepatocytes, as expected given their dominance in the liver cellular population (Figure 1.13.C and Figure 1.13.E). Among non-parenchymal cells, macrophages showed the highest tendency to develop p21-expressing senescence (Figure 1.13.E), consistent with our visceral fat dataset (42). Notably, we further observed differences in senescence development across macrophage states, with *Cxcl13*-expressing inflamed macrophages showing the highest $p21^+$ ratio, nearly twice that of resident macrophages (Kupffer) (Figure 1.13.E). Activated HSCs also exhibited a higher tendency to express p21 compared with resting HSCs, although the sample size was small and additional validation may be needed (Figure 1.13.E).

Overall, these results suggest that senescence develops in parallel across multiple cell types and that cellular state may influence p21-associated senescence in non-parenchymal populations.

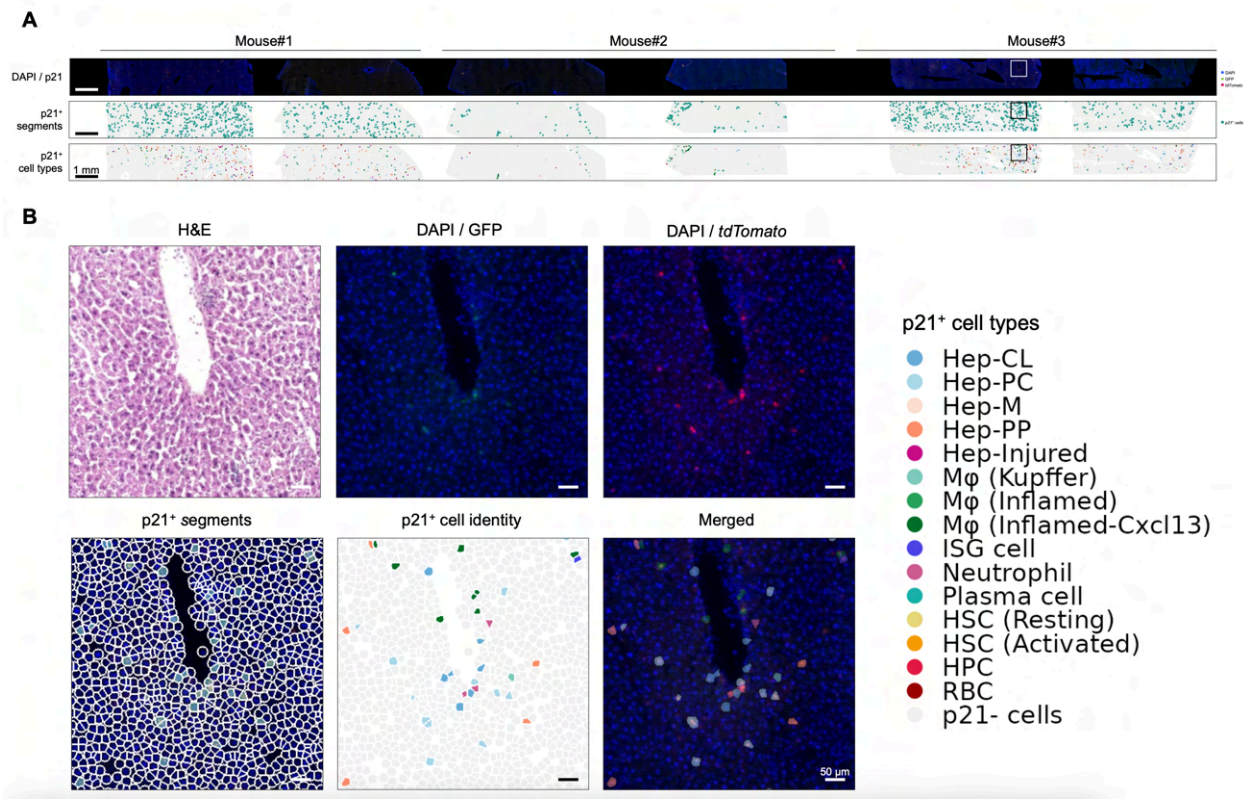


Figure 1.12 p21-Cre fluorescence guides cell-type assignment of senescent cells

(A) Overview of Seq-Scope–profiled liver sections with a focus on $p21^+$ cells. From top to bottom, images are displayed as DAPI/GFP/*tdTomato* fluorescence, $p21^+$ segments, and spatial projection of $p21^+$ cell types based on the clusters defined in Figure 1.13.B. (B) Higher-magnification spatial maps of the boxed regions in (A).

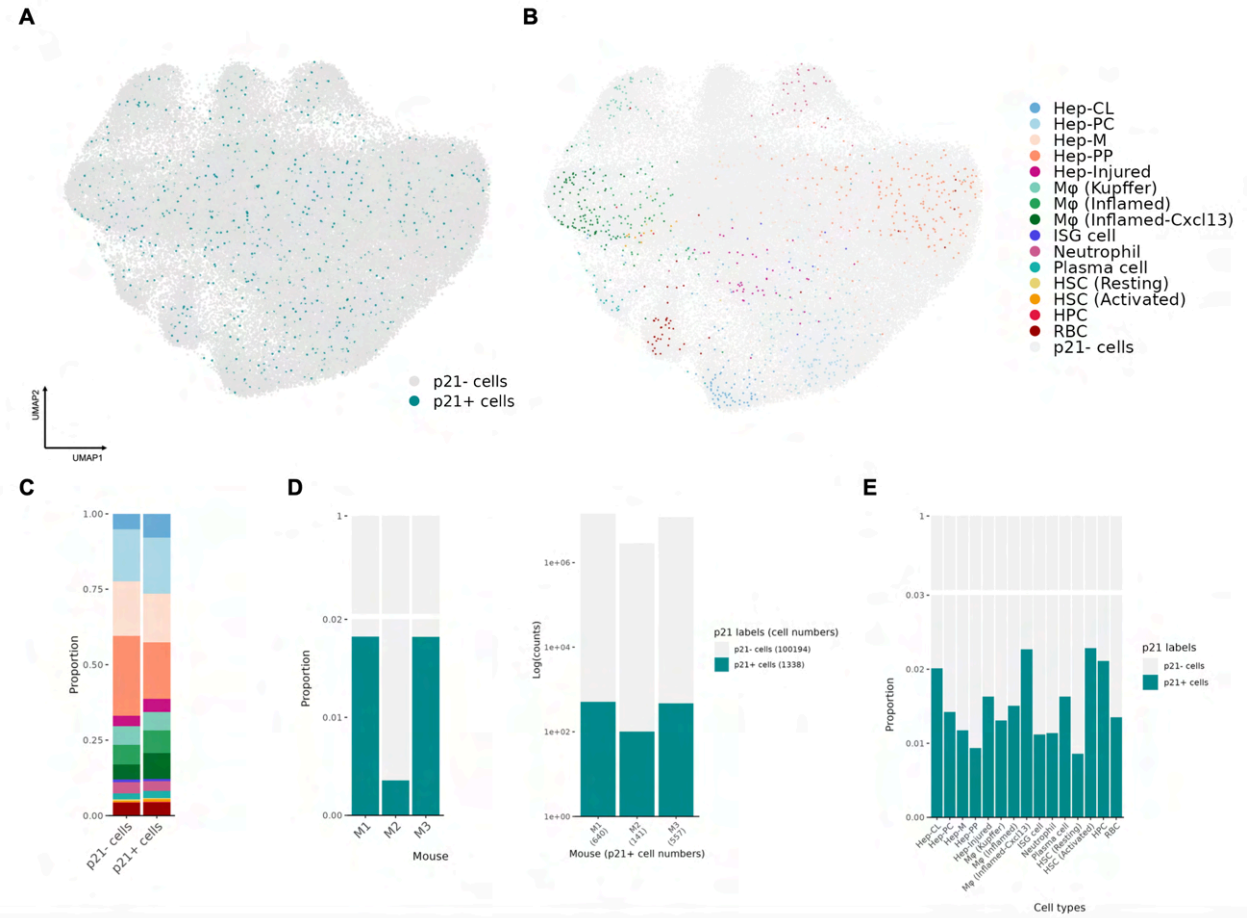


Figure 1.13 Senescence emerges in parallel across multiple liver lineages in aged liver

(A-B) UMAP embedding highlighting $p21^+$ cells (A) or coloring $p21^+$ cells by the cell-type clusters defined in Figure 1.10.B (B). (C) Distribution of cell types within the $p21^-$ and $p21^+$ cell groups. (D) Frequency of p21 positivity across mice, shown as a ratio (left) and as log(counts) (right). (E) Frequency of p21 positivity across cell types, shown as a ratio.

Distinct SASP programs reveal heterogeneity among p21-expressing senescent cells

Cellular senescence is widely defined not only by stable cell-cycle arrest, but also by acquisition of a senescence-associated secretory phenotype, a characteristic program that includes inflammatory signaling, extracellular matrix remodeling, and other paracrine signals (40). Given this complexity, even a single cell type can adopt distinct SASP pro-grams across different microenvironments.

Here, by leveraging the high-resolution feature of Seq-Scope, we scanned the transcriptome of each $p21^+$ cell individually in the tissue. We identified two morpho-logically similar cell aggregates within the $p21^+$ niche that nevertheless expressed two distinct SASP programs (Figure 1.14.A-B). Based on histology, both niches appeared as non-parenchymal cell aggregates. Transcriptome data further pointed to their identities as activated HSCs and macrophages, supported by mixed local expression of *Col1a1*, *Col3a1*, *Vcam1*, and *Cd74* (Figure 1.14.A-B, top row). Their SASP signatures, however, differed. While one niche predominantly expressed *Gpnmb* (seno-antigen) (48,49), surrounded by inflammatory SASPs, such as *Cxcl9* and *Cxcl10* (Figure 1.14.A, bottom row), the other niche more prominently expressed *Ccl8* and *Mmp3*, reflecting SASP programs associated with inflammation and tissue remodeling, with less pronounced expression of *Gpnmb* (Figure 1.14.B, bottom row). By visualizing the spatial expression of selected SASP genes, these two otherwise similar microenvironments were shown to be transcriptionally distinct, indicating heterogeneity of senescence even within the same $p21^+$ niche.

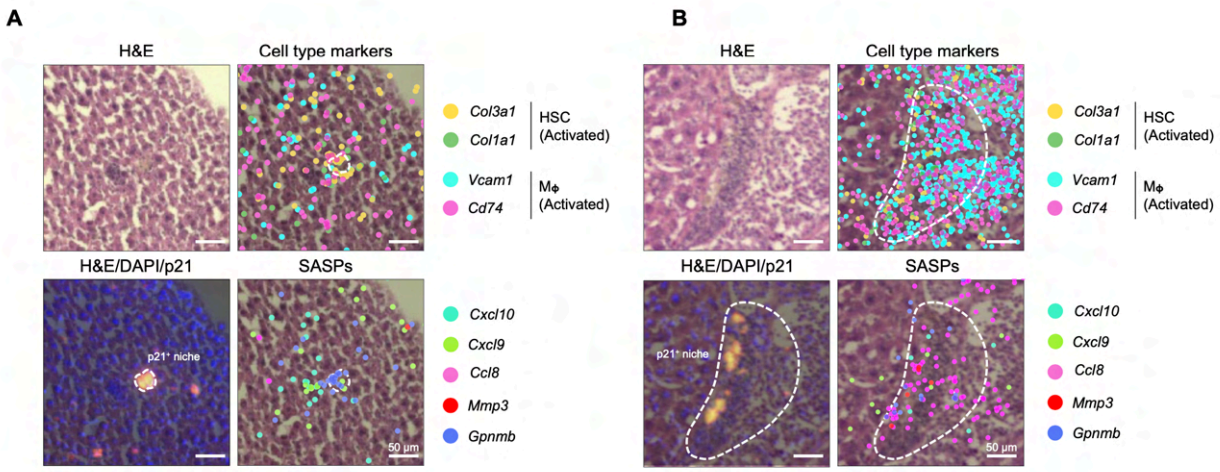


Figure 1.14 Distinct SASP programs reveal heterogeneity among p21-expressing senescent cells

(A-B) Two $p21^{+}$ senescence niches are shown. Panels display histology (top left), an H&E/DAPI/GFP/tdTomato overlay (bottom left) with the $p21^{+}$ niche outlined by a white dashed boundary, cell-type marker expression (top right), and selected SASP genes (bottom right). Genes are plotted as color dots.

Cell types exhibit distinct transcriptome profiles within the senescent niche

To further investigate the senescence microenvironment, we collected cells that were spatially located immediately adjacent to $p21^+$ cells (Figure 1.15.A, bottom row; Figure 1.15.B). In total, 4,902 neighboring cells were isolated. The cell-type composition of these neigh-boring cells was similar to that of the $p21^+$ population, with no single cell type dominating (Figure 1.15.C).

We next performed differential expression (DE) analyses comparing $p21^+$ cells, neighboring cells, and other cells within each cell type to identify spatially patterned transcriptional changes associated with the senescent niche (Figure 1.15.D). This analysis revealed position- and lineage-specific enrichment of genes that match to canonical senescence-related programs, including inflammatory sensing, proteostasis remodeling, and metabolic stress adaptation.

In parenchymal populations, Hep-CL $p21^+$ cells showed significant enrichment of *Itga2* (a collagen-binding integrin associated with extracellular matrix sensing and tissue remodeling in inflammatory conditions) and *C1rb* (a complement-pathway protease family gene involved in innate inflammatory activation). Hep-M $p21^+$ cells were marked by elevated *Lcn2* (a secreted injury-associated factor induced in oxidative stress states) as well as *Procr* (a mediator in cytoprotective and inflammatory-response pathways). In Hep-PC $p21^+$ cells, *Tnfsf10* was significantly upregulated; this TRAIL-family cytokine has been implicated in liver inflammation and injury responses.

Among immune-lineage populations, $p21^+$ inflamed *Cxcl13*$^+$ macrophages showed significant enrichment of *Gpnmb*, *Kcnn4* (an ion-channel gene reported to shape macrophage inflammatory programs), *Nupr1* (a stress-induced transcriptional regulator connected to oxidative-stress adaptation), and *Scimp* (a macrophage adaptor that promotes selective Toll-like receptor-induced proinflammatory cytokine responses). In contrast, neighboring inflamed *Cxcl13*$^+$ macrophages showed significant upregulation of *Tnfsf10*, suggesting a distinct inflammatory or injury-associated program.

In neutrophils, $p21^+$ cells were enriched for *Crispld2* (a negative modulator of pro-inflammatory cytokine responses), *Dpep2* (a leukotriene-metabolizing enzyme linked to inflammatory signaling), *Gzma* (a granzyme that can function extracellularly to amplify inflammatory responses), and *Lum* (a mediator of TNFα-induced cell cycle arrest). By contrast,

neighboring neutrophils showed significant upregulation of *Il1b*, a central inflammatory cytokine that also contributes to senescence-associated secretory signaling. In plasma cells, $p21^+$ cells showed increased *Clic1* (a protein linked to oxidative stress and NLRP3 inflammasome activation) together with *Mgst2* (a leukotriene-pathway and redox-stress enzyme associated with ER stress-induced oxidative DNA damage).

Together, the DE result indicated that $p21^+$ cells and their immediate neighbors engage distinct, cell type–specific programs that align with senescence-associated stress, inflammatory, and remodeling axes rather than a single shared phenotype restricted to only the senescent cell itself (Figure 1.15.D).

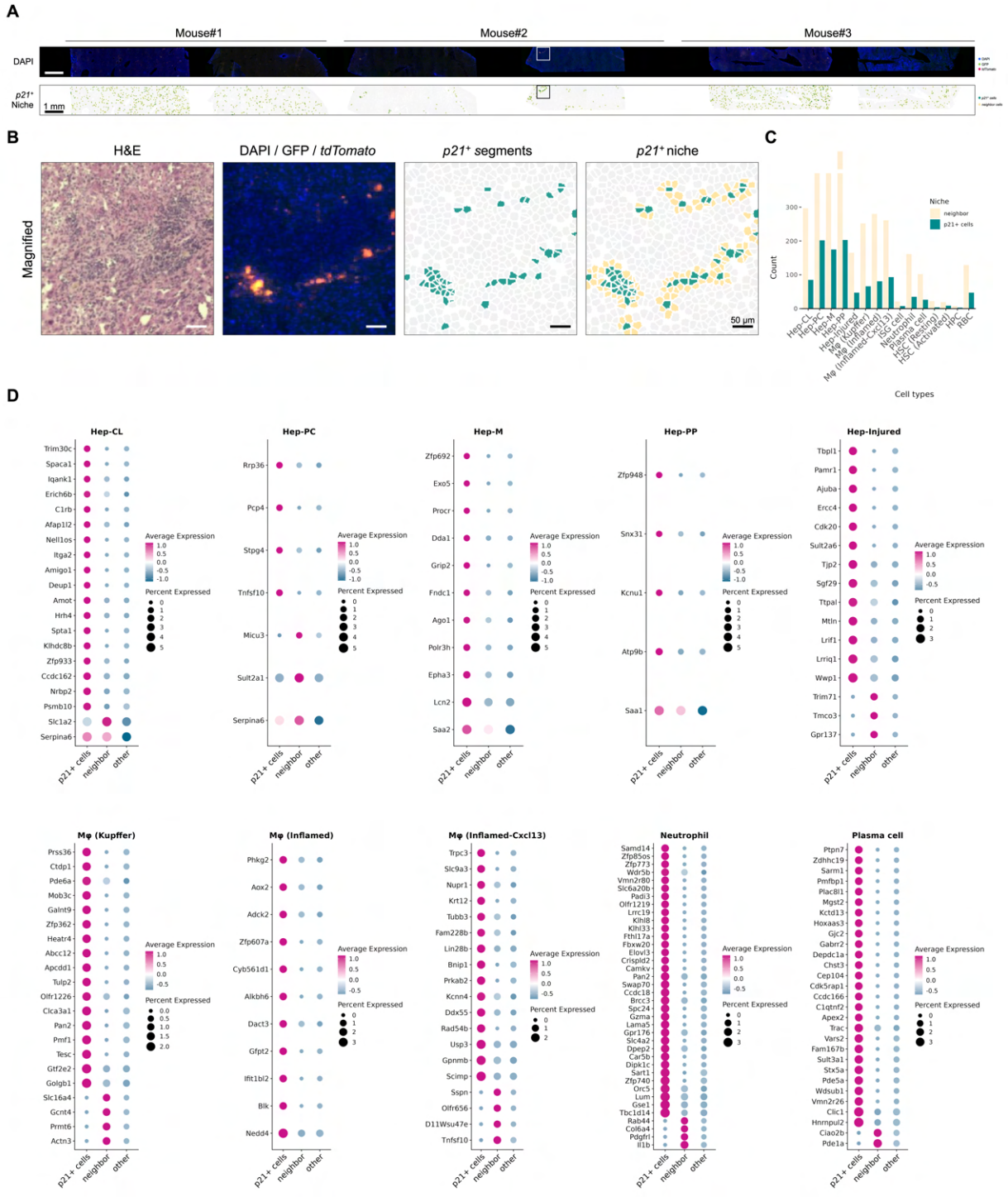


Figure 1.15 Cell types exhibit distinct transcriptome profiles within the senescent niche

(A) Overview of Seq-Scope–profiled liver sections with a focus on p21$^+$ niches. From top to bottom, images are displayed as DAPI/GFP/*tdTomato* fluorescence and cells residing within p21$^+$ niches. (B) Higher-magnification spatial maps of the boxed regions in (A). (C) Quantification of the prevalence of p21$^+$ cells (green) and neighboring cells (yellow) across cell types. (D) Representative expression patterns of genes selectively upregulated in p21$^+$ cells or in neighboring cells across cell types (adjusted p-values < 0.05).

Senescence undergoes transcriptional shifts across distinct stages

Several studies have reported the dynamic change of p21 expression over the course of senescence, with an initial increase followed by attenuation over time. To capture stage differences along this trajectory, our p21-Cre reporter system includes two complementary readouts of p21 status. In this model, the Cre-GFP cassette is transcribed upon immediate p21 promoter activity, indicating ongoing p21 transcriptional signals (Figure 1.16.A, top row), whereas the Cre-dependent loxP-*tdTomato* cassette is permanently activated following p21 promoter-driven Cre activity, representing a history of p21 expression (Figure 1.16.A, bottom row).

Since the relative intensity of these two reporters can vary from cell to cell, we performed systematic normalization and quantification of GFP and *tdTomato* fluorescence in each $p21^+$ cell. Over 90% of $p21^+$ cells showed higher normalized *tdTomato* than normalized GFP signal (Figure 1.16.B), consistent with the temporal behavior of p21 expression during senescence progression. GFP-only spots were rare, as most GFP signal was ac-companied by *tdTomato* expression. In contrast, a subset of $p21^+$ cells contained *tdTomato* signal with little to no detectable GFP, suggesting a later-stage state after attenuation of ongoing p21 transcription.

To investigate transcriptional differences across senescence progression, we separated $p21^+$ cells with low-to-undetectable GFP (normalized GFP < 0.01) from cells with detectable GFP to represent a later-stage, post-attenuation subset (Figure 1.16.C). Both subsets were similarly represented across the three biological replicates, making batch effects an unlikely explanation for the later analytical result (Figure 1.16.C). In total, 422 $p21^{tdTomato}$ cells (31.5%) were separated from 916 $p21^{GFP/tdTomato}$ cells (68.5%) (Figure 1.16.D). Differential expression analysis was then performed against the two subsets for the identification of potential transcriptional changes in two distinct senescent stages (Figure 1.16.E). This analysis revealed stage-specific gene enrichment patterns consistent with core senescence-associated programs.

The active p21-expressing subset was enriched genes such as *Serpina6*, *Pon1*, and *Rgn*, all of which have been linked to cellular aging and senescence-related phenotypes in protein and transcript-level studies (50–52). In the same early-stage cluster, the expression of *H2-Ab1* suggested an emerging immune-interacting feature that have been observed in aging-associated transcriptomic states (53). In contrast, the subset representing later-stage senescence after p21 signal attenuation showed a more overt secretory acute-phase and redox-stress signature,

dominated by the expression of *Saa1/Saa2*, *Hp*, and *Mt1* (54–57). Together, these results point to a tightly regulated progression of senescence, in which cells adopt distinct transcriptional programs that both respond to and reshape the local microenvironment at different stages of the senescent state.

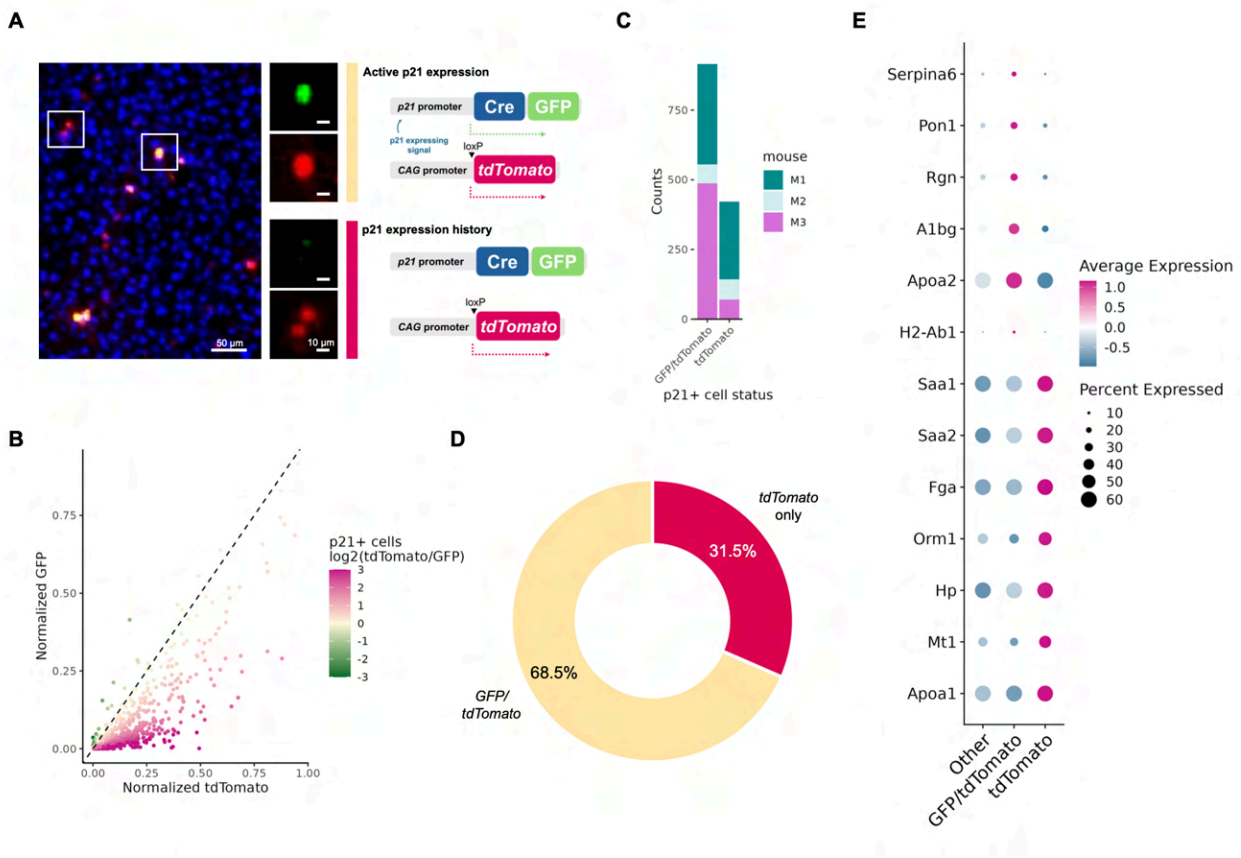


Figure 1.16 Senescence undergoes transcriptional shifts across distinct stages

(A) Schematic of the p21-Cre dual-reporter system. A representative DAPI/GFP/*tdTomato* view is shown (selected from Figure 1.10.A). Boxed regions indicate senescent cells with active p21 transcription (top row) or senescent cells with attenuated p21 expression (bottom row). (B) Distributions of normalized GFP and *tdTomato* signals. Each dot represents one $p21^{+}$ cell and is colored by the *tdTomato*/GFP signal ratio. (C) Quantification of the prevalence of $p21^{GFP/tdTomato}$ cells and $p21^{tdTomato}$ cells across mice. (D) Overall relative proportions of $p21^{GFP/tdTomato}$ cells and $p21^{tdTomato}$ cells. (E) Representative expression patterns of genes that are upregulated in $p21^{GFP/tdTomato}$ cells or $p21^{tdTomato}$ cells.

Interferon-stimulated gene activation in aging is independent of p21 status

Interferon-stimulated genes are a transcriptional program induced downstream of type I interferon signaling that can be activated not only by infection, but also by DNA damaging stress (46,47). It has been reported that ISG activity is a recurrent component of senescence biology, with roles in mediating DNA damage response and shaping inflammatory signaling (47,58).

In our aged liver dataset, we were able to identify this ISG-expressing cluster (Figure 1.17.A) as well, with a distinct transcriptional signature. We summarized this program using a cumulative ISG score and assessed its relative expression across cells (Figure 1.17.B-C). The individual ISGs contributing to the score are shown in Figure 1.17.D, with *Rsad2* exhibiting the most pronounced change. In addition to canonical ISGs, inflammatory chemokines such as *Cxcl10* and *Cxcl9* were also upregulated in this cluster, suggesting a locally activated inflammatory niche.

Spatial mapping further revealed aggregated foci of ISG-expressing cells (Figure 1.17.E-F) in the aged liver. Based on histology, these cells are likely hepatocytes, despite reduced expression of canonical hepatic markers (Figure 1.17.D and 1.17.F). Notably, $p21^{+}$ cells showed relatively low overlap with the ISG-expressing population by fluorescence and cell-type matching (Figure 1.13.E and 1.17.F), supporting a model in which type I interferon signaling and p21 activation are plausibly controlled in independent and parallel regulatory axes during senescence development.

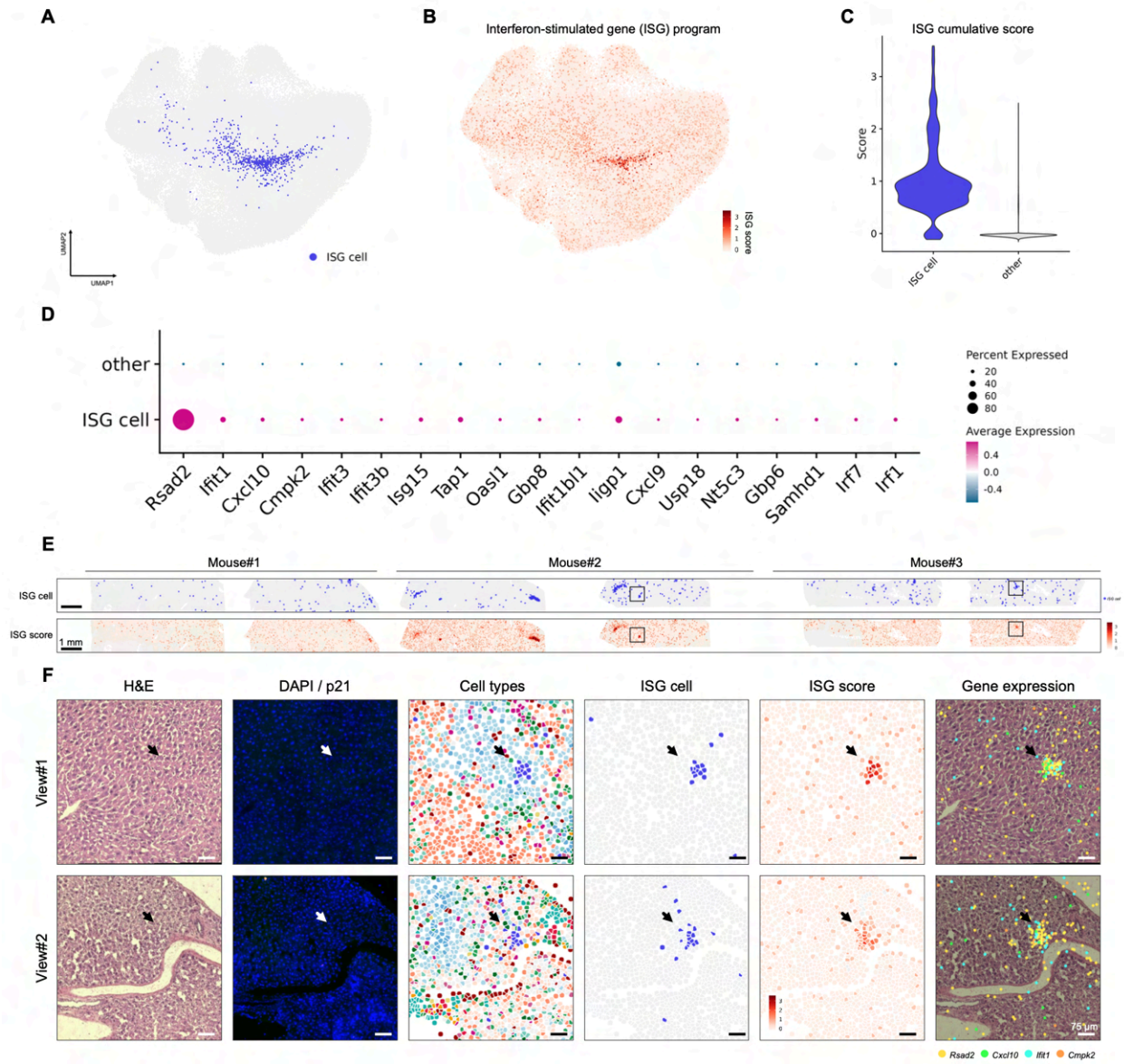


Figure 1.17 Interferon-stimulated gene activation in aging is independent of p21 status

(A-B) UMAP embedding colored by the ISG cluster (A) or by the cumulative ISG gene score (B). (C) Quantification of the cumulative ISG gene score. (D) Representative expression patterns of ISG genes. (E) Overview of liver sections colored by ISG cluster (top row) or by cumulative ISG gene score (bottom row). (F) Higher-magnification spatial maps of the boxed regions in (E). Arrows indicate ISG cells. Expression of the indicated ISG genes is shown as color dots in gene-expression maps.

1.4 Discussion

The data presented here demonstrate that Seq-Scope can visualize the histological organization of the transcriptome architecture at multiple scales, including at the tissue zonation level, the cellular level, and even the subcellular level. Equipped with an ultra-high-resolution output and an outstanding transcriptome capture output, Seq-Scope drew a clear boundary between different tissue zones, cell types and subcellular components. Previously existing technologies could not provide this level of clarity due to their low-resolution output and/or inefficiency in transcriptome capture.

Several factors could have contributed to Seq-Scope's high transcriptome capture efficiency. First, the dense and tight arrangement of barcoded clusters in Seq-Scope could have increased the transcriptome capture rate since they almost eliminated "blind spot" areas between the spatial features. Second, unlike some methods that produce a bumpy array surface, Seq-Scope produces a flat array surface, enabling direct interaction between the capture probe and tissue sample. Third, solid-phase amplification, limited by molecular crowding (59), might have provided the two-dimensional concentration of RNA-capture probes ideal for the molecular interaction with tissue-derived RNA. Finally, biochemical strategies specific to our protocol, such as the secondary strand synthesis, retrieval, and amplification methods, could have increased the yield of transcriptome recovery.

Another benefit of Seq-Scope is its scalability and adaptability. In our initial proof-of-concept study, we used the MiSeq platform for the HDMI-array generation (10). Over the years, we have upgraded Seq-Scope multiple times through sequencing platforms that use spatially localized amplification, such as Illumina HiSeq (22,23), and NovaSeq (34), to generate the HDMI-array, providing a much bigger uninterrupted imaging area.

In terms of the cost, the current MiSeq-based HDMI-array can be generated at approximately $150/mm2. The cost could be further reduced to $11/mm2 in HiSeq2500 or $2.6/mm2 in NovaSeq, based on current costs of sequencing. As for turnaround time, the HDMI-array generation takes a day after 1st-Seq, and library preparation can be completed in two days. A single MiSeq machine can finish 1st-Seq in ~3 hours since it only involves cluster generation and 25bp single-end sequencing steps. An experienced researcher can disassemble the 1st-Seq flow cell within 5-10 min. The procedure is straightforward and not laborious or technically

demanding. Therefore, Seq-Scope can make the ultra-high-resolution ST accessible for any type and scale of basic science and clinical work.

Convenience in the data analysis pipeline is another strength of Seq-Scope. Most of the Seq-Scope analyses were seamlessly performed with widely-used standard software tools, such as Illumina RTA (60), STARsolo (61) and Seurat (62). Being relatively effortless from an analytic perspective will be a hugely attractive factor for many experimental biologists.

However, it is worth noting that the MiSeq flow cell was not originally designed for ST (60); therefore, exposing the cluster surface was initially challenging. In the liver dataset, scratch-associated data losses were often observed due to the damages during disassembly. When generating the colon dataset, we minimized the damage by protecting the HDMI-array with hydrogel filling. Therefore, the colon result was almost scratch-free and revealed higher numbers of UMI per area than the liver result. In the future, designing a detachable flow cell for 1st-Seq could make this process even more straightforward.

The current HDMI-array is not encoded by the UMI sequence; therefore, we used random priming positions during the secondary strand synthesis as the alternative UMI. Based on our library size diversity (400-850bp), the UMI diversity available for a single gene is estimated to be ~400. In each HDMI, the ratios between the gene and UMI numbers are very close to 1:1, indicating that the current UMI diversity (~400) is far from saturation and should be more than enough to reliably de-duplicate sequencing reads without the risk of over-collapsing.

Due to the extremely high number of HDMI and relatively low number of UMI per HDMI, HDMI-UMI information needs to be aggregated in some way to produce an interpretable result. In the ST field, the 10 μm feature size is considered a sweet spot for spatial single-cell analysis (63). Consistent with this idea, data binning with 10 μm grids performed well for identifying various cell types from the liver and colon datasets, while smaller grids did not perform well. To overcome this limitation and fully utilize Seq-Scope's high resolution, we employed three independent approaches: (i) Histology-guided image segmentation method for spatial single-cell analysis, (ii) Multiscale sliding windows analysis for high-resolution cell type mapping, and (iii) Direct spatial plotting to monitor spatial gene expression at high resolution. The results from these analyses demonstrated the utility of Seq-Scope in performing high-resolution spatial single-cell/subcellular analysis and identifying biological information that former technologies were unable to approach.

Our results also indicate that Seq-Scope has the potential to improve and complement current scRNA-seq approaches. Conventional scRNA-seq of solid tissues typically requires extensive dissociation and cell-sorting steps, which inevitably lead to loss of tissue architecture, a feature that often plays a critical role in pathophysiology. In several situations, such as acne formation and senescence niches, cells are tightly joined within a microenvironment that is not amenable to conventional scRNA-seq. By capturing the transcriptome directly from a frozen tissue slice, Seq-Scope can recover single-cell transcriptome signatures from cell types that have previously been difficult to work with.

Despite the robust nature of Seq-Scope, several limitations should be acknowledged. First, the current Seq-Scope study focused exclusively on the poly(A)-tagged transcriptome and therefore did not capture information beyond that. This limitation can be overcome through further research; details are discussed in Chapter 4. Second, cellular regulation often extends beyond transcription, and prior work has reported cases in which transcriptomic changes do not align with proteomic readouts. It therefore remains unclear whether the mRNA differences we observe can be translated into corresponding changes in protein abundance. Additional validation using complementary technologies is therefore encouraged. For example, the presence of TREM2 macrophages in acne lesions is supported not only by Seq-Scope, but also by single-cell RNA sequencing and independent biomedical experiments that validate the underlying mechanism. Third, pathophysiology is highly context dependent, and inter-individual variation can produce non-uniform readouts due to differences in lifetime exposures and physiological history (38). Larger cohorts are often needed to strengthen the conclusions.

Still, Seq-Scope technology provides a versatile solution for spatial single-cell and subcellular analyses. A single run of Seq-Scope could produce the microscopic gene expression imaging data for the whole transcriptome. The vast amount of information produced by Seq-Scope would accelerate scientific discoveries to illustrate biological complexity and heterogeneity beyond traditional cellular classification, leading to a new paradigm in molecular diagnosis.

1.5 Methods

Human skin biopsy

The collection of skin biopsy was performed in accordance with protocols approved by the institutional review board at University of California, Los Angeles. All patients provided written informed consent. Acne donors were recruited from the University of California, Los Angeles. Patients were excluded from the study if they had been using acne medication, hormonal regulation medication, or hormone-related implants in the past three months. Skin samples were obtained from 4-mm punch biopsies of early (< 24 hour) papules on the back (22).

p21-Cre Dual-Reporter Mice Model

p21-Cre dual-reporter mice on C57BL/6 background were generated as previously described (42,43,45). In brief, a p21 promoter fragment driving a Cre recombinase and GFP reporter was synthesized by GenScript and cloned into the pBBT378 vector for site-specific recombination at the mouse H11 genomic locus. Positive embryonic clones were implanted into C57BL/6 females to generate p21-Cre-GFP mice. p21-Cre-GFP mice were then crossed with floxed knock-in *tdTomato* mice (strain no. 007914, The Jackson Laboratory) bearing a loxP-stop-loxP *tdTomato* cassette under the control of the CAG promoter. The offspring, p21-Cre-GFP/*tdTomato* mice (p21-Cre dual-reporter mice), were validated and maintained according to Institutional Animal Care and Use Committee (IACUC) protocol.

Seq-Scope Array Preparation (1st-Seq)

Seq-Scope procedure was described in detail previously (10,34). Seq-Scope is a solid-phase transcriptome-capturing system build upon Illumina sequencing platforms with synthetic barcoded single-stranded oligonucleotide library (HDMI32-DraI, Eurofins). Optimal concentration of HDMI32-DraI oligonucleotides (MiSeq & HiSeq: 100 pM; NovaSeq: 1-2nM per lane) was seeded onto the flow cell and amplified through synthesis cycles to form barcoded clusters on the surface. Custom sequencing primer (Read1-DraI, Eurofins) was used at the sequence-by-synthesis stage to read the barcode sequence. Sequencer was manually set to stop after 37bp single-end reading. Following the run, the flow cell and the output data were retrieved. The output FASTQ file will provide the sequence and the XY coordinates of the barcodes.

The retrieved flow cell requires preprocessing to become a Seq-Scope array. The flow cell was washed with nuclease-free water three times initially, followed by overnight incubation of DraI (R0129, NEB) and CIAP (M0525, NEB) enzyme mixture at 37 °C. The flow cell was treated with exonuclease I (M2903, NEB) cocktail at 37 °C for 45 min the next day to remove remaining flow cell-attached primer. The flow cell was washed three times with nuclease-free water, three times with 0.1 N NaOH (5 min each), and three times with 0.1 M Tris (pH 7.5). The cover was then disassembled with a tungsten carbide tip scriber (IMT-8806, IMT), exposing the array surface for tissue attachment. For MiSeq and HiSeq flow cells, an agarose gel is recommended to be placed in the channel before disassembly to prevent damaging the array surface during the process.

Tissue Preparation, Sectioning, and processing

Tissues were freshly dissected, embedded into OCT compound (23-730-571, Fisher Scientific), and snap-frozen by submerging into liquid nitrogen pre-chilled 2-Methylbutane (MX0760, Sigma-Aldrich). OCT-mounted frozen tissues were cryosectioned (Leica CM3050S, −15 °C) at a 5° cutting angle to obtain 10-µm sections. Sections were placed on the array surface and rewarmed at room temperature for complete attachment. Attached sections were fixed in 4% formaldehyde (15170, Electron Microscopy Sciences) at room temperature for 10 min. Fixing solution was washed away with nuclease-free water. If needed, the tissue can be optionally stained with 0.1 ug/ml DAPI solution (62248, Thermal Scientific) 10 min at room temperature to reveal nuclear location. Stained tissue sections were mounted in 85% glycerol (BP229-1, Fisher Scientific) with coverslips for fluorescence imaging using Keyence digital darkroom system. Afterward, the array was retrieved, cleaned, and subjected to hematoxylin and eosin (H&E) staining according to our protocol (34). H&E images were also captured by the Keyence digital darkroom system.

Seq-Scope RNA Library Generation and Sequencing (2nd-Seq)

Seq-Scope library preparation was also described in detail previously (10,34). In brief, tissue permeabilization was performed at 37 °C using 0.2 U/µL collagenase I (17018-029, Thermofisher), and 1 mg/mL pepsin (P7000, Sigma) in 0.1M HCl with incubation time of 20 min and 10 min each. The permeabilized tissue sections were equilibrated with 1X Maxima RT

buffer (EP0751, Thermofisher), followed by overnight incubation with reverse transcription mixture (1X RT buffer (EP0751, Thermofisher), 4% Ficoll PM-400 (F4375-10G, Sigma), 1mM dNTPs (N0477L, NEB), RNase inhibitor (30281, Lucigen), Maxima H-RTase (EP0751, Thermofisher)) in a humidified chamber at 42 °C.

On the following day, sections were incubated with Exonuclease I (M2903, NEB) at 37 °C for 45 min to remove unused single-stranded DNA probes. Sections were then digested in tissue lysis cocktail (100 mM Tris pH 8.0, 100 mM NaCl, 2% SDS, 5 mM EDTA, 16 U/mL Proteinase K (P8107S, NEB)) at 37 °C for 40 min. Upon the completion of digestion, the array was washed sequentially with nuclease-free water, 0.1N NaOH (5 min), and 0.1M Tris pH7.5, three times each. The array was then loaded with library synthesis mixture (1X NEBuffer-2 (NEB), 10 uM TruSeq Read2-conjugated Random Primer (IDT), 1mM dNTPs (N0477, NEB), Klenow Fragment (M0212, NEB), and nuclease-free water) and incubated in a humidified chamber at 37 °C for 2 hr. The array was cleaned with nuclease-free water after the completion of the reaction. The array was then incubated with 0.1N NaOH for 5 min to elute the barcoded cDNA library. The elution was neutralized by 3 M potassium acetate (pH5.5) and purified using AMPure XP beads (1.8X bead/sample ratio, A63881, Beckman Coulter) according to the manufacturer's instruction.

Library amplification was carried out in two PCR steps using Kapa HiFi Hotstart Readymix (KK2602, KAPA Biosystems). In PCR1, TruSeq forward and reverse primers were added, and PCR products were purified using AMPure XP beads (1X bead/sample ratio). In PCR2, TruSeq indexing primers were used, followed by AMPure XP-based size selection (0.6X bead/sample ratio). Libraries were assessed on an Agilent 2100 Bioanalyzer and re-purified when necessary, before sequencing with paired-end 100-cycle reads.

Sequencing Data Processing

Data were processed as described previously using NovaScope pipeline (34). A 1st-Seq data table was first generated from the 1st-Seq FASTQ files, containing filtered barcode sequences and their corresponding spatial coordinates. The 2nd-Seq FASTQ reads were then processed against this table by (i) mapping reads to the spatial barcode map using the spatial barcode sequences, (ii) filtering barcoded reads based on validated barcode sequences, and (iii) assigning spatial coordinates to the retained reads. Reads with assigned spatial information were aligned to the

reference genome using STAR (61), and the resulting alignments were used to generate an SGE matrix.

Alignment between histology and spatial dataset

Aligned transcripts in the SGE matrix were plotted spatially based on the coordinates for visualization. SGE images were then subjected to semi-automatic alignment with the H&E image using QGIS (version 3.22.9) georeferencer function or *historef* (34).

Single Cell Segmentation (DAPI-based, optional)

DAPI staining was enhanced for signal recognition optimization to create a DAPI vector mask. Each vector point was dilated uniformly with a 6-pixel radius to create cell segment boundaries. Transcripts within each segment were aggregated into a single datapoint, which was treated as a single cell with a given segment ID. Aggregated datapoints were stored in a new spatial DGE matrix for downstream analysis.

Uniform hexagonal gridding

Spatial hexagon grids (10-24 μm, non-overlapping) were generated using the NOVASCOPE pipeline (34), where transcripts within each grid were aggregated and treated as a single unit, with spatial coordinates assigned to the hexagon center.

Data Analysis and Visualization

Single-cell SGE matrix was analyzed in the Seurat package (62,64). Cells with low unique feature counts were removed to optimize clustering performance. Batches were normalized with SCTransform, followed by integration using SCT-normalized values. Principal components were computed using RunPCA, and high-quality components were selected to generate UMAP embeddings. Cells were clustered using FindNeighbors followed by FindClusters. Cell types were annotated based on marker gene expression identified with FindMarkers and FindAllMarkers functions. Data visualization was supported by plotting functions in Seurat and ggplot2. Cell types were projected into spatial plots based on their segment ID using custom python scripts. Spatial gene expression plots were generated with a custom software platform that displays histology and SGE matrix simultaneously.

1.6 References

1. Ståhl PL, Salmén F, Vickovic S, Lundmark A, Navarro JF, Magnusson J, Giacomello S, Asp M, Westholm JO, Huss M, et al. Visualization and analysis of gene expression in tissue sections by spatial transcriptomics. Science. 2016 Jul 1;353(6294):78–82. doi:10.1126/science.aaf2403 PubMed PMID: 27365449.

2. Bergenstråhle J, Larsson L, Lundeberg J. Seamless integration of image and molecular analysis for spatial transcriptomics workflows. BMC Genomics. 2020 Jul 14;21(1):482. doi:10.1186/s12864-020-06832-3 PubMed PMID: 32664861; PubMed Central PMCID: PMC7386244.

3. Liu Y, Yang M, Deng Y, Su G, Enninful A, Guo CC, Tebaldi T, Zhang D, Kim D, Bai Z, et al. High-Spatial-Resolution Multi-Omics Sequencing via Deterministic Barcoding in Tissue. Cell. 2020 Dec 10;183(6):1665-1681.e18. doi:10.1016/j.cell.2020.10.026 PubMed PMID: 33188776; PubMed Central PMCID: PMC7736559.

4. Stickels RR, Murray E, Kumar P, Li J, Marshall JL, Di Bella DJ, Arlotta P, Macosko EZ, Chen F. Highly sensitive spatial transcriptomics at near-cellular resolution with Slide-seqV2. Nat Biotechnol. 2021 Mar;39(3):313–9. doi:10.1038/s41587-020-0739-1 PubMed PMID: 33288904; PubMed Central PMCID: PMC8606189.

5. Rodriques SG, Stickels RR, Goeva A, Martin CA, Murray E, Vanderburg CR, Welch J, Chen LM, Chen F, Macosko EZ. Slide-seq: A scalable technology for measuring genome-wide expression at high spatial resolution. Science. 2019 Mar 29;363(6434):1463–7. doi:10.1126/science.aaw1219 PubMed PMID: 30923225; PubMed Central PMCID: PMC6927209.

6. Marco Salas S, Kuemmerle LB, Mattsson-Langseth C, Tismeyer S, Avenel C, Hu T, Rehman H, Grillo M, Czarnewski P, Helgadottir S, et al. Optimizing Xenium In Situ data utility by quality assessment and best-practice analysis workflows. Nat Methods. 2025 Apr;22(4):813–23. doi:10.1038/s41592-025-02617-2 PubMed PMID: 40082609; PubMed Central PMCID: PMC11978515.

7. He S, Bhatt R, Brown C, Brown EA, Buhr DL, Chantranuvatana K, Danaher P, Dunaway D, Garrison RG, Geiss G, et al. High-plex imaging of RNA and proteins at subcellular resolution in fixed tissue by spatial molecular imaging. Nat Biotechnol. 2022 Dec;40(12):1794–806. doi:10.1038/s41587-022-01483-z PubMed PMID: 36203011.

8. Zhang M, Pan X, Jung W, Halpern AR, Eichhorn SW, Lei Z, Cohen L, Smith KA, Tasic B, Yao Z, et al. Molecularly defined and spatially resolved cell atlas of the whole mouse brain. Nature. 2023 Dec;624(7991):343–54. doi:10.1038/s41586-023-06808-9 PubMed PMID: 38092912; PubMed Central PMCID: PMC10719103.

9. Slovin S, Carissimo A, Panariello F, Grimaldi A, Bouché V, Gambardella G, Cacchiarelli D. Single-Cell RNA Sequencing Analysis: A Step-by-Step Overview. Methods Mol Biol. 2021;2284:343–65. doi:10.1007/978-1-0716-1307-8_19 PubMed PMID: 33835452.

10. Cho CS, Xi J, Si Y, Park SR, Hsu JE, Kim M, Jun G, Kang HM, Lee JH. Microscopic examination of spatial transcriptome using Seq-Scope. Cell. 2021 Jun 24;184(13):3559-3572.e22. doi:10.1016/j.cell.2021.05.010 PubMed PMID: 34115981; PubMed Central PMCID: PMC8238917.

11. 10x Genomics [Internet]. [cited 2026 Feb 17]. Visium HD: Whole transcriptome spatial discovery at single cell scale. Available from: https://www.10xgenomics.com/library/8012d2

12. Chen A, Liao S, Cheng M, Ma K, Wu L, Lai Y, Qiu X, Yang J, Xu J, Hao S, et al. Spatiotemporal transcriptomic atlas of mouse organogenesis using DNA nanoball-patterned arrays. Cell. 2022 May 12;185(10):1777-1792.e21. doi:10.1016/j.cell.2022.04.003 PubMed PMID: 35512705.

13. Fu X, Sun L, Dong R, Chen JY, Silakit R, Condon LF, Lin Y, Lin S, Palmiter RD, Gu L. Polony gels enable amplifiable DNA stamping and spatial transcriptomics of chronic pain. Cell. 2022 Nov 23;185(24):4621-4633.e17. doi:10.1016/j.cell.2022.10.021 PubMed PMID: 36368323; PubMed Central PMCID: PMC9691594.

14. Macosko EZ, Basu A, Satija R, Nemesh J, Shekhar K, Goldman M, Tirosh I, Bialas AR, Kamitaki N, Martersteck EM, et al. Highly Parallel Genome-wide Expression Profiling of Individual Cells Using Nanoliter Droplets. Cell. 2015 May 21;161(5):1202–14. doi:10.1016/j.cell.2015.05.002 PubMed PMID: 26000488; PubMed Central PMCID: PMC4481139.

15. BD Rhapsody™ System mRNA Whole Transcriptome Analysis (WTA) Library Preparation Protocol.

16. Salmén F, Ståhl PL, Mollbrink A, Navarro JF, Vickovic S, Frisén J, Lundeberg J. Barcoded solid-phase RNA capture for Spatial Transcriptomics profiling in mammalian tissue sections. Nat Protoc. 2018 Nov;13(11):2501–34. doi:10.1038/s41596-018-0045-2 PubMed PMID: 30353172.

17. 10x Genomics [Internet]. [cited 2026 Feb 17]. Visium Spatial Gene Expression Reagent Kits User Guide | Official 10x Genomics Support. Available from: https://www.10xgenomics.com/support/spatial-gene-expression-fresh-frozen/documentation/steps/library-construction/visium-spatial-gene-expression-reagent-kits-user-guide

18. 10x Genomics [Internet]. [cited 2026 Feb 17]. Visium Spatial Tissue Optimization Reagents Kits User Guide | Official 10x Genomics Support. Available from: https://www.10xgenomics.com/support/spatial-gene-expression-fresh-frozen/documentation/steps/tissue-optimization/visium-spatial-tissue-optimization-reagents-kits-user-guide

19. Benjamin Kaminow, Dinar Yunusov, Alexander Dobin. STARsolo: accurate, fast and versatile mapping/quantification of single-cell and single-nucleus RNA-seq data. bioRxiv; 2021. doi:10.1101/2021.05.05.442755

20. Xi J, Lee JH, Kang HM, Jun G. STtools: A Comprehensive Software Pipeline for Ultra-high Resolution Spatial Transcriptomics Data. Bioinforma Adv. 2022;2(1):vbac061. doi:10.1093/bioadv/vbac061 PubMed PMID: 36284674; PubMed Central PMCID: PMC9590442.

21. Hsu JE, Ruiz L, Hwang Y, Guzman S, Cho CS, Cheng W, Si Y, Macpherson P, Schrank M, Jun G, et al. High-Resolution Spatial Transcriptomic Atlas of Mouse Soleus Muscle: Unveiling Single Cell and Subcellular Heterogeneity in Health and Denervation. bioRxiv; 2024. doi:10.1101/2024.02.26.582103

22. Do TH, Ma F, Andrade PR, Teles R, de Andrade Silva BJ, Hu C, Espinoza A, Hsu JE, Cho CS, Kim M, et al. TREM2 macrophages induced by human lipids drive inflammation in acne lesions. Sci Immunol. 2022 Jul 22;7(73):eabo2787. doi:10.1126/sciimmunol.abo2787 PubMed PMID: 35867799; PubMed Central PMCID: PMC9400695.

23. Ma F, Plazyo O, Billi AC, Tsoi LC, Xing X, Wasikowski R, Gharaee-Kermani M, Hile G, Jiang Y, Harms PW, et al. Single cell and spatial sequencing define processes by which keratinocytes and fibroblasts amplify inflammatory responses in psoriasis. Nat Commun. 2023 Jun 12;14(1):3455. doi:10.1038/s41467-023-39020-4 PubMed PMID: 37308489; PubMed Central PMCID: PMC10261041.

24. Schott M, León-Periñán D, Splendiani E, Strenger L, Licha JR, Pentimalli TM, Schallenberg S, Alles J, Samut Tagliaferro S, Boltengagen A, et al. Open-ST: High-resolution spatial transcriptomics in 3D. Cell. 2024 Jul 25;187(15):3953-3972.e26. doi:10.1016/j.cell.2024.05.055 PubMed PMID: 38917789.

25. Poovathingal S, Davie K, Borm LE, Vandepoel R, Poulvellarie N, Verfaillie A, Corthout N, Aerts S. Nova-ST: Nano-patterned ultra-dense platform for spatial transcriptomics. Cell Rep Methods. 2024 Aug 19;4(8):100831. doi:10.1016/j.crmeth.2024.100831 PubMed PMID: 39111312; PubMed Central PMCID: PMC11384075.

26. Hao Y, Stuart T, Kowalski MH, Choudhary S, Hoffman P, Hartman A, Srivastava A, Molla G, Madad S, Fernandez-Granda C, et al. Dictionary learning for integrative, multimodal and scalable single-cell analysis. Nat Biotechnol. 2024 Feb;42(2):293–304. doi:10.1038/s41587-023-01767-y

27. Wolf FA, Angerer P, Theis FJ. SCANPY: large-scale single-cell gene expression data analysis. Genome Biol. 2018 Feb 6;19(1):15. doi:10.1186/s13059-017-1382-0 PubMed PMID: 29409532; PubMed Central PMCID: PMC5802054.

28. Si Y, Lee C, Hwang Y, Yun JH, Cheng W, Cho CS, Quiros M, Nusrat A, Zhang W, Jun G, et al. FICTURE: scalable segmentation-free analysis of submicron-resolution spatial transcriptomics. Nat Methods. 2024 Oct;21(10):1843–54. doi:10.1038/s41592-024-02415-2

29. Soille P, Vincent LM. Determining watersheds in digital pictures via flooding simulations. In: Visual Communications and Image Processing ’90: Fifth in a Series

[Internet]. SPIE; 1990 [cited 2026 Feb 18]. p. 240–50. Available from: https://www.spiedigitallibrary.org/conference-proceedings-of-spie/1360/0000/Determining-watersheds-in-digital-pictures-via-flooding-simulations/10.1117/12.24211.full doi:10.1117/12.24211

30. Pachitariu M, Stringer C. Cellpose 2.0: how to train your own model. Nat Methods. 2022 Dec;19(12):1634–41. doi:10.1038/s41592-022-01663-4

31. Stringer C, Wang T, Michaelos M, Pachitariu M. Cellpose: a generalist algorithm for cellular segmentation. Nat Methods. 2021 Jan;18(1):100–6. doi:10.1038/s41592-020-01018-x

32. Dries R, Zhu Q, Dong R, Eng CHL, Li H, Liu K, Fu Y, Zhao T, Sarkar A, Bao F, et al. Giotto: a toolbox for integrative analysis and visualization of spatial expression data. Genome Biol. 2021 Mar 8;22(1):78. doi:10.1186/s13059-021-02286-2 PubMed PMID: 33685491; PubMed Central PMCID: PMC7938609.

33. Palla G, Spitzer H, Klein M, Fischer D, Schaar AC, Kuemmerle LB, Rybakov S, Ibarra IL, Holmberg O, Virshup I, et al. Squidpy: a scalable framework for spatial omics analysis. Nat Methods. 2022 Feb;19(2):171–8. doi:10.1038/s41592-021-01358-2

34. Kim Y, Cheng W, Cho CS, Hwang Y, Si Y, Park A, Schrank M, Hsu JE, Anacleto A, Xi J, et al. Seq-Scope: repurposing Illumina sequencing flow cells for high-resolution spatial transcriptomics. Nat Protoc. 2025 Mar;20(3):643–89. doi:10.1038/s41596-024-01065-0

35. Bahar Halpern K, Caspi I, Lemze D, Levy M, Landen S, Elinav E, Ulitsky I, Itzkovitz S. Nuclear Retention of mRNA in Mammalian Tissues. Cell Rep. 2015 Dec 29;13(12):2653–62. doi:10.1016/j.celrep.2015.11.036 PubMed PMID: 26711333; PubMed Central PMCID: PMC4700052.

36. Baratta JL, Ngo A, Lopez B, Kasabwalla N, Longmuir KJ, Robertson RT. Cellular organization of normal mouse liver: a histological, quantitative immunocytochemical, and fine structural analysis. Histochem Cell Biol. 2009 Jun;131(6):713–26. doi:10.1007/s00418-009-0577-1 PubMed PMID: 19255771; PubMed Central PMCID: PMC2761764.

37. Donne R, Saroul-Aïnama M, Cordier P, Celton-Morizur S, Desdouets C. Polyploidy in liver development, homeostasis and disease. Nat Rev Gastroenterol Hepatol. 2020 Jul;17(7):391–405. doi:10.1038/s41575-020-0284-x

38. Gorgoulis V, Adams PD, Alimonti A, Bennett DC, Bischof O, Bishop C, Campisi J, Collado M, Evangelou K, Ferbeyre G, et al. Cellular Senescence: Defining a Path Forward. Cell. 2019 Oct 31;179(4):813–27. doi:10.1016/j.cell.2019.10.005 PubMed PMID: 31675495.

39. Wang B, Han J, Elisseeff JH, Demaria M. The senescence-associated secretory phenotype and its physiological and pathological implications. Nat Rev Mol Cell Biol. 2024 Dec;25(12):958–78. doi:10.1038/s41580-024-00727-x PubMed PMID: 38654098.

40. Coppé JP, Patil CK, Rodier F, Sun Y, Muñoz DP, Goldstein J, Nelson PS, Desprez PY, Campisi J. Senescence-associated secretory phenotypes reveal cell-nonautonomous functions of oncogenic RAS and the p53 tumor suppressor. PLoS Biol. 2008 Dec 2;6(12):2853–68. doi:10.1371/journal.pbio.0060301 PubMed PMID: 19053174; PubMed Central PMCID: PMC2592359.

41. Noda A, Ning Y, Venable SF, Pereira-Smith OM, Smith JR. Cloning of senescent cell-derived inhibitors of DNA synthesis using an expression screen. Exp Cell Res. 1994 Mar;211(1):90–8. doi:10.1006/excr.1994.1063 PubMed PMID: 8125163.

42. Wang B, Wang L, Gasek NS, Kuo CL, Nie J, Kim T, Yan P, Zhu J, Torrance BL, Zhou Y, et al. Intermittent clearance of p21-highly-expressing cells extends lifespan and confers sustained benefits to health and physical function. Cell Metab. 2024 Aug 6;36(8):1795-1805.e6. doi:10.1016/j.cmet.2024.07.006 PubMed PMID: 39111286.

43. Wang B, Wang L, Gasek NS, Zhou Y, Kim T, Guo C, Jellison ER, Haynes L, Yadav S, Tchkonia T, et al. An inducible p21-Cre mouse model to monitor and manipulate p21-highly-expressing senescent cells in vivo. Nat Aging. 2021 Oct;1(10):962–73. doi:10.1038/s43587-021-00107-6 PubMed PMID: 35024619; PubMed Central PMCID: PMC8746571.

44. Ogrodnik M, Carlos Acosta J, Adams PD, d'Adda di Fagagna F, Baker DJ, Bishop CL, Chandra T, Collado M, Gil J, Gorgoulis V, et al. Guidelines for Minimal Information on Cellular Senescence Experimentation in vivo. Cell. 2024 Aug 8;187(16):4150–75. doi:10.1016/j.cell.2024.05.059 PubMed PMID: 39121846; PubMed Central PMCID: PMC11790242.

45. Gasek NS, Yan P, Zhu J, Purushothaman KR, Kim T, Wang L, Wang B, Flynn WF, Sun M, Guo C, et al. Clearance of p21 highly expressing senescent cells accelerates cutaneous wound healing. Nat Aging. 2025 Jan;5(1):21–7. doi:10.1038/s43587-024-00755-4 PubMed PMID: 39537987; PubMed Central PMCID: PMC12205026.

46. Schneider WM, Chevillotte MD, Rice CM. Interferon-stimulated genes: a complex web of host defenses. Annu Rev Immunol. 2014;32:513–45. doi:10.1146/annurev-immunol-032713-120231 PubMed PMID: 24555472; PubMed Central PMCID: PMC4313732.

47. Yu Q, Katlinskaya YV, Carbone CJ, Zhao B, Katlinski KV, Zheng H, Guha M, Li N, Chen Q, Yang T, et al. DNA damage-induced type I interferon promotes senescence and inhibits stem cell function. Cell Rep. 2015 May 5;11(5):785–97. doi:10.1016/j.celrep.2015.03.069 PubMed PMID: 25921537; PubMed Central PMCID: PMC4426031.

48. Suda M, Shimizu I, Katsuumi G, Yoshida Y, Hayashi Y, Ikegami R, Matsumoto N, Yoshida Y, Mikawa R, Katayama A, et al. Senolytic vaccination improves normal and pathological age-related phenotypes and increases lifespan in progeroid mice. Nat Aging. 2021 Dec;1(12):1117–26. doi:10.1038/s43587-021-00151-2

49. Hsiao CL, Katsuumi G, Yoshida Y, Furihata T, Joki Y, Furuuchi R, Liang JQ, Nakagami H, Minamino T. Vaccination targeting senescence-associated transmembrane protein alleviated cardiovascular pathology in the mice. Eur Heart J. 2024 Oct 28;45(Supplement_1):ehae666.3654. doi:10.1093/eurheartj/ehae666.3654

50. Irvine KM, Skoien R, Bokil NJ, Melino M, Thomas GP, Loo D, Gabrielli B, Hill MM, Sweet MJ, Clouston AD, et al. Senescent human hepatocytes express a unique secretory phenotype and promote macrophage migration. World J Gastroenterol WJG. 2014 Dec 21;20(47):17851–62. doi:10.3748/wjg.v20.i47.17851 PubMed PMID: 25548483; PubMed Central PMCID: PMC4273135.

51. Lee YS, Park CO, Noh JY, Jin S, Lee NR, Noh S, Lee JH, Lee KH. Knockdown of paraoxonase 1 expression influences the ageing of human dermal microvascular endothelial cells. Exp Dermatol. 2012 Sep;21(9):682–7. doi:10.1111/j.1600-0625.2012.01555.x PubMed PMID: 22897574.

52. Fujisawa K, Terai S, Hirose Y, Takami T, Yamamoto N, Sakaida I. Senescence marker protein 30 (SMP30)/regucalcin (RGN) expression decreases with aging, acute liver injuries and tumors in zebrafish. Biochem Biophys Res Commun. 2011 Oct 22;414(2):331–6. doi:10.1016/j.bbrc.2011.09.067 PubMed PMID: 21951853.

53. Marin I, Boix O, Garcia-Garijo A, Sirois I, Caballe A, Zarzuela E, Ruano I, Attolini CSO, Prats N, López-Domínguez JA, et al. Cellular Senescence Is Immunogenic and Promotes Antitumor Immunity. Cancer Discov. 2023 Feb 6;13(2):410–31. doi:10.1158/2159-8290.CD-22-0523 PubMed PMID: 36302218; PubMed Central PMCID: PMC7614152.

54. Ebert R, Benisch P, Krug M, Zeck S, Meißner-Weigl J, Steinert A, Rauner M, Hofbauer L, Jakob F. Acute phase serum amyloid A induces proinflammatory cytokines and mineralization via toll-like receptor 4 in mesenchymal stem cells. Stem Cell Res. 2015 Jul 1;15(1):231–9. doi:10.1016/j.scr.2015.06.008

55. Pabis K, Chiari Y, Sala C, Straka E, Giacconi R, Provinciali M, Li X, Brown-Borg H, Nowikovsky K, Valencak TG, et al. Elevated metallothionein expression in long-lived species mediates the influence of cadmium accumulation on aging. GeroScience. 2021 Jun 11;43(4):1975–93. doi:10.1007/s11357-021-00393-3 PubMed PMID: 34117600; PubMed Central PMCID: PMC8492847.

56. Bertaggia E, Scabia G, Dalise S, Lo Verso F, Santini F, Vitti P, Chisari C, Sandri M, Maffei M. Haptoglobin Is Required to Prevent Oxidative Stress and Muscle Atrophy. PLoS ONE. 2014 Jun 24;9(6):e100745. doi:10.1371/journal.pone.0100745 PubMed PMID: 24959824; PubMed Central PMCID: PMC4069100.

57. Hari P, Millar FR, Tarrats N, Birch J, Quintanilla A, Rink CJ, Fernández-Duran I, Muir M, Finch AJ, Brunton VG, et al. The innate immune sensor Toll-like receptor 2 controls the senescence-associated secretory phenotype. Sci Adv. 2019 Jun;5(6):eaaw0254. doi:10.1126/sciadv.aaw0254 PubMed PMID: 31183403; PubMed Central PMCID: PMC6551188.

58. Wang D, Chen K, Wang Z, Wu H, Li Y. Research progress on interferon and cellular senescence. FASEB J. 2024;38(16):e70000. doi:10.1096/fj.202400808RR

59. Mercier JF, Slater GW. Solid phase DNA amplification: a Brownian dynamics study of crowding effects. Biophys J. 2005 Jul;89(1):32–42. doi:10.1529/biophysj.104.051904 PubMed PMID: 15821160; PubMed Central PMCID: PMC1366531.

60. Ravi RK, Walton K, Khosroheidari M. MiSeq: A Next Generation Sequencing Platform for Genomic Analysis. Methods Mol Biol. 2018;1706:223–32. doi:10.1007/978-1-4939-7471-9_12 PubMed PMID: 29423801.

61. Dobin A, Davis CA, Schlesinger F, Drenkow J, Zaleski C, Jha S, Batut P, Chaisson M, Gingeras TR. STAR: ultrafast universal RNA-seq aligner. Bioinformatics. 2013 Jan 1;29(1):15–21. doi:10.1093/bioinformatics/bts635

62. Hao Y, Hao S, Andersen-Nissen E, Mauck WM, Zheng S, Butler A, Lee MJ, Wilk AJ, Darby C, Zager M, et al. Integrated analysis of multimodal single-cell data. Cell. 2021 Jun 24;184(13):3573-3587.e29. doi:10.1016/j.cell.2021.04.048

63. Marx V. Method of the Year: spatially resolved transcriptomics. Nat Methods. 2021 Jan;18(1):9–14. doi:10.1038/s41592-020-01033-y

64. Stuart T, Butler A, Hoffman P, Hafemeister C, Papalexi E, Mauck WM, Hao Y, Stoeckius M, Smibert P, Satija R. Comprehensive Integration of Single-Cell Data. Cell. 2019 Jun 13;177(7):1888-1902.e21. doi:10.1016/j.cell.2019.05.031 PubMed PMID: 31178118.

Chapter 2 High-Resolution Spatial Transcriptomic Atlas of Mouse Soleus Muscle: Unveiling Single-Cell and Subcellular Heterogeneity in Health and Denervation

2.1 Abstract

Skeletal muscle exhibits pronounced cellular and subcellular heterogeneity, but comprehensive spatial mapping has been constrained by cell/nuclei dissociation-based methods that lose tissue architecture and by spatial platforms with insufficient resolution or limited transcriptome coverage. Here we present a high-resolution spatial transcriptomic atlas of mouse soleus muscle in longitudinal sections with unbiased whole-transcriptome coverage, enabling myofiber-resolved transcriptomes while preserving subcellular expression domains across the length of fibers. Combining histology-guided myofiber segmentation with unbiased grid-based mapping, we recover canonical fiber types and reveal widespread hybrid myofiber states in situ, including type IIb-associated signatures that are rare in soleus muscle and evident only when intramyofiber heterogeneity is assessed. At subcellular scale, we delineate the neuromuscular junction (NMJ) as a multi-compartment niche comprising postsynaptic myonuclei and spatially distinct peri-synaptic and myelinating Schwann cell-associated regions, each with characteristic gene programs. Applying this framework to denervation (3 and 7 days) identifies robust fiber-type-specific stress responses, coordinated remodeling of macrophage and fibroblast transcriptomes, and marked intramyofiber heterogeneity, including spatially nonuniform activation of damage-response genes along individual myofibers, with distinct transcriptional domains proximal and distal to the NMJ and associated degenerative histological features. Together, this atlas provides a high-resolution reference for muscle biology and clarifies how denervation reshapes myofiber, synaptic, and stromal-immune programs across cells and within cells in intact tissue.

2.2 Introduction

Skeletal muscle plays a vital role in myriad physiological processes, including movement, posture maintenance, and metabolic regulation (1). This complex tissue,

characterized by its ability to convert chemical energy into mechanical force, is essential not only for physical activity but also for overall health and well-being. The architecture of skeletal muscle is remarkably intricate, featuring a variety of myofiber types, each with distinct functional and metabolic properties, and is interspersed with non-myocyte cells such as satellite cells, immune cells, fibroblasts, and endothelial cells. These diverse elements contribute to the muscle's cellular heterogeneity, with each type playing a specific role in muscle physiology and response to stimuli (2-4).

Skeletal muscle exhibits a profound dependency on neural inputs; innervation is crucial for maintaining muscle tone and function (5). Denervation, the loss of neural input, leads to rapid atrophy and functional impairment, a process that is not only relevant to traumatic injuries and in various neuromuscular diseases but also plays a significant role in the aging process (6). This dynamic interplay between muscle and nerve highlights the importance of understanding muscle biology in a holistic manner. The molecular makeup of skeletal muscles, which includes a diverse array of proteins, enzymes, and signaling molecules, further underpins their dynamic adaptability to various physical demands and stressors, as well as their response to changes in innervation status. Thus, a comprehensive understanding of the detailed structure and function of skeletal muscle, encompassing its heterogeneity and complex interactions with neural inputs, is pivotal. Such knowledge is essential not only for advancing our understanding of muscle physiology but also for developing targeted therapies for muscle-related diseases and addressing the challenges of muscle deterioration with aging.

Single-cell transcriptomic technologies have brought significant insights into cellular heterogeneity across various biological systems, yet their application in skeletal muscle research is challenged by the unique nature of muscle tissue. The elongated and multinucleate structure of myofibers is not amenable to standard fluidics or microwell-based cell sorting techniques, which are designed for smaller, mononucleate cells. In response to these challenges, single-nucleus RNA sequencing (snRNA-seq) has emerged as an alternative, focusing on the analysis of individual nuclei instead of whole cells (4). While snRNA-seq was successfully able to reveal transcriptome heterogeneity in muscle cells (7-11), it falls short in providing a complete picture of the transcriptomic activity of muscle fibers and overall tissues. Primarily, it captures only the nuclear transcriptome, potentially missing critical information contained within the cytoplasm.

This exclusion is particularly significant in muscle fibers, where key elements of the cellular machinery and signaling pathways are located in the cytoplasm. More importantly, snRNA-seq provides no information on the spatial organization of these nuclei within different regions of the muscle fibers, an aspect crucial to understanding the complex interactions and functionality of skeletal muscle.

The limitations of single-cell and single-nucleus approaches have led researchers to explore spatial transcriptomics, a technique that preserves the spatial context of gene expression within tissues. Spatial transcriptomics provides a two-dimensional map of transcriptomic data, allowing researchers to visualize gene expression patterns in relation to the tissue architecture (12-14). However, this method also faces significant challenges when applied to skeletal muscle research. One major limitation is the resolution; current spatial transcriptomics techniques, such as the 10X Visium platform, offer a resolution that is often too coarse to distinguish individual cells or subcellular structures, such as the intricate arrangement of muscle fibers and neuromuscular junctions, as in recently published studies (15-22). This limitation means that the heterogeneity and complex interactions within skeletal muscle tissue can be obscured, with the resulting data representing a mixture of signals from multiple cell types. Furthermore, these data were captured from horizontal tissue sections, making it even more difficult to resolve cell types at specialized regions, such as the neuromuscular junctions. Consequently, while spatial transcriptomics adds valuable context to transcriptomic analysis, its current resolution constraints limit its ability to provide the detailed insights necessary for a complete understanding of the nuanced cellular and molecular dynamics of skeletal muscle.

To overcome the limitations of traditional single-cell and spatial transcriptomics in skeletal muscle research, we employed Seq-Scope, a cutting-edge method that dramatically enhances resolution and analytical depth (12-14, 23, 24). Seq-Scope, characterized by its ability to provide ultra-high-resolution transcriptomic data, allows for the precise mapping of gene expression at the subcellular level. This advanced technology enabled us to conduct a comprehensive profiling of both normal skeletal muscle and its response to denervation along the longitudinal axis of muscle fibers. Our findings, with unprecedented detail, reveal not only the intricate structure of neuromuscular junctions (NMJs) but also previously underappreciated heterogeneity in the individual muscle fiber responses to denervation. Furthermore, our high-resolution data illuminate the complex interactions between myofibers and non-myocyte cells,

both of which undergo substantial changes in their transcriptome phenotypes during denervation responses. This study thus represents a significant advancement in the field of muscle biology, providing a foundation for future research into the molecular mechanisms of muscle function and disease.

2.3 Results

2.3.1 Overview of the experiments and dataset

Skeletal muscle poses unique challenges for single-cell and spatial transcriptomic analyses due to the extreme length and multinucleated architecture of myofibers (4, 7-11). Among skeletal muscles, the mouse soleus represents an especially suitable model for spatial transcriptomic interrogation because of its mixed composition of type I and type II fibers, which exhibit distinct metabolic and functional properties (25). Type I fibers are enriched in mitochondria and optimized for sustained, oxidative activity, whereas type II fibers encompass a spectrum of glycolytic and oxidative phenotypes adapted for rapid force generation (3). In addition, the mouse soleus muscle is well characterized histologically and displays a relatively simple and ordered architecture, with individual fibers extending over more than 70% of the muscle length and aligned parallel to the longitudinal axis. Neuromuscular junctions are positioned at stereotyped locations along each fiber and collectively form a narrow transverse band across the muscle. These anatomical features make the mouse soleus muscle well suited for comprehensive spatial mapping of myofiber and synaptic transcriptomes.

Using the HiSeq implementation of Seq-Scope, which provides a continuous imaging area of approximately 1.5 mm × 60 mm (26), we profiled mouse soleus muscles sectioned along the longitudinal axis. To characterize denervation-induced remodeling, we analyzed muscles collected at 3 and 7 days following surgical denervation. In each animal, the left soleus muscle was denervated through sciatic nerve transection, while the contralateral right muscle served as an innervated control (Figure 2.1.A). In total, 32 longitudinal sections from 11 animals were analyzed, including untreated controls (C0; 3 mice, 13 sections), innervated controls at 3 days (C3; 1 mouse, 2 sections) and 7 days (C7; 1 mouse, 2 sections), as well as denervated muscles at 3 days (D3; 2 mice, 6 sections) and 7 days (D7; 4 mice, 9 sections) (Figure 2.1.B-C).

Seq-Scope enables simultaneous acquisition of hematoxylin and eosin-stained images and spatially resolved RNA capture from the same tissue section (Figure 2.1.D-E). Across all

samples, we detected a total of 76.6 million unique reads mapped to the transcriptome. Spatial distributions of detected transcripts revealed a characteristic pattern, with lower transcript density in the central regions of myofibers and markedly higher density at the fiber periphery (Figure 2.1.D-E; magnified views). This pattern is consistent with muscle ultrastructure, in which the central fiber core is densely packed with myofibrils, whereas nuclei and most transcriptionally active cytoplasmic compartments are concentrated near the sarcolemma.

For downstream analysis, the spatial transcriptome was segmented into a grid of hexagonal bins with 14 μm sides. After excluding mitochondrial genes and hypothetical gene models and applying a minimum threshold of 100 detected gene features per bin to restrict analysis to tissue-covered regions (Figure 2.2.A), we obtained 121,191 hexagonal units. Each unit contained a median of 248 detected transcripts, with a mean ± SD of 311 ± 200 transcripts (Figure 2.2.B). These spatial units were subjected to unsupervised multidimensional clustering to identify major cellular and tissue compartments (Figure 2.1.F-I).

Clustering analysis demonstrated clear separation between control tissues (C0, C3, and C7) and denervated tissues at 3 and 7 days (Figure 2.1.G). Importantly, biological and technical replicates within each experimental group showed strong integration, indicating minimal batch effects across experiments (Figure 2.1.H). These results confirm that the dataset robustly captures biologically meaningful transcriptional changes associated with denervation while maintaining high technical reproducibility.

Annotation of cluster identities revealed major myofiber types present in the soleus muscle, including type I, type IIa, and type IIx fibers, labeled as MF1, MF2A, and MF2X, respectively. In addition, multiple non-myocyte populations were identified, including macrophages, fibroblasts, smooth muscle cells, and adipocytes, each defined by canonical marker gene expression (Figure 2.1.I, Figure 2.2.C). Spatial projection of these clusters using FICTURE, a segmentation-free approach that infers transcriptomic patterns at sub-micrometer resolution (27), recapitulated the microscopic organization of muscle tissue observed by histology. This analysis accurately delineated myofiber boundaries and highlighted localized regions of immune infiltration, fibroblast expansion, and vascular structures (Figure 2.1.F, magnified panels).

Although non-myocyte populations were consistently detected across experimental conditions (Figure 2.2.D), tissue sections (Figure 2.2.E), and technical batches (Figure 2.2.F),

myofiber clusters exhibited strong condition specificity. Distinct myofiber transcriptomic states were observed in control muscles (MF-N), 3-day denervated muscles (MF-D3), and 7-day denervated muscles (MF-D7) (Figure 2.2.D-F), indicating substantial denervation-induced alteration of myofiber gene expression. Application of batch correction and data integration methods successfully unified datasets across all conditions, recovering the canonical myofiber types (MF1, MF2A, and MF2X) and major non-myocyte populations covering all samples (Figure 2.3). However, this integration also attenuated biologically meaningful condition-specific differences and eliminated populations unique to individual experimental states, underscoring the importance of complementary condition-aware analyses for capturing denervation-specific transcriptional programs.

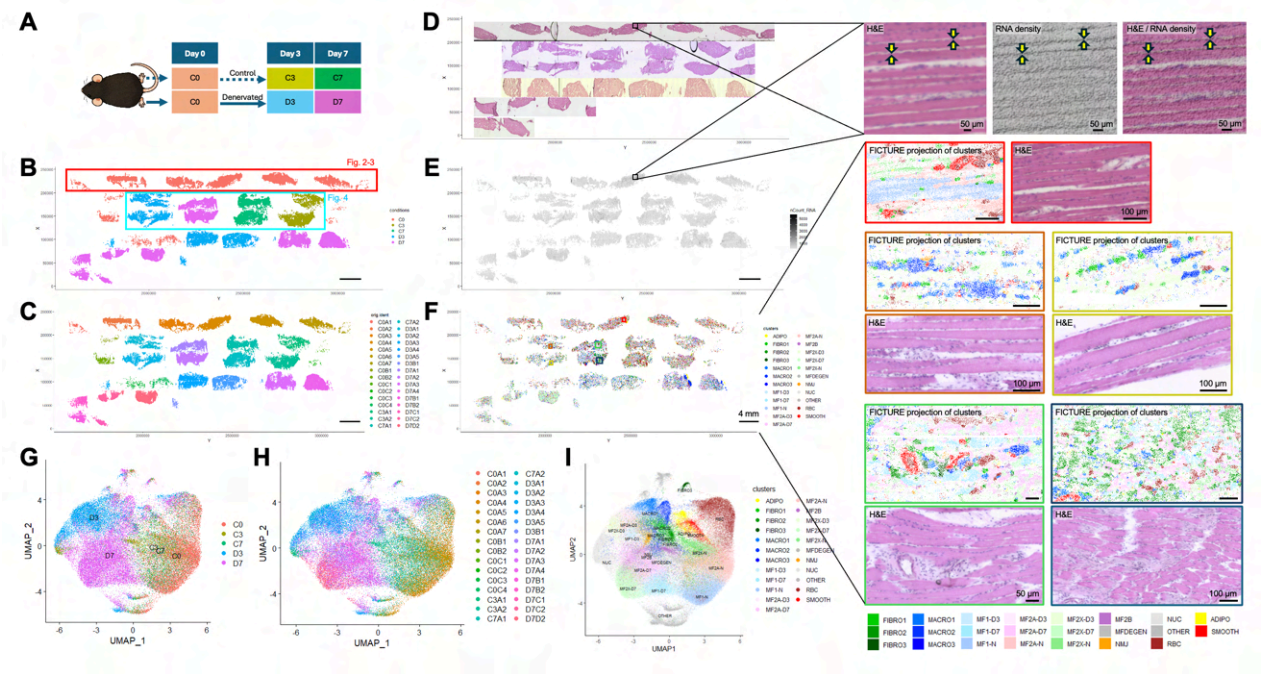


Figure 2.1 High-resolution spatial transcriptomic analysis of mouse soleus muscle in healthy and denervated conditions

(A) Schematic of the muscle denervation experiment. In each mouse, the left hindlimb was denervated, while the right hindlimb served as the control. Tissues were collected at baseline and at 3 and 7 days after denervation. (B-F) Spatial maps colored by experimental condition (B), individual section identity (C), hematoxylin and eosin (H&E) histology (D), captured RNA density (E), and transcriptome clustering results (F). Individual section identities in (C) are encoded by four letters, with the first two letters indicating experimental condition as in (A) and the third and fourth letters denoting animal and section identity, respectively. Boxed regions in (D-F) are shown at higher magnification on the right. Colored boxes in (F) correspond to magnified views of the same color, generated using pixel-level FICTURE projection of clusters. (G-I) UMAP embeddings colored by experimental condition (G), individual section identity (H), and transcriptome clustering results (I), corresponding to (B), (C), and (F), respectively.

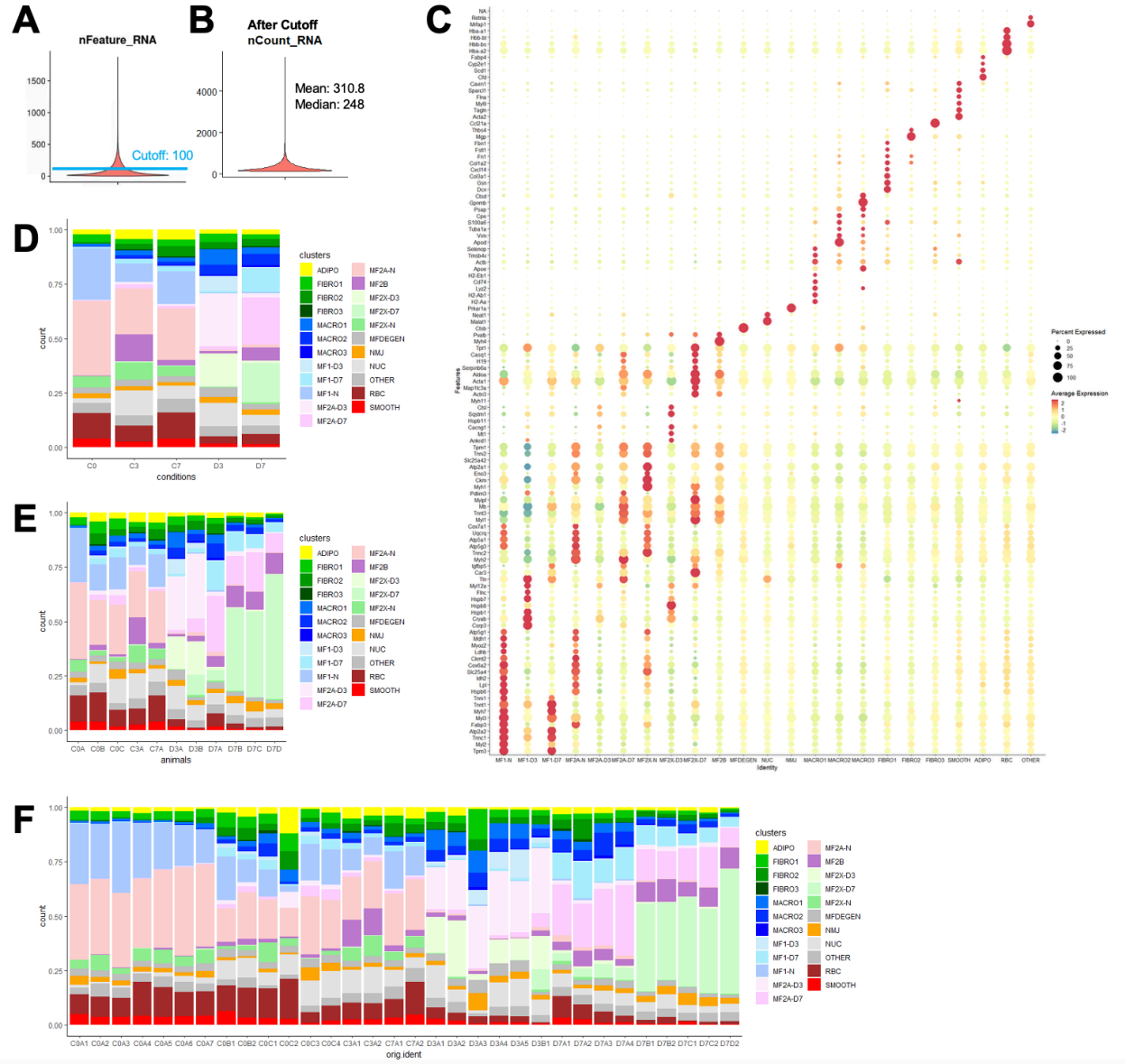


Figure 2.2 Transcriptome-based identification of cell types from Seq-Scope data

(A, B) Myofiber spatial transcriptomes were segmented into hexagonal grids with 14 μm side length and 24 μm flat-to-flat height. (A) Violin plot showing the distribution of gene features per hexagon (nFeature_RNA). A cutoff of 100 gene features (blue line) was applied to obtain high-quality transcriptomes. (B) Violin plot showing the distribution of unique transcript counts per hexagon (nCount_RNA) after applying the 100 gene feature cutoff. (C) Expression of cluster-specific marker genes used for cell type mapping shown in Figure 2.1.F and Figure 2.1.I. (D-F) Distribution of identified clusters across experimental conditions (D), animal identity (E), and section identity (F). Individual section identities in (F) are encoded by four letters, with the first two letters indicating experimental condition as in Figure 2.1.A and the third and fourth letters denoting animal and section identity, respectively.

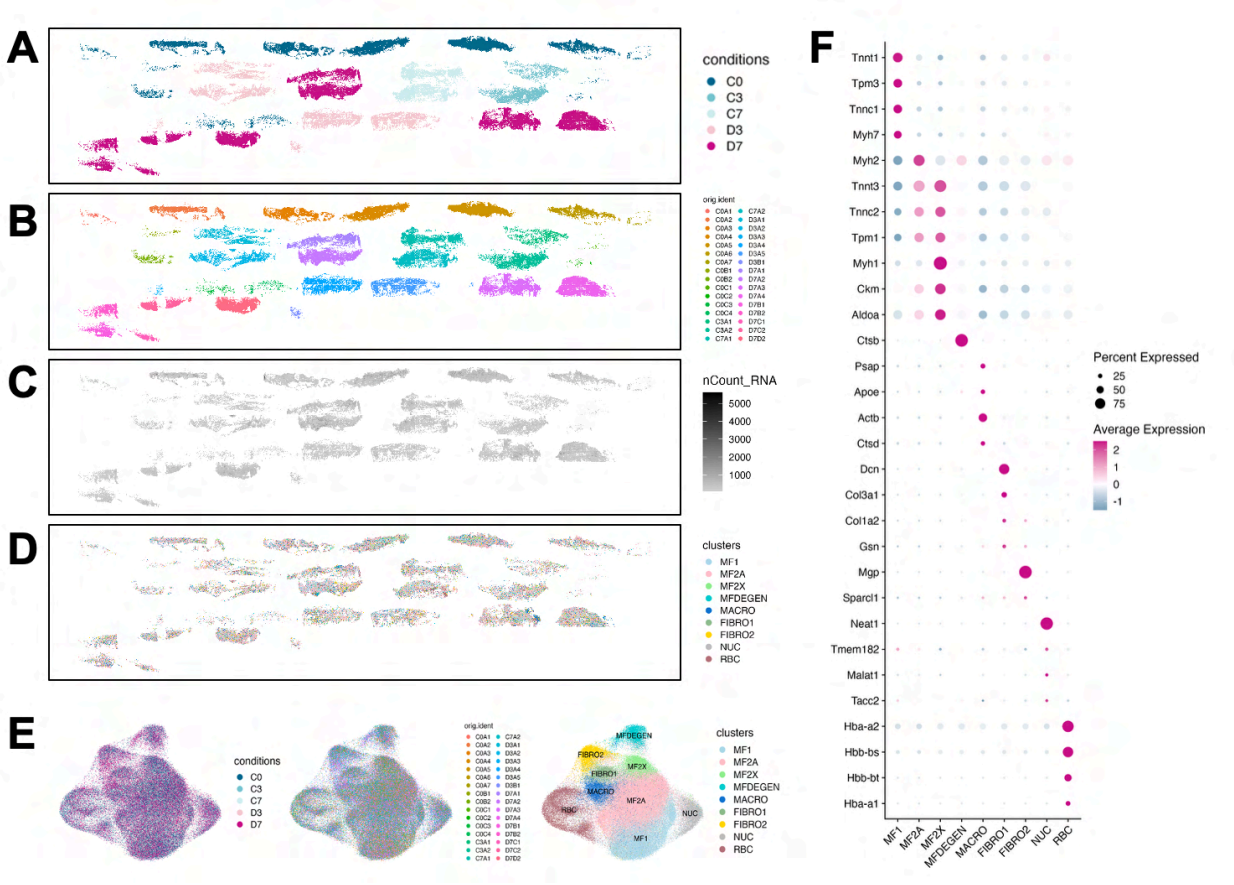


Figure 2.3 Data integration identifies canonical myofiber types and major muscle cell populations

(A-F) Spatial distribution of experimental conditions (A), individual section identities (B), unique transcript density (C), and transcriptome clustering results (D) following integration (E). In (E), UMAP embeddings of the integrated dataset are colored by experimental condition (left), individual section identity (middle), and cluster assignment (right), demonstrating effective batch correction. Expression of cell type markers across integrated clusters is shown in a dot plot (F). Individual section identities in (B, E) are encoded by four letters, with the first two letters denoting experimental condition as in Figure 2.1.A and the third and fourth letters indicating animal and section identity, respectively.

2.3.2 Single-myofiber transcriptome analysis of normal muscle

From high-quality longitudinal sections of normal soleus muscle (Figure 2.1.B, red box), individual myofiber boundaries were delineated using H&E-guided segmentation (Figure 2.4.A) to enable single-myofiber transcriptome analysis. After applying a minimum cutoff of 300 detected gene features, 1,355 myofiber transcriptomes were obtained. Each myofiber revealed a median of 2,732 unique transcripts after excluding mitochondrial genes, hemoglobins, and hypothetical gene models (Figure 2.4.B-C). Variability in transcript counts reflected differences in the extent of longitudinal fiber representation within individual sections.

Unsupervised clustering resolved three major fiber type groups corresponding to MF1, MF2A, and MF2X (Figure 2.4.D-E). These groups were defined by expected fiber type-associated markers (Figure 2.5.A-C), including myosin heavy chain isoforms (Figure 2.5.D, first row), tropomyosins and troponins (Figure 2.5.D, second row), and ER calcium pumps and metabolic enzymes (Figure 2.5.D, third row). Fiber type-specific marker sets were largely consistent with prior snRNA-seq analyses of mouse soleus muscle (7, 8), while also revealing additional enriched genes not previously detected (Figure 2.4.F, Figure 2.5.E).

Because fiber identities were assigned in spatial context, each fiber type could be mapped back onto histological space, enabling direct visualization of their anatomical distribution (Figure 2.4.D). Inclusion of mitochondrial and hypothetical genes increased overall transcript counts but did not alter fiber type assignments (Figure 2.5.F). Notably, MF2X fibers expressed high levels of mitochondria-encoded transcripts despite their glycolytic role in soleus muscle (Figure 2.5.G-H)

2.3.3 Subcellular anatomy of the hybrid myofiber transcriptome

To assess intra-myofiber transcriptomic heterogeneity, we analyzed spatial transcriptomes using 14-µm-sided hexagonal grids and focused this analysis on normal muscle tissue (Figure 2.4.G-J, Figure 2.6). Hexagonal clustering recapitulated the major myofiber types (Figure 2.4.H) and their characteristic markers (Figure 2.6.A), including myosin heavy chain isoforms (Figure 2.6.B), consistent with segmentation-based analysis (Figure 2.6.C) and prior snRNA-seq studies (Figure 2.6.D).

Despite this overall agreement, hexagonal clustering additionally detected small clusters with type IIb-associated signatures marked by *Myh4*, which are rare in the oxidative mouse

soleus (Figure 2.4.H, Figure 2.6.A-B). To investigate this discrepancy, we examined the spatial distribution of hexagon-assigned myofiber types. High-resolution spatial mapping using multiscale sliding windows (24, 28) revealed that, while the overall spatial pattern of myofiber types resembled that obtained from segmentation-based analysis, hexagonal data uncovered transcriptomic heterogeneity within individual myofibers (Figure 2.4.G).

Specifically, distinct myofiber-type transcriptomes were detected within the same myofiber area, consistent with previously described hybrid myofibers (7, 8). We observed mixtures of MF2A and MF2X, as well as MF2X and MF2B, within individual fibers (Figure 2.4.I). As expected, given the rarity of MF2B fibers in mouse soleus, MF2B signatures were detected only in combination with MF2X within individual myofibers and were therefore not resolved as a distinct cluster by segmentation-based analysis, leading to their classification as MF2X (Figure 2.4.D-E).

In addition, we detected a small subset of hexagonal clusters characterized by elevated expression of cathepsin B, designated as MFDEGEN (Figure 2.6.E). Similar transcriptional signatures have been previously associated with exercise-induced remodeling (29) or muscle degeneration (30). In normal muscle, MFDEGEN-associated regions were sparsely distributed and did not exhibit a consistent spatial pattern along myofibers, suggesting that this signature reflects a localized transcriptional state rather than a distinct fiber type or organized anatomical compartment.

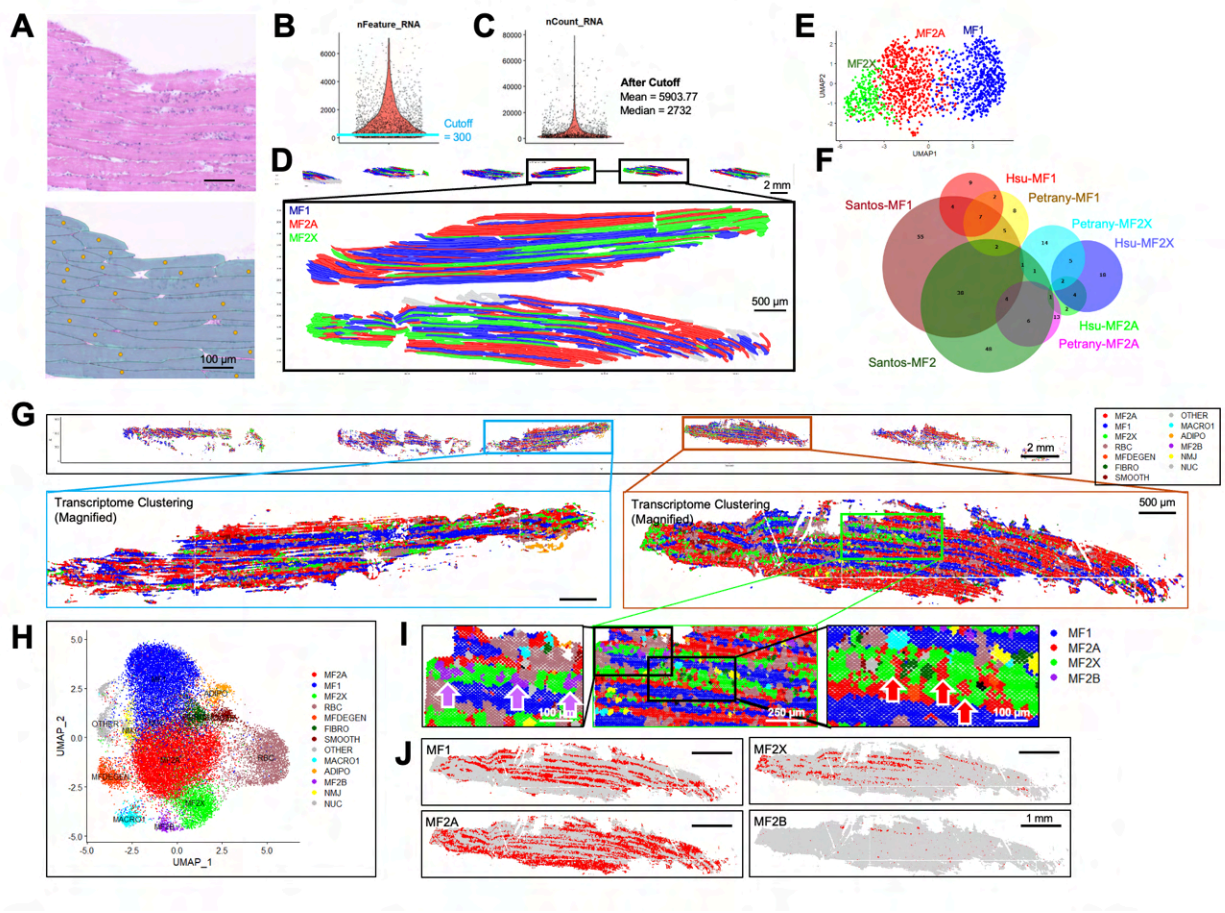


Figure 2.4 Single-myofiber transcriptome analysis of normal muscle

(A) Example of myofiber segmentation based on an H&E-stained image (top), with segmented fibers shown below. All transcriptomic data within each segmented region were aggregated into a single data point (yellow circle) for individual myofiber analysis. (B) Distribution of the number of gene features per segmented fiber (nFeature_RNA). A cutoff of 300 gene features was applied to retain high-quality transcriptomes. (C) Distribution of the number of unique transcripts per segmented fiber (nCount_RNA) after applying the 300 gene feature cutoff. (D) Projection of segmented myofiber transcriptome clusters from (E) into histological space based on the segmented regions. The upper panel shows the full analysis area, and the lower panels show magnified views of the fourth and fifth sections. (E) UMAP representation of the segmented myofiber transcriptome, revealing three major fiber types (MF1, MF2A, MF2X) by multidimensional clustering. (F) Comparison of marker gene sets for each myofiber type identified in the segmentation-based analysis with those reported in two prior single-nucleus RNA sequencing studies (7, 8), using a Venn diagram generated with DeepVenn (54). (G) Spatial plot of a uniform hexagonal grid with 14 µm sides, with cell types projected from the clustering results in (H). Boxed regions are shown at higher magnification. (H) UMAP embedding of hexagonal grid-based transcriptome clustering colored by identified cell types. (I) Magnified regions from (G) highlighting hybrid fibers. (J) Spatial projection of individual myofiber type distributions, shown in red.

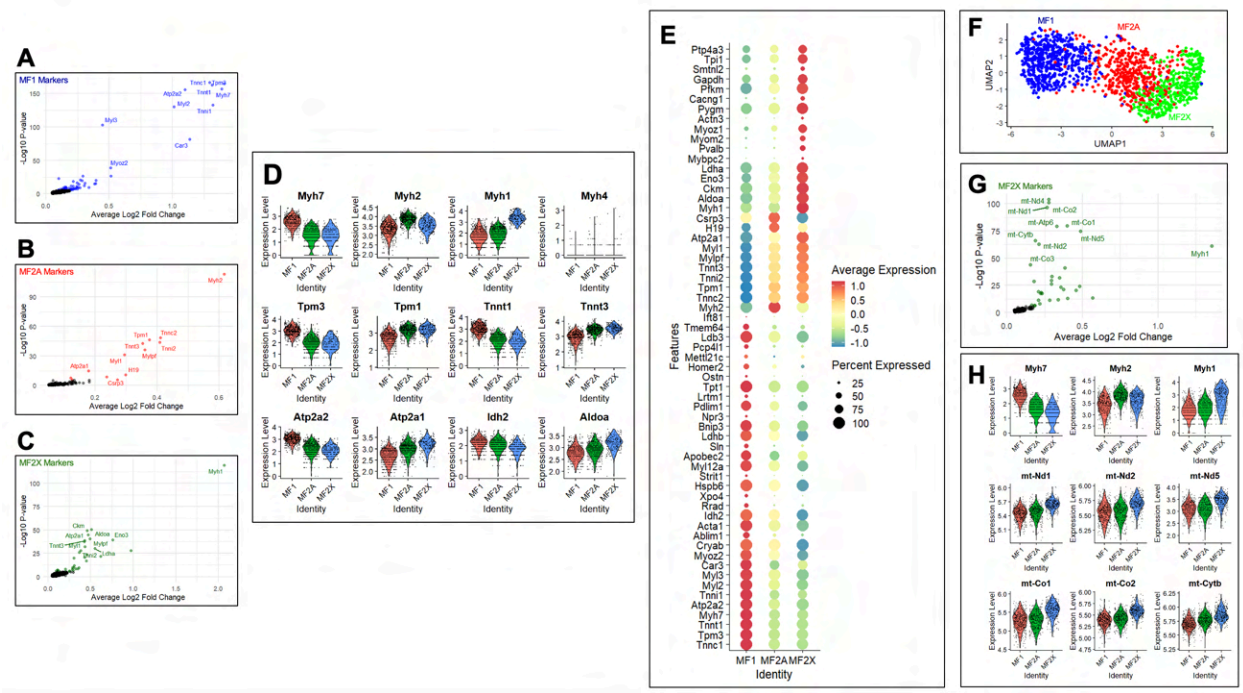


Figure 2.5 Fiber type-specific gene expression in single-segmented myofibers

(A-C) Volcano plots showing genes enriched in individual myofiber clusters, MF1 (A), MF2A (B), and MF2X (C). The top 20 marker genes are highlighted using the same color scheme as in Figure 2.4.E. (D) Violin plots illustrating expression of selected genes across myofiber populations, including myosin heavy chain genes (top), tropomyosins and troponins (middle), and endoplasmic reticulum calcium pumps and metabolic enzymes (bottom). (E) Dot plot showing expression of additional marker genes enriched in the myofiber clusters identified in Figure 2.4.E. (F) UMAP representation of the myofiber transcriptome derived from a dataset that includes mitochondrial and hypothetical genes. The clustering pattern is largely consistent with the analysis excluding these genes shown in Figure 2.4.E. (G) Volcano plot identifying marker genes enriched in MF2X fibers from (F), highlighting elevated expression of mitochondrial genes. (H) Violin plots showing expression patterns of myosin heavy chain genes and selected mitochondrially encoded genes across the myofiber populations identified in (F).

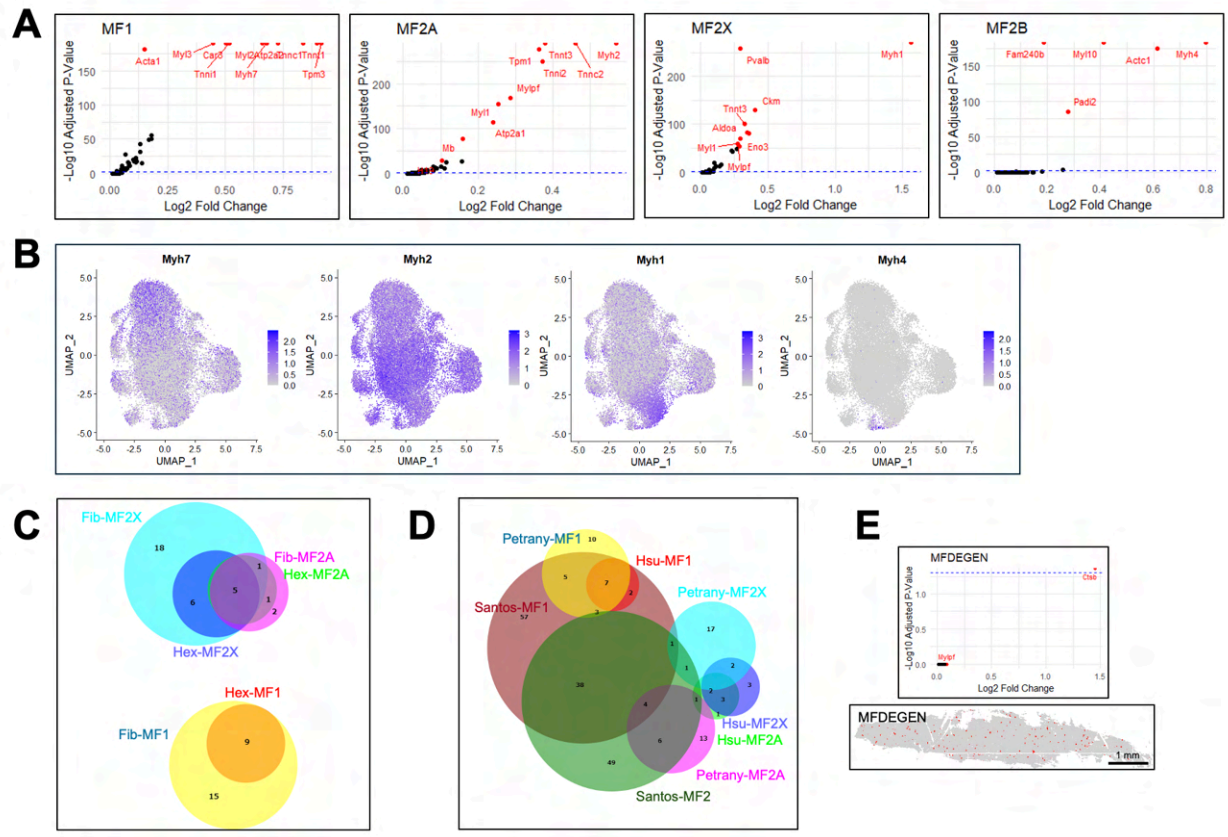


Figure 2.6 Characterization of myofiber type transcriptomes using hexagonal grid analysis

(A) Volcano plots showing genes upregulated in the indicated myofiber types. (B) Expression of fiber type-specific myosin heavy chain isoforms projected onto the UMAP manifold. (C) Comparison of marker gene sets for each myofiber transcriptome between the hexagonal grid-based analysis (Hex) shown in Figure 2.4.G-H and the segmentation-based analysis (Fib) shown in Figure 2.4.E, using Venn diagrams. (D) Comparison of marker gene sets identified in the hexagonal grid-based myofiber transcriptomes with those reported in two previous single-nucleus RNA sequencing studies (7, 8), using a Venn diagram generated with DeepVenn (54). (E) Volcano plot identifying marker genes enriched in MFDEGEN cluster (top) and their spatial distribution in histological space (bottom).

2.3.4 Identification of neuromuscular junction (NMJ) transcriptome

Beyond myofiber type-associated transcriptomes, hexagonal binning of the Seq-Scope dataset revealed additional transcriptomic clusters corresponding to subcellular domains. Among these, a prominent cluster was characterized by high expression of the nuclear noncoding RNAs *Malat1* and *Neat1*, defining a nuclear (NUC) subdomain (Figure 2.4.H; Figure 2.7.A, blue) (31). Adjacent to the NUC cluster in low-dimensional embedding, we identified a distinct transcriptomic cluster spatially localized to neuromuscular junctions (NMJs) (Figure 2.7.A, red). This cluster was defined by enrichment of canonical postsynaptic genes, including *Prkar1a*, *Etv5*, *Ufsp1*, and *Chrna1* (Figure 2.7.B), consistent with its localization to postsynaptic myonuclei at the NMJ. Spatial projection showed that NMJ-associated transcriptomic regions aligned precisely with the stereotyped midline localization of NMJs in soleus muscle (Figure 2.7.C). At higher magnification, these regions overlapped with histological endplate structures corresponding to clusters of postsynaptic myonuclei (Figure 2.7.D). NMJ markers identified in the Seq-Scope dataset showed partial overlap with postsynaptic nuclear markers previously identified by snRNA-seq (Figure 2.7.E), indicating that the NMJ transcriptome identified by Seq-Scope is consistent with known postsynaptic programs but also reveals distinct features not captured by snRNA-seq.

2.3.5 Spatial resolution of postsynaptic and schwann cell-associated NMJ domains

Although the NMJ cluster was defined by postsynaptic gene expression, not all NMJ-associated transcriptomic regions overlapped with histological endplates. Several genes enriched in the NMJ cluster, including *Mpz* and *Smoc2*, are known markers of myelinating and non-myelinating Schwann cells, respectively (32). Subclustering of the NMJ population did not separate these components and instead reflected fiber type-specific transcriptional signatures (Figure 2.7.F-G), indicating that NMJ-associated postsynaptic muscle transcriptomes retain fiber type-associated gene expression patterns.

We therefore examined the spatial distribution of individual NMJ marker genes at its raw resolution. This analysis revealed clear spatial separation between postsynaptic nuclear markers such as *Prkar1a*, *Etv5*, and *Ufsp1* and Schwann cell-associated markers *Mpz* and *Smoc2* (Figure 2.7.H-I). In contrast, acetylcholine receptor transcripts exhibited strong colocalization with postsynaptic nuclear regions marked by *Prkar1a* expression (Figure 2.8.A). These observations

indicate that the NMJ-associated transcriptome comprises multiple spatially distinct domains that cannot be resolved by clustering alone but are separable through high-resolution spatial mapping.

2.3.6 Distinct transcriptomic programs within the NMJ microenvironment

Based on the spatial segregation of *Prkar1a*, *Smoc2*, and *Mpz*, we segmented three NMJ-associated regions representing postsynaptic myonuclei, a perisynaptic region, and a myelinating Schwann cell-associated region (Figure 2.7.H and Figure 2.7.J). Differential expression analysis between these compartments revealed distinct transcriptional programs (Figure 2.7.K-N). The perisynaptic region exhibited high expression of *Lum*, *Apod*, *Dcn*, and *Smoc2* (Figure 2.7.M), closely matching non-myelinating Schwann cell transcriptomes described from brachial plexus and sciatic nerve tissues (32) (Figure 2.7.L, left). In contrast, the myelinating Schwann cell-associated region expressed genes involved in myelination, including *Mpz* (32), *Pmp22* (33), and *Ndrg1* (34) (Figure 2.7.N), showing strong concordance with myelinating Schwann cell transcriptomes derived from the same peripheral nerve dataset (Figure 2.7.L, right) (32).

Some of the genes we identified from the perisynaptic region, such as *ApoD* (Figure 2.7.M), were not identified in recently reported perisynaptic terminal Schwann cell transcriptome datasets (35, 36). However, this expression pattern has been independently validated by RNAscope, which demonstrated high *ApoD* expression in terminal Schwann cells as well as in myelinating Schwann cells of intramuscular nerves (37). In our analysis, *ApoD* emerged as a prominent marker of the perisynaptic region and was detected in both terminal and myelinating Schwann cell-associated regions (Figure 2.7.M-N). In addition, *Smoc2* and *Dcn*, which were enriched in the perisynaptic region (Figure 2.7.M), are not only expressed in non-myelinating Schwann cells (32) but also in nerve-associated fibroblasts (38-40), indicating transcriptomic heterogeneity among cell populations adjacent to the NMJ.

Spatial visualization of compartment-specific markers revealed a geometric organization of postsynaptic nuclei, perisynaptic regions, and myelinating Schwann cell-associated domains that closely mirrors the known anatomical arrangement at the neuromuscular junction (Figure 2.7.J, Figure 2.8.B). Together, these results demonstrate that high-resolution Seq-Scope resolves the NMJ as a multi-compartment transcriptomic niche in intact skeletal muscle.

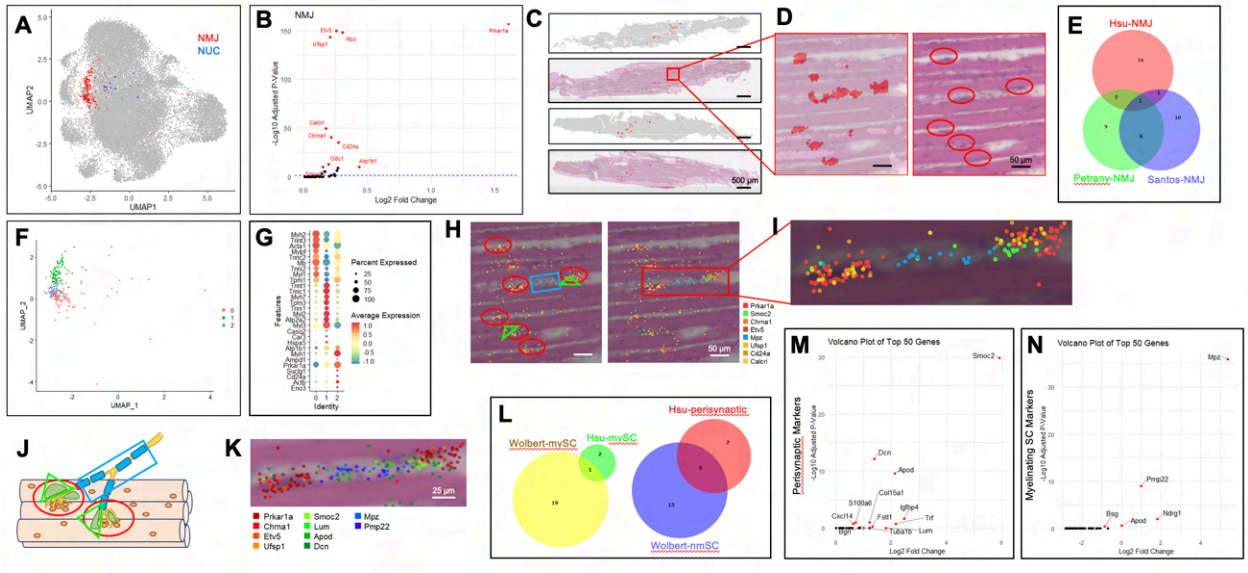


Figure 2.7 High-resolution spatial profiling of neuromuscular junction-associated transcriptomes

(A) Identification of neuromuscular junction (NMJ, red) and nuclear (NUC, blue) transcriptome clusters from the UMAP embedding of the hexagonal dataset. (B) Volcano plot showing genes enriched in the NMJ cluster. (C, D) Spatial plots of NMJ clusters shown in red in the first and third rows of (C), overlaid with histology in the second and fourth rows. The boxed region in (C) is magnified in (D, left) and shown with the corresponding H&E image (D, right). NMJ endplate structures in the histology are highlighted with red ovals. (E) Comparison of NMJ marker gene sets identified in the current hexagonal analysis with those from two previous single-nucleus RNA sequencing studies (7, 8), using a Venn diagram generated with DeepVenn (54). (F, G) UMAP manifold of isolated NMJ transcriptomes (F), subclustered into three groups shown in different colors (0 = red, 1 = green, 2 = blue), corresponding to Type IIa, Type I, and Type IIx myofibers based on marker gene expression (G). These results suggest that postsynaptic NMJ nuclei retain their myofiber-type identities. (H-J) Spatial gene expression plots in the indicated colors, with gene detection represented as dots (H). Postsynaptic regions are indicated by red ovals, perisynaptic regions by green triangles, and myelinating Schwann cell regions by blue rectangles (H, left). The boxed region in (H, right) is magnified in (I). A schematic illustration of NMJ structure is shown in (J). (K-N) Identification of additional markers representing distinct NMJ-associated cell types. Markers enriched in the perisynaptic region (M) and myelinating Schwann cell region (N) are highlighted and compared with published marker lists (the top 20 significant genes) for non-myelinating and myelinating Schwann cells (L) (32). Ten prominent markers were selected and projected onto the magnified NMJ spatial map (K), which displays architectural similarity to the canonical NMJ structure (J).

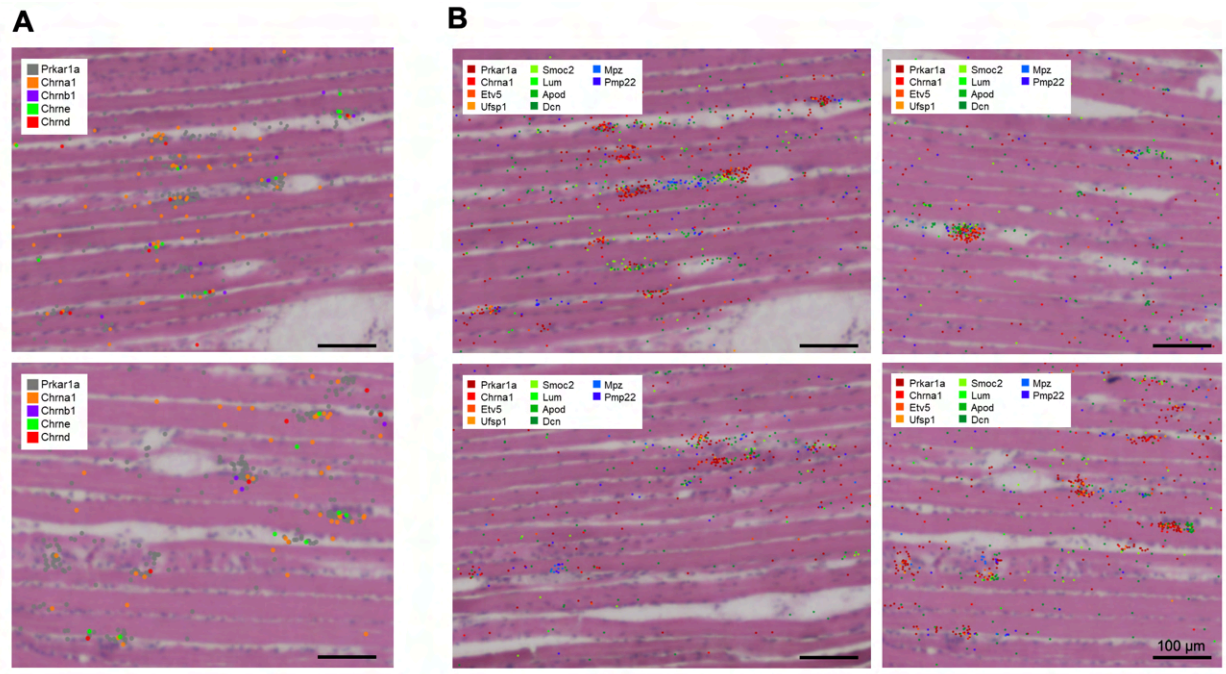


Figure 2.8 Expression of distinct marker genes in the neuromuscular junction region

(A) Spatial expression of acetylcholine receptor isoforms around postsynaptic nuclei identified by *Prkar1a* expression. (B) Spatial expression of cell type-specific marker genes identified in the analysis shown in Figure 2.7 across distinct NMJ-associated regions.

2.3.7 Characterization of non-myocytes in the Seq-Scope dataset

High-resolution hexagonal analysis identified multiple non-myocyte transcriptomic populations within the soleus muscle, including macrophages, fibroblasts, adipocytes, smooth muscle cells, and erythrocytes (Figure 2.9.A-D). These populations exhibited distinct spatial localization patterns that aligned with tissue microanatomy. For example, smooth muscle transcriptomes were specifically localized around arterial structures (Figure 2.9.E, left panel), while adipocyte transcriptomes were confined to lipid-rich regions (Figure 2.9.E, right panel).

Seq-Scope enabled robust detection of cell populations that are difficult to capture using nucleus-based approaches. Macrophage transcriptomes, marked by *Cd74* and MHC components, were readily detected and spatially resolved across tissue sections (Figure 2.9.A-D), despite being largely absent from snRNA-seq datasets (7, 8). Similarly, erythrocyte-associated transcripts, including hemoglobins, were uniquely identifiable due to the whole-transcriptome and spatial nature of Seq-Scope.

Fibroblast transcriptomes enriched for extracellular matrix genes, including *Dcn*, *Gsn*, and collagens, were broadly distributed in interstitial regions and showed close correspondence to fibro-adipogenic progenitor-like signatures described in snRNA-seq studies (Figure 2.9.F). Likewise, smooth muscle-specific gene expression, including *Acta2*, *Myl9*, *Tagln*, and *Mylk* (Figure 2.9.D), were robustly detected, while prior snRNA-seq datasets isolated different set of markers (Figure 2.9.G). In contrast, certain cell types reported in snRNA-seq datasets, such as satellite cells, myotendinous junction-associated nuclei, and tenocytes, were underrepresented in the Seq-Scope dataset, likely reflecting volumetric sampling limitations inherent to thin tissue sections.

Taken together, analyses of normal soleus muscle demonstrate that Seq-Scope captures myofiber type diversity, intra-fiber transcriptomic heterogeneity, neuromuscular junction subdomains, and multiple non-myocyte populations within intact tissue. This spatially resolved baseline provides a reference for examining how these transcriptional programs and tissue architectures are altered following denervation.

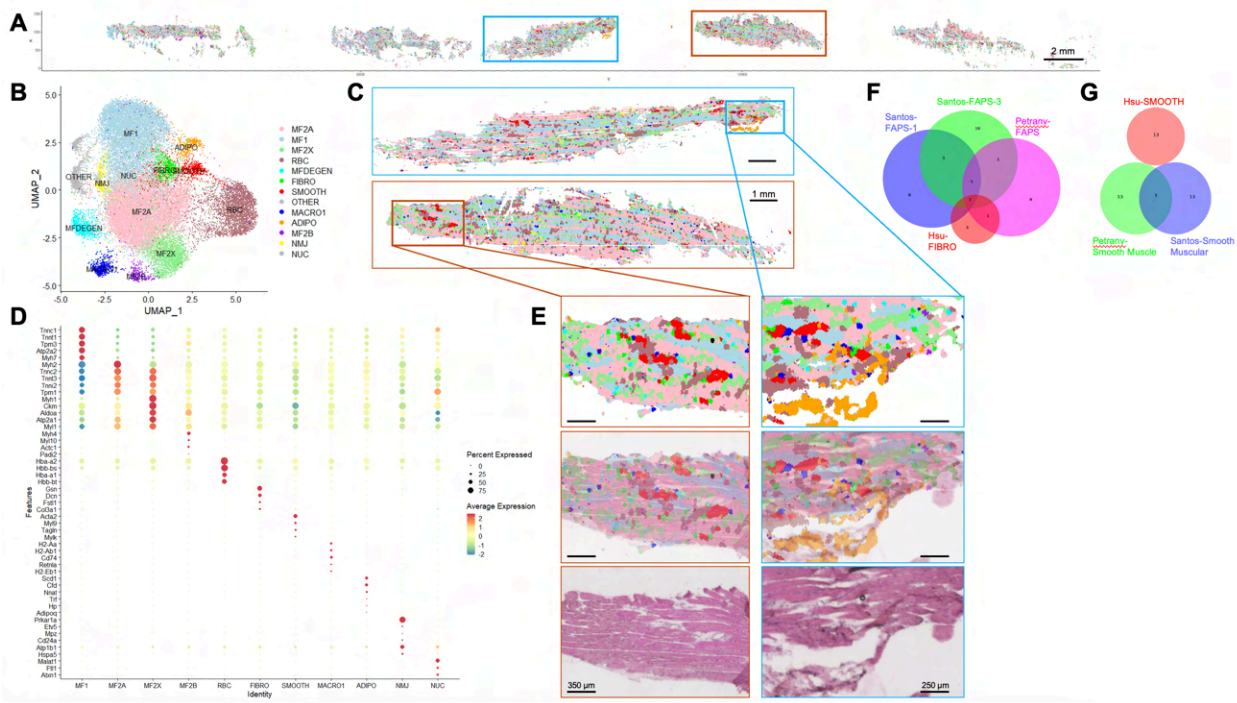


Figure 2.9 Non-myocyte transcriptomic heterogeneity revealed in the Seq-Scope dataset

(A, B) Spatial map (A) and UMAP manifold (B) from Figure 2.4.G and 2.4.H, recolored to emphasize non-myocyte transcriptomes. (C) Magnified spatial views from the boxed regions in (A) shown with corresponding cluster colors. (D) Dot plots showing expression of top cluster-specific marker genes across non-myocyte clusters. (E) Further magnification of boxed regions in (C) as indicated by guidelines. Left panels highlight arteries, while right panels highlight adipose tissue. (F, G) Comparison of marker gene sets for fibroblasts or fibro-adipogenic progenitors (FAPs) (F) and smooth muscle cells (G) between the current hexagonal analysis and two previous single-nucleus RNA sequencing studies (7, 8). The top 20 significant genes were included in the analysis.

2.3.8 Fiber type-specific responses to denervation

To examine fiber type-specific responses to denervation, we performed another round of segmentation-based single-myofiber analysis, using four tissues that produced high-quality histology and transcriptome data (Figure 2.10.A). After applying a gene feature cutoff of 300, we obtained 3908 segmented myofiber transcriptomes from control and denervated fibers at 3 days (1337 and 620, respectively) and 7 days (1127 and 824, respectively). After removing all mitochondrial, hypothetical and hemoglobin-encoding transcripts, the median and mean numbers of transcripts in each myofiber was 1738 and 3274 ± 5332 respectively (Figure 2.10.B). As observed from hexagonal analysis (Figure 2.1), denervated fibers at 3 and 7 days exhibited transcriptomes substantially different from control fibers, while fibers from control muscles at 3 and 7 days integrated very well into each other (Figure 2.11.A), indicating that the experimental batch effect is minimal and the differences we observed could be explained largely by the biological effects of denervation. Some of the fibers in day 7 denervated fibers contained a fibrotic signature, likely due to effects from fibroblast transcriptome nearby the myofibers. As we focused on myofiber transcriptomes, the fibers displaying fibrotic signatures were excluded from the fiber type-specific analysis (FIBRO in Figure 2.10.B; NA in Figure 2.10.C). In all muscles, we were able to identify three major myofiber types, corresponding to MF1, MF2A and MF2X fibers (Figure 2.10.B), based on fiber-type markers isolated from normal muscle (Figure 2.11.B).

Even though classical markers, including myosin heavy chain, troponin and tropomyosin isoforms, were relatively highly expressed in their corresponding myofiber types within the same section, allowing us to identify their original fiber types, their level was strongly diminished in day 3 denervated myofibers compared to control myofibers (Figure 2.11.B). In contrast, differential expression analyses identified a number of genes that were strongly upregulated in day 3 denervated fibers, but also explicitly upregulated in specific myofiber types, such as oxidative type I or glycolytic type IIx fibers (Figure 2.10.C and Figure 2.11.C). Markers enriched for day 3 denervated myofiber type I (D3-MF1) include several heat shock proteins (e.g. *Hspb1*, *Hspa8*), crystallins (*Cryab*) and muscle stress response proteins (e.g. *Csrp3*, *Ankrd1*). These were proteins previously shown to be upregulated upon denervation through proteomics (41); however, our analyses show that their upregulation is highly specific to oxidative MF1 fibers (Figure 2.10.C and Figure 2.11.C-D). In addition to these genes, many markers of damaged

myofibers (e.g. *Xirp1*, *Flnc*, *Enah,* and *Otud1*; see references (7, 9, 42)) were also specifically upregulated in D3-MF1 (Figure 2.11.D). In contrast, day 3 denervated myofiber type IIx (D3-MF2X) exhibited stronger upregulation of different genes such as heat shock proteins (e.g. *Hspb8*) and metallothioneins (*Mt1*, *Mt2*) (Figure 2.11.E).

We also identified markers enriched for day 7 denervated fibers. Some classical type I myofiber markers, such as *Myh7* and *Tnnt1*, were upregulated in D7-MF1 (Figure 2.11.F), while other genes such as *Krt18*, *Cdkn1a,* and *Ctsb* were upregulated in D7-MF2X (Figure 2.11.G). In addition to these, day 7 denervated fibers exhibited upregulation of various stress-responding genes such as autophagy controllers (Figure 2.11.H), atrophy inducers (Figure 2.11.I), a chromatin modulator (*Hdac3*) and oxygen metabolism genes (*Mb* and *Car3*; Figure 2.11.J), as well as DNA damage-responsive transcripts (*Cdkn1a*, *Gadd45a,* and *Mdm2*; Figure 2.11.K), which show variable fiber type specificities in regulation.

2.3.9 Subcellular heterogeneity in denervation responses

Myofiber damage-response markers enriched in the D3-MF1 state, including *Xirp1*, *Enah*, and *Flnc* (42-44), have been reported previously in aged muscle and in myofibers undergoing dystrophic remodeling (7, 9), suggesting that their induction reflects acute structural or mechanical stress. Although the transcriptomic state defined as D3-MF1 was primarily observed in muscle tissue at 3 days after denervation, it was also detected in a subset of fibers at 7 days (Figure 2.10.D), indicating that the response is not exclusively specific to the early phase and can persist to the chronic phase. High-resolution spatial analysis revealed that these fibers often exhibited hybrid transcriptional states, with discrete intramyofiber regions expressing either D3-MF1 or D7-MF1 gene programs (Figure 2.10.E).

Importantly, these transcriptional domains were associated with distinct histological features. Regions expressing D3-MF1 markers showed pale and degenerative H&E staining patterns (Figure 2.10.E-G, yellow arrows), whereas adjacent regions expressing D7-MF1 markers retained a more preserved myofiber morphology (Figure 2.10.E-G, blue arrows). This spatial concordance between transcriptomic state and histological appearance indicates that

denervation elicits localized, rather than uniform, remodeling responses along individual myofibers.

Notably, D3-MF1 damage-response transcripts were frequently enriched near the neuromuscular junction. While postsynaptic NMJ markers such as *Prkar1a* remained sharply confined to the endplate region, D3-MF1-associated transcripts extended beyond the synaptic core and radiated into adjacent segments of the same myofiber (Figure 2.10.F). This pattern suggests that early denervation-induced transcriptional responses are spatially organized around the NMJ and propagate into peri-synaptic regions, even in the absence of active neural input. Together, these findings demonstrate that denervation triggers pronounced subcellular heterogeneity within myofibers, linking localized structural degeneration, spatially restricted transcriptional programs, and the anatomical position of the NMJ.

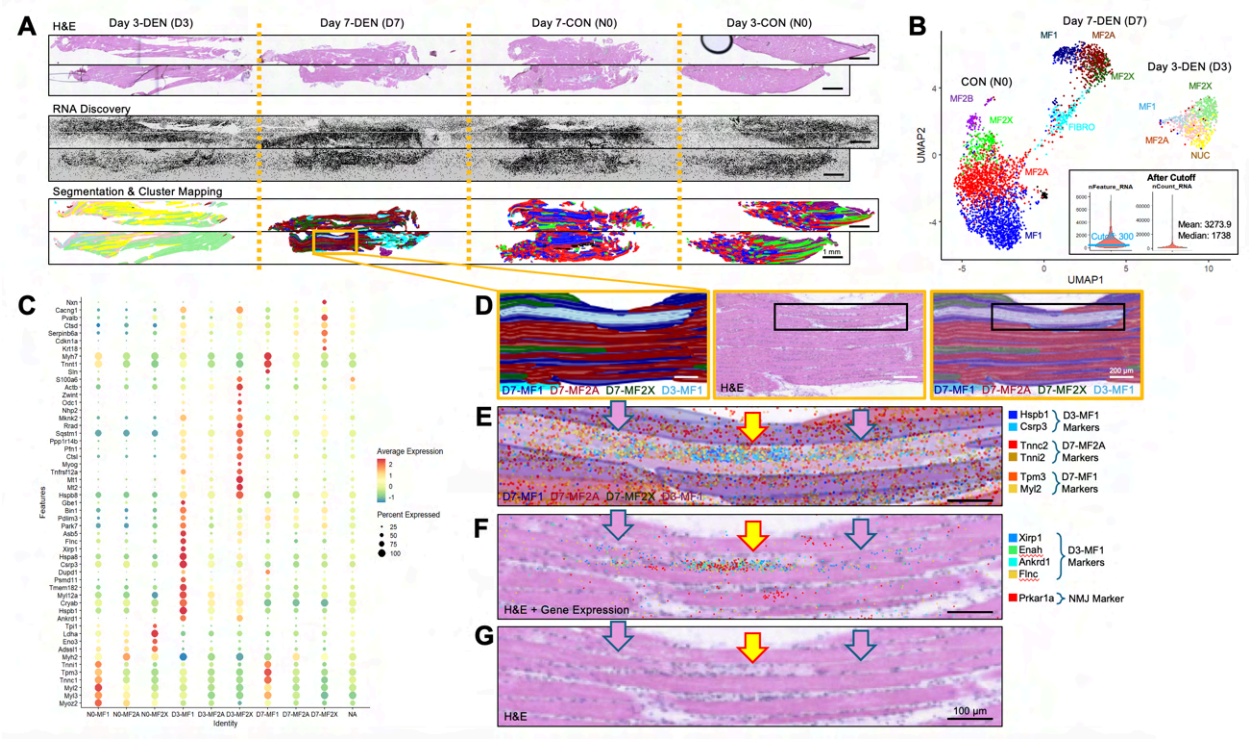


Figure 2.10 Heterogeneous transcriptome responses to denervation in single myofibers

(A) Longitudinal sections of mouse skeletal muscle from different denervation groups (DEN, denervated leg; CON, control leg), arranged as H&E histology (top), spatial RNA discovery plots (middle), and H&E-based segmented myofibers (bottom) projected with the fiber clustering colors shown in (B). (B) UMAP manifold of segmented myofiber transcriptomes, revealing heterogeneous denervation responses within three major fiber types identified by multidimensional clustering. Insets show the distribution of gene features per fiber (nFeature_RNA, left) and the distribution of unique transcript counts per fiber (nCount_RNA, right) after applying the gene feature cutoff of 300. (C) Visualization of cluster-specific top marker gene expression across myofiber clusters, highlighting fiber type-specific responses to denervation. (D-G) Identification of myofibers exhibiting intracellular heterogeneity in transcriptomic responses to denervation. Myofiber transcriptomes identified by segmentation of the H&E image (D, center) are projected into histological space (D, left) and overlaid onto the corresponding H&E image (D, right). Although the tissue was collected 7 days after denervation, a subset of myofibers exhibits a D3-MF1 (day 3 MF1-type) transcriptomic signature. The boxed region in (D) is magnified in (E-G). Selected denervation-induced genes and NMJ markers are plotted in the magnified regions (E, F), revealing close spatial proximity between degenerative responses and the NMJ area. Overlay with H&E histology shows that regions with high D3-MF1 signature (yellow arrow) display pale eosin staining, whereas regions exhibiting a D7-MF1 transcriptome (pink arrows) show normal myofiber staining (G).

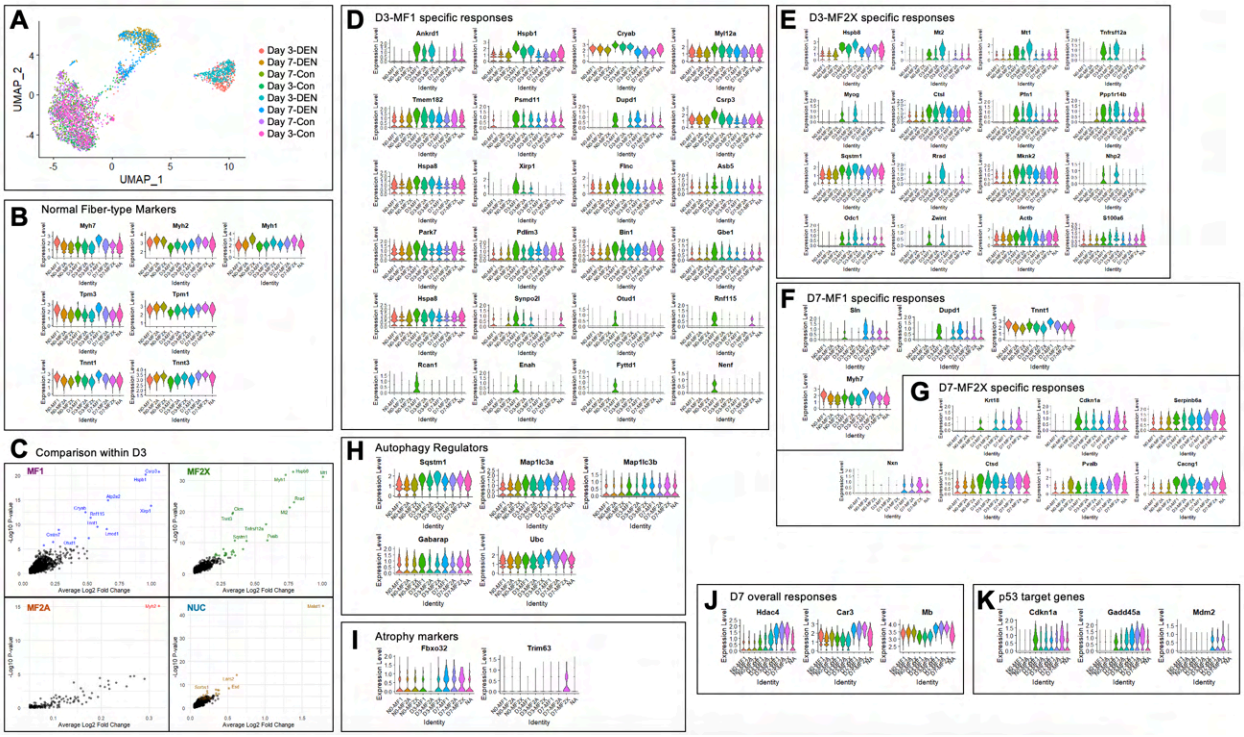


Figure 2.11 Fiber type-specific denervation responses

(A) UMAP manifold of the myofiber transcriptome colored by experimental condition. Control samples integrate well, whereas day 3 and day 7 denervated samples form distinct clusters corresponding to their respective time points. (B) Expression of myosin heavy chain isoforms, tropomyosins, and troponins across myofiber types in the denervated segmented myofiber dataset. (C) Identification of myofiber type-specific denervation response genes. Genes highly expressed in each myofiber type within the day 3 denervated dataset are highlighted. (D-K) Gene induction across myofiber types in the denervated dataset, grouped as day 3 myofiber type I-specific responses (D), day 3 myofiber type IIx-specific responses (E), day 7 myofiber type I-specific responses (F), day 7 myofiber type IIx-specific responses (G), autophagy-related responses (H), atrophy-related responses (I), day 7 global responses (J), and DNA damage responses (K).

2.3.10 Denervation preserves postsynaptic NMJ identity while inducing extrajunctional acetylcholine receptors

We next examined postsynaptic NMJ responses to denervation by focusing on the NMJ cluster identified in the hexagonal grid analysis covering the entire dataset (Figure 2.12.A; Figure 2.1.I). In the UMAP manifold, NMJ-associated transcriptomes were distributed across multiple subclusters, reflecting their strong similarity to the surrounding myofiber transcriptomes within the same tissue sections (Figure 2.12.A). Consistent with global myofiber responses (Figure 2.10), NMJ-associated regions exhibited induction of stress-responsive genes, including heat shock proteins and crystallins, following denervation (Figure 2.13.A-B).

Despite these changes, the transcriptional identity of postsynaptic NMJs remained remarkably stable. Core postsynaptic markers, including *Prkar1a*, *Etv5*, and *Ufsp1*, maintained robust and spatially restricted expression at the endplate throughout the denervation time course (Figure 2.12.B-C and Figure 2.13.D). The overall abundance of NMJ-associated regions in the dataset was not substantially altered by denervation (Figure 2.12.B), indicating preservation of NMJ structural organization at the transcriptional level.

In contrast, acetylcholine receptor gene expression underwent marked remodeling, consistent with established models where neuronal activity suppresses acetylcholine receptor transcription in extrasynaptic regions (45). While acetylcholine receptor transcripts were largely confined to the NMJ in control muscle, denervation led to strong induction of multiple receptor subunits, including *Chrna1*, *Chrnb1*, and *Chrng*, throughout the myofiber (Figure 2.12.D). Notably, extrajunctional expression of *Chrnb1* and *Chrng* exceeded their baseline levels at the NMJ.

Importantly, not all receptor subunits exhibited the same spatial regulation. *Chrne* expression remained strictly confined to postsynaptic NMJ nuclei even after denervation (Figure 2.12.D), consistent with prior evidence that *Chrne* expression is developmentally regulated and controlled at individual endplates (46). Spatial visualization further illustrated this dichotomy, showing persistent localization of postsynaptic markers such as *Prkar1a*, *Etv5*, and *Ufsp1* (red colors) at NMJs, alongside widespread induction of *Chrna1* and *Chrng* (yellow colors) across denervated muscle tissue (Figure 2.12.E). Together, these results demonstrate that denervation

preserves postsynaptic NMJ identity while selectively derepressing extrajunctional acetylcholine receptor expression.

2.3.11 Denervation elicits robust extracellular matrix remodeling in the perisynaptic NMJ microenvironment

We next examined denervation-induced transcriptional changes in non-myofiber compartments associated with the NMJ microenvironment. In contrast to normal muscle (Figure 2.7), transcriptomic signatures corresponding to myelinating Schwann cells, marked by *Mpz* and *Pmp22*, were not readily detected in denervated tissues. Nevertheless, perisynaptic regions defined by non-myelinating or terminal Schwann cell-associated markers remained identifiable in close proximity to postsynaptic NMJs (Figure 2.12.E).

Following denervation, perisynaptic marker expression became more spatially extensive compared to control muscles (Figure 2.12.E), suggesting expansion or activation of this compartment. Using marker-based segmentation analogous to that applied in normal muscle (Figure 2.7), we isolated postsynaptic and perisynaptic NMJ regions and performed differential expression analysis between control and denervated conditions. This analysis revealed robust and selective upregulation of genes involved in extracellular matrix remodeling, tissue repair, and injury responses within the perisynaptic compartment (Figure 2.12.F-I).

Spatial mapping confirmed that these extracellular matrix-associated transcripts were enriched in regions surrounding NMJs in denervated muscle (Figure 2.12.J). Given that many of these genes are expressed by fibroblasts and macrophages, it is possible that additional cell populations recruited to the NMJ following denervation contribute to the observed remodeling response. It is also possible that terminal Schwann cells underwent activation, proliferation, and extracellular matrix remodeling in response to neuronal injury (47-50). Collectively, these results identify the perisynaptic NMJ microenvironment as a dynamic and transcriptionally active niche that undergoes pronounced extracellular matrix remodeling in response to denervation.

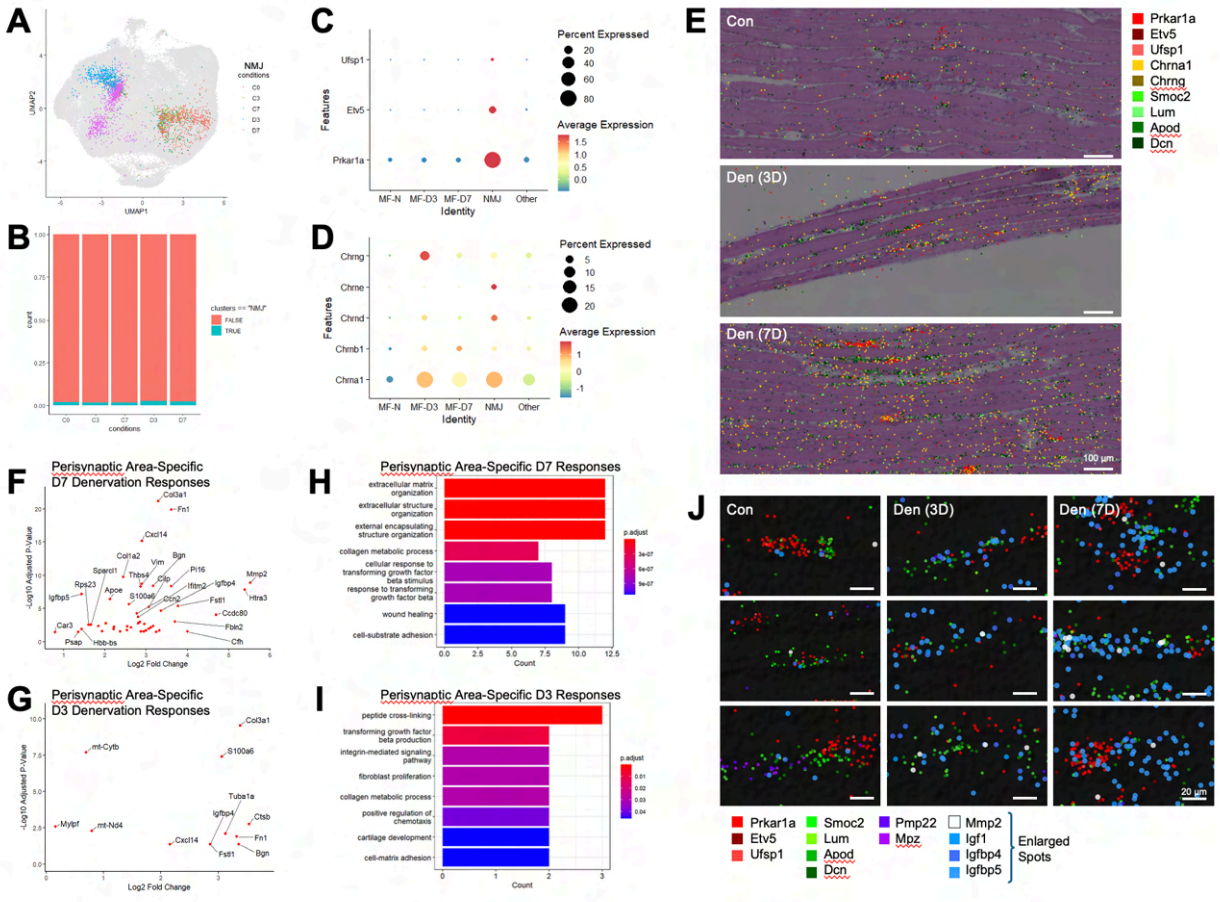


Figure 2.12 Denervation-induced changes in the neuromuscular junction region

(A) UMAP manifold from Figure 2.1.I highlighting the NMJ cluster, colored by experimental condition. All other clusters are shown in gray in the background. (B) Relative abundance of the NMJ cluster across experimental conditions. (C, D) Dot plots displaying differential expression of postsynaptic nuclei marker genes (C) and acetylcholine receptor isoforms (D) across myofiber types at different time points after denervation. (E) Spatial expression of postsynaptic nuclei markers (warm colors) and non-myelinating perisynaptic Schwann cell markers (greens) in control, 3-day denervated, and 7-day denervated myofibers, overlaid onto corresponding H&E images. (F-I) Perisynaptic area-specific transcriptional responses at 7 days (F, H) and 3 days (G, I) after denervation, identified by comparison with control perisynaptic regions. Genes that were also regulated in the postsynaptic area were excluded from the analysis. Results are shown as volcano plots (F, G) and gene ontology enrichment analyses (H, I). (J) Spatial expression of postsynaptic nuclei markers (reds), perisynaptic area markers (greens), myelinating Schwann cell area markers (purples), *Mmp2* (white), and *Igf* and *Igfbp* genes (blues), indicating enhanced extracellular matrix remodeling and IGF pathway activity around the NMJ following denervation.

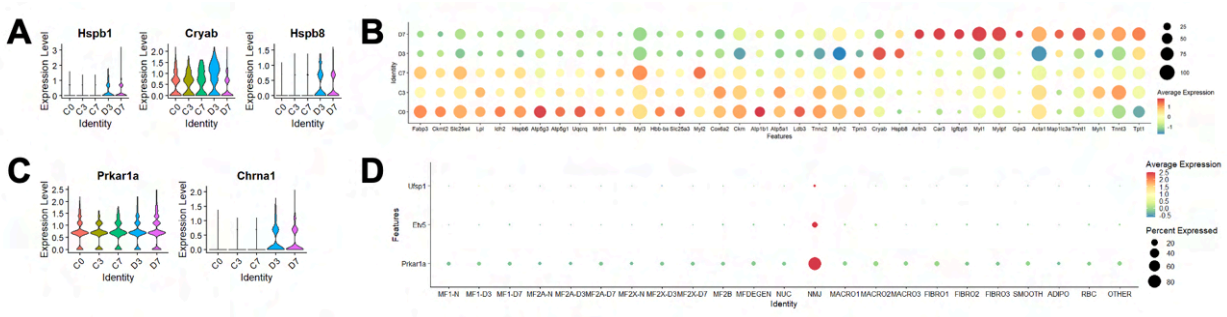


Figure 2.13 Neuromuscular junction responses to denervation

(A-C) Expression of the indicated genes across different experimental conditions, visualized using ViolinPlot (A, C) and DotPlot (B). (D) Differential expression of postsynaptic nuclei marker genes across different clusters, visualized by DotPlot analysis.

2.3.12 Non-myocyte responses to denervation

Finally, we examined transcriptional responses of macrophages and fibroblasts, two non-myocyte populations closely associated with myofiber integrity and tissue remodeling. In the hexagonal grid analysis (Figure 2.1.I and Figure 2.2.C-F), three subclusters were identified for each population, designated MACRO1-3 and FIBRO1-3 (Figure 2.14.A-I and Figure 2.14.J-S, respectively).

Across experimental conditions, macrophage populations showed a general trend toward increased abundance following denervation, albeit with different kinetics (Figure 2.14.D-F), despite substantial variability in overall cell-type representation across samples (Figure 2.1.D-F). Concordantly, expression of macrophage-associated marker genes increased after denervation, with the highest levels observed at 7 days (Figure 2.14.G-I). These trends were evident across all three macrophage subclusters (MACRO1-3), indicating a broadly coordinated macrophage response rather than expansion of a single macrophage subtype.

In contrast, fibroblast populations did not exhibit a clear or consistent change in overall abundance following denervation (Figure 2.14.M-O). However, transcriptional profiling revealed pronounced condition-dependent remodeling within the FIBRO1 subcluster (Figure 2.14.J, 2.14.M, 2.14.P, and 2.14.S). Although the relative contribution of FIBRO1 cells remained largely stable at both 3 and 7 days after denervation (Figure 2.14.M), their gene expression profiles shifted substantially in a time-dependent manner.

At 3 days after denervation, FIBRO1 cells exhibited increased expression of genes associated with early injury and inflammatory responses, including the collagen, *Col3a1*, the chemokine, *Cxcl14*, and the lysosomal protease, *Ctsl* (Figure 2.14.P and 2.14.S). By 7 days, this transcriptional program transitioned toward enrichment of extracellular matrix-associated genes, including *Fn1*, *Mgp*, and *Dcn*, consistent with matrix remodeling processes (Figure 2.14.P and 2.14.S). These expression patterns were reproducibly observed across individual samples, despite moderate inter-sample variability (Figure 2.14.S).

Together, these data indicate that non-myocyte populations respond to denervation through distinct and temporally structured transcriptional programs. Macrophages exhibit a progressive increase in abundance and activation, whereas fibroblasts, particularly the FIBRO1 subpopulation, undergo dynamic transcriptional remodeling without marked changes in population size. These findings highlight the importance of condition-dependent, cell type-

specific gene regulation in shaping the non-myocyte contribution to denervation-induced muscle remodeling.

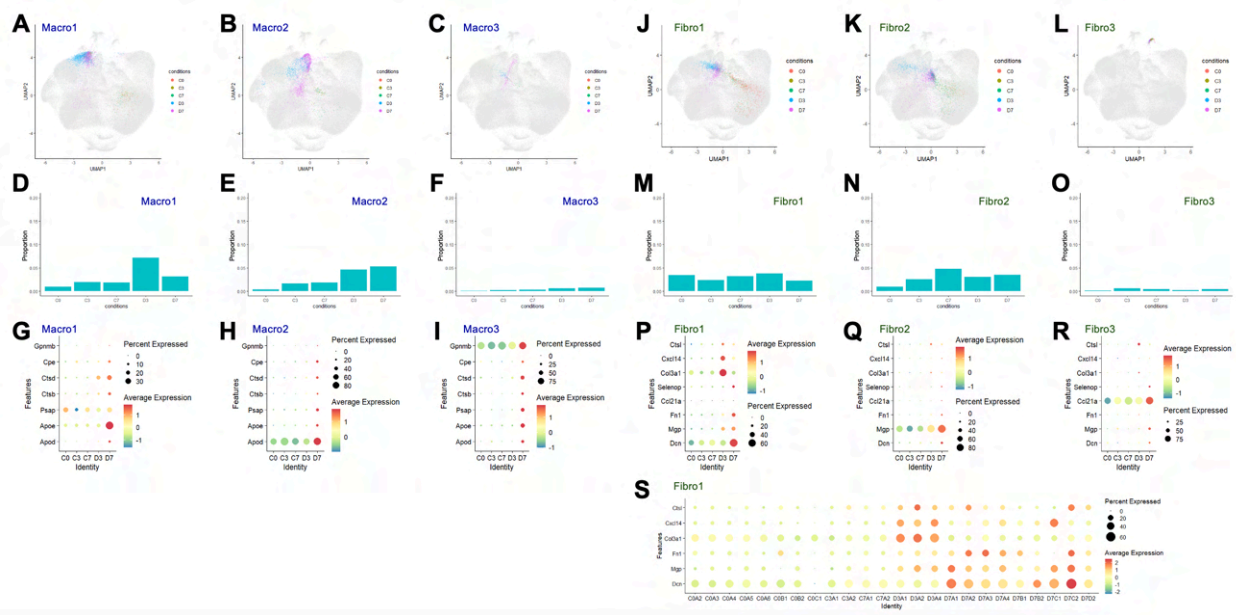


Figure 2.14 Denervation responses in non-myocytes

(A-C) UMAP manifold from Figure 2.1.I highlighting the indicated macrophage clusters, colored by experimental condition. All other clusters are shown in gray in the background. (D-F) Population shares of the indicated macrophage clusters across experimental conditions. (G-I) Differential expression of cluster-specific marker genes in macrophage subclusters across experimental conditions. (J-L) UMAP manifold from Figure 2.1.I highlighting the indicated fibroblast clusters, colored by experimental condition. All other clusters are shown in gray in the background. (M-O) Population shares of the indicated fibroblast clusters across experimental conditions. (P-R) Differential expression of cluster-specific marker genes in fibroblast subclusters across experimental conditions. (S) Expression of the indicated cluster-specific marker genes in fibroblast subclusters across individual samples.

2.4 Discussion

Skeletal muscle function is central to movement, metabolic homeostasis, and overall organismal health. A defining feature of this tissue is its pronounced cellular and subcellular heterogeneity, coupled with a strong dependence on neural input for maintenance of structure and function. Understanding how this complex architecture is organized in intact tissue and how it is remodeled following denervation is therefore essential for elucidating mechanisms underlying neuromuscular disease, aging-associated muscle decline, and recovery from nerve injury. Recent advances in transcriptomic technologies have created new opportunities to address these questions (51), yet each approach has inherent limitations that have constrained their application to skeletal muscle. In this study, we employed Seq-Scope, an ultra-high-resolution spatial transcriptomic platform, to generate a comprehensive atlas of normal and denervated mouse soleus muscle with single-cell and subcellular resolution.

To our knowledge, this work represents the first transcriptome-wide spatial atlas of skeletal muscle that combines microscopic spatial resolution with unbiased gene coverage in longitudinal sections. Previous transcriptomic studies of skeletal muscle have relied primarily on scRNA-seq or snRNA-seq, which necessarily disrupt tissue architecture and eliminate spatial context, or on spatial platforms such as 10X Visium, whose limited resolution precludes reliable discrimination of individual myofibers or subcellular domains (15-22). As a result, prior spatial transcriptomic studies of skeletal muscle have been restricted to transverse sections and were unable to assess transcriptomic variation along the longitudinal axis of myofibers. More recently, imaging-based approaches such as 10X Xenium have achieved cellular-scale resolution in skeletal muscle (52); however, these methods rely on targeted gene panels and therefore capture only a small fraction (<400 genes) of the transcriptome. By contrast, Seq-Scope provides sub-micrometer spatial resolution together with whole-transcriptome coverage, enabling direct visualization of transcriptional organization within intact myofibers and across tissue microenvironments in longitudinal sections.

To extract biological insight from the resulting high-dimensional dataset, we employed two complementary analytical strategies: histology-guided myofiber segmentation and unbiased hexagonal grid-based spatial binning. These approaches produced convergent yet distinct results. Segmentation-based analysis enabled robust classification of major myofiber types and supported comprehensive fiber type-specific differential gene expression analyses. In contrast,

grid-based spatial analysis localized transcriptomic phenotypes without reliance on predefined cellular boundaries, revealing hybrid myofiber states, subcellular transcriptional domains, and localized degenerative signatures that were not resolved by segmentation alone. Importantly, this approach also captured spatially organized non-myocyte populations, including macrophages, fibroblasts, smooth muscle cells, and adipocytes, as well as specialized structures such as neuromuscular junctions and partially degenerating myofiber regions. Together, these complementary strategies provide a holistic molecular view of skeletal muscle architecture across the longitudinal histological axis.

Our results further underscore the complexity of denervation-induced remodeling in skeletal muscle. At the level of myofibers, denervation elicited robust and fiber type-specific transcriptional responses, most prominently at early time points. These responses included induction of stress-associated pathways involving heat shock proteins, crystallins, metallothioneins, autophagy regulators, and genes related to oxygen metabolism. Notably, these transcriptional changes were not uniformly distributed along myofibers. Instead, high-resolution spatial analysis revealed localized domains of damage-response gene expression, frequently enriched near neuromuscular junctions and associated with histological features of partial degeneration. Such spatially restricted responses are difficult to detect using dissociation-based approaches or low-resolution spatial methods (15-22) and are not accessible through targeted imaging-based assays (52).

Non-myocyte populations also exhibited distinct and temporally structured responses to denervation. Macrophages showed a progressive increase in abundance and expression of macrophage-associated genes, consistent with their established roles in injury response and tissue remodeling. Fibroblasts, in contrast, did not display a consistent change in population size but instead underwent pronounced transcriptional remodeling within a defined subpopulation. Early denervation was associated with increased expression of collagens, chemokines, and proteases, whereas later stages were characterized by upregulation of extracellular matrix components, suggesting a transition from early injury-associated signaling to matrix remodeling. These findings indicate that denervation-induced changes in non-myocyte compartments are driven largely by dynamic gene regulation rather than simple shifts in cellular abundance.

At the neuromuscular junction, Seq-Scope resolved coordinated yet distinct transcriptional responses across postsynaptic, perisynaptic, and Schwann cell-associated

domains. Denervation preserved the transcriptional identity of postsynaptic NMJ nuclei while inducing widespread extrajunctional expression of select acetylcholine receptor subunits across myofibers, consistent with established activity-dependent regulation of these genes (45, 46). In parallel, perisynaptic regions exhibited expansion and robust induction of extracellular matrix and injury-response genes, in agreement with previous reports describing activation of terminal Schwann cells and associated remodeling processes following nerve injury (36, 47-50). The ability to spatially disentangle these compartment-specific responses highlights the strength of high-resolution spatial transcriptomics for dissecting multicellular niches within intact tissue.

In conclusion, this study provides a detailed spatial and transcriptional framework for understanding skeletal muscle organization and its remodeling following denervation. By leveraging the resolution and transcriptome coverage of Seq-Scope, we uncover heterogeneity across fiber types, within individual myofibers, and among diverse non-myocyte populations, revealing spatially structured responses that are not accessible with previous transcriptomic approaches. While these findings are derived from a murine model and will require validation in human tissue and disease contexts, this atlas establishes a reference for future studies of neuromuscular pathology, aging, and regeneration. More broadly, it demonstrates the power of high-resolution spatial transcriptomics to advance understanding of complex, multinucleated tissues and their dynamic responses to physiological perturbation.

2.5 Methods

Mice Muscle Injury Model

All animal procedures were subject to the regulations established by the University of Michigan Institutional Animal Care and Use Committee (IACUC). C57BL/6J mice littermates, approximately 6 months of age, underwent sciatic nerve transection (SNT) on their left hindlimb and were randomly assigned to a 3-day or 7-day recovery group. Mice were anesthetized using 5% isoflurane (MWI Animal Health) followed by continuous 2% isoflurane administration to ensure an unresponsive state to tactile stimuli. Preoperative analgesia was administered using 5 mg/kg carprofen (MWI Animal Health). The hindlimbs were shaved and cleaned with chlorhexidine and 70% alcohol. A small incision (<10 mm) was made 1 mm posterior and parallel to the femur to expose the sciatic nerve. The sciatic nerve was transected with a removal

of a 5 mm segment, and the incision was closed with wound clips (Autoclip, BD Clay Adams). A sham procedure was replicated on the contralateral leg. Mice were placed on a heating pad after the procedure and monitored until full recovery from anesthesia. Mice recovered for either three or seven days before being sacrificed and tissue collection.

Seq-Scope array construction (1st-Seq)

Seq-Scope array was constructed as described previously (24). Seq-Scope array is a solid phase transcriptome capturing system, which was constructed on the HiSeq2000 (Illumina) platform with HDMI32-DraI, a single-stranded oligonucleotide library (Eurofins), and Read1-DraI sequencing primer. Through sequence-by-synthesis strategy, 100pM HDMI32-DraI oligonucleotides were placed and formed into clusters on the flow cell surface. Sequencer was manually set to perform 37bp single-end reading with a custom Read1-DraI primer. The run was completed right after 37 cycles, and the flow cell was retrieved. The output FASTQ file from the run will provide the sequence and the XY coordinates of the barcodes. The retrieved flow cell was further processed into ready-to-use Seq-Scope array. The flow cell was washed with nuclease-free water three times and incubated with DraI (R0129, NEB) and CIAP (M0525, NEB) enzyme mixture at 37 °C overnight to expose oligo-dT end. The flow cell was then treated with exonuclease I (M2903, NEB) cocktail at 37 °C for 45 min to remove non-specific single-stranded DNA. In the last step, the flow cell underwent a series of washing steps, including three times with nuclease-free water, three times with 0.1N NaOH for 5 min each, and three times with 0.1M Tris pH7.5. The cover of the flow cell was then disassembled using Tungsten Carbide Tip Scriber (IMT-8806, IMT) to expose the surface of the array for tissue attachment.

Tissue Preparation, Sectioning, and processing

Mice subjected to SNT were anesthetized through intraperitoneal injection of 0.5 mg/g avertin (2,2,2,- Tribromoethanol 97%, Sigma #T48402, and 2-methyl-2-butanol 99%, Sigma #240486-100ml). Soleus muscles were freshly dissected and embedded into O.C.T compound (23-730-571, Fisher Scientific). The OCT blocks were snap-frozen by submerging into liquid nitrogen pre-chilled 2-Methylbutane (MX0760, Sigma-Aldrich). The sectioning of the OCT-mounted frozen tissue was performed in a cryostat (Leica CM3050S, -15 °C) at a 5° cutting angle with each section 10 μm thick. Sections were attached to the array and re-warmed at room

temperature. Attached sections were then fixed in 4% formaldehyde (15170, Electron Microscopy Sciences) at room temperature for 10 min, followed by hematoxylin and eosin (H&E) staining that was described previously (24). H&E images were captured under the Keyence digital darkroom system.

Seq-Scope RNA Library Generation and Sequencing (2nd-Seq)

Seq-Scope library construction was constructed as described previously (24). In brief, tissue sections were permeabilized with 0.2 U/μL collagenase I (17018-029, Thermo Fisher) at 37 °C for 20 min, followed with 1mg/mL pepsin (P7000, Sigma) in 0.1M HCl at 37 °C for 10 min. Permeabilized tissue sections were then washed with 1X Maxima RT buffer (EP0751, Thermofisher). Reverse transcription was conducted on the array through the incubation of RT mixture (1X RT buffer (EP0751, Thermofisher), 4% Ficoll PM-400 (F4375-10G, Sigma), 1mM dNTPs (N0477L, NEB), RNase inhibitor (30281, Lucigen), Maxima H-RTase (EP0751, Thermofisher)) in a humidified chamber at 42 °C overnight.

Tissue sections were treated with exonuclease I (#M2903, NEB) cocktail the next day at 37 °C for 45 min to remove unused single-stranded DNA probes. Sections were then incubated in tissue digestion cocktail (100 mM Tris pH 8.0, 100 mM NaCl, 2% SDS, 5 mM EDTA, 16 U/mL Proteinase K (P8107S, NEB)) at 37 °C for 40 min. After the tissues were digested, the array was washed three times with nuclease-free water, three times with 0.1N NaOH for 5 min each, and three times with 0.1M Tris pH7.5.

Secondary stand synthesis was conducted following the washing step. The array was loaded with secondary strand synthesis mixture (1X NEBuffer-2 (NEB), 10 uM TruSeq Read2-conjugated Random Primer (IDT), 1mM dNTPs (N0477, NEB), Klenow Fragment (M0212, NEB), and nuclease-free water) and incubated in a humidified chamber at 37 °C for 2 hr. Solution was removed upon the completion of the reaction, and the array was washed with nuclease-free water three times. The array was then treated with 0.1N NaOH for 5 min to elute the barcoded cDNA library. The pH of the elution was neutralized by 3 M potassium acetate, pH5.5. Eluted library was then further purified using AMPure XP beads (1.8X bead/sample ratio, A63881, Beckman Coulter) according to the manufacturer's instruction.

Library amplification was conducted through two rounds of PCR. First round PCR was performed using Kapa HiFi Hotstart Readymix (KK2602, KAPA Biosystems), 2μM forward and

reverse primers as described in our previous paper (24), and the total eluted library. PCR product was purified using AMPure XP beads (A63881, Beckman Coulter) with 1.2X beads/sample ratio. Second round PCR was performed using Kapa HiFi Hotstart Readymix (KK2602, KAPA Biosystems), indexing primers described in (24), and 2nM of the first round PCR product. PCR product was purified again using AMPure XP beads (A63881, Beckman Coulter) with 0.6X beads/sample ratio. The size of the library was selected between 400-850bp through agarose gel electrophoresis. Selected library was purified using Zymoclean Gel DNA Recovery Kit (D4001, Zymo Research). The library was then sequenced with a paired-end (100-150bp) setup.

Generation of Spatial Digital Gene Expression (SGE) Matrix

Data are processed as described previously (24, 28), combing both 1st-Seq and 2nd-Seq FASTQ results. In the processing, 2nd-Seq FASTQ results were first filtered for their presence in 1st-Seq data table, so that the alignment and data processing could be more efficient. Then alignment was performed in STAR to produce spatial digital gene expression matrix matching individual gene expression with spatial coordinates identified through HDMI matching between 1st-Seq and 2nd-Seq.

Alignment between histology and spatial dataset

From the dataset, spatial transcriptome density is visualized through hillshade function. The hillshade image was semi-automatically aligned with H&E image using QGIS (version 3.22.9) georeferencer function, through manually marking salient spatial features common in both images.

Myofiber Segmentation and Hexagonal Gridding

Myofiber segmentation was performed on QGIS by manually drawing polygons on H&E images, according to myofiber boundary lines. Transcripts within each fiber were aggregated into a single datapoint, which was treated as a single cell located at a point on surface of the polygon. For hexagonal gridding, spatial data are aggregated toward a non-overlapping array of hexagons with 14μm sides, which was treated as a single cell located at the center of each hexagon.

Data Analysis and Visualization

The aggregated DGE matrix was analyzed in the Seurat package (53). Feature number threshold was applied to remove the grids (as indicated in the figure and the text) that corresponded to the area that was not overlaid by the tissue. Data were normalized using SCTransform function. After discovering principal components through RunPCA and generating UMAP manifold using RunUMAP, clustering was performed using the shared nearest neighbor modularity optimization implemented in Seurat's FindNeighbors and FindClusters function and then annotated to specific myofiber and cell types based on marker gene expression. For clustering segmented myofiber transcriptome from control/denervated dataset, clustering was sequentially performed, first to differentiate experimental conditions, and then to identify myofiber subtypes in each of experimental condition-dependent clusters. Clusters were visualized in histological space through plotting hexagonal centers using ggplot2 package (hexagonal dataset) or through plotting the whole polygonal area using geopandas and matplotlib package (segmentation dataset). FindMarkers and FindAllMarkers functions were used to identify Top markers from each cluster, and volcano plot was generated using the output of these functions using ggplot2. Level of gene expression was visualized though Seurat functions such as VlnPlot, DotPlot and FeaturePlot, and spatial gene expression was visualized through a custom visualization software which visualizes discovered genes as colored dots in the coordinate space. Area-proportional Venn diagrams were made using DeepVenn (54).

Overlapping hexagonal grid were generated to allow for multiscale sliding windows analysis (24, 28). To make a projection, annotations provided from non-overlapping hexagonal analysis were fine-tuned using FindTransferAnchors and TransferData in Seurat. Separately, factors learned from clusters of non-overlapping hexagonal analysis were projected into raw pixel-level dataset through FICTURE as described in our recent work (55).

2.6 References

1. Mukund K, Subramaniam S. Skeletal muscle: A review of molecular structure and function, in health and disease. Wiley Interdiscip Rev Syst Biol Med. 2020;12(1):e1462.

2. Ritso M, Tung LW, Rossi FMV. Emerging skeletal muscle stromal cell diversity: Functional divergence in fibro/adipogenic progenitor and mural cell populations. Exp Cell Res. 2022;410(1):112947.

3. Schiaffino S, Reggiani C. Fiber types in mammalian skeletal muscles. Physiol Rev. 2011;91(4):1447-531.

4. Williams K, Yokomori K, Mortazavi A. Heterogeneous Skeletal Muscle Cell and Nucleus Populations Identified by Single-Cell and Single-Nucleus Resolution Transcriptome Assays. Front Genet. 2022;13:835099.

5. Ehmsen JT, Hoke A. Cellular and molecular features of neurogenic skeletal muscle atrophy. Exp Neurol. 2020;331:113379.

6. Soendenbroe C, Andersen JL, Mackey AL. Muscle-nerve communication and the molecular assessment of human skeletal muscle denervation with aging. Am J Physiol Cell Physiol. 2021;321(2):C317-C29.

7. Petrany MJ, Swoboda CO, Sun C, Chetal K, Chen X, Weirauch MT, et al. Single-nucleus RNA-seq identifies transcriptional heterogeneity in multinucleated skeletal myofibers. Nat Commun. 2020;11(1):6374.

8. Dos Santos M, Backer S, Saintpierre B, Izac B, Andrieu M, Letourneur F, et al. Single-nucleus RNA-seq and FISH identify coordinated transcriptional activity in mammalian myofibers. Nat Commun. 2020;11(1):5102.

9. Kim M, Franke V, Brandt B, Lowenstein ED, Schowel V, Spuler S, et al. Single-nucleus transcriptomics reveals functional compartmentalization in syncytial skeletal muscle cells. Nat Commun. 2020;11(1):6375.

10. Orchard P, Manickam N, Ventresca C, Vadlamudi S, Varshney A, Rai V, et al. Human and rat skeletal muscle single-nuclei multi-omic integrative analyses nominate causal cell types, regulatory elements, and SNPs for complex traits. Genome Res. 2021;31(12):2258-75.

11. Lin H, Ma X, Sun Y, Peng H, Wang Y, Thomas SS, et al. Decoding the transcriptome of denervated muscle at single-nucleus resolution. J Cachexia Sarcopenia Muscle. 2022;13(4):2102-17.

12. Tian L, Chen F, Macosko EZ. The expanding vistas of spatial transcriptomics. Nat Biotechnol. 2023;41(6):773-82.

13. Bressan D, Battistoni G, Hannon GJ. The dawn of spatial omics. Science. 2023;381(6657):eabq4964.

14. Kang HM, Lee JH. Spatial Single-Cell Technologies for Exploring Gastrointestinal Tissue Transcriptome. Compr Physiol. 2023;13(3):4709-18.

15. D'Ercole C, D'Angelo P, Ruggieri V, Proietti D, Virtanen L, Parisi C, et al. Spatially resolved transcriptomics reveals innervation-responsive functional clusters in skeletal muscle. Cell Rep. 2022;41(12):111861.

16. Heezen LGM, Abdelaal T, van Putten M, Aartsma-Rus A, Mahfouz A, Spitali P. Spatial transcriptomics reveal markers of histopathological changes in Duchenne muscular dystrophy mouse models. Nat Commun. 2023;14(1):4909.

17. Larouche JA, Wallace EC, Spence BD, Buras E, Aguilar CA. Spatiotemporal mapping of immune and stem cell dysregulation after volumetric muscle loss. JCI Insight. 2023;8(7).

18. Ruoss S, Esparza MC, Vasquez-Bolanos LS, Nasamran CA, Fisch KM, Engler AJ, et al. Spatial transcriptomics tools allow for regional exploration of heterogeneous muscle pathology in the pre-clinical rabbit model of rotator cuff tear. J Orthop Surg Res. 2022;17(1):440.

19. Stec MJ, Su Q, Adler C, Zhang L, Golann DR, Khan NP, et al. A cellular and molecular spatial atlas of dystrophic muscle. Proc Natl Acad Sci U S A. 2023;120(29):e2221249120.

20. Patsalos A, Halasz L, Oleksak D, Wei X, Nagy G, Tzerpos P, et al. Spatiotemporal transcriptomic mapping of regenerative inflammation in skeletal muscle reveals a dynamic multilayered tissue architecture. J Clin Invest. 2024;134(20).

21. Coulis G, Jaime D, Guerrero-Juarez C, Kastenschmidt JM, Farahat PK, Nguyen Q, et al. Single-cell and spatial transcriptomics identify a macrophage population associated with skeletal muscle fibrosis. Sci Adv. 2023;9(27):eadd9984.

22. Lequain H, Degletagne C, Streichenberger N, Valantin J, Simonet T, Schaeffer L, et al. Spatial Transcriptomics Reveals Signatures of Histopathological Changes in Muscular Sarcoidosis. Cells. 2023;12(23).

23. Gurkar AU, Gerencser AA, Mora AL, Nelson AC, Zhang AR, Lagnado AB, et al. Spatial mapping of cellular senescence: emerging challenges and opportunities. Nat Aging. 2023;3(7):776-90.

24. Cho C-S, Xi J, Si Y, Park S-R, Hsu J-E, Kim M, et al. Microscopic examination of spatial transcriptome using Seq-Scope. Cell. 2021;184(13):3559-72. e22.

25. Pette D, Spamer C. Metabolic properties of muscle fibers. Fed Proc. 1986;45(13):2910-4.

26. Do TH, Ma F, Andrade PR, Teles R, de Andrade Silva BJ, Hu C, et al. TREM2 macrophages induced by human lipids drive inflammation in acne lesions. Sci Immunol. 2022;7(73):eabo2787.

27. Si Y, Lee C, Hwang Y, Yun JH, Cheng W, Cho CS, et al. FICTURE: scalable segmentation-free analysis of submicron-resolution spatial transcriptomics. Nat Methods. 2024;21(10):1843-54.

28. Xi J, Lee JH, Kang HM, Jun G. STtools: a comprehensive software pipeline for ultra-high-resolution spatial transcriptomics data. Bioinformatics Advances. 2022;2(1).

29. Gokce E, Gun N. The Relationship Between Exercise, Cathepsin B, and Cognitive Functions: Systematic Review. Percept Mot Skills. 2023;130(4):1366-85.

30. Kar NC, Pearson CM. Early elevation of cathepsin B1 in human muscle disease. Biochem Med. 1977;18(1):126-9.

31. West JA, Davis CP, Sunwoo H, Simon MD, Sadreyev RI, Wang PI, et al. The long noncoding RNAs NEAT1 and MALAT1 bind active chromatin sites. Mol Cell. 2014;55(5):791-802.

32. Wolbert J, Li X, Heming M, Mausberg AK, Akkermann D, Frydrychowicz C, et al. Redefining the heterogeneity of peripheral nerve cells in health and autoimmunity. Proc Natl Acad Sci U S A. 2020;117(17):9466-76.

33. Pantera H, Moran JJ, Hung HA, Pak E, Dutra A, Svaren J. Regulation of the neuropathy-associated Pmp22 gene by a distal super-enhancer. Hum Mol Genet. 2018;27(16):2830-9.

34. Berger P, Sirkowski EE, Scherer SS, Suter U. Expression analysis of the N-Myc downstream-regulated gene 1 indicates that myelinating Schwann cells are the primary disease target in hereditary motor and sensory neuropathy-Lom. Neurobiol Dis. 2004;17(2):290-9.

35. Castro R, Taetzsch T, Vaughan SK, Godbe K, Chappell J, Settlage RE, et al. Specific labeling of synaptic schwann cells reveals unique cellular and molecular features. Elife. 2020;9.

36. Guzman SD, Abu-Mahfouz A, Davis CS, Ruiz LP, Macpherson PC, Brooks SV. Decoding muscle-resident Schwann cell dynamics during neuromuscular junction remodeling. JCI Insight. 2025.

37. Seaberg BL, Purao S, Rimer M. Validation of terminal Schwann cell gene marker expression by fluorescent in situ hybridization using RNAscope. Neurosci Lett. 2022;771:136468.

38. Zhang S, Cai B, Li Z, Wang K, Bao L, Li C, et al. Fibroblastic SMOC2 Suppresses Mechanical Nociception by Inhibiting Coupled Activation of Primary Sensory Neurons. J Neurosci. 2022;42(20):4069-86.

39. Schuler SC, Kirkpatrick JM, Schmidt M, Santinha D, Koch P, Di Sanzo S, et al. Extensive remodeling of the extracellular matrix during aging contributes to age-dependent impairments of muscle stem cell functionality. Cell Rep. 2021;35(10):109223.

40. De Micheli AJ, Swanson JB, Disser NP, Martinez LM, Walker NR, Oliver DJ, et al. Single-cell transcriptomic analysis identifies extensive heterogeneity in the cellular composition of mouse Achilles tendons. Am J Physiol Cell Physiol. 2020;319(5):C885-C94.

41. Lang F, Aravamudhan S, Nolte H, Turk C, Holper S, Muller S, et al. Dynamic changes in the mouse skeletal muscle proteome during denervation-induced atrophy. Dis Model Mech. 2017;10(7):881-96.

42. Otten C, van der Ven PF, Lewrenz I, Paul S, Steinhagen A, Busch-Nentwich E, et al. Xirp proteins mark injured skeletal muscle in zebrafish. PLoS One. 2012;7(2):e31041.

43. Molt S, Buhrdel JB, Yakovlev S, Schein P, Orfanos Z, Kirfel G, et al. Aciculin interacts with filamin C and Xin and is essential for myofibril assembly, remodeling and maintenance. J Cell Sci. 2014;127(Pt 16):3578-92.

44. Leber Y, Ruparelia AA, Kirfel G, van der Ven PF, Hoffmann B, Merkel R, et al. Filamin C is a highly dynamic protein associated with fast repair of myofibrillar microdamage. Hum Mol Genet. 2016;25(13):2776-88.

45. Tsay HJ, Schmidt J. Skeletal muscle denervation activates acetylcholine receptor genes. J Cell Biol. 1989;108(4):1523-6.

46. Yumoto N, Wakatsuki S, Sehara-Fujisawa A. The acetylcholine receptor gamma-to-epsilon switch occurs in individual endplates. Biochem Biophys Res Commun. 2005;331(4):1522-7.

47. Proietti D, Giordani L, De Bardi M, D'Ercole C, Lozanoska-Ochser B, Amadio S, et al. Activation of skeletal muscle-resident glial cells upon nerve injury. JCI Insight. 2021;6(7).

48. Love FM, Thompson WJ. Schwann cells proliferate at rat neuromuscular junctions during development and regeneration. J Neurosci. 1998;18(22):9376-85.

49. Sugiura Y, Lin W. Neuron-glia interactions: the roles of Schwann cells in neuromuscular synapse formation and function. Biosci Rep. 2011;31(5):295-302.

50. Huang X, Jiang J, Xu J. Denervation-Related Neuromuscular Junction Changes: From Degeneration to Regeneration. Front Mol Neurosci. 2021;14:810919.

51. Min BD, Hwang CY, Kim D, Kim SY, Jayasinghe JNC, Tran MN, et al. Advancing muscle aging and sarcopenia research through spatial transcriptomics. Osteoporos Sarcopenia. 2025;11(2 Suppl):22-31.

52. Umek N, Meznaric M, Sink Z, Blagotinsek Cokan K, Prosenc Zmrzljak U, Horvat S. In situ spatial transcriptomic analysis of human skeletal muscle using the Xenium platform. Cell Tissue Res. 2025;399(3):291-302.

53. Hao Y, Stuart T, Kowalski MH, Choudhary S, Hoffman P, Hartman A, et al. Dictionary learning for integrative, multimodal and scalable single-cell analysis. Nat Biotechnol. 2023.

54. Hulsen T. DeepVenn--a web application for the creation of area-proportional Venn diagrams using the deep learning framework Tensorflow. js. arXiv preprint arXiv:221004597. 2022.

55. Si Y, Lee C, Hwang Y, Yun JH, Cheng W, Cho CS, et al. FICTURE: scalable segmentation-free analysis of submicron-resolution spatial transcriptomics. Nat Methods. 2024;21(10):1843–54.

Chapter 3 Histopathology and Spatial Transcriptomics Jointly Map Myofiber-specific Pathological Programs in mTORC1-driven Myopathy

3.1 Abstract

Skeletal muscle is a structurally organized and functionally diverse organ composed of heterogeneous myofiber types and supporting non-myocyte populations that act in concert to generate force, regulate metabolism, and maintain systemic homeostasis. Myopathies occur in many different diseases, but the mechanisms that drive these muscle pathologies are still largely unknown, partly because conventional approaches cannot link histopathological features to molecular states at single-fiber resolution. To address this challenge, we brought histopathology and spatial transcriptomics together by applying high-resolution Seq-Scope technology to a rodent model of mTORC1 hyperactivation, which produces diverse pathological alterations within individual myofibers. Cross-sections from extensor digitorum longus (EDL) and soleus (SOL), two muscles with distinct fiber-type compositions, were profiled to determine how transcriptome changes are linked to histopathological outcomes. Our analyses reveal that mTORC1 hyperactivation elicits distinct, fiber-type–dependent pathological programs. Type I and IIa fibers, abundant in SOL but scarce in EDL, were largely resistant to mTORC1-induced pathology, exhibiting only minimal morphological alterations and no fiber type-specific responses beyond those commonly observed throughout the tissue. In contrast, type IIx fibers, shared between both muscles, diverged into opposing fates: in SOL, they underwent abnormal enlargement driven by sustained growth signaling, cytoskeletal remodeling, and impaired proteostasis with defective autophagy; whereas in EDL, they developed basophilia characterized by lipid-supported respiration fueling excessive ribonucleotide synthesis and RNA accumulation. Within the same muscle, type IIb fibers displayed striking heterogeneity with discrete transcriptional states encompassing canonical stress responses, oxidative metabolic activation, and developmental reprogramming. In parallel, non-myocytic populations, including activated macrophages and fibroblasts, accumulated preferentially in SOL, forming a fibrotic microenvironment supporting inflammation, tissue remodeling and hypertrophy. Taken together,

these findings reveal that sustained mTORC1 signaling disrupts muscle homeostasis through distinct metabolic and structural routes, directly linking histopathological phenotypes to their molecular states at single-fiber resolution.

3.2 Introduction

Skeletal muscle is a multifunctional organ that drives movement while being critical for maintaining metabolic homeostasis. This balanced control of essential functions is critical for maintaining health and relies on the heterogeneity of myofibers with respect to contraction and energy metabolism. Differences between myofibers underlie the classic classification into slow and fast, and oxidative and glycolytic fiber types, a framework that has long explained variation in endurance, contractile speed, and fatigue resistance. (1). At the molecular level, this classification is largely determined by the expression of distinct myosin heavy chain (MyHC) isoforms, which define the major fiber types: type I (MF1; slow oxidative), type IIa (MF2A; fast oxidative), type IIx (MF2X; intermediate fast glycolytic), and type IIb (MF2B; fast glycolytic). The functional specialization of each fiber type allows skeletal muscle as a whole to support diverse physiological demands (2).

Mammalian target of rapamycin complex 1 (mTORC1) is a central regulator of cell growth and anabolism that senses inputs from nutrient, growth factor, and energy signals (3). Its kinase activity is activated at the lysosomal surface through the small GTPase RHEB, which is inhibited by the TSC1/TSC2 complex during growth factor deprivation or energy depletion. In parallel, mTORC1 recruitment to lysosomes is controlled by amino acid availability. Under amino acid insufficiency, the GATOR1 complex (DEPDC5, NPRL2, and NPRL3) maintains the Rag GTPases (RRAGA/B and RRAGC/D) in their inactive GDP-bound state, thereby preventing mTORC1 from translocating to the lysosomal surface and becoming activated (4,5). Disruption of either TSC1 or DEPDC5 elevates mTORC1 activity, but full constitutive activation requires disruption of both pathways due to the presence of negative feedback mechanisms (6–8). Once active, mTORC1 phosphorylates downstream targets such as S6K1 and 4E-BP1 to promote mRNA translation, while simultaneously suppresses autophagy initiation through inhibitory phosphorylation of ULK1 (9–11). By linking environmental inputs to biosynthetic outputs, mTORC1 ensures that cell growth and anabolic metabolism occur only under permissive conditions.

In skeletal muscle, appropriate mTORC1 activity is indispensable for growth, maintenance, and repair (12). Muscle-specific deletion of Raptor, an essential subunit of mTORC1, results in profound atrophy and impaired force generation (13), highlighting the importance of proper mTORC1 activity in maintaining muscle homeostasis. On the contrary, sustained hyperactivation of mTORC1, whether induced experimentally through muscle-specific TSC1 deletion or arising naturally during aging, leads to progressive myopathy marked by fiber degeneration, metabolic stress, impaired proteostasis, and loss of regenerative capacity (8). In our previous work, we produced a mouse strain with depletion of both TSC1 and DEPDC5 in muscle tissue (*Ckm-Cre Tsc1*$^{F/F}$ *Depdc5*$^{F/F}$) to enforce constitutive hyperactivated mTORC1 signaling pathway (6,14). Unlike single-knockout models (7,8), which showed little pathology in young mice, *Ckm-Cre Tsc1*$^{F/F}$ *Depdc5*$^{F/F}$ mice develop severe early-onset myopathy and skeletal muscle dysfunction. This phenotype was associated with excessive oxidative stress, impaired proteostasis, and accumulation of the autophagy adaptor SQSTM1/p62, resulting in dysregulation of myofiber homeostasis.

With recent advances in technologies, single-cell (sc) and single-nucleus (sn) RNA-seq resources have mapped aging muscle across lifespan and diseases, providing valuable insights into cellular composition and aging-associated shifts in regenerative, immune, and fibrotic states (15–26). Spatial transcriptomic and imaging-based methods such as MERFISH (27) and smFISH (28) have further visualized the distribution of specific transcripts within intact myofibers and tissue sections, while multiplex proteomic platforms like CODEX (29) have profiled fiber-type mosaics at the protein level. Together, these approaches have greatly expanded our understanding of muscle biology and aging. However, they fall short in resolving the fiber-type complexity of myopathy. Sc/snRNA-seq relies on tissue dissociation and cannot resolve intact myofibers, while spatial methods to date have been constrained to targeted panels or low resolution, making it difficult to capture the full complexity of fiber-type heterogeneity in the myopathic process.

To directly address this gap, we applied Seq-Scope, a high-resolution spatial transcriptome profiling technology that we recently developed (30,31). Its sub-micrometer resolution with unbiased whole-transcriptome coverage enables high-fidelity mapping of transcriptional diversity at the single-myofiber level. Using Seq-Scope, we profiled cross sections of extensor digitorum longus (EDL) muscles and soleus (SOL) muscles, two

anatomically distinct tissues encompassing the major myofiber types, from *Ckm-Cre Tsc1*$^{F/F}$ *Depdc5*$^{F/F}$ and control littermates. Our analyses revealed that mTORC1 hyperactivation elicits both global stress responses and fiber-type-specific remodeling programs. Comparison between EDL and SOL demonstrated striking context-dependent plasticity of MF2X, which engaged distinct metabolic and cytoskeletal remodeling pathways in each muscle. Within the same muscle, MF2B fibers reprogrammed their classical glycolytic transcriptome, acquiring either MF2X-like oxidative signatures or undifferentiated myofiber-like developmental signatures. In addition, classical myopathic features, such as abnormal myofiber enlargement and basophilic fibers, were each linked to characteristic transcriptomic profiles with predicted functional outcomes. Overall, this study provides a histopathology-guided, single-fiber spatial framework for dissecting fiber-type-specific remodeling under mTORC1 hyperactivation, offering molecular insight into the developmental processes of myopathies and a foundation for future mechanistic studies of muscle physiology and disease.

3.3 Results

3.3.1 Seq-Scope enables combined analysis of histopathology and single-myofiber transcriptomics

We have formerly generated a mouse model of unregulated mTORC1 hyperactivation by concomitantly deleting *Tsc1* and *Depdc5*, thereby achieving maximal activation of both Rheb and Rag arms of mTORC1 signaling (Figure 3.1.A). mTORC1 hyperactivation in skeletal muscle severely disrupted tissue homeostasis, leading to loss of muscle function associated with various pathologies, including basophilic fibers, enlarged fibers, and centrally nucleated fibers (Figure 3.1.A; white, black and green arrows, respectively). To capture the molecular changes underlying these phenotypes at the resolution of individual myofibers, we used Seq-Scope, a spatial transcriptomics platform with sub-micrometer resolution (average 0.5–0.7 μm), which we have recently developed and optimized (30,31). By aggregating transcripts according to the histology-based myofiber segmentation, the spatial transcriptome could be precisely assigned to individual myofibers. This approach preserved fiber morphology and spatial context while revealing and mapping transcriptomic diversity.

In this study, four *Ckm-Cre Tsc1*$^{F/F}$ *Depdc5*$^{F/F}$ (muscle-specific deletion of *Tsc1* and *Depdc5*) and four *Tsc1*$^{F/F}$ *Depdc5*$^{F/F}$ (Cre-negative control) littermates were sacrificed at 10 weeks of age. EDL and SOL muscles were harvested, embedded in OCT, freshly frozen, and sectioned. A total of 16 cross-sections (two muscles per mouse) were placed onto Seq-Scope arrays for spatial transcriptomic profiling. The exact same sections were subjected to H&E staining and DAPI/WGA imaging on the array surface prior to transcript capture and library generation (Figure 3.1.B; first and second row, respectively). Sequencing of the Seq-Scope library yielded a total of 700 million unique reads that successfully aligned to the mm10 reference genome with valid spatial barcodes. The resulting RNA density map (Figure 3.1.B, third row) revealed strong localization of transcripts at the periphery of myofibers, consistent with known muscle architecture. Using WGA imaging data and Cellpose segmentation algorithm to delineate cellular membranes, we segmented 8,616 individual myofibers across 16 tissue sections (Figure 3.1.B, fourth row, Figure 3.3.A). Data from each sample was considered independent, integrated and clustered to assign myofiber identities. The data showed minimal batch effects, aside from the expected separation of SOL and EDL with their distinct myofiber compositions (Figure 3.1.C and Figure 3.3.B-D). Myofiber types were also clearly distinguished by the expression of their corresponding myosin heavy chain isoforms (Figure 3.1.D and Figure 3.3.C) and by metabolic genes associated with oxidative (MF1/MF2A) or glycolytic (MF2B) pathways (Figure 3.3.E-F).

To systematically assess the histopathological features observed in mutant muscle, we quantified the prevalence of basophilic fibers, enlarged fibers, and centrally nucleated fibers across all sections (Figure 3.2.A). Basophilic fibers were further classified by staining patterns: transitional basophilic fibers showed scattered dark particles (Figure 3.2.A, right panel, top row), whereas developed basophilic fibers displayed dense, strip-like filling (Figure 3.2.A, right panel, bottom row). Strikingly, basophilic fibers were observed only in mutant EDL muscle, while enlarged fibers were restricted to mutant SOL muscle (Figure 3.2.B, left panel). Fibers with central nuclei were also more frequent in mutant SOL muscle. When stratified by fiber type, we found that MF2X fibers showed the highest frequency of pathological features relative to other fiber types, suggesting that MF2X fibers exhibit the strongest pathological response to mTORC1 hyperactivation (Figure 3.2.B, right panel, 3.3.G).

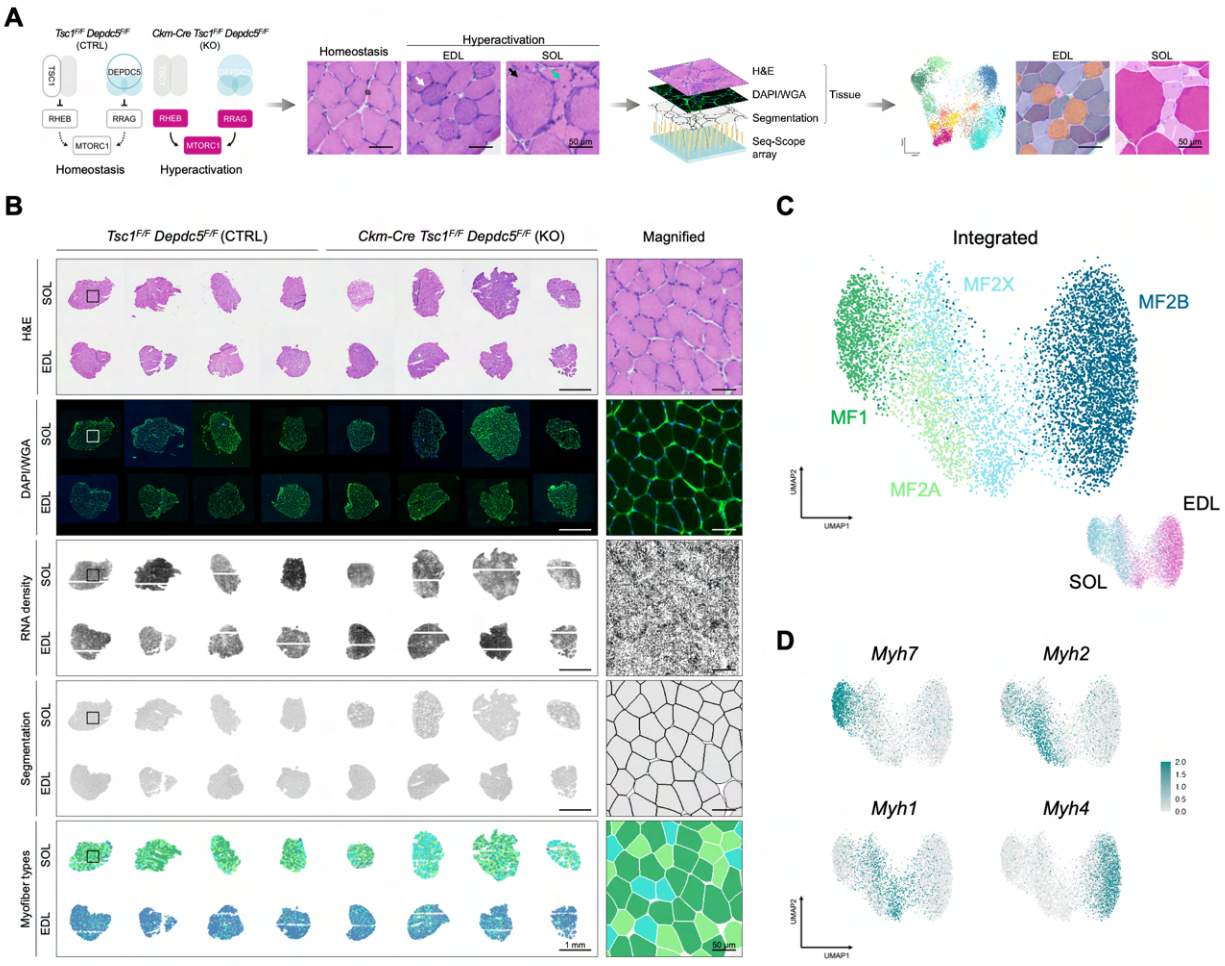


Figure 3.1 Seq-Scope enables histopathology-guided single-myofiber transcriptome analysis

(A) Schematic of the experimental workflow. Arrows indicate pathological phenotypes including basophilia (white), hypertrophy (black), and central nuclei (green). Hematoxylin and eosin (H&E) histology, DAPI/wheat germ agglutinin (WGA) imaging, and Seq-Scope whole transcriptome analysis are performed on the same slide, which allows precise segmentation and single-myofiber transcriptome analysis. (B) Cross-sections of control and mutant skeletal muscles examined by Seq-Scope. From top to bottom, images are displayed as H&E histology, DAPI/WGA staining, RNA density map from Seq-Scope transcriptome data, single-myofiber segmentation, and spatial myofiber type projection, according to the clusters identified in (C). *Tsc1*$^{F/F}$ *Depdc5*$^{F/F}$: control; *Ckm-Cre Tsc1*$^{F/F}$ *Depdc5*$^{F/F}$: mutant. SOL: soleus muscle; EDL: extensor digitorum longus muscle. MF1: myofiber type I; MF2A: myofiber type IIa; MF2X: myofiber type IIx; MF2B: myofiber type IIb. (C) UMAP manifolds displaying the major myofiber types identified by multidimensional clustering. Datasets were integrated across mice. Each point (n = 8616) represents an individual myofiber and is colored according to its corresponding myofiber type (center) or its originating muscle depot (lower right). (D) UMAP manifold colored by the expression levels of myosin heavy chain (*Myh*) isoforms that represent each myofiber type.

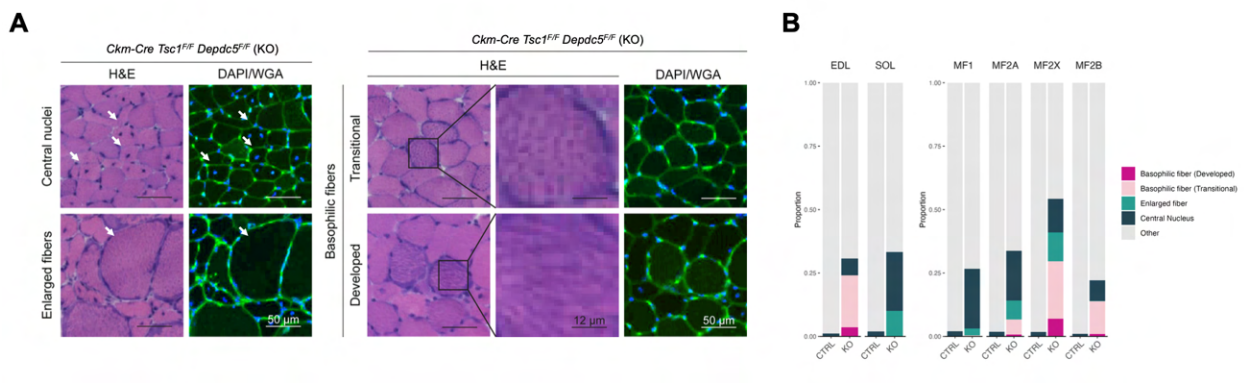


Figure 3.2 mTORC1 hyperactivation-induced muscular pathologies

(A) Pathological phenotypes observed in mTORC1 hyperactivated skeletal muscle. Left panel: centrally nucleated myofibers (arrows in the top row) and hypertrophic fibers (arrows in the bottom row). Right panel: transitional basophilic fibers (top row, scattered dark particles) and developed basophilic fibers (bottom row, dense and strip-like filling). Boxed areas are magnified on the right. (B) Quantification of pathological phenotype prevalence by muscle depot (left) or by myofiber type (right). "Other" includes myofibers from control muscles as well as morphologically normal fibers from mutant muscles. CTRL, control; KO, mutant.

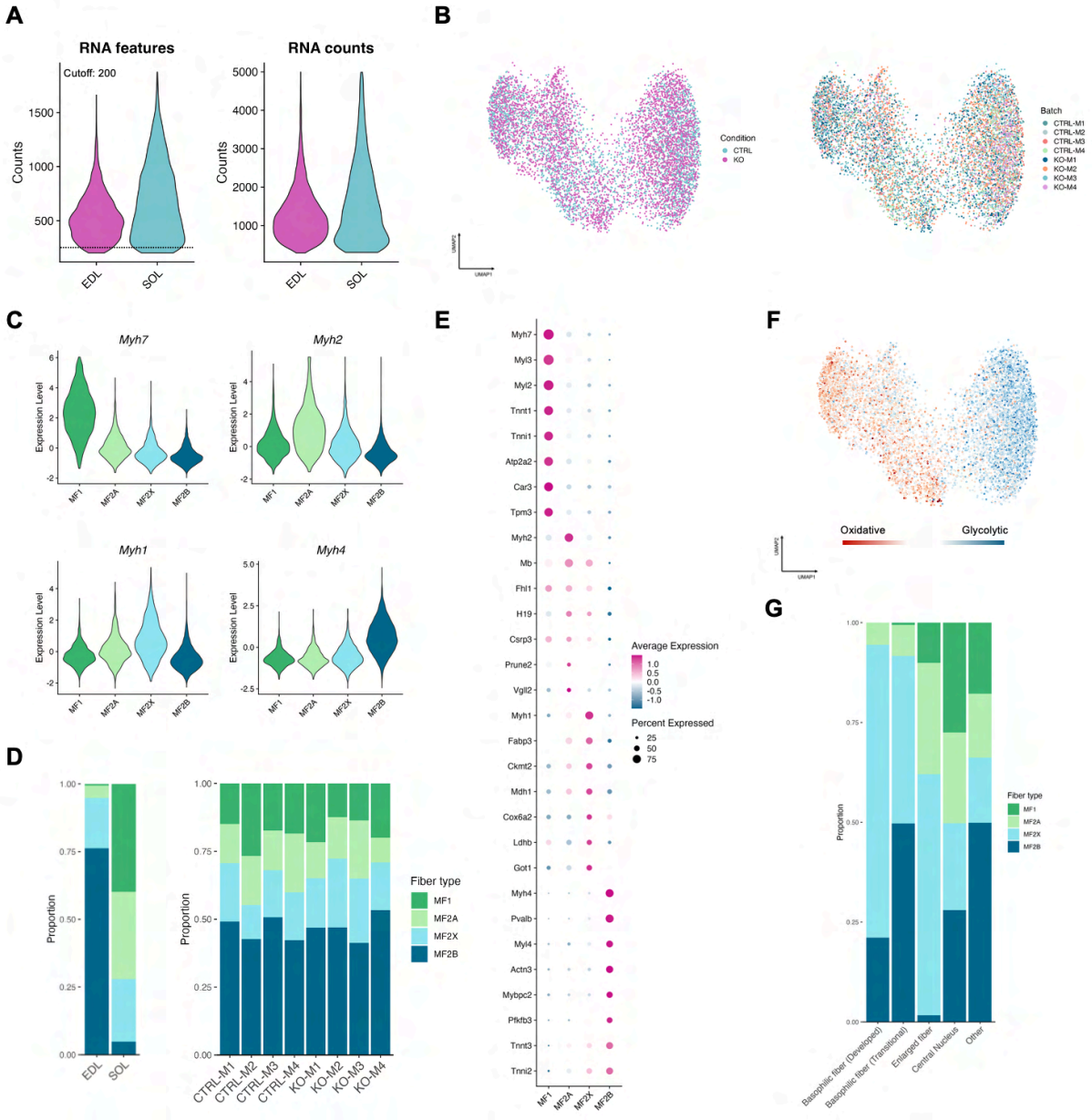


Figure 3.3 Stratification of single-myofiber transcriptome into classical myofiber types

(A) Distribution of unique RNA features (number of detected genes; left) and transcript counts (right) per segmented myofiber, shown separately for EDL and SOL. A minimum cutoff of 200 unique RNA features was applied prior to integration and downstream analyses. (B) Data integration performance. The UMAP manifold is colored according to the conditions (left) and batches (right) of individual myofibers. All eight biological replicates, from either control or mutant mice, contributed to all clusters with similar proportions. (C) Expression of myofiber-specific myosin heavy chain isoforms across designated myofiber types. (D) Proportion of myofiber types across muscles (left) and batches (right). (E) Dot plot representing the expression of fiber type-specific marker genes in each myofiber type cluster. Dot size represents the proportion of myofibers expressing each gene, and dot color represents the average expression level. (F) UMAP manifold colored according to the combined scores of metabolic-related genes across the oxidative (red) and glycolytic (blue) axis. (G) Distribution of myofiber types within each pathological phenotype category.

3.3.2 Identification of fiber type-specific responses to mTORC1 hyperactivation

Skeletal muscle fiber types differ not only in contractile speed but also in metabolic specialization (1). These intrinsic differences suggest that individual fiber types may respond unevenly to stress. To test this, we conducted differential gene expression analysis to compare transcriptomic signatures of each myofiber cluster between control (homeostasis) and mutant (hyperactivation) muscle (Figure 3.4.A and Figure 3.6.A). Even though many genes were commonly upregulated in response to mTORC1 hyperactivation, representing conserved response pathways, substantial number of genes showed myofiber type–specific signatures (Figure 3.4.B). As described in the Methods, we have classified the genes upregulated under mTORC1 hyperactivation into global response (expressed across all four fiber types, 25%); partially specific response (expressed in two or three fiber types, 49.2% in sum); and responses specific for MF2A (5.6%, 7 genes), MF2X (4.0%, 5 genes), and MF2B (16.1%, 20 genes) fiber types (Figure 3.5.A and Figure 3.6.B-C). Notably, MF1 transcriptome only showed global responses, without any unique signatures, consistent with its well-documented resilience to metabolic and structural stress (32).

To systematically evaluate the functional implications of both global and fiber-type–specific signatures, we performed gene ontology (GO) enrichment analysis. Globally expressed genes were enriched in pathways related to ion transport regulation, muscle differentiation, cytoskeletal and synaptic remodeling, protein localization to membranes, and proteostasis (Figure 3.5.B). These pathways, directly linked to mTORC1 hyperactivation-induced proteostasis disruption and damage responses, were also observed in our previous bulk RNA-seq findings (6), highlighting the reproducibility of our analysis across different platforms.

In contrast, enabled by the Seq-Scope technology, the present study revealed novel findings of fiber type–specific responses (Figure 3.4.B and Figure 3.5.C). CompareGO clustering showed that MF2B myofibers, despite experiencing the same mTORC1-driven stress as other fiber types, exhibited little enrichment of oxidative stress or detoxification processes. Instead, their response was dominated by reinforcement of carbohydrate metabolic pathways with the upregulation of *Pkm*, *Phka1*, *Agl*, and *Pfkb3*, indicating a rigid glycolytic program even under pathological conditions. By contrast, MF2A myofibers enriched heavily in stress-response and protein quality-control pathways, reflected by the induction of *Tfrc* (transferrin receptor, iron uptake), *Mt1* (metallothionein, oxidative stress buffering), *Psmd4*, and *Psmc3* (proteasome-

related subunits), alongside regulators such as *Igfbp5* (insulin growth factor binding protein) and *Sln* (sarcolipin, calcium handling) that mark contractile and developmental specialization. MF2X myofibers, on the other hand, exhibited strong remodeling signatures with elevated *Asb15* (E3 ubiquitin ligase adaptor in myogenesis), *Sparcl1* (extracellular matrix glycoprotein), and *Actc1* (cardiac α-actin, muscle development marker), accompanied by stress regulators *Ctsb* (cathepsin B) and *Gpx3* (glutathione peroxidase), suggesting greater transcriptional plasticity in structural and oxidative adaptation. Together, these results establish a clear correspondence between gene-level signatures and higher-order functional pathways (Figure 3.5.D), validating the concept that different fiber types deploy distinct transcriptional programs in response to mTORC1 hyperactivation.

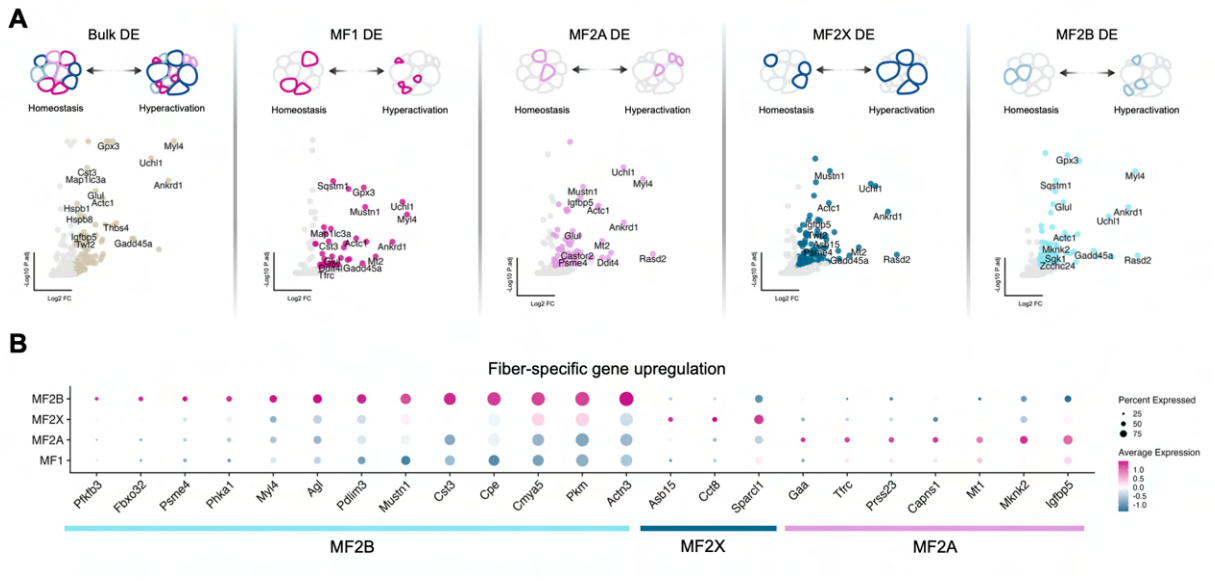


Figure 3.4 Identification of fiber type-specific responses to mTORC1 hyperactivation

(A) Schematic of the analytical workflow for fiber type-specific differential expression (DE) analysis comparing control (homeostasis) and mutant (hyperactivation) muscle. Upregulated genes are shown (adjusted p-value < 0.05, log2FC > 1.5). (B) Representative expression patterns of genes that are exclusively upregulated in individual myofiber types, selected from a broader set (Figure 3.6.B). Exclusivity was determined by the Kruskal-Wallis test (adjusted p-value < 0.05). Exclusively expressed genes were not identified in mutant MF1 fibers.

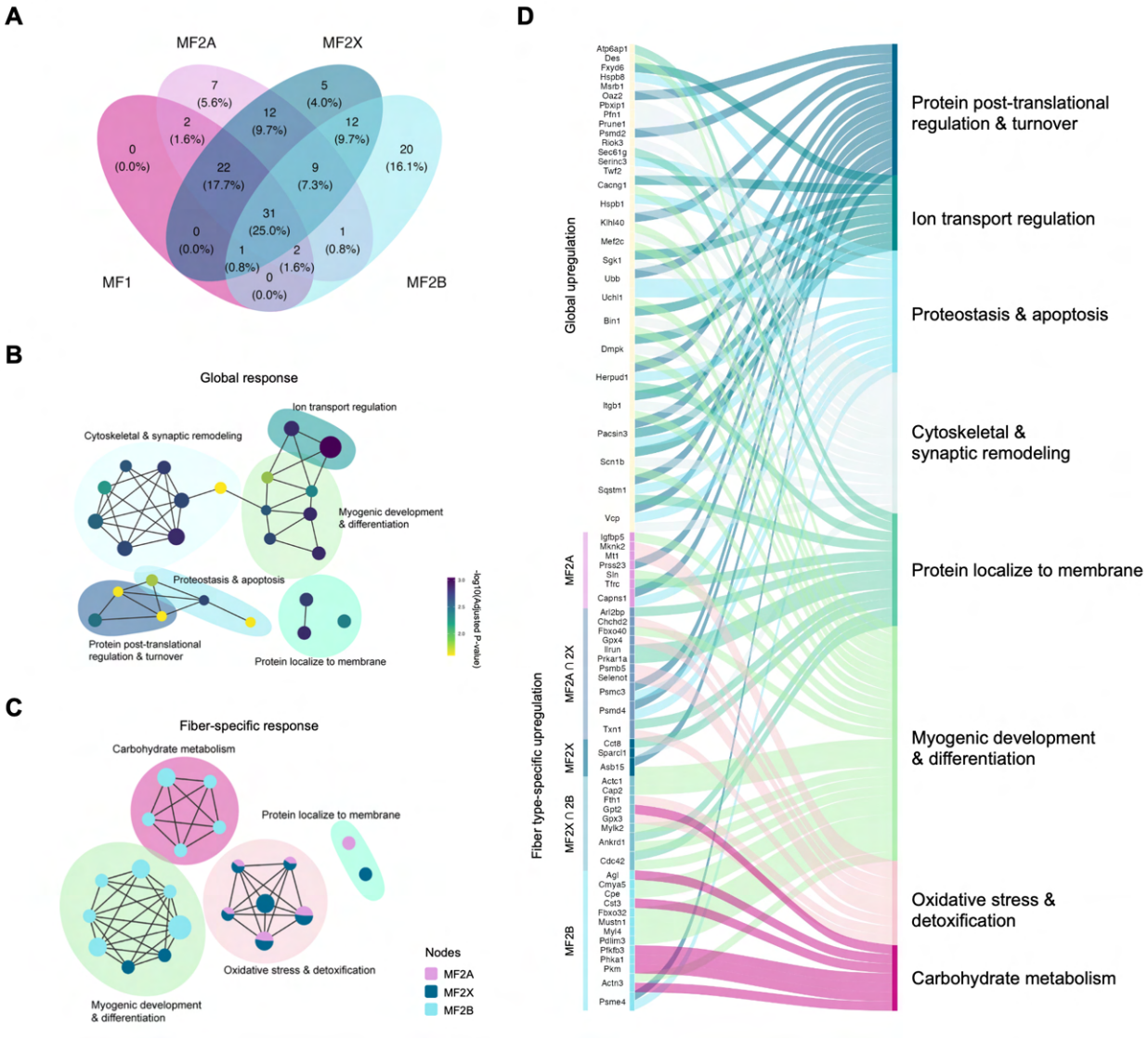


Figure 3.5 Functional analysis of fiber type-specific responses to mTORC1 hyperactivation

(A) Venn diagram depicting the uniqueness and overlap of upregulated genes across different myofiber types, with numbers and percentages shown for both shared and unique gene sets. (B) Genes upregulated across all four fiber types (Global Response) were analyzed by gene ontology (GO) enrichment and visualized as a network. Each node represents a GO term, grouped by functional proximity within the enrichment hierarchy. Node size indicates the number of genes associated with the term, and node color reflects enrichment significance (adjusted p-value). (C) Genes selectively upregulated in specific fiber types were analyzed using compareGO. GO terms were grouped by functional proximity. Node size reflects the number of contributing genes, and node colors are shown as pie charts indicating the relative enrichment strength (adjusted p-value) contributed by each fiber type. (D) Genes globally upregulated across all fiber types and genes selectively upregulated in specific fiber types were mapped to enriched GO groups. The origin of each gene set is indicated by the stratum, and connecting threads represent gene-to-pathway relationships, colored by GO term identity.

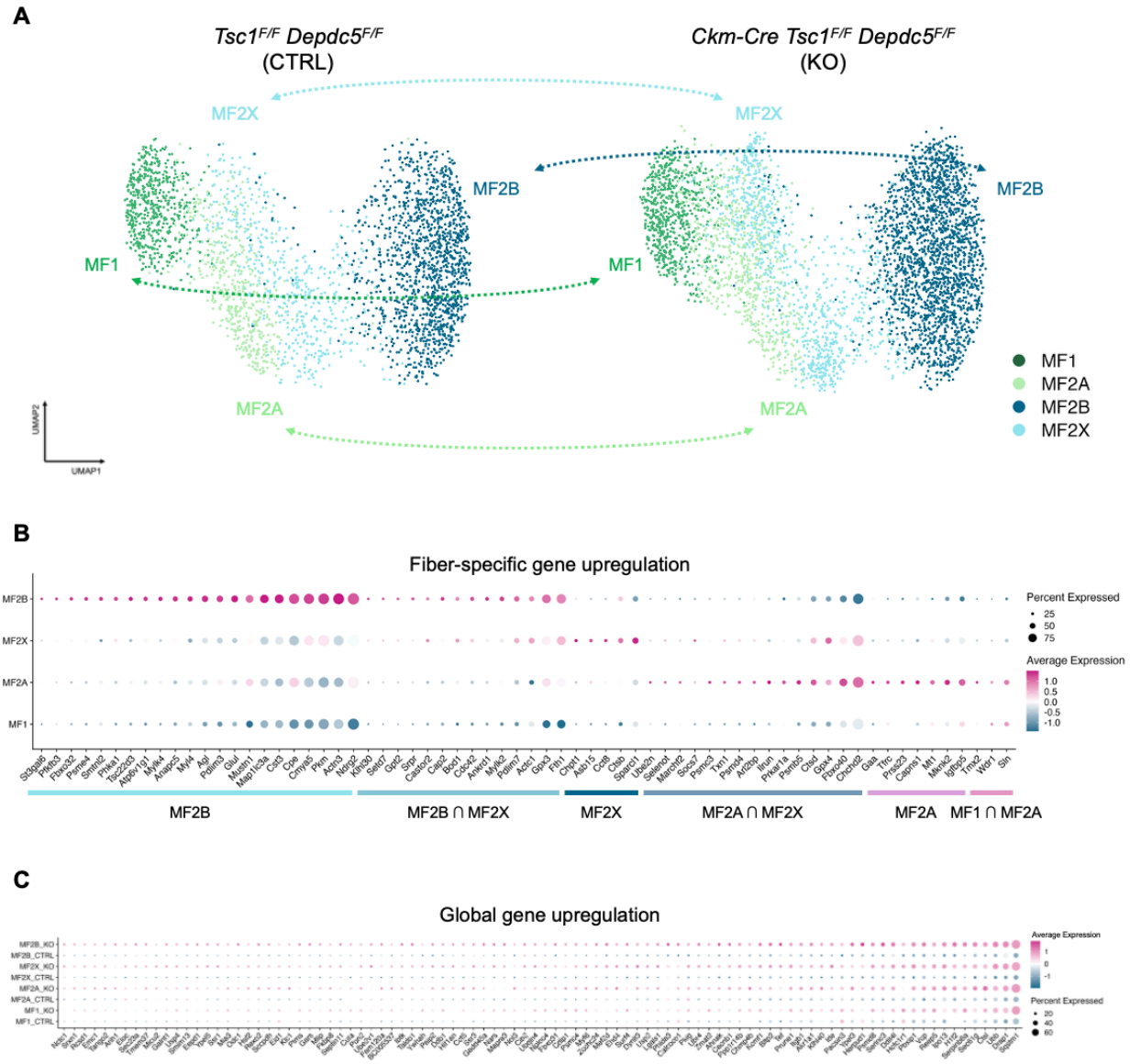


Figure 3.6 Validation of fiber type-specific and global gene expression comparisons

(A) From the UMAP manifold showing fiber type identities (Figure 3.1.C), two condition-specific manifolds were generated. Dotted double-arrow lines indicate the fiber type–matched comparisons used for differential expression analysis. (B) Expression of mTORC1 hyperactivation-induced genes that are upregulated only in specific myofiber types in mutant muscle. The intersection symbol (∩) indicates genes that are upregulated in both of the indicated myofiber types. (C) Expression of globally upregulated genes induced by mTORC1 hyperactivation across all myofiber types.

3.3.3 Distinct mTORC1-driven adaptations of type IIx myofibers in different muscles

Myofibers type IIx (MF2X), known to express *Myh1* isoform, are often viewed as an intermediate fast-twitch population positioned between oxidative MF2A and glycolytic MF2B with respect to contractile and metabolic features (1). Importantly, MF2X represents the only fiber type consistently present in both the predominantly oxidative SOL muscle and the glycolytic EDL muscle, positioning it as a shared node across otherwise distinct fiber-type compositions (33). Recent snRNA-seq studies in both mouse and human muscle have confirmed that MF2X nuclei form a distinct transcriptional cluster, separable from myofiber MF2A and MF2B, and that their representation and state can shift under different physiological and pathological contexts such as regeneration or denervation (17,28). These datasets highlight that MF2X are not a homogeneous class but instead display notable context-specific divergence.

To investigate how such a dynamic fiber type responds to mTORC1 hyperactivation, we isolated total of 1,447 MF2X myofibers from the dataset, representing all different tissue samples that integrated well with each other (Figure 3.3.B, Figure 3.7.A, and Figure 3.9.A). Although control MF2X fibers from SOL and EDL are mixed well in the UMAP manifold (Figure 3.7.A, left), mTORC1-hyperactivated MF2X fibers showed two distinct clusters, representing damage-associated MF2X-SOL and MF2X-EDL fibers (Figure 3.7.A, right). Notably, MF2X-SOL was predominantly associated with myofiber enlargement (Figure 3.7.B, top panel) while MF2X-EDL often exhibited basophilia (Figure 3.7.C, bottom panel).

Differential expression analysis between control and mTORC1-hyperactivated MF2X-SOL or MF2X-EDL revealed fiber type-specific transcriptional responses (Figure 3.9.B). Among 216 genes highly upregulated by hyperactive mTORC1, 26 genes were classified to be EDL-specific, while 72 genes were classified to be SOL-specific (Figure 3.7.D-E and Figure 3.9.C). Other genes were similarly upregulated in MF2X from both muscles. Gene score analysis demonstrated that mTORC1 hyperactivation was the predominant driver of these transcriptional changes (Figure 3.7.F, right), while such differences were minimal in control muscle (Figure 3.7.F, left). Histology and spatial profiling of the MF2X myofibers further validated the distinct transcriptional and morphological separation between mutant SOL and EDL muscles (Figure 3.8.A and Figure 3.9.D). While MF2X-EDL fibers remained small or normal in size, MF2X-SOL fibers frequently exhibited noticeable hypertrophy (Figure 3.8.A and Figure 3.9.E).

Using the SOL- and EDL-specific mTORC1-responsive genes (Figure 3.7.D-E and Figure 3.9.C), we performed gene set enrichment analysis (Figure 3.8.B and Figure 3.9.F). Three categories of pathways emerged: those enriched in global MF2X response (proteostasis & apoptosis, muscle contraction, myogenic development, and oxidative stress response), SOL-specific MF2X response (cytoskeletal complex assembly, and glucose homeostasis), and EDL-specific MF2X response (ribonucleotide/purine metabolism, and monosaccharide catabolism). Together, these findings demonstrate that, even within a shared fiber class, mTORC1 hyperactivation elicits divergent muscle-specific adaptations, underscoring the context-dependent plasticity of type IIx myofibers.

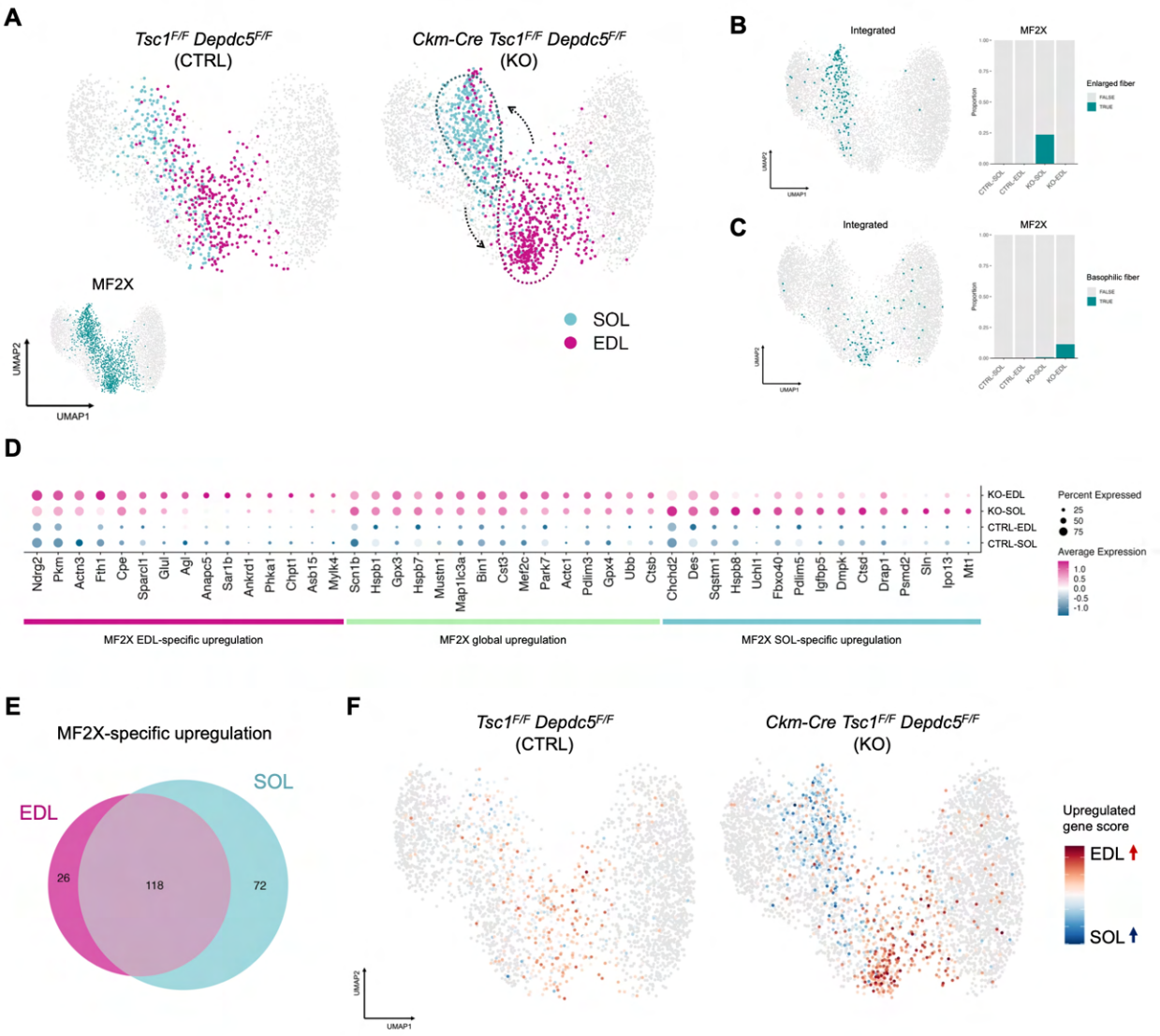


Figure 3.7 Distinct hyperactive mTORC1 responses of type IIx myofibers in different muscles

(A) UMAP visualization of myofiber datapoints separated as control (left) or mutant (right) groups, with muscle identity (EDL: red, or SOL: blue) annotated within the original MF2X depot (lower left). All other fiber types were greyed out. Dotted arrows and shapes indicate the bidirectional shift of the MF2X subclusters in response to mTORC1 hyperactivation. (B-C) Enlarged fibers (B) and developed basophilic fibers (C) were marked in the UMAP manifold (left). Their proportions were quantified from MF2X cluster of indicated muscles and presented in a bar graph (right). (D) Representative expression patterns of genes that are upregulated in response to mTORC1 hyperactivation in all MF2X fibers (MF2X global upregulation) or specifically in MF2X of EDL or MF2X of SOL, selected from a broader set (Figure 3.9.C). Exclusivity was determined using pairwise Wilcoxon tests (adjusted p-value < 0.05). (E) Venn diagram depicting the uniqueness and overlap of genes upregulated in MF2X of SOL and MF2X of EDL. (F) Cumulative module score of muscle-specific upregulated genes displayed in integrated UMAP manifold with control (left) and mutant (right) myofiber datapoints separated.

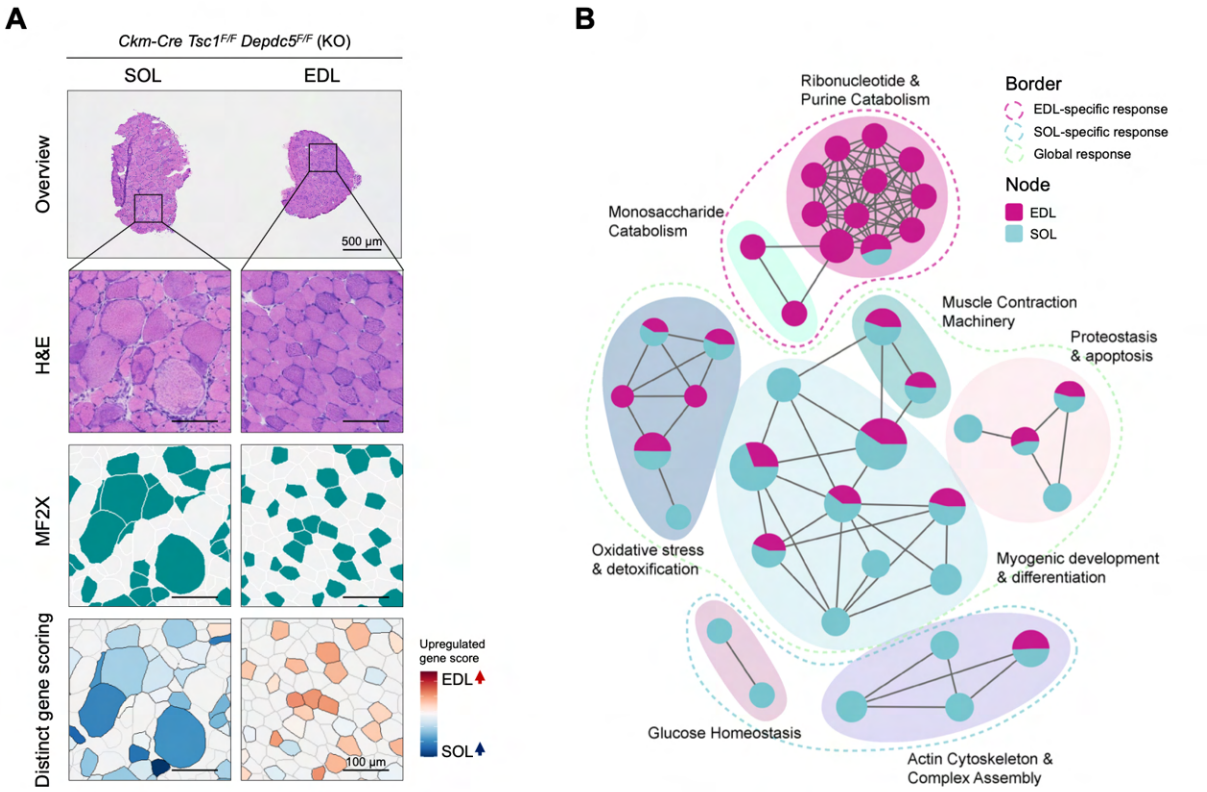


Figure 3.8 Systematic revelation of distinct responses from type IIx myofibers in different muscles

(A) Spatial images of representative mutant sections from each muscle. Boxed areas are magnified below (H&E). MF2X myofiber identity (MF2X) and cumulative module scores (Distinct gene scoring) representing the axis of SOL- and EDL-specific responses are also visualized at the myofiber level. (B) GO enrichment network representing group of genes that are upregulated in response to mTORC1 hyperactivation in all MF2X fibers (Global response) or specifically in MF2X of EDL (EDL-specific) or MF2X of SOL (SOL-specific). Pathways were grouped by functional similarity. Node size reflects the number of genes associated with each pathway, and node colors are shown as pie charts indicating the relative enrichment significance (adjusted p-values) contributed by each muscle-specific gene set. For the complete results with GO term names, see Figure 3.9.F.

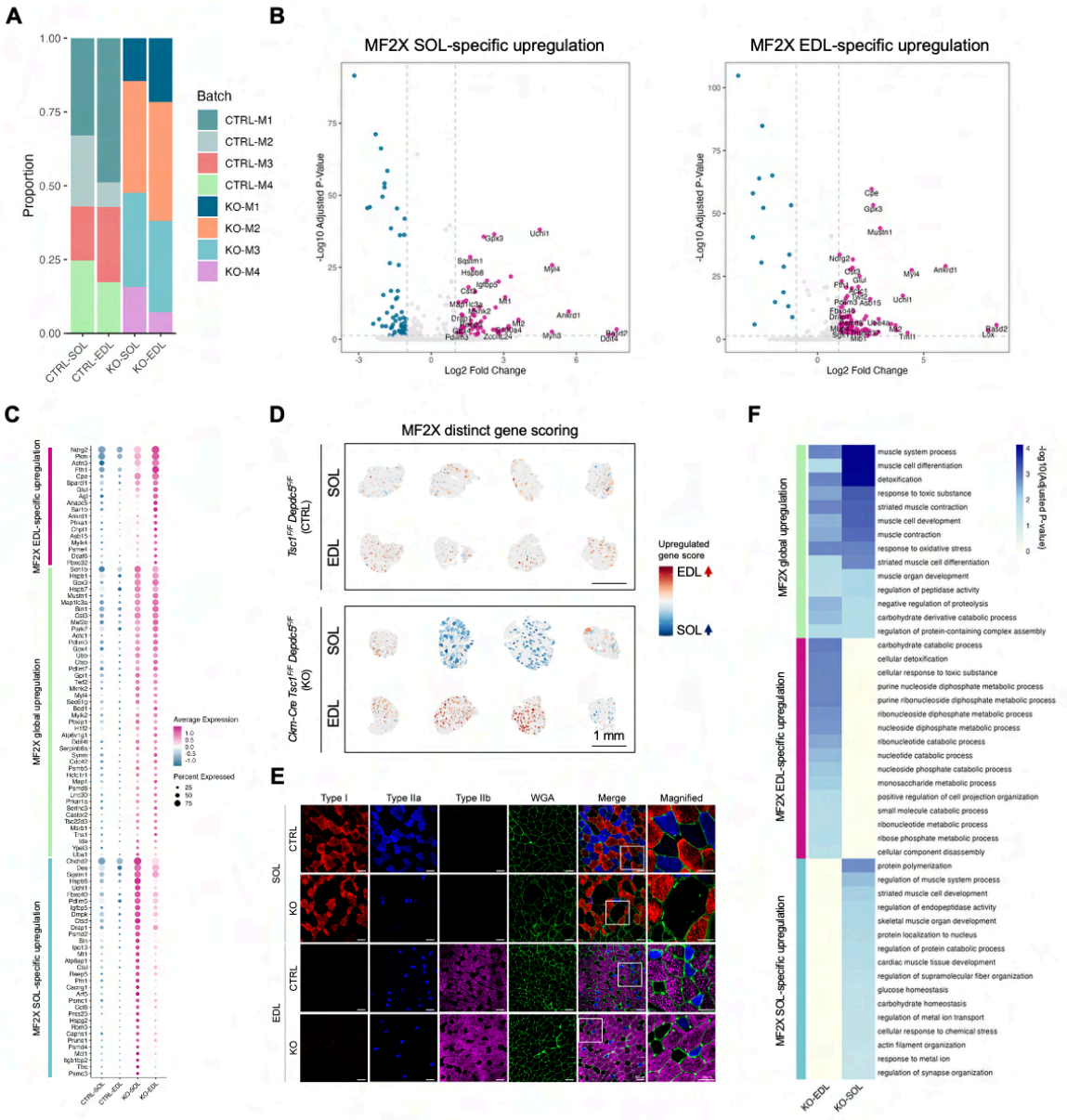


Figure 3.9 Validation of MF2X fiber responses under mTORC1 hyperactivation

(A) Contribution of different experimental batches to each indicated dataset of MF2X myofibers. (B) Differential expression analyses of MF2X fibers in SOL (left) or EDL (right) between control and mutant mice. Significantly upregulated or downregulated genes (adjusted p-values < 0.05, Log2FC > or < 1.5) are highlighted. (C) Expression of the complete list of genes that are upregulated in response to mTORC1 hyperactivation in all MF2X fibers (MF2X global upregulation) or specifically in MF2X of EDL or MF2X of SOL. Exclusivity was determined using pairwise Wilcoxon tests (adjusted p-value < 0.05). (D) Spatial images of muscle-specific MF2X cumulative module scores (MF2X distinct gene scoring) representing the axis of SOL- and EDL-specific responses. (E) Immunostaining of indicated fiber types in control or mutant EDL or SOL muscle. Type I (red), IIa (blue) and IIb (magenta) fibers are visualized through specific antibody staining while type IIx fibers appear unstained (black). WGA staining (green) outlines myofiber membranes and extracellular matrix. Boxed areas in Merge column are magnified at right. (F) Heatmap showing the result of gene set enrichment analysis of genes upregulated in response to mTORC1 hyperactivation in all MF2X fibers (MF2X global upregulation) or specifically in MF2X of EDL or MF2X of SOL. Color represents the enrichment significance (adjusted p-values). The result was used to construct the GO enrichment network shown in Figure 3.8.B.

3.3.4 Type IIx myofibers in Soleus undergo hypertrophy with structural remodeling

Abnormal myofiber enlargement is a pathological hallmark observed in diverse muscle disorders and experimental models (1). As mTORC1 hyperactivation induced myofiber enlargement specifically in SOL muscle (Figure 3.2.B), we investigate its molecular basis by re-analyzing 2,972 SOL myofibers, with a focus on the difference between control and mTORC1-hyperactivated muscle tissues (Figure 3.10.A). In mutant SOL muscles, enlarged fibers were mainly recognized as MF2X, with only a small contribution from MF2A (Figure 3.10.A-B). Fiber size distributions derived from cross-sectional segmentation confirmed that while most MF2X fibers in mutant muscle expanded several-fold compared with controls, MF1 and the majority of MF2A shrank instead (Figure 3.10.C and Figure 3.12.A). These observations are consistent with IHC validation (Figure 3.9.E) and previously reported immunostaining quantification (8). We further noted a universal increase in *Myh1* expression and decrease in *Myh7/2* expression (Figure 3.12.B). The proportion of MF2X fibers in general were elevated in mutant SOL muscle (Figure 3.12.C). Importantly, this shift was observed consistently across independent batches, suggesting a potential fiber-type shift during stress.

In addition to exhibiting prominent hypertrophy, MF2X fibers also displayed more pronounced changes at the molecular level. Among the genes differentially expressed between control and mutant SOL tissues, MF2X fibers showed the strongest overall expression changes compared with other fiber types (Figure 3.12.D). Since MF2X fibers showed both abnormal enlargement and transcriptome alterations, we further evaluated the molecular basis underlying the mTORC1-driven enlarged fibers, which occurs only in a subset of MF2X. To address this, we directly compared enlarged and non-enlarged fibers, enabling clearer identification of genes associated with mTORC1-driven hypertrophy (Figure 3.10.D). These genes were generally expressed at low levels in non-hypertrophic fibers and their expressions showed strong positive correlations with myofiber sizes (Figure 3.10.E), even after normalization to each myofiber's RNA content (Figure 3.12.E).

Genes strongly correlated with fiber enlargement included classical autophagy regulators such as *Sqstm1* (p62), *Map1lc3a* (LC3A) and *Ubb*, as well as proteasome or protease components such as *Psmb5* and *Ctsd*, suggesting an association between myofiber hypertrophy and mTORC1 hyperactivation-driven proteostasis disruption. Genes involved in muscle growth and regeneration (e.g., *Igfbp5*, *Mustn1* and *Ankrd1*) and structural genes indicating sarcomeric

and cytoskeletal remodeling (e.g., *Actc1*, *Myl4*, *Mylpf*, *Actn3*, *Tpm1* and *Mybpc3*) were also specifically upregulated in hypertrophic myofibers from mTORC1-hyperactivated muscles.

In addition, *Uchl1*, a ubiquitin C-terminal hydrolase, was strongly correlated with fiber enlargement. Notably, *Uchl1* has been shown to act as a brake on mTORC1 signaling in skeletal muscle, where its deletion results in sustained mTORC1 activation, impaired autophagy, and progressive muscle atrophy (34). Consistent with this, UCHL1 is also required for maintaining ubiquitin homeostasis and proper differentiation in myotubes, with knockdown leading to protein aggregation (35). Its elevated expression in enlarged fibers therefore suggests a compensatory role in managing proteostasis and restraining excessive mTORC1 activity under hyperactivation.

Importantly, the specific upregulation of *p62*, *Igfbp5*, *Actc1*, and *Uchl1* in hypertrophic myofibers was confirmed through IHC staining of their protein products (Figure 3.10.F). This coordinated program, combining impaired proteostasis, persistent growth signaling, and cytoskeletal remodeling, was reflected in our GO network analysis (Figure 3.11.A and Figure 3.12.F). Together, these results connect the molecular changes to the enlargement myopathy observed in SOL muscle (Figure 3.11.B).

3.3.5 Central nuclei are prevalent across various types of myofibers

The presence of centrally located nuclei in skeletal myofibers is a well-recognized histopathological feature, commonly associated with regeneration, myopathies, and various muscle stress conditions (36,37). Histological analysis revealed a higher proportion of centrally nucleated myofibers in mutant SOL compared with mutant EDL muscles (Figure 3.1.F and Figure 3.13.A, left panel). Although no strong fiber-type specificity was detected, oxidative fibers, such as MF1 and MF2A, had a subtle tendency to show more frequent central nuclei compared to the glycolytic fibers (Figure 3.3.G, Figure 3.13.A, and Figure 3.13.B, right panel). To assess whether central nuclei regions display distinct transcriptional features, we segmented 430 central nuclei from 2 mutant EDL and 2 mutant SOL muscles using combined H&E, DAPI, and WGA staining. Nuclei were dilated by 2, 4, or 6 μm to capture sufficient transcripts, and their transcriptomes were compared with 24-μm hexagon profiles from the 4 selected sections to generate a spatial single-nuclei–like dataset (Figure 3.14.C-D). The analysis did not reveal strong enrichment for a specific gene or pathway, likely reflecting that the central nuclei feature could happen for a variety of different myofibers without representing a specific pathway. However,

we were able to identify several zinc finger proteins, such as *Zfp93* and *Zfp429*, which were significantly enriched in central nucleic regions and may be involved in positioning the nucleus during the injury (Figure 3.14.E).

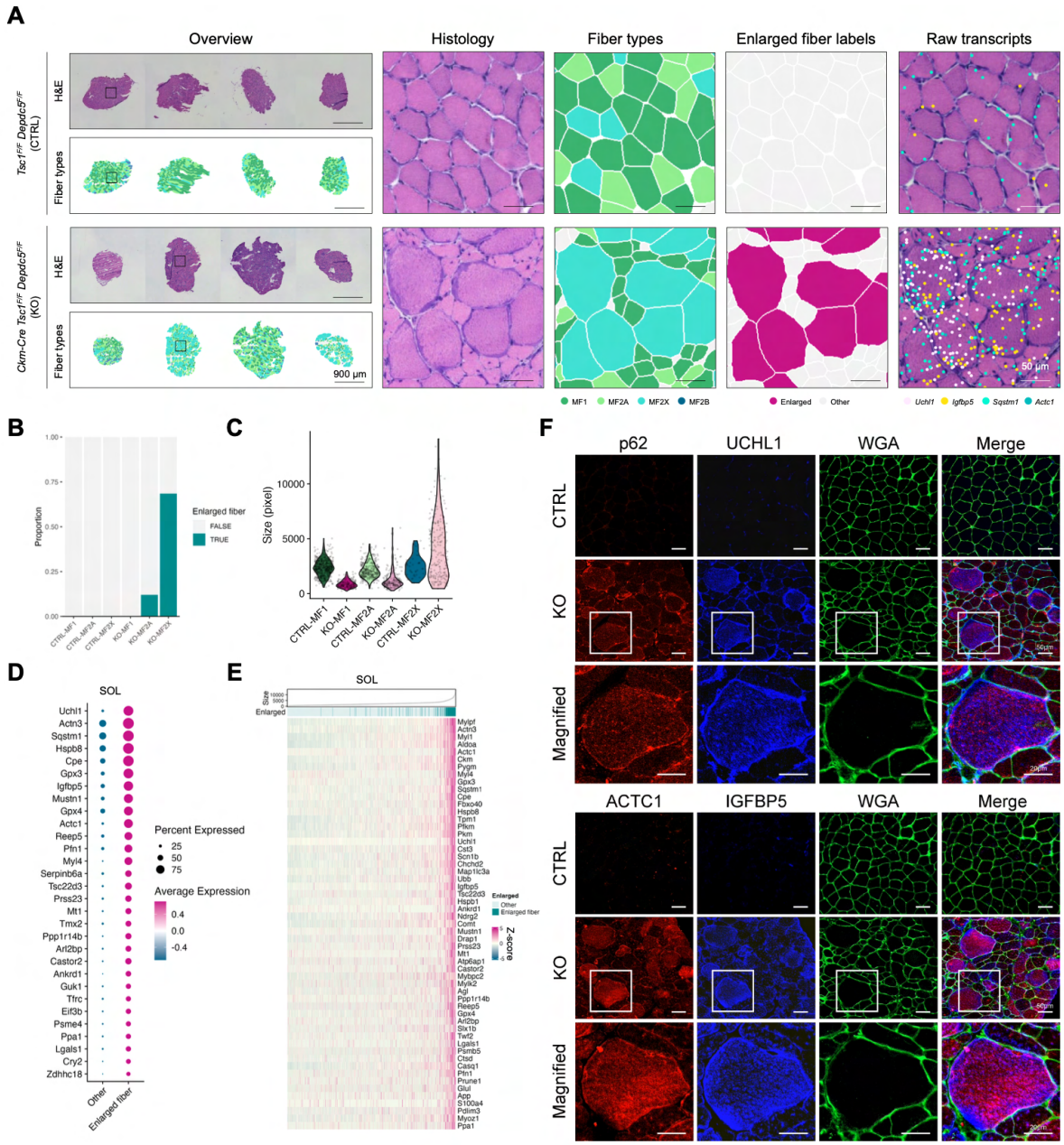


Figure 3.10 Type IIx myofibers in Soleus undergo hypertrophy with structural remodeling

(A) Spatial images of SOL sections. Left: histology overview of 4 control sections (top) and 4 mutant sections (bottom) overlaid with fiber type images. Right: Spatial images of magnified boxed area from corresponding overview, presenting from left to right as histology, fiber types, enlarged fiber labels, and raw transcripts plotted as colored dots. (B) Prevalence of enlarged fibers in different myofiber clusters of SOL was quantified and presented as a bar graph. (C) Size of fibers in different myofiber clusters of SOL was calculated and presented as a violin plot. One pixel corresponds to ~0.57 μm^2. (D) Expression of genes highly upregulated in enlarged fibers were presented in a dot plot. (E) Correlation between fiber size and gene expression. Myofibers (x-axis) are ordered from small to large. Positively correlated genes (y-axis) are ranked by correlation strength. The expression level of the genes is colored based on z-scores. RNA counts within single fiber were normalized by fiber size to estimate RNA density. (F) Immunostaining of indicated proteins in control or mutant SOL muscle. WGA staining (green) outlines myofiber borders. Staining was performed on two serial sections (top and bottom). Boxed areas highlighting an enlarged fiber are magnified at the bottom.

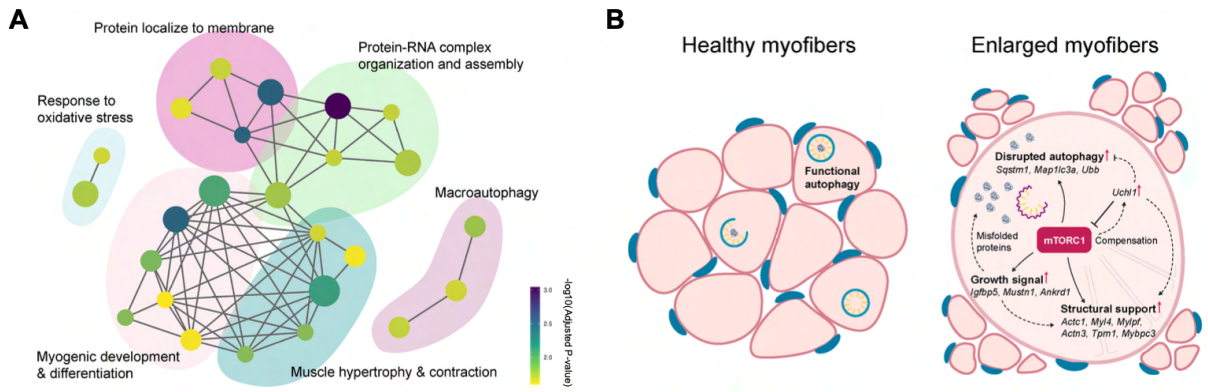


Figure 3.11 Schematic of soleus Type IIx hypertrophy with structural remodeling

(A) GO enrichment network based on genes upregulated in enlarged fibers. Pathways were grouped by functional similarity. Node size corresponds to the number of genes associated with each pathway, and node color reflects enrichment significance (adjusted p-value). For the complete results with GO term names, see Figure 3.12.F. (B) Schematic diagram illustrating transcriptome regulation underlying pathological hypertrophy in mTORC1-activated type IIx myofibers in SOL.

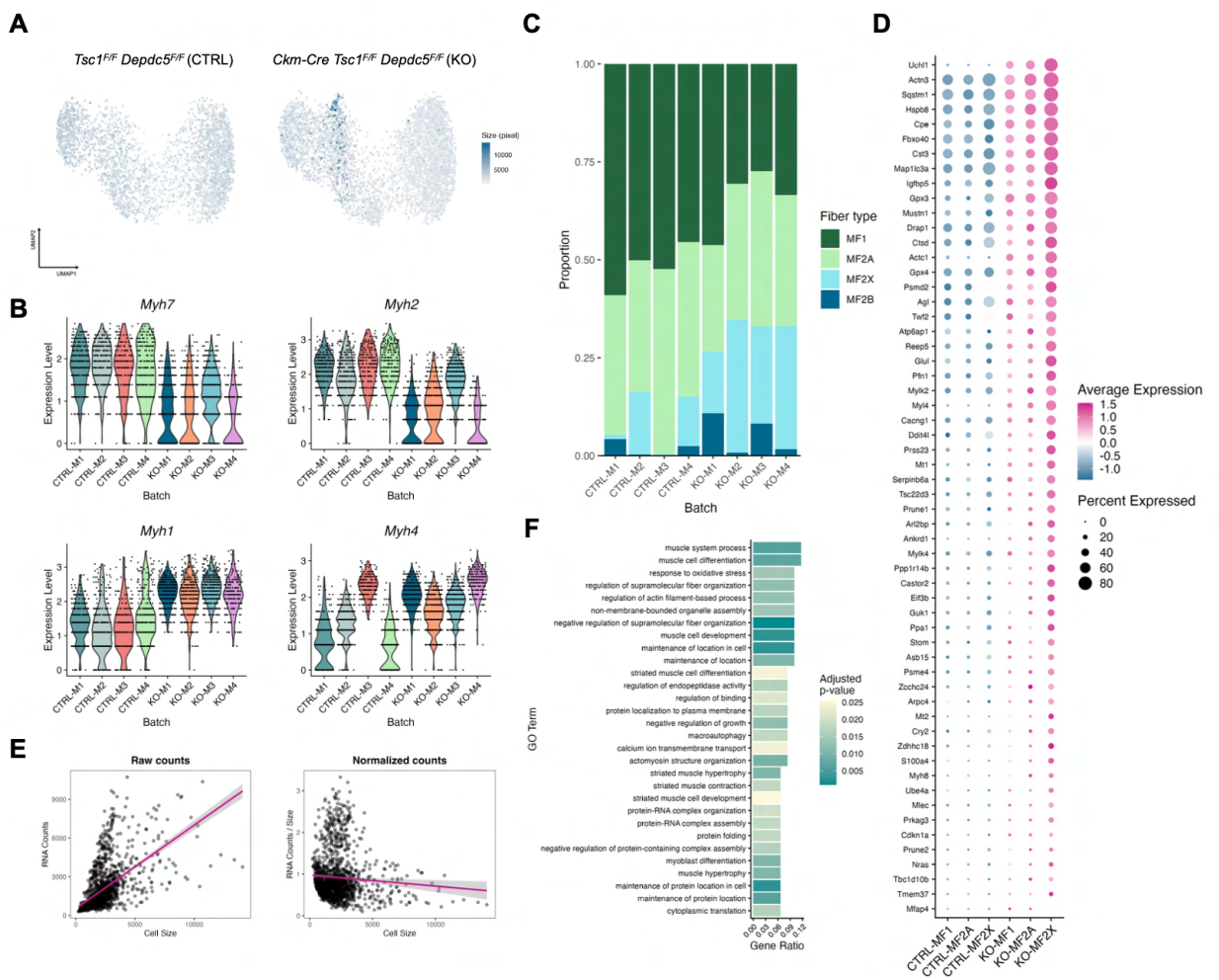


Figure 3.12 Transcriptomic characteristics of pathological features in myofiber enlargement

(A) Myofiber size visualized in integrated UMAP space, shown separately for control (left) and mutant (right) groups. (B) Expression of myofiber-specific myosin heavy chain isoforms across control and mutant SOL muscle batches. (C) Proportion of myofiber types in control and mutant SOL muscle batches. (D) Expression of mTORC1 hyperactivation-driven upregulated genes in SOL myofiber types. Most of these genes show highest expression in MF2X fibers in mutant mice. (E) RNA count-fiber size correlation. Right: correlation between transcript counts per myofiber (RNA Counts) and fiber size. Left: correlation between size-normalized transcript density (RNA Counts / myofiber) and fiber size (Cell size). (F) GO enrichment analysis of genes upregulated in enlarged fibers, corresponding to the GO network shown in Figure 3.11.A.

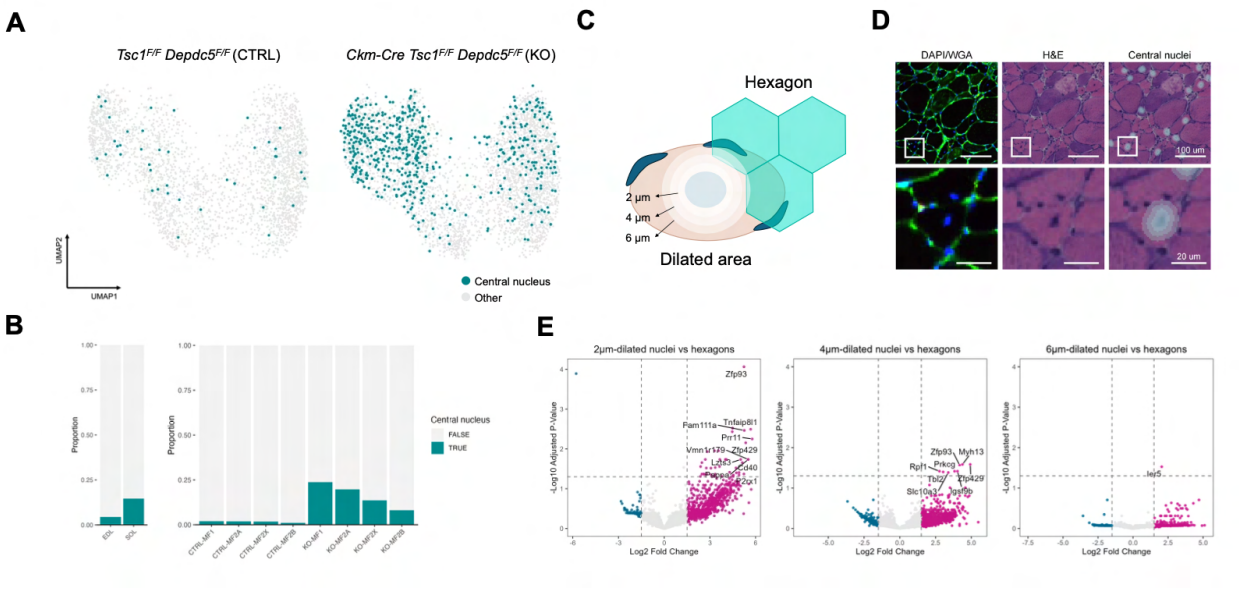


Figure 3.13 Transcriptomic characteristics of pathological features in central nuclei

(A) Centrally nucleated myofibers are marked in integrated UMAP space, separated by control (left) and mutant (right) groups. (B) Proportion of centrally nucleated myofibers in indicated subsets. (C) Histology-based spatial single-nuclei–like analysis. Central nuclei were identified from the histology images, and central nuclear transcriptome was extracted from spatial transcriptome with different radial ranges, reflecting lateral diffusion of transcripts. Analysis compared whole-tissue transcriptomes (segmented by 24 μm hexagon gridding) with central-nuclei transcriptomes. (D) Identification of centrally nucleated fibers by combining DAPI/WGA and H&E staining. Central nuclei with different radial ranges are visualized in a gradient on top of H&E images. Boxed areas are magnified below. (E) Comparison of central-nuclei transcriptomes with whole-tissue transcriptomes. Differentially expressed genes between tissue transcriptome and central nuclei transcriptomes of different radial ranges were shown in volcano plots. Upregulated (red) and downregulated genes (green) ($Log_2FC > 1.5$ on either side) are highlighted; significantly upregulated genes (adjust p-value < 0.05) are labeled.

3.3.6 Basophilic fibers activate lipid and oxidative metabolism to sustain elevated RNA synthesis

Basophilic fibers represent a distinctive histological phenotype, defined by enhanced hematoxylin accumulation in the cytoplasm, reflecting elevated nucleotide content and often emerging under stress conditions (38). Here, based on H&E histology, we identified and isolated 48 developed basophilic fibers and 387 transitional basophilic fibers where the majority were restricted to MF2X fibers in mutant EDL muscle (Figure 3.14.A-C and Figure 3.16.A, left panel). To validate the notion that more hematoxylin staining reflects elevated nucleotide content, we quantified RNA abundance in single fibers by counting unique transcripts from the spatial transcriptome dataset. Raw counts showed only modest increases in some developed basophilic fibers (Figure 3.16.B) likely due to the presence of hypertrophic fibers, which occupied more fiber volumes in histology, in non-basophilic fiber group. After normalizing RNA counts by fiber area to measure RNA concentration, we then observed a robust elevation of RNA content across both transitional and developed basophilic fibers (Figure 3.14.D-E).

We next examined which genes were specifically expressed in basophilic fibers using differential expression analysis. Mitochondrial genome–encoded genes (Figure 3.14.F; those beginning with ‘mt-’) were strongly upregulated, along with numerous additional transcripts. To systematically understand the molecular characteristics of basophilic fibers, we performed GO pathway enrichment analysis (Figure 3.15.A). The result revealed a strong enrichment of genes mediating lipid metabolism, mitochondrial transport, tricarboxylic acid (TCA) cycle, electron transportation, and nucleotide synthesis (Figure 3.15.A). These findings suggested a pronounced upregulation of a coordinated programs in basophilic fibers.

With further investigation, we identified multiple fatty acid and lipid metabolism-related genes, including *Fabp3* (fatty acid transport), *Acadl* (long-chain β-oxidation), *Oxct1* (ketone body catabolism), *Mfn2* (mitochondrial fusion and lipid exchange), *Chpt1* (phosphatidylcholine biosynthesis), and *Gpx4* (lipid peroxide detoxification), prominently upregulated in basophilic fibers (Figure 3.14.F), reflecting a broad program enhancing lipid handling and mitochondrial lipid utilization. *Ckmt2* (mitochondrial creatine kinase) additionally linked lipid-derived energy flux to ATP buffering, bridging fatty acid oxidation with downstream energy production. Elevated expression of *Mb* (myoglobin), multiple *Cox* subunits (cytochrome c oxidase), *Atp*

genes (ATP synthase), and several mitochondrially encoded respiratory chain components, as mentioned above, highlighted elevated mitochondrial respiration.

Enrichment of ribonucleotide metabolic pathways was also observed (Figure 3.14.F, Figure 3.15.A, and Figure 3.16.C). Several TCA-associated enzymes contributed both energy and building blocks for nucleotide production: *Idh2* (isocitrate dehydrogenase, generating NADPH for biosynthesis), *Ogdh* (α-ketoglutarate dehydrogenase, producing NADH while channeling carbon through the cycle), *Mdh1/Mdh2* (malate dehydrogenases, regenerating oxaloacetate that serves as a source of aspartate for nucleotide rings), and *Ldhb* (lactate dehydrogenase B, maintaining NAD^+/NADH balance and controlling substrate flow into mitochondria). In parallel, *Mpc2* (mitochondrial pyruvate carrier) supported entry of glycolytic carbon into the cycle, while *Nmrk2* (nicotinamide riboside kinase 2) contributed to NAD^+ salvage, sustaining redox reactions required for biosynthesis. Together, these signatures point to a coordinated program in which fatty-acid oxidation and respiration not only supply ATP but also drive TCA cycle flux that yields reducing power and carbon intermediates, thereby fueling purine nucleotide synthesis and ultimately resulting in the elevated RNA content of basophilic fibers (Figure 3.15.B).

To illustrate this framework within a histological context, *Fabp3*, *Mb*, and *Mdh1* were highlighted as representative markers of lipid handling, oxidative respiration, and ribonucleotide metabolism, respectively (Figure 3.15.C, raw transcripts view). In parallel, A selection of genes corresponding to these three pathways were combined into cumulative scores, and their relative expression levels were assessed and visualized (Figure 3.15.C, Figure 3.16.A, right panel, and Figure 3.16.D). This analysis confirmed the specific activation of all three pathways in basophilic fibers, which correspond to MF2X in EDL muscle. Taken together, our results indicate that mTORC1 hyperactivation reprograms MF2X fibers in EDL muscle toward lipid-supported respiration and nucleotide synthesis, giving rise to the basophilic phenotype.

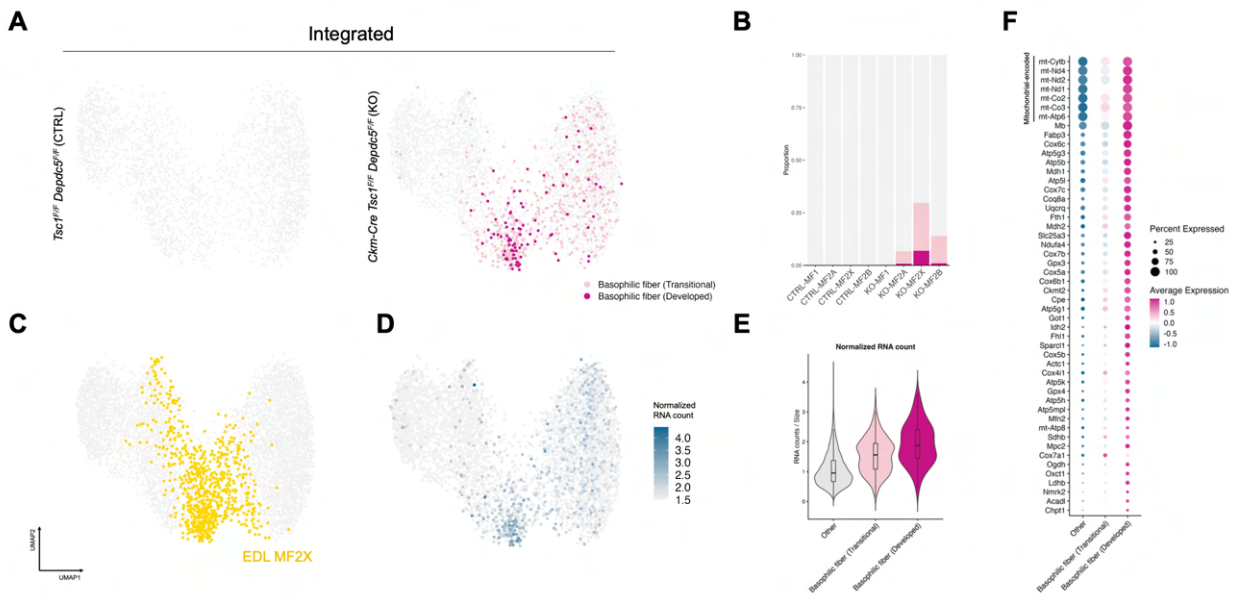


Figure 3.14 EDL myofiber type IIx develops basophilia with high RNA content

(A) Integrated UMAP manifold, colored with transitional (pink) and developed (red) basophilic fibers, shown separately for control (left) and mutant (right) groups. (B) The prevalence of basophilia was quantified for each fiber type cluster. (C) UMAP manifold displaying MF2X myofibers originated from EDL muscles (yellow). (D) UMAP manifold displaying RNA density (size-normalized RNA count) of each myofiber. (E) Violin plot visualizing the distribution of size-normalized RNA counts for transitional (pink) and developed (red) basophilic fibers as well as other fibers (grey). (F) Dot plot visualizing the expression of genes upregulated in basophilic fibers.

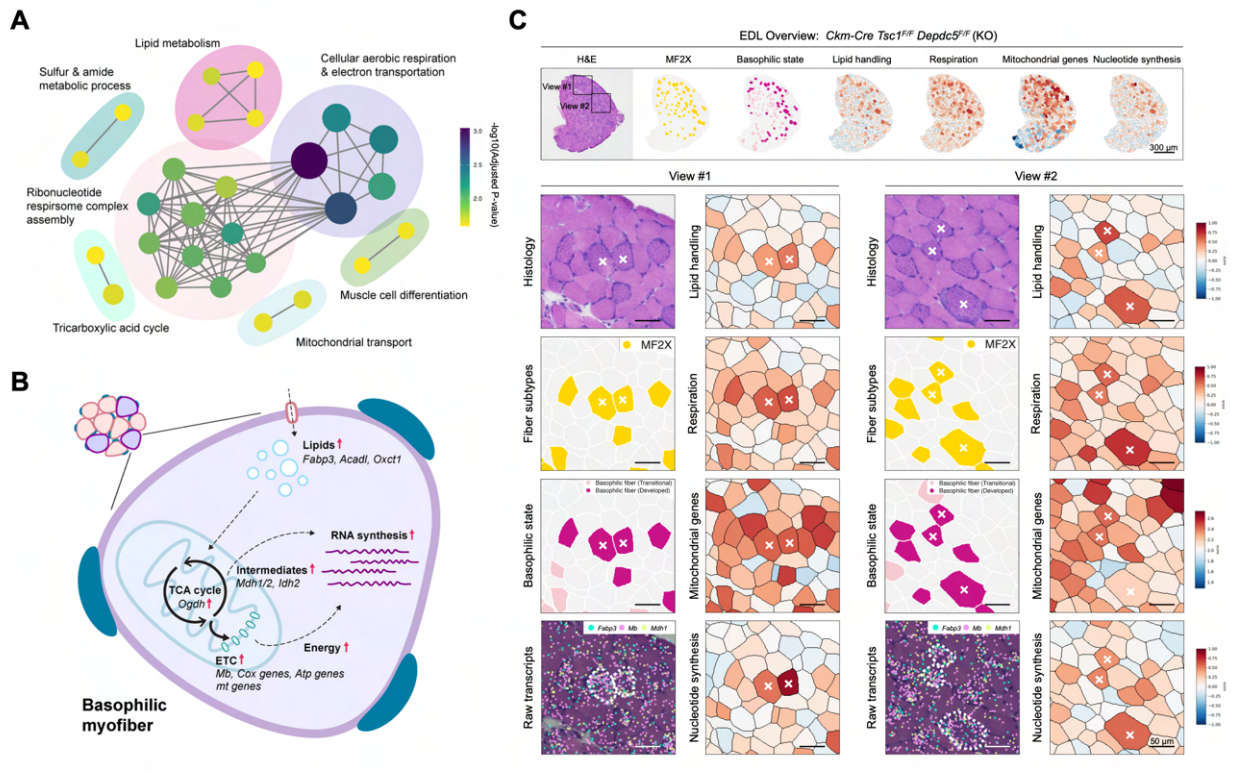


Figure 3.15 Basophilic fibers activate lipid and oxidative metabolism to sustain elevated RNA synthesis

(A) GO enrichment network analysis based on genes specifically upregulated in basophilic fibers. Pathways were grouped by functional similarity. Node size corresponds to the number of genes associated with each pathway, and node color reflects enrichment significance (adjusted p-value). For the complete results with GO term names, see Figure 3.16.C. (B) Schematic diagram illustrating transcriptome regulation underlying mTORC1-induced basophilia in type IIx fibers in EDL. (C) Spatial images of a representative section from mutant EDL. Top: overview images presenting from left to right as H&E histology, MF2X identity, basophilic states, and cumulative score maps for following genes. Lipid handling score: *Fabp3*, *Acadl*, *Oxct1*, *Mfn2*, *Chpt1*, *Gpx4*, and *Ckmt2*. Respiration score: *Mb*, *Cox* genes, and *Atp* genes (see Figure 3.14.F). Mitochondrial gene score: mitochondrial genome-encoded genes (see Figure 3.14.F). Nucleotide synthesis score: *Idh2*, *Ogdh*, *Mdh1/Mdh2*, *Ldhb*, *Mpc2*, and *Nmrk2*. Bottom: representative basophilic fibers magnified in two views, corresponding to the boxes above in the H&E image. Raw transcripts are shown in colored dots as indicated in insets. Crosses and dotted borders highlight representative MF2X fibers. For the images from other mutant EDL sections, see Figure 3.16.A.

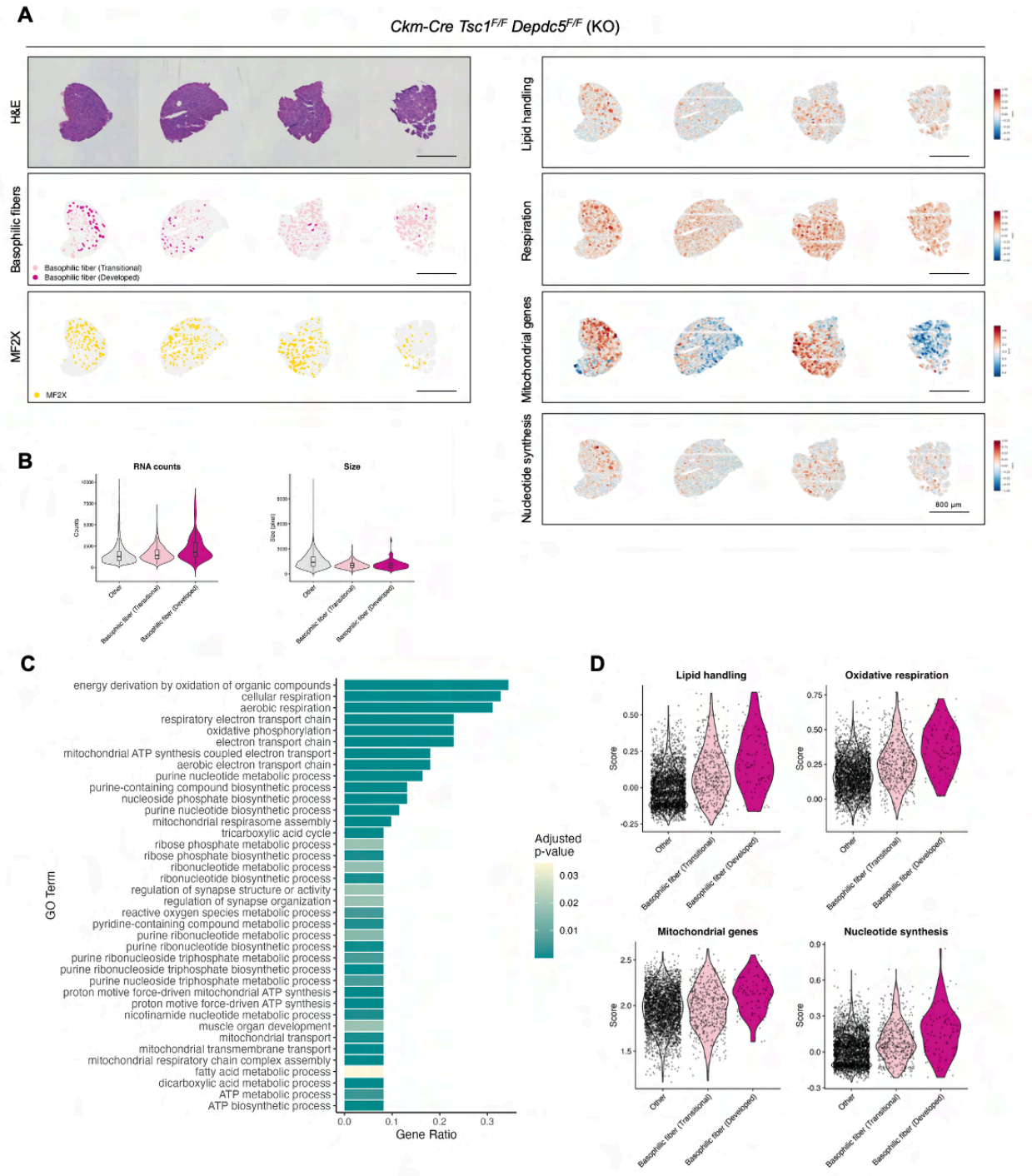


Figure 3.16 Supporting data for oxidative metabolism and RNA synthesis in basophilic fibers

(A) Spatial images of mutant EDL sections (full set). Left panel from top to bottom: H&E histology, basophilia map, and MF2X cluster map. Right panel from top to bottom: maps of lipid-handling module score, respiration module score, mitochondrial gene module score, and nucleotide synthesis module score, calculated as in Figure 3.15.C. (B) Distribution of RNA counts and fiber sizes across basophilic fiber states. (C) Enriched GO terms corresponding to nodes in the basophilic fiber functional network (Figure 3.15.A). (D) Distribution of cumulative module scores across basophilic fiber states.

3.3.7 Stress-induced reprogramming of type IIb fibers in EDL reveals transcriptional adaptability

Type IIb fibers (MF2B), typically defined as the most glycolytic and fast-contracting population, have recently been shown to exhibit transcriptional variation under different contexts (19, 32). With deeper investigation of raw transcriptome data, we identified an internal heterogeneity among MF2B fibers that was masked by an aggressive batch correction applied during integration. To uncover this subtle yet critical diversity, we isolated and sub-clustered 4,182 myofibers from EDL, a muscle predominantly composed of MF2B fibers, without applying any batch correction (Figure 3.19.A-E). Control EDL samples displayed minimal batch variation, whereas mutant samples showed somewhat greater variability across biological replicates, likely reflecting individual-specific responses or differences in mTORC1 hyperactivation-induced injury stages. Nonetheless, two mutant batches (KO-M1 & KO-M3) integrated well even without any batch correction, which could represent a reproducible transcriptome heterogeneity of MF2B myofibers (Figure 3.19.C-D).

From this dataset, we identified a clear mTORC1 hyperactivation–driven subdivision of MF2B into three transcriptionally distinct groups among the two EDL replicates (Figure 3.17.A-B). All three MF2B subgroups in mutant EDL exhibited elevated RNA content compared with controls, indicating active transcriptional responses (Figure 3.19.F). Gene profiling revealed divergent programs: MF2B subtype-1 (58% of mutant MF2B) expressed stress-response transcripts resembling the global mTORC1 hyperactivation signature; MF2B subtype-2 (22%) largely escaped the stress response and instead showed increased expression of genes controlling mitochondrial and oxidative metabolism; and MF2B subtype-3 (20%) was characterized by re-expression of developmental and remodeling genes, including *Actc1* and *Myl4* (Figure 3.17.C).

Among these subtypes, we focused on MF2B subtype-2, which suppressed stress response and rather upregulated oxidative metabolism. To quantitatively evaluate the mitochondrial content and activity, we generated a composite mitochondrial score based on all detectable mitochondrially encoded mt genes. The result confirmed that MF2B subtype-2 exhibited a relatively high mitochondrial level that is comparable to basophilic MF2X fibers, the oxidative population in EDL muscles (Figure 3.17.C-D and Figure 3.20.B). However, interestingly, unlike basophilic MF2X fibers, MF2B subtype-2 fibers largely maintained normal morphology (Figure 3.17.E-F). These findings suggest that a fraction of MF2B adopts oxidative

metabolism without altering its myosin isoforms or developing pathological morphology in response to mTORC1 hyperactivation.

MF2B subtype-3, highlighted by developmental and de-differentiation signatures, did not display any obvious morphological phenotypes (Figure 3.17.E, G). Transcriptional spatial mapping and quantitative analyses validated the elevated expression of *Actc1* and *Myl4* in this subgroup (Figure 3.17.G, right column and Figure 3.20.C). Co-immunostaining of ACTC1 and MYL4 revealed both overlapping and non-overlapping fibers (Figure 3.18.A), pointing to a more complex downstream regulatory mechanism.

Despite these wide variations in transcriptome differences between MF2B subtypes, they maintained their MF2B identity by robustly expressing its characteristic *Myh4* isoform (Figure 3.19.B); *Myh4* expression level was very high across all MF2B subtypes without any notable differences between the subtypes.

Together, these findings demonstrate that type IIb fibers diverge into distinct transcriptional trajectories under mTORC1 hyperactivation (Figure 3.18.B) while maintaining their fiber-type identity, highlighting previously unrecognized heterogeneity and transcriptional adaptability within a fiber type that was traditionally considered uniform.

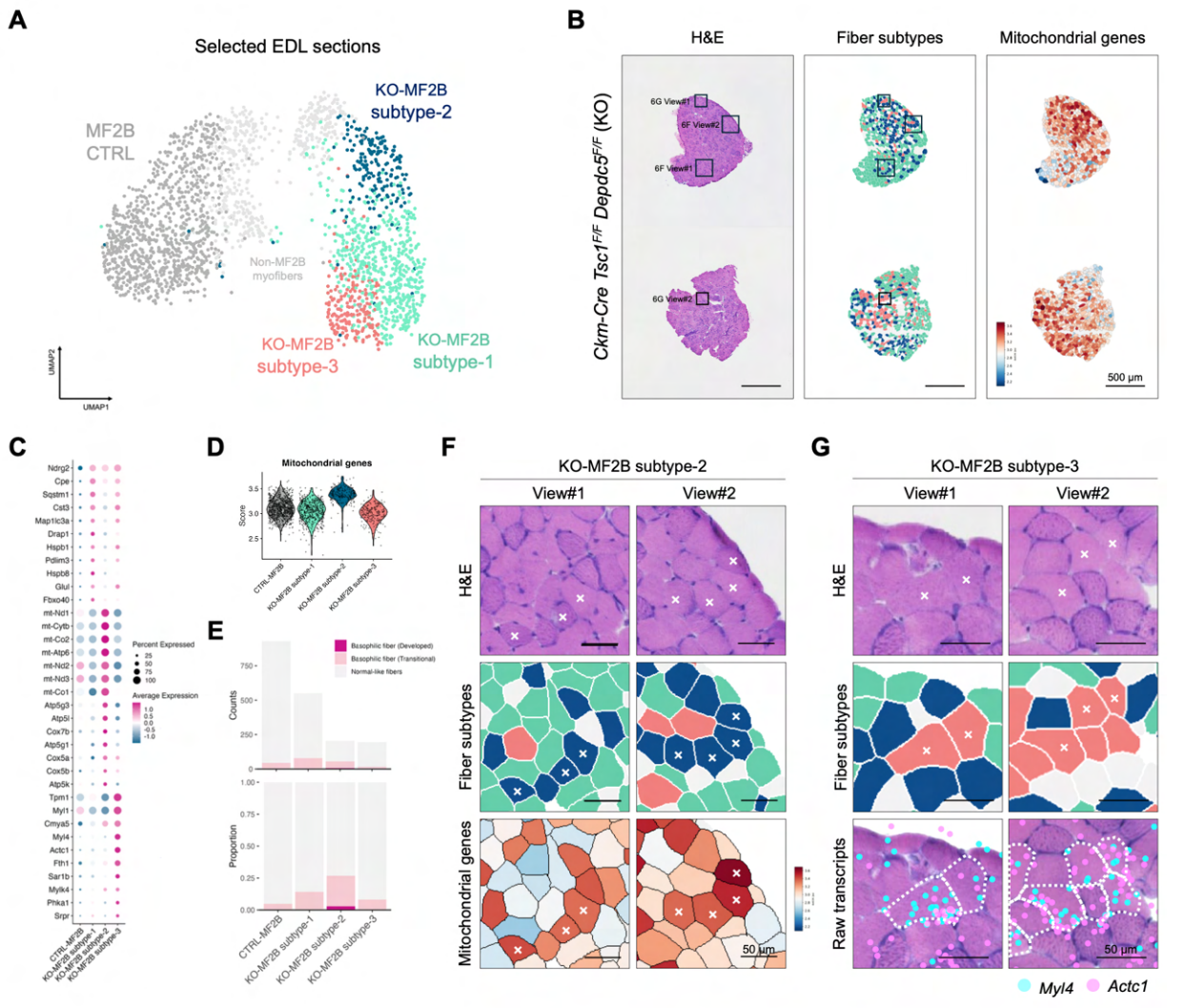


Figure 3.17 Type IIb fibers in EDL exhibit three distinct stress adaptation states without gross morphological alterations

Myofibers from EDL muscles were subset and analyzed to reveal MF2B heterogeneity. (A) UMAP manifold showed MF2B clusters in selected control and mutant EDL sections (n = 2). Control MF2B cluster and non-MF2B clusters are labeled in dark gray and light gray, respectively. For full analysis, see Figure 3.19. (B) Spatial images of selected mutant EDL sections. Left: H&E histology. Middle: MF2B fiber subtype map, according to the clustering presented in (A). Right: Spatial map of a cumulative score created with the expression level of mitochondrial genome-encoded genes. Boxed areas in H&E images are magnified in (F-G). (C) Expression of genes upregulated in each KO-MF2B subtype (1-3). (D) mitochondrial gene cumulative score compared between control and mutant MF2B subtypes. (E) Frequency of basophilic fibers in control and mutant MF2B subtypes. (F) Representative views of MF2B subtype-2 with histology (H&E), fiber-subtype map, and mitochondrial gene cumulative score map. Crosses indicate representative subtype-2 myofibers. (G) Representative views of MF2B subtype-3 with histology (H&E), fiber-subtype map, and raw transcript plots of indicated genes. Crosses and dotted borders highlight representative subtype-3 myofibers.

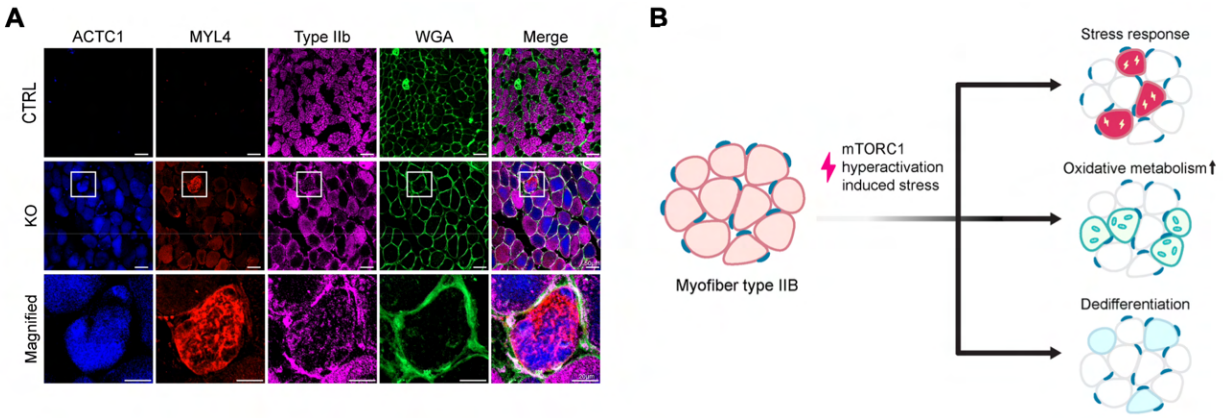


Figure 3.18 Overview of distinct stress adaptation states in EDL Type IIb fibers

(A) Immunostaining of indicated proteins in control and mutant EDL muscles. WGA staining (green) delineates myofiber membranes. Boxed areas are magnified at the bottom. (B) Schematic diagram illustrating differential adaptation responses of MF2B fibers to mTORC1 hyperactivation-induced stress.

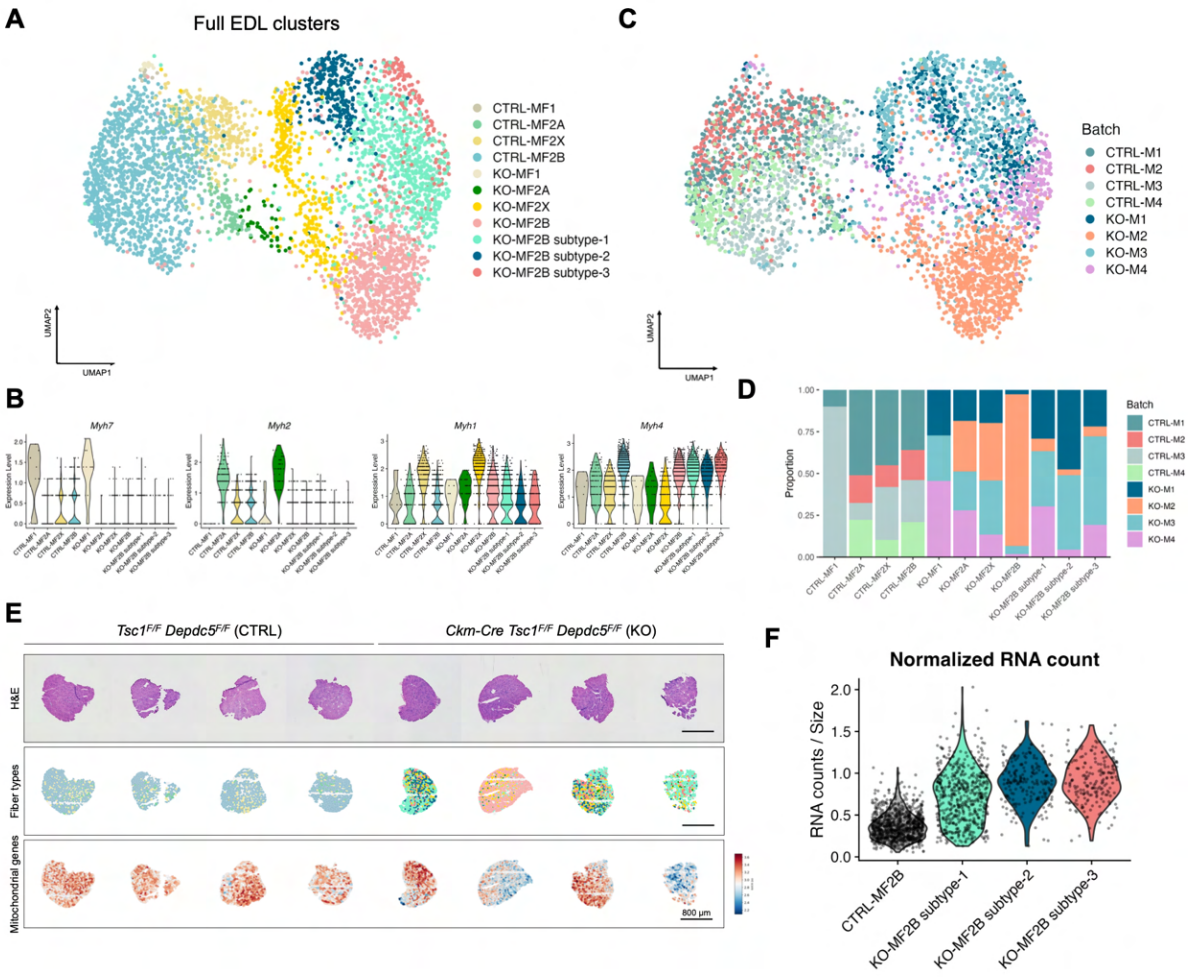


Figure 3.19 Diversification of MF2B responses to mTORC1 hyperactivation

(A) UMAP manifold displaying myofiber types from all EDL sections, constructed without batch correction. (B) Expression of myofiber-specific myosin heavy chain isoforms across designated myofiber types. All MF2B myofiber subtypes express *Myh4*, a key marker of MF2B. (C) UMAP manifold displaying experimental batches from all EDL sections, constructed without batch correction. (D) Proportion of individual batches in different myofiber types, presented in a bar graph. (E) Spatial images of 8 EDL sections (4 control and 4 mutant) used for the analyses in (A-D). H&E histology (top), fiber type map (middle), and mitochondrial gene cumulative score map (bottom) are shown. (F) Distribution of size-normalized RNA counts in different MF2B subclusters.

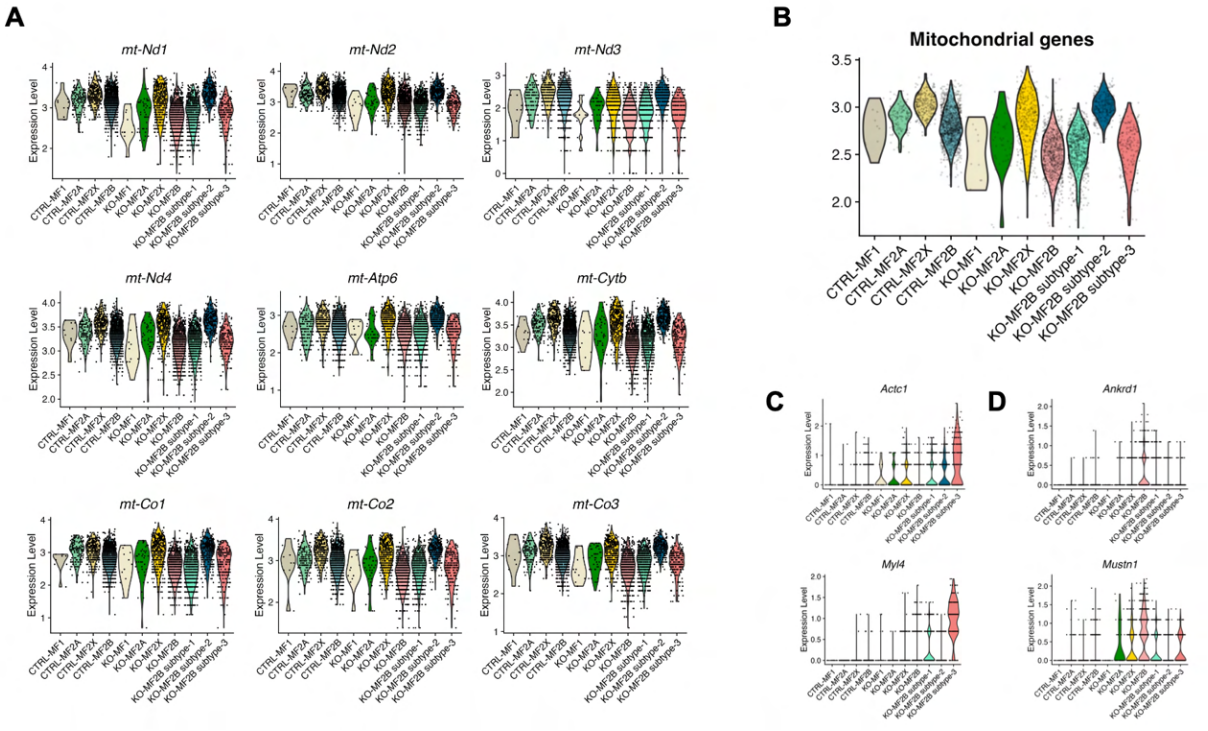


Figure 3.20 Expression of genes in MF2B subtypes in response to mTORC1 hyperactivation

(A) Expression of mitochondrial genome-encoded genes in different myofiber clusters of EDL. (B) Mitochondrial gene cumulative score in different myofiber clusters of EDL. (C-D) Expression of indicated genes in different myofiber clusters in EDL, representing the mutant MF2B subtype-3 (C) or the KO-M3 batch effect (D).

3.3.8 mTORC1 hyperactivation drives macrophage–fibroblast accumulation in soleus muscle

Aside from myofibers, or myocytes, many non-myocytic cell types, including fibroblasts, endothelial cells, and immune cells, reside within skeletal muscle, where they provide essential support for tissue maintenance and homeostasis. To investigate how these populations respond to mTORC1 hyperactivation, we profiled non-myocytes using 24-μm diameter (flat-to-flat width) hexagon spatial gridding. This revealed diverse cell types, including macrophages, fibroblasts, neuromuscular junctions (NMJs), and erythrocytes (RBCs) (Figure 3.21.A-B).

While resting non-myocytic cell types are equally presented in all batches (Figure 3.22.A-B), activated macrophages and fibroblasts were highly and specifically enriched in mutant SOL muscle (Figure 3.21.C and Figure 3.22.C). The macrophage cluster strongly expressed *Apoe*, marking them as tissue-resident macrophages (TRMs), whereas activated fibroblasts, separated from *Gsn*-expressing interstitial fibroblasts, expressed *Mgp*, *Thbs4*, *Col1a1*, and *Col3a1*, along with relatively low *Gsn* expression (Figure 3.21.B and Figure 3.22.D). These observations indicated the development of a fibrotic environment in the mTORC1-hyperactivated mutant SOL muscles, which are enriched with histopathological features such as myofiber hypertrophy and central nucleus. Importantly, activated TRMs were often found in close proximity to activated fibroblasts (Figure 3.21.D), a spatial relationship that aligns with the established role of macrophages in driving fibrotic programs through paracrine signals that stimulate fibroblast activation and matrix deposition (39–41).

Overall, these results demonstrate that mTORC1 hyperactivation in myofibers not only drives intrinsic fiber pathology but also elicits secondary responses in non-myocytes within a specific muscle. The recruitment and activation of these cells are speculated to be triggered by altered tissue architecture and hypertrophic myofiber secretory signaling, creating a complex and interdependent pathological microenvironment.

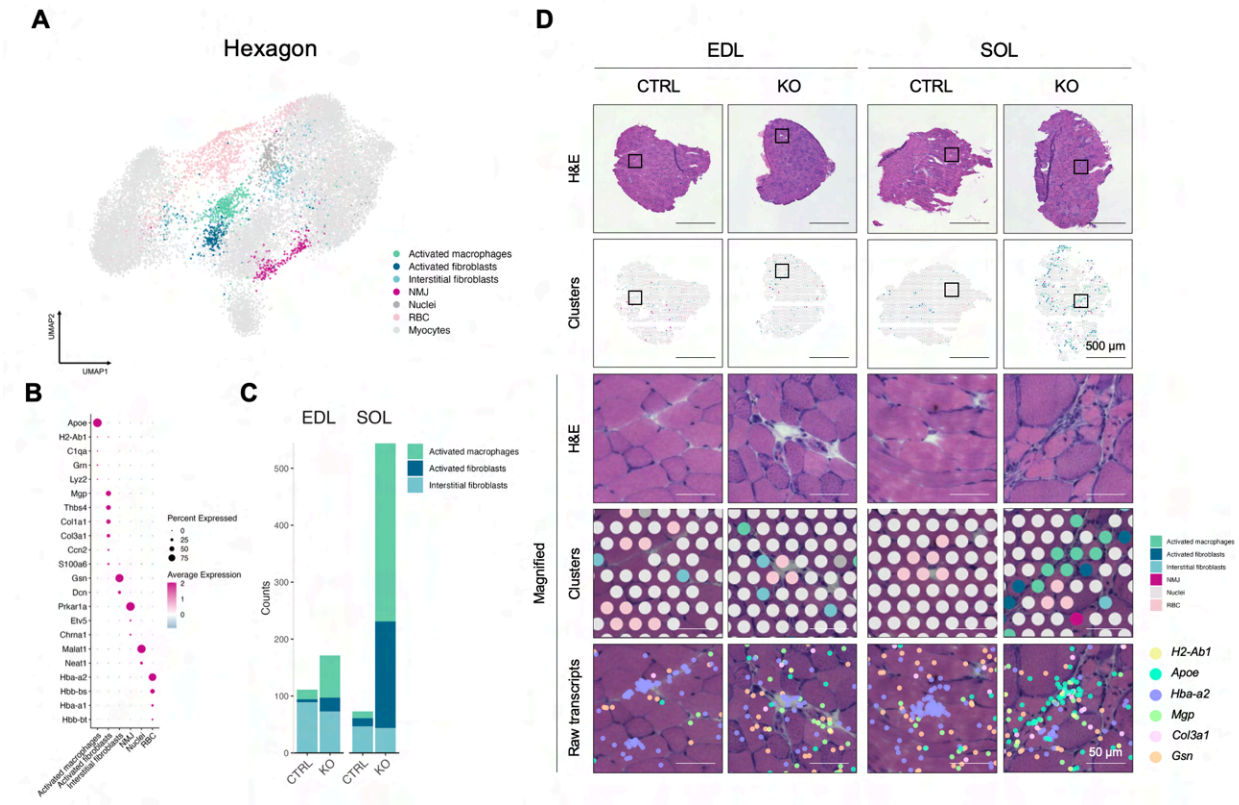


Figure 3.21 mTORC1 hyperactivation drives macrophage-fibroblast accumulation in SOL muscle

Non-myocytes were identified in skeletal muscle using 24 µm non-overlapping hexagon gridding. (A) UMAP manifold of the hexagonal grid dataset displaying non-myocyte clusters, conducted without batch correction. (B) Expression of non-myocyte markers in different cell types. (C) Quantification of macrophage and fibroblast cell type prevalence in control and mutant mice. (D) Spatial images showing H&E histology and cluster maps in representative muscle sections from each group. Boxed areas are magnified. Transcript expression is displayed as indicated color dots.

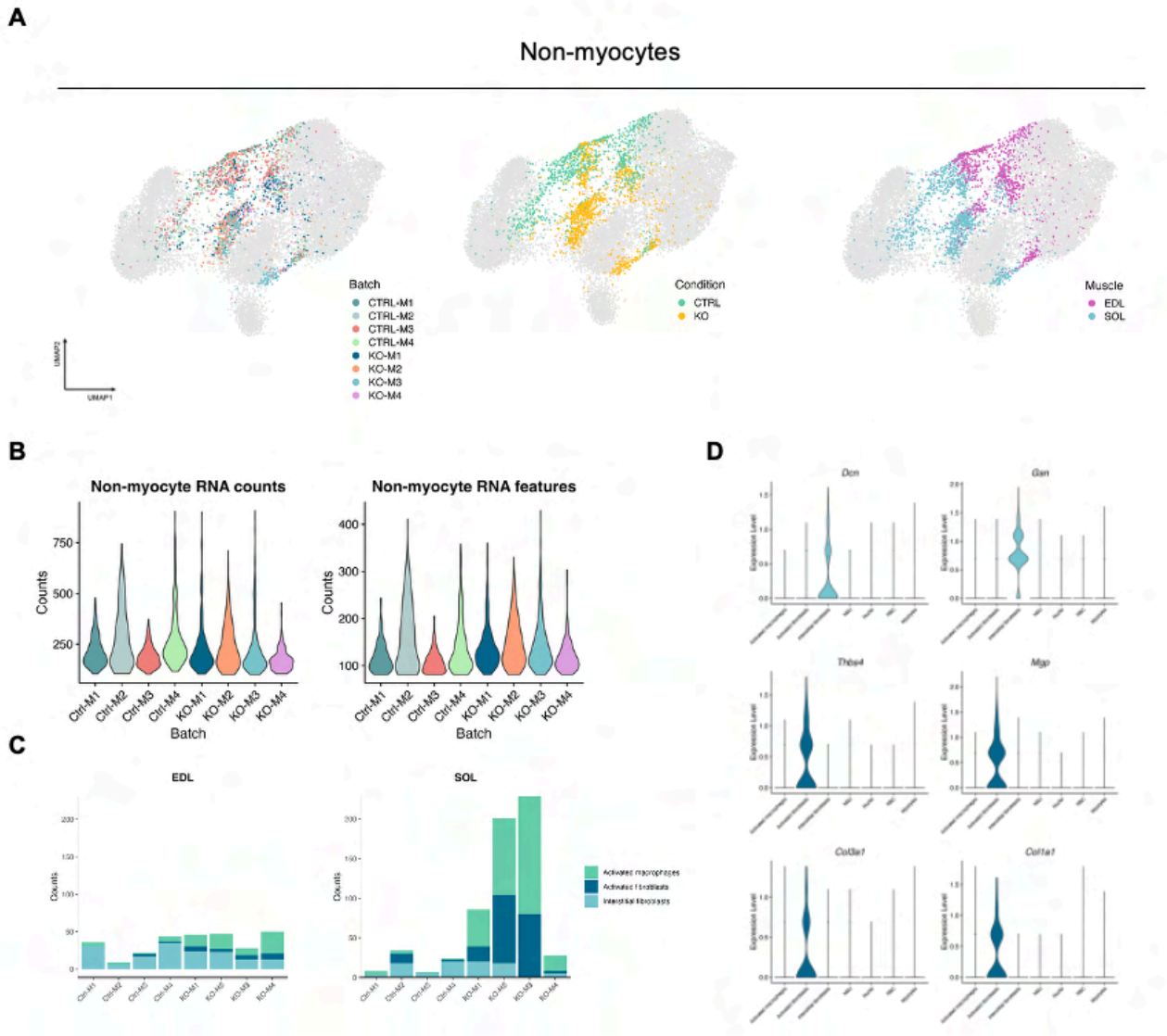


Figure 3.22 Hexagonal grid analyses of non-myocyte populations

(A) UMAP manifold, colored with batches (left), conditions (middle), or muscle (right), constructed without batch correction. Non-myocytes are highlighted in indicated colors, while myocytes are greyed out. (B) Distribution of unique transcript counts (left) and gene numbers (RNA features, right) per non-myocytes of indicated batches. (C) Quantification of macrophage and fibroblast cell type prevalence in indicated batches. (D) Expression of fibroblast activity-associated genes across non-myocyte clusters.

3.4 Discussion

Histopathological features such as basophilic fibers, fiber enlargement, and central nuclei have long served as hallmarks of skeletal muscle disease (38,42,43), yet the molecular programs underlying these morphologies remain poorly understood. Traditional approaches have struggled to connect phenotype with transcriptional state at the level of single fibers, while scRNA and snRNA sequencing lose their associated histological information (15–26). By combining high-resolution spatial transcriptomics with image-guided fiber segmentation, we establish a framework to directly link morphological phenotypes with their transcriptomes. This pathology-guided, single-fiber analysis reveals how sustained mTORC1 hyperactivation drives diverse and fiber-type–specific pathological responses across distinct muscle groups.

Even though the difference in susceptibility between EDL and SOL has long been recognized (44–46), our study is among the first to show that pathology-induced transcriptomic outcomes diverge sharply between these two muscles. In SOL, MF2X fibers predominantly underwent abnormal enlargement, whereas in EDL, MF2X fibers developed a basophilic phenotype. These contrasting trajectories indicate that MF2X fibers do not adopt a uniform pathological program but instead respond in a muscle-dependent manner. Given the distinct baseline fiber-type compositions and metabolic environments of SOL and EDL, it is plausible that local tissue context modulates how MF2X fibers respond to mTORC1 hyperactivation. In particular, the continuous activation and loading of SOL may contribute to its growth phenotype, whereas the relatively low usage of EDL might favor alternative pathological outcomes. It is also possible that MF2X fibers arising during development contain latent differences in identity, even if their baseline transcriptomes appear highly similar, which could contribute to muscle-specific outcomes under stress. Overall, these findings highlight the context-dependent plasticity of MF2X fibers and suggest that muscle-specific factors shape their adaptive responses to perturbation.

Through gene enrichment analysis, abnormally enlarged fibers were identified as engaging sustained growth signaling, disrupted autophagic homeostasis, and structural remodeling (Figure 3.11.A), which is in line with the results from a previous study using bulk tissues (8). These processes were also shown to drive physiological myofiber hypertrophy in the context of mechanical overload (47). However, under continuous mTORC1 activation, they may tip the balance away from normal growth toward pathological remodeling. Even though

hyperactive mTORC1 drives ongoing anabolic activity, including increased protein synthesis and ribosomal biogenesis, it simultaneously suppresses autophagy, thereby compromising proteostasis. This impaired capacity to clear damaged proteins and organelles likely exacerbates the imbalance between growth and quality control. Alongside these defects, cytoskeletal remodeling signatures, including reorganization of actin filaments and contractile apparatus components, suggest structural adaptation aimed at accommodating increased fiber size. Together, these processes form a foundation for hypertrophic expansion, but one that is unstable, as the combined disruption of proteostasis and autophagy predisposes the fibers to dysfunction and degeneration.

In EDL, MF2X fibers predominantly developed the basophilic phenotype, marked by lipid-supported respiration fueling nucleotide synthesis and culminating in elevated RNA content (Figure 3.15.B). Even though previous study has marked basophilia as a regenerative and metabolically oxidative phenotype (38), why these fibers adopt oxidative features in a glycolytic-dominant muscle under mTORC1 hyperactivation remains an open question. One possibility is that the oxidative shift arises as a means of redox management: by enhancing oxidative phosphorylation, fibers increase NADH and $FADH_2$ turnover, thereby alleviating oxidative stress. This process inevitably generates TCA intermediates that could, in principle, be directed into multiple metabolic fates. However, under mTORC1 hyperactivation, where anabolic programs strongly promote RNA and protein synthesis, these intermediates are likely funneled preferentially toward nucleotide production. Alternatively, the oxidative shift may serve a more directed purpose with fibers deliberately engaging lipid-supported respiration as the most efficient pathway to sustain nucleotide and protein synthesis. In either case, the phenomenon underscores the metabolic plasticity of MF2X fibers, which appear capable of recruiting oxidative programs to meet the demands of pathological growth within an otherwise glycolytic muscle environment.

Beyond basophilic and enlarged fibers, we also assessed additional pathological features commonly associated with myopathy. Fibers with central nuclei were more frequent in mutant muscle, consistent with regenerative remodeling (42), but our transcriptomic analysis did not yield a broad set of differentially expressed gene signatures for this nuclei population, likely reflecting technical difficulties or biological heterogeneity. However, we identified a small group of genes, including several zinc finger proteins, that were selectively enriched in central-nucleus

fibers, suggesting potential roles in mediating central-nuclei–associated muscle pathology. We also noted that different muscle tissues display variability in phenotype prevalence, which we attribute to differences in the stage of mTORC1 hyperactivation across muscles. While all the sections were included in the integrative analysis, a subset of tissues were more extensively focused on to reveal fine-level heterogeneity that was masked during aggressive batch correction procedures.

In addition to these pathological features, our analysis also uncovered unexpected adaptability within MF2B fibers (Figure 3.18.B). Traditionally viewed as the most glycolytic and least flexible fiber type (48,49), MF2B in EDL diverged into three distinct subgroups under mTORC1 hyperactivation. One subgroup displayed the canonical stress-response program, consistent with the global transcriptomic changes induced by mTORC1 activation. The second subgroup, however, showed elevated expression of mitochondrial and oxidative genes while retaining a morphologically normal appearance. We speculate that this reflects a compensatory shift, in which a fraction of MF2B fibers adopt oxidative features to support aerobic metabolism that would normally be contributed by MF2X fibers, which are diverted into the basophilic trajectory. The third subgroup re-expressed developmental and structural regulators such as *Actc1* and *Myl4*, pointing to a remodeling program that may reflect partial de-differentiation or activation of regenerative pathways. These divergent outcomes suggest that mTORC1 hyperactivation does not impose a uniform response in glycolytic fibers but instead interacts with local or intrinsic cues to channel MF2B into distinct transcriptional trajectories. With responses largely independent from overt morphological pathologies, we speculate that these heterogeneous programs may be shaped and affected by surrounding non-myocytes or neighboring fibers. Importantly, despite these wide variations in transcriptome response, they maintained their MF2B identity by expressing their characteristic myosin isoform *Myh4* at robust levels. These findings reveal that MF2B fibers, long considered metabolically rigid, can mount heterogeneous transcriptional responses when challenged, suggesting a previously underappreciated capacity for remodeling within this fiber type.

In conclusion, our study provides a comprehensive view of how sustained mTORC1 hyperactivation reshapes skeletal muscle at single-fiber resolution. By integrating pathology-guided segmentation with spatial transcriptomics, we uncovered fiber-type–specific adaptations, including divergent MF2X trajectories and unexpected heterogeneity within MF2B, as well as

non-myocytic responses that promote fibrotic remodeling. These findings extend our understanding of the molecular programs that underlie classic histopathological features of myopathy and emphasize the plasticity of fiber types under stress. A limitation of our study is that it was performed in murine models of mTORC1 hyperactivation, and further work will be needed to determine whether similar adaptive programs operate in other pathological contexts or human diseases. Nonetheless, this work highlights the value of spatially resolved transcriptomics for linking morphology to molecular state and establishes a framework for future investigations into the mechanisms that govern muscle pathology.

3.5 Methods

Sex as a biological variable

In this study, spatial transcriptomic analyses were performed in male mice. Our previous characterization of the same mouse model showed that mTORC1-driven myopathy and associated cardiac and respiratory defects occur in both male and female mice (6,14), indicating that the core pathological consequences of mTORC1 hyperactivation are not sex restricted. Many functional and molecular assays in that work were carried out in males, and the present study builds on that dataset by adding high-resolution, fiber type-specific and muscle-specific transcriptional information in the same sex. Consequently, the spatial and single-myofiber programs described here are defined in male skeletal muscle, and it remains unknown whether the detailed histopathological and transcriptional trajectories are identical in females. Future studies that include both sexes and are prospectively powered for sex-stratified analyses will be required to determine whether sex modifies susceptibility to mTORC1 hyperactivation, the responses of individual fiber types, or associated non-myocytic remodeling.

Rodent muscular mTORC1 hyperactivation model

As previously described (6,14), *Tsc1*$^{F/F}$ and *Ckm-Cre* mice (C57BL/6J background) were obtained from Jackson Laboratories (stock no. 005680), and *Depdc5*$^{F/F}$ mice were collected from the European Mouse Mutant Archive (EM:10459). *Tsc1*$^{F/F}$ *Depdc5*$^{F/F}$ double knockout mice were generated by interbreeding, and progeny were subsequently crossed with Ckm-Cre mice to produce skeletal muscle–specific knockout animals. All mice were maintained under protocols

approved by the University of Michigan Institutional Animal Care and Use Committee (IACUC). To minimize batch effects, four control and four knockout littermates were selected for tissue harvest. Immediately after dissection, muscle tissues were embedded in O.C.T. compound (23-730-571, Fisher Scientific) and snap-frozen in liquid nitrogen–cooled 2-methylbutane (MX0760, Sigma-Aldrich).

Seq-Scope array production (1st-Seq)

Seq-Scope procedures were described in detail previously (30,31). Seq-Scope is a solid-phase transcriptome spatial capture system that has undergone several upgrades. The latest version was built upon Illumina NovaSeq 6000 platform with a 7 mm × 7 mm imaging area. Barcoded capture probe clusters on the array surface were generated using HDMI32-DraI, a custom single-stranded oligonucleotide library (IDT), and Read1-DraI sequencing primer through a sequence-by-synthesis strategy. The sequencing output FASTQ file generated during array construction contained the barcode sequences and their corresponding XY coordinates.

The array originated from Illumina NovaSeq 6000 flow cell contains four channels with 7 mm × 70 mm imaging areas. Arrays were split and diced into suitable sizes for storage and experimental use. Before application, arrays required several preprocessing steps. Arrays were first washed three times with nuclease-free water, followed by overnight incubation at 37 °C with a DraI (R0129, NEB) / CIAP (M0525, NEB) enzyme mixture. The following day, arrays were treated with Exonuclease I (M2903, NEB) for 45 min at 37 °C, then washed sequentially: three times with nuclease-free water, three times with 0.1 N NaOH for 5 min each, and three times with 0.1 M Tris (pH 7.5).

Seq-Scope spatial transcriptome library generation and sequencing (2nd-Seq)

Seq-Scope library generation was performed according to our previous paper (30). OCT-mounted frozen muscle blocks stored at –80 °C were equilibrated in a cryostat (Leica CM3050S) at –15 °C for 1 h prior to sectioning. Sections were cut at 10 μm thickness with a 5° cutting angle and placed onto cold Seq-Scope arrays, then warmed to room temperature to promote tight attachment. Tissue fixation was performed on the array with 4% formaldehyde (15170, Electron Microscopy Sciences) at room temperature for 10 min, followed by three PBS washes. Sections were then co-stained with DAPI (Invitrogen, D21490) and Alexa Fluor-488 WGA (Invitrogen,

W11261) for 15 min at room temperature, washed three times with PBS, mounted in 5% glycerol, and imaged on a Keyence digital darkroom system for whole-tissue DAPI/WGA capture. The coverslip was then gently removed to avoid tissue damage, after which hematoxylin and eosin (H&E) staining was performed and whole-tissue H&E images were captured with a Keyence microscope.

Tissue permeabilization was carried out by incubating sections with 0.2 U/μL collagenase I (17018-029, Thermo Fisher) at 37 °C for 20 min, followed by 1 mg/mL pepsin (P7000, Sigma) in 0.1 M HCl at 37 °C for 10 min. Reverse transcription was performed between the permeabilized tissue and array surface using an RT mixture [1× RT buffer (EP0751, Thermo Fisher), 4% Ficoll PM-400 (F4375-10G, Sigma), 1 mM dNTPs (N0477L, NEB), RNase inhibitor (30281, Lucigen), Maxima H-RTase (EP0751, Thermo Fisher)] and incubated overnight at 42 °C in a humidified chamber. The following day, unbound single-stranded DNA probes were digested with Exonuclease I (M2903, NEB). Tissue was removed by incubation with a digestion cocktail (100 mM Tris, pH 8.0; 100 mM NaCl; 2% SDS; 5 mM EDTA; 16 U/mL Proteinase K, P8107S, NEB) at 37 °C for 40 min. Arrays were then washed three times each with nuclease-free water, 0.1 N NaOH (5 min per wash), and 0.1 M Tris, pH 7.5.

Library generation was performed immediately after washing. Arrays were incubated for 2 h at 37 °C in a humidified chamber with a library synthesis mixture [1× NEBuffer-2 (NEB), 10 μM TruSeq Read2-conjugated random primer (IDT), 1 mM dNTPs (N0477, NEB), Klenow Fragment (M0212, NEB), nuclease-free water]. The arrays were then washed with nuclease-free water, and libraries were collected twice by 0.1 N NaOH elution (5 min each). Eluates were neutralized with 3 M potassium acetate, pH 5.5, and purified with AMPure XP beads (1.2× bead/sample ratio, A63881, Beckman Coulter) according to the manufacturer's instructions.

Libraries were amplified in two rounds of PCR using Kapa HiFi HotStart ReadyMix (KK2602, KAPA Biosystems). The first round used 2 μM TruSeq forward and reverse primers as described previously (30,31), and products were purified with AMPure XP beads (1× bead/sample ratio). In the second round, TruSeq indexing primers were applied, and products were size selected with AMPure XP beads (0.6× bead/sample ratio). Library quality was assessed on an Agilent 2100 Bioanalyzer (Agilent), with additional purification performed if necessary. Final libraries were sequenced using paired-end 100-cycle reads.

Raw data processing

Seq-Scope data processing was using the NovaScope pipeline, as described in detail previously (30). 1st-Seq data table was generated from the 1st-Seq FASTQ files, containing array region lookup indices, quality-filtered barcode sequences, and corresponding spatial coordinates. The 2nd-Seq FASTQ reads were then processed against this table by (i) assigning array indices through region lookup, (ii) mapping reads to the spatial barcode map using spatial barcode sequences (HDMI), (iii) filtering barcoded reads with validated barcode sequences, and (iv) assigning spatial coordinates to the identified reads. Reads with assigned spatial information were aligned to the genome using STAR (50), and a spatial digital gene expression (SGE) matrix was generated.

Histology and SGE alignment

H&E images were aligned to SGE matrix using the *historef* package (version 0.1.3), which detects fiducial marks visible in both modalities to guide image registration, as described previously (30). DAPI/WGA images were subsequently aligned to the processed H&E images using Georeferencer function in QGIS (version 3.22.9).

Myofiber segmentation and hexagon gridding

Myofiber segmentation was performed in Cellpose (51) using WGA-stained myofiber membranes as input. A custom segmentation model was trained to optimize fiber identification, and manual adjustments were applied when necessary. Segmentation masks generated by Cellpose were exported as NumPy arrays and processed with custom Python scripts to label and isolate individual fibers. Transcripts within each segmented myofiber were aggregated and stored as an aggregated spatial digital gene expression matrix. Longitudinal and oblique myofibers, which are minimally presented within the cross sections, were ruled out during pixel size counting.

For non-myocyte analysis, spatial hexagon grids (24 μm, non-overlapping) were generated using NovaScope, where transcripts within each grid were aggregated and treated as a single unit, with spatial coordinates assigned to the hexagon center.

Data Analysis and Visualization

Single-myofiber datasets were analyzed using Seurat package (52,53). Myofibers with low feature counts (nFeature cutoff: 200) were removed to optimize clustering performance. Each batch was normalized with SCTransform, and datasets were integrated using SCT-normalized values. Principal components were calculated using the RunPCA function, and high-quality components were selected to generate UMAP embeddings, followed by cluster identification with the FindNeighbors and FindClusters functions. Myofiber clusters were annotated based on marker gene expression, and unique transcript signatures were identified with the FindMarkers and FindAllMarkers functions.

Gene ontology enrichment analysis was performed with ClusterProfiler (54) using the org.Mm.eg.db annotation (Carlson, M., Bioconductor). Data visualization was supported by various R packages including Seurat, ggplot2, ggvenn (Yan, G., version 0.1.10), ggVennDiagram (55), ComplexUpset (krassowski, M., version 1.3.3), ComplexHeatmap (56) and enrichplot (54). Spatial myofiber projections were generated from segmentation NumPy arrays using custom python scripts. Raw spatial gene expression was visualized with a custom software platform that displayed both histology and the SGE matrix.

Hexagon-based spatial transcriptomes (24 μm non-overlapping grids) were analyzed independently without dataset integration, primarily to detect non-myocytes. Each hexagon was treated as a single cell. Normalization and clustering were performed in Seurat using SCTransform, RunPCA, and RunUMAP function, followed by marker-based annotation.

Statistics

Genes significantly upregulated in mutant muscle comparing to control muscle were first filtered using stringent cutoffs on expression level and fold-change, followed by systematic classification on fiber types using a combination of Kruskal–Wallis and pairwise Wilcoxon tests. The Kruskal–Wallis test identified genes with significantly higher expression in their top-expressing fiber type, thereby defining fiber type–specific signatures (adjusted p.value < 0.05). The Pairwise Wilcoxon tests were subsequently conducted to compare expression levels across fiber types, allowing us to define partially shared gene groups as well as globally enriched transcripts (adjusted p.value < 0.05).

Immunohistochemistry

Frozen muscle sections were equilibrated to room temperature before processing. Sections were permeabilized with 0.5% Triton X-100 in PBS for 5 min, followed by three PBS washes (5 min each). Fiber-type immunostaining was performed using the Mouse on Mouse (M.O.M.) Immunodetection Kit (VectorLabs, BMK-2202) according to the manufacturer's instructions. Briefly, sections were incubated overnight at 4 °C with M.O.M. Mouse Ig Blocking Reagent, then with primary antibodies diluted in M.O.M. Diluent at optimized concentrations. Alexa Fluor–conjugated secondary antibodies (Invitrogen) were diluted in M.O.M. Diluent and applied for 60 min at room temperature. For membrane visualization, sections were incubated with Alexa Fluor 488–conjugated WGA (Invitrogen, W11261) for 10 min prior to mounting with ProLong Gold Antifade Mountant (Invitrogen, P36934). Images were acquired using a Zeiss LSM 980 confocal microscope equipped with an Airyscan 2 detector (Carl Zeiss Microscopy). Primary antibodies: BA-D5 (MF1), SC-71 (MF2A), BF-F3 (MF2B) were acquired from Developmental Studies Hybridoma Bank (DSHB), University of Iowa. ACTC1 (66125-1-IG) and MYL4 (67533-1-IG) were purchased from ProteinTech. UCHL1 (PA5-29012) and IGFBP5 (PA5-37369) were purchased from Invitrogen. SQSTM1/p62 (5114) were purchased from Cell Signaling.

3.6 References

1. Schiaffino S, Reggiani C. Fiber Types in Mammalian Skeletal Muscles. Physiol Rev. 2011;91(4):1447-531.

2. Pette D, Staron RS. Myosin isoforms, muscle fiber types, and transitions. Microsc Res Tech. 2000;50(6):500-9.

3. Zoncu R, Efeyan A, Sabatini DM. mTOR: from growth signal integration to cancer, diabetes and ageing. Nat Rev Mol Cell Biol. 2011;12(1):21-35.

4. Dibble CC, Manning BD. Signal integration by mTORC1 coordinates nutrient input with biosynthetic output. Nat Cell Biol. 2013;15(6):555-64.

5. Bar-Peled L, Chantranupong L, Cherniack AD, Chen WW, Ottina KA, Grabiner BC, et al. A tumor suppressor complex with GAP activity for the Rag GTPases that signal amino acid sufficiency to mTORC1. Science. 2013;340(6136):1100-6.

6. Cho CS, Kim Y, Park SR, Kim B, Davis C, Hwang I, et al. Simultaneous loss of TSC1 and DEPDC5 in skeletal and cardiac muscles produces early-onset myopathy and cardiac

dysfunction associated with oxidative damage and SQSTM1/p62 accumulation. Autophagy. 2022;18(10):2303-22.

7. Graber TG, Fry CS, Brightwell CR, Moro T, Maroto R, Bhattarai N, et al. Skeletal muscle–specific knockout of DEP domain containing 5 protein increases mTORC1 signaling, muscle cell hypertrophy, and mitochondrial respiration. J Biol Chem. 2019;294(11):4091-102.

8. Castets P, Lin S, Rion N, Di Fulvio S, Romanino K, Guridi M, et al. Sustained activation of mTORC1 in skeletal muscle inhibits constitutive and starvation-induced autophagy and causes a severe, late-onset myopathy. Cell Metab. 2013;17(5):731-44.

9. Kim J, Kundu M, Viollet B, Guan KL. AMPK and mTOR regulate autophagy through direct phosphorylation of Ulk1. Nat Cell Biol. 2011;13(2):132-41.

10. Ghosh J, Kapur R. Role of mTORC1-S6K1 signaling pathway in regulation of hematopoietic stem cell and acute myeloid leukemia. Exp Hematol. 2017;50:13-21.

11. Holz MK, Ballif BA, Gygi SP, Blenis J. mTOR and S6K1 mediate assembly of the translation preinitiation complex through dynamic protein interchange and ordered phosphorylation events. Cell. 2005;123(4):569-80.

12. Bodine SC. The role of mTORC1 in the regulation of skeletal muscle mass. Fac Rev. 2022;11:32.

13. Bentzinger CF, Romanino K, Cloëtta D, Lin S, Mascarenhas JB, Oliveri F, et al. Skeletal muscle-specific ablation of raptor, but not of rictor, causes metabolic changes and results in muscle dystrophy. Cell Metab. 2008;8(5):411-24.

14. Cho CS, Kowalsky AH, Namkoong S, Park SR, Wu S, Kim B, et al. Concurrent activation of growth factor and nutrient arms of mTORC1 induces oxidative liver injury. Cell Discov. 2019;5(1):60.

15. Kedlian VR, Wang Y, Liu T, Chen X, Bolt L, Tudor C, et al. Human skeletal muscle aging atlas. Nat Aging. 2024;4(5):727-44.

16. Walter LD, Orton JL, Ntekas I, Fong EHH, Maymi VI, Rudd BD, et al. Transcriptomic analysis of skeletal muscle regeneration across mouse lifespan identifies altered stem cell states. Nat Aging. 2024;4(12):1862-81.

17. Petrany MJ, Swoboda CO, Sun C, Chetal K, Chen X, Weirauch MT, et al. Single-nucleus RNA-seq identifies transcriptional heterogeneity in multinucleated skeletal myofibers. Nat Commun. 2020;11(1):6374.

18. De Micheli AJ, Spector JA, Elemento O, Cosgrove BD. A reference single-cell transcriptomic atlas of human skeletal muscle tissue reveals bifurcated muscle stem cell populations. Skelet Muscle. 2020;10(1):19.

19. Oprescu SN, Yue F, Qiu J, Brito LF, Kuang S. Temporal Dynamics and Heterogeneity of Cell Populations during Skeletal Muscle Regeneration. iScience. 2020;23(4):100993.

20. De Micheli AJ, Laurilliard EJ, Heinke CL, Ravichandran H, Fraczek P, Soueid-Baumgarten S, et al. Single-Cell Analysis of the Muscle Stem Cell Hierarchy Identifies Heterotypic Communication Signals Involved in Skeletal Muscle Regeneration. Cell Rep. 2020;30(10):3583-3595.e5.

21. Rubenstein AB, Smith GR, Raue U, Begue G, Minchev K, Ruf-Zamojski F, et al. Single-cell transcriptional profiles in human skeletal muscle. Sci Rep. 2020;10:229.

22. Scripture-Adams DD, Chesmore KN, Barthélémy F, Wang RT, Nieves-Rodriguez S, Wang DW, et al. Single nuclei transcriptomics of muscle reveals intra-muscular cell dynamics linked to dystrophin loss and rescue. Commun Biol. 2022;5:989.

23. Giordani L, He GJ, Negroni E, Sakai H, Law JYC, Siu MM, et al. High-Dimensional Single-Cell Cartography Reveals Novel Skeletal Muscle-Resident Cell Populations. Mol Cell. 2019;74(3):609-621.e6.

24. Xi H, Langerman J, Sabri S, Chien P, Young CS, Younesi S, et al. A Human Skeletal Muscle Atlas Identifies the Trajectories of Stem and Progenitor Cells across Development and from Human Pluripotent Stem Cells. Cell Stem Cell. 2020;27(1):158-176.e10.

25. Saleh KK, Xi H, Switzler C, Skuratovsky E, Romero MA, Chien P, et al. Single cell sequencing maps skeletal muscle cellular diversity as disease severity increases in dystrophic mouse models. iScience. 2022;25(11):105415.

26. Ham AS, Lin S, Tse A, Thürkauf M, McGowan TJ, Jörin L, et al. Single-nuclei sequencing of skeletal muscle reveals subsynaptic-specific transcripts involved in neuromuscular junction maintenance. Nat Commun. 2025;16:2220.

27. Chen L, Kong X, Johnston KG, Mortazavi A, Holmes TC, Tan Z, et al. Single-cell spatial transcriptomics reveals a dystrophic trajectory following a developmental bifurcation of myoblast cell fates in facioscapulohumeral muscular dystrophy. Genome Res. 2024;34(5):665-79.

28. Dos Santos M, Backer S, Saintpierre B, Izac B, Andrieu M, Letourneur F, et al. Single-nucleus RNA-seq and FISH identify coordinated transcriptional activity in mammalian myofibers. Nat Commun. 2020;11(1):5102.

29. Wang YX, Holbrook CA, Hamilton JN, Garoussian J, Afshar M, Su S, et al. A single cell spatial temporal atlas of skeletal muscle reveals cellular neighborhoods that orchestrate regeneration and become disrupted in aging. bioRxiv. 2022.

30. Kim Y, Cheng W, Cho CS, Hwang Y, Si Y, Park A, et al. Seq-Scope: repurposing Illumina sequencing flow cells for high-resolution spatial transcriptomics. Nat Protoc. 2025;20(3):643-89.

31. Cho CS, Xi J, Si Y, Park SR, Hsu JE, Kim M, et al. Microscopic examination of spatial transcriptome using Seq-Scope. Cell. 2021;184(13):3559-3572.e22.

32. Tang H, Inoki K, Brooks SV, Okazawa H, Lee M, Wang J, et al. mTORC1 underlies age-related muscle fiber damage and loss by inducing oxidative stress and catabolism. Aging Cell. 2019;18(3):e12943.

33. Talbot J, Maves L. Skeletal muscle fiber type: using insights from muscle developmental biology to dissect targets for susceptibility and resistance to muscle disease. Wiley Interdiscip Rev Dev Biol. 2016;5(4):518-34.

34. Gao H, Freeling J, Wu P, Liang AP, Wang X, Li Y. UCHL1 regulates muscle fibers and mTORC1 activity in skeletal muscle. Life Sci. 2019;233:116699.

35. Gao H, Hartnett S, Li Y. Ubiquitin C-Terminal Hydrolase L1 regulates myoblast proliferation and differentiation. Biochem Biophys Res Commun. 2017;492(1):96-102.

36. Meyer GA. Evidence of induced muscle regeneration persists for years in the mouse. Muscle Nerve. 2018;58(6):858-62.

37. Hastings RL, Massopust RT, Haddix SG, Lee Y il, Thompson WJ. Exclusive vital labeling of myonuclei for studying myonuclear arrangement in mouse skeletal muscle tissue. Skelet Muscle. 2020;10(1):15.

38. Neerunjun JS, Dubowitz V. Concomitance of basophilia, ribonucleic acid and acid phosphatase activity in regenerating muscle fibres. J Neurol Sci. 1977;33(1-2):95-109.

39. Wynn TA, Vannella KM. Macrophages in Tissue Repair, Regeneration, and Fibrosis. Immunity. 2016;44(3):450-62.

40. Tidball JG. Regulation of muscle growth and regeneration by the immune system. Nat Rev Immunol. 2017;17(3):165-78.

41. Wosczyna MN, Rando TA. A Muscle Stem Cell Support Group: Coordinated Cellular Responses in Muscle Regeneration. Dev Cell. 2018;46(2):13-43.

42. Folker ES, Baylies MK. Nuclear positioning in muscle development and disease. Front Physiol. 2013;4:363.

43. Dubowitz V, Sewry CA, Oldfors A. Muscle biopsy: a practical approach. Fifth edition. Elsevier; 2021.

44. Mendias CL, Marcin JE, Calerdon DR, Faulkner JA. Contractile Properties of EDL and Soleus Muscles of Myostatin-Deficient Mice. J Appl Physiol Bethesda Md 1985. 2006;101(3):898-905.

45. Moens P, Baatsen PH, Maréchal G. Increased susceptibility of EDL muscles from mdx mice to damage induced by contractions with stretch. J Muscle Res Cell Motil. 1993;14(4):446-51.

46. Carvalho AJ, McKee NH, Green HJ. Metabolic and contractile responses of fast and slow twitch rat skeletal muscles to ischemia and reperfusion. Plast Reconstr Surg. 1997;99(1):163-71.

47. Goodman CA. The role of mTORC1 in regulating protein synthesis and skeletal muscle mass in response to various mechanical stimuli. Rev Physiol Biochem Pharmacol. 2014;166:43-95.

48. Herbison GJ, Jaweed MM, Ditunno JF. Muscle fiber types. Arch Phys Med Rehabil. 1982;63(5):227-30.

49. Qaisar R, Bhaskaran S, Van Remmen H. Muscle fiber type diversification during exercise and regeneration. Free Radic Biol Med. 2016;98:56-67.

50. Dobin A, Davis CA, Schlesinger F, Drenkow J, Zaleski C, Jha S, et al. STAR: ultrafast universal RNA-seq aligner. Bioinformatics. 2013;29(1):15-21.

51. Stringer C, Wang T, Michaelos M, Pachitariu M. Cellpose: a generalist algorithm for cellular segmentation. Nat Methods. 2021;18(1):100-6.

52. Hao Y, Hao S, Andersen-Nissen E, Mauck WM, Zheng S, Butler A, et al. Integrated analysis of multimodal single-cell data. Cell. 2021;184(13):3573-3587.e29.

53. Stuart T, Butler A, Hoffman P, Hafemeister C, Papalexi E, Mauck WM, et al. Comprehensive Integration of Single-Cell Data. Cell. 2019;177(7):1888-1902.e21.

54. Wu T, Hu E, Xu S, Chen M, Guo P, Dai Z, et al. clusterProfiler 4.0: A universal enrichment tool for interpreting omics data. The Innovation. 2021;2(3):100141.

55. Gao CH, Yu G, Cai P. ggVennDiagram: An Intuitive, Easy-to-Use, and Highly Customizable R Package to Generate Venn Diagram. Front Genet. 2021;12:706907.

56. Gu Z, Eils R, Schlesner M. Complex heatmaps reveal patterns and correlations in multidimensional genomic data. Bioinformatics. 2016;32(18):2847-9.

Chapter 4 Conclusions and Future Directions

4.1 Summary

Spatial transcriptomics is a powerful approach for systematically profiling cellular RNA expression within intact tissue, revealing critical information that is otherwise masked by histological architecture (1). In this thesis, I described the development and methodology of Seq-Scope, a cutting-edge spatial transcriptomics platform established in our laboratory (2,3). Seq-Scope enables unbiased transcript capture while maintaining sub-micrometer resolution, offering a comprehensive single-cell spatial view of gene expression. I also presented four applications of Seq-Scope in pathophysiology, covering skin acne (4), liver senescence, muscle denervation (5), and mTORC1-driven myopathies (6), described at different levels of depth. Together, these studies demonstrated the versatility of Seq-Scope as both a technology and a discovery tool, while also inspiring important follow-up questions in different aspects.

4.2 The future of Seq-Scope: beyond spatial transcriptomics

The field of spatial omics has expanded rapidly over the past decade (7). Researchers have increasingly sought to incorporate spatial context into omics studies as the complexity and heterogeneity of tissue microenvironments become more evident. As both a contributor to and a competitor in spatial transcriptomics, Seq-Scope has achieved unprecedented resolution while remaining relatively straightforward to implement in other laboratories (2,3). Still, it is important to acknowledge a key limitation of Seq-Scope: it currently operates primarily within the transcriptomic space, whereas other platforms have advanced toward integrated multi-omics capabilities (8–10).

The expansion of Seq-Scope is necessary and ongoing. We proposed redesigning the Seq-Scope first-seq synthetic library that is capable of incorporating additional probes beyond the original poly(A)-capture probe. By modifying the capture head of these add-on probes, Seq-Scope can be adapted to collect information beyond the host poly(A) transcriptome. Over the

past few years, several promising projects branching from the standard Seq-Scope workflow have been initiated.

(i) *Seq-Scope CRISPR-Cas9 in situ screening*. CRISPR screening has become a well-established approach for studying the expansion of somatic mutations that drive cancer progression (11,12). In this system, researchers deliver pooled sgRNA libraries into Cas9-expressing mice, generating single-gene deletions in individual cells. Over time, cells harboring advantageous deletions expand within the target tissue, often accompanied by additional mutations acquired during uncontrolled proliferation, eventually giving rise to malignant tumor microenvironments. This powerful technology has provided valuable insights into somatic mutation biology. However, the equally important spatial context underlying these processes remains largely inaccessible. One potential solution is to design add-on probes within the Seq-Scope platform that target conserved regions of sgRNAs used in CRISPR systems. By applying sgRNA-Cas9 tissues to a customized Seq-Scope array, it would become possible to capture not only the identity of the sgRNA within a given cell, but also that cell's transcriptome together with the transcriptomes of surrounding cells. This integration would enable in situ identification of transcriptional shifts associated with specific knockouts by directly linking each cell's transcriptome to its corresponding sgRNA sequence.

(ii) *Seq-Scope Microbiome.* Microbiota are increasingly recognized as critical regulators of physiology, participating in diverse processes across tissues ranging from barrier surfaces such as the skin and colon to more protected organs such as the brain. However, due to the current limitation in technology, it is still challenging to grasp the complex regulatory interactions mediated by diverse microbial populations. Here, we propose extending Seq-Scope into this area, where it could provide a powerful framework for simultaneously capturing microbial identity and host transcriptional responses. By designing add-on probes targeting conserved regions of bacterial 16S rRNA (13,14), Seq-Scope could enable simultaneous spatial profiling of gut microbiota composition and host transcriptomes. This combined readout would provide a framework for examining microbiome-host crosstalk within intact tissue contexts.

(iii) *Seq-Scope Epitranscriptome.* A major limitation of Seq-Scope is its current restriction to transcriptomic profiling. Yet studies have shown that post-transcriptional, or epi-transcriptional, modifications can be just as important as transcript abundance in shaping cellular physiology. In this thesis, I further propose extending Seq-Scope into the epitranscriptomic

space. Achieving this goal would require substantial modification of the standard workflow, because epitranscriptional marks on mRNA cannot be directly preserved through conventional reverse transcription into complementary DNA. Rather than reverse-transcribing cDNA directly on the barcoded probe, as in the original setup, we propose building the spatial barcodes onto the probe-bound mRNA itself. This strategy would preserve endogenous RNA modifications while spatially barcoding the transcripts, thereby enabling downstream isolation of modified RNAs through immunoprecipitation-based methods such as methylated RNA immunoprecipitation (meRIP) (15). The locations of these modifications on transcripts could be further resolved using artificial bases and specialized polymerases during library construction. If successful, this technological upgrade would allow Seq-Scope to extend into the epitranscriptomic space and provide an additional layer of information on cellular regulatory mechanisms.

While these projects remain technically challenging and are progressing at a slower pace, it is important to note that each carries tremendous potential to advance its corresponding field. If successful, these efforts would further elevate Seq-Scope as a leading platform and substantially broaden its impact across the spatial omics landscape.

4.3 Muscle atlas and muscular microenvironments

In Chapter 2, this thesis describes the construction of a rodent skeletal muscle atlas and the discovery of myofiber and sub-myofiber heterogeneity during denervation (5). While this work provided the first comprehensive view of skeletal muscle transcriptomic organization, it is fully acknowledged as exploratory and therefore limited in mechanistic insight. Follow-up investigations in multiple directions could be established. For instance, the identification of fiber-type-specific stress responses during denervation motivates studies aimed at defining how and why distinct myofiber types exhibit divergent responses. In addition, the localized transcriptional shifts at the neuromuscular junction could inspire research explaining the drivers of regionally enriched extracellular matrix remodeling programs. Overall, the work presented here is not the final answer of muscle physiology, but a foundation on which future mechanistic studies can build upon.

4.4 mTORC1 hyperactivation-driven myopathies

In Chapter 3, this thesis documents the integration of histopathology and transcriptomics to dissect muscle pathophysiology in a rodent model of sustained mTORC1 hyperactivation (6). This study is distinctive in that it linked morphological outcomes to molecular states at single-fiber resolution. A central finding is the divergent fate of type IIx fibers across muscles: hypertrophy accompanied by impaired proteostasis in soleus, versus basophilia associated with lipid-supported respiration and RNA accumulation in EDL. Compared with the earlier chapters, these results provide clearer mechanistic insight into how sustained mTORC1 signaling reshapes myofiber states.

Important questions remain regarding the drivers of these two trajectories. One possibility is that differences in fiber-type compositions between soleus and EDL create distinct microenvironments that drives myofiber type IIx toward different pathological outcomes. Future studies could test this idea through targeted interventions that alter muscle identity, such as co-transfecting *Six1* and *Eya1* expression vectors into soleus to induce a slow-to-fast transition. This manipulation has been reported to promote replacement of MyHC I/IIa with faster isoforms, activate fast-fiber gene programs, and shift metabolism toward glycolysis (16).

4.5 Perspectives

This thesis introduces Seq-Scope as a scalable spatial transcriptomics technology with subcellular-level resolution and shows how it can connect tissue histology to underlying regulatory programs. Through case studies in skin acne, liver senescence, and skeletal muscle biology and pathology, the work lays out a broadly applicable strategy to map how gene expression is regulated inside cells, among cell populations, and within local microenvironments in health and disease.

4.6 References

1. Ståhl PL, Salmén F, Vickovic S, Lundmark A, Navarro JF, Magnusson J, et al. Visualization and analysis of gene expression in tissue sections by spatial transcriptomics. Science. 2016;353(6294):78–82.

2. Kim Y, Cheng W, Cho CS, Hwang Y, Si Y, Park A, et al. Seq-Scope: repurposing Illumina sequencing flow cells for high-resolution spatial transcriptomics. Nat Protoc. 2025;20(3):643–89.

3. Cho CS, Xi J, Si Y, Park SR, Hsu JE, Kim M, et al. Microscopic examination of spatial transcriptome using Seq-Scope. Cell. 2021;184(13):3559-3572.e22.

4. Do TH, Ma F, Andrade PR, Teles R, Silva BJ de A, Hu C, et al. TREM2 macrophages induced by human lipids drive inflammation in acne lesions. Sci Immunol. 2022;7(73):eabo2787.

5. Hsu JE, Ruiz L, Hwang Y, Guzman S, Cho CS, Cheng W, et al. High-Resolution Spatial Transcriptomic Atlas of Mouse Soleus Muscle: Unveiling Single Cell and Subcellular Heterogeneity in Health and Denervation. bioRxiv; 2024.

6. Hsu JE, Zhao Q, Cheng W, Kang HM, Brooks SV, Kim M, et al. Histopathology and spatial transcriptomics jointly map myofiber-specific pathological programs in mTORC1-driven myopathy. BioRxiv Prepr Serv Biol. 2025;2025.12.03.692123.

7. Marx V. Method of the Year: spatially resolved transcriptomics. Nat Methods. 2021;18(1):9–14.

8. Russell AJC, Weir JA, Nadaf NM, Shabet M, Kumar V, Kambhampati S, et al. Slide-tags enables single-nucleus barcoding for multimodal spatial genomics. Nature. 2024;625(7993):101–9.

9. Liu Y, Yang M, Deng Y, Su G, Enninful A, Guo CC, et al. High-Spatial-Resolution Multi-Omics Sequencing via Deterministic Barcoding in Tissue. Cell. 2020;183(6):1665-1681.e18.

10. Zhang D, Deng Y, Kukanja P, Agirre E, Bartosovic M, Dong M, et al. Spatial epigenome–transcriptome co-profiling of mammalian tissues. Nature. 2023;616(7955):113–22.

11. Replogle JM, Norman TM, Xu A, Hussmann JA, Chen J, Cogan JZ, et al. Combinatorial single-cell CRISPR screens by direct guide RNA capture and targeted sequencing. Nat Biotechnol. 2020;38(8):954–61.

12. Zhu M, Lu T, Jia Y, Luo X, Gopal P, Li L, et al. Somatic Mutations Increase Hepatic Clonal Fitness and Regeneration in Chronic Liver Disease. Cell. 2019;177(3):608-621.e12.

13. Lötstedt B, Stražar M, Xavier R, Regev A, Vickovic S. Spatial host–microbiome sequencing reveals niches in the mouse gut. Nat Biotechnol. 2024;42(9):1394–403.

14. Saarenpää S, Shalev O, Ashkenazy H, Carlos V, Lundberg DS, Weigel D, et al. Spatial metatranscriptomics resolves host–bacteria–fungi interactomes. Nat Biotechnol. 2024;42(9):1384–93.

15. Liu J, Li K, Cai J, Zhang M, Zhang X, Xiong X, et al. Landscape and Regulation of m6A and m6Am Methylome across Human and Mouse Tissues. Mol Cell. 2020;77(2):426-440.e6.

16. Grifone R, Laclef C, Spitz F, Lopez S, Demignon J, Guidotti JE, et al. Six1 and Eya1 Expression Can Reprogram Adult Muscle from the Slow-Twitch Phenotype into the Fast-Twitch Phenotype. Mol Cell Biol. 2004;24(14):6253–67.